TECHNISCHE UNIVERSITÄT WIEN

Dissertation

Enhancement of Biomechanical and Morphometric Tools for the Inference of Habitual Activity from Bone Microstructure

carried out for the purpose of obtaining the degree Doctor technicae (Dr.techn.), submitted at TU Wien, Faculty of Mechanical and Industrial Engineering, by

Dipl.-Ing. Sebastian BACHMANN, BSc

Immatriculation Number: 00925947

under the supervision of

Univ.Prof. Dipl.-Ing. Dr.techn. Dieter H. PAHR

Institute of Lightweight Design and Structural Biomechanics, E317

Vienna, January 2023

reviewed by

Sen.Lect. Enrico DALL'ARA, PhD
Department of Oncology and Metabolism
Insigneo Institute for In Silico Medicine
University of Sheffield, United Kingdom

Assoc.Prof. Saulo MARTELLI, PhD
School of Mechanical, Medical & Process Engineering
Queensland University of Technology, Australia

"*If bone is the answer, then what is the question?*"

Rik Huiskes

This work was supported by the European Research Council (ERC) under the European Union's Horizon 2020 research and innovation program within the framework of the project "NewHuman" (Grant Agreement No. 819960).

I confirm, that going to press of this thesis
needs the confirmation of the examination committee.

Affidavit

I declare in lieu of oath, that I wrote this thesis and performed the associated research myself, using only literature cited in this volume. If text passages from sources are used literally, they are marked as such.

I confirm that this work is original and has not been submitted elsewhere for any examination, nor is it currently under consideration for a thesis elsewhere.

I acknowledge that the submitted work will be checked electronically-technically using suitable and state-of-the-art means (plagiarism detection software). On the one hand, this ensures that the submitted work was prepared according to the high-quality standards within the applicable rules to ensure good scientific practice "Code of Conduct" at the TU Wien. On the other hand, a comparison with other student theses avoids violations of my personal copyright.

Vienna, January 2023

Sebastian Bachmann

Acknowledgements

This thesis would not have been possible without the support of countless people. Their contributions to this work are not only scientific (“*If I have seen further than others, it is by standing on the shoulders of giants*” – Isaac Newton) but also mental (“*Friendship is a wildly underrated medication*” – Anna Deavere Smith).

First and foremost, I thank my supervisor, Dieter Pahr, and co-supervisor, Alexander Synek, for their tremendous support over the past years. Without them, I probably would never have started this endeavour. Both shared their knowledge with me on many occasions and helped me to solve tricky tasks, but they were also available for a cozy chat.

I would also like to thank the members of our group, both in Vienna and Krems. I also thank all members of the ILSB (current and former!) for sharing their expertise with me and for exhilarating meetings near the coffee machine and off-work activities. It is great to have so many knowledgeable people at the institute, who you can ask about almost anything and get an answer to. Special shout-outs go to Lukas for answering many questions to bootstrap some tools used in this thesis and to Pia and Katja, who contributed exceedingly to the good working atmosphere.

During my doctorate, I met many people who were part of the “NewHuman” project. Unfortunately, all of these meetings were only possible online (eventually, there was still a pandemic going on). Nevertheless, it was always great fun in these meetings, especially (but not only!) because of our project leader Matt. Special thanks go to Chris and Marine for their time for discussions, helpful comments, and exciting projects to work on together.

A huge thanks go to all of my friends – especially Alex, Patrick, and Stefan for so many hours of joy, good food & coffee, sport-activities, and good talks. Last but not least, I thank my family for their never-ending support and uplifting words. Particularly, I want to send a large kiss to my fiancée Maria, who has encouraged me in my work and has given me the time to pursue it.

♡

Contents

List of Figures

List of Tables

List of Abbreviations

μCT micro-CT

μFE micro finite element

1D one-dimensional

2D two-dimensional

3D three-dimensional

3D GM 3D geometric morphometrics

aBMD areal bone mineral density

aDNA ancient DNA

ANN artificial neural network

BMD bone mineral density

BMU bone multicellular unit

BS bone surface

BSTV bone surface over total volume

BV bone volume

BVTV bone volume over total volume

CCC concordance correlation coefficient

cHMA canonical holistic morphometric analysis

CPU central processing unit

CT computed tomography

Ct.Ar cortical area

Ct.Po cortical porosity

Ct.Th cortical thickness

CV coefficient of variation

DA degree of anisotropy

DEXA dual-energy X-ray absorptiometry

DMR dorsal metacarpal ridge

DNA deoxyribonucleic acid

DoF degrees of freedom

FE finite element

FEA finite element analysis

FWER family-wise error-rate

HA hydroxyapatite

hFE homogenised finite element

HMA holistic morphometric analysis

HR-pQCT high resolution peripheral quantitative CT

IBR inverse bone remodelling

KUBC kinematic uniform boundary condition

LCN lacuno-canalicular network

MRI magnetic resonance imaging

MSD mean surface distance

MV marrow volume

n-μCT neutron μCT

PCA principal component analysis

PMUBC periodicity compatible mixed uniform boundary condition

PVE partial volume effect

QCT quantitative CT

QUS quantitative ultrasound

rBVTV relative bone volume over total volume

RFT random field theory

RMSE root mean squared error

ROI region of interest

RVE representative volume element

SDM statistical deformation model

SDTM statistical deformation and texture model

SED strain energy density

SR-μCT synchrotron-radiation μCT

STL StereoLithography

Tb.N trabecular number

Tb.Sp trabecular spacing

Tb.Th trabecular thickness

TMD tissue mineral density

TV total volume

VE volume element

VOI volume of interest

Abstract

Motivation. Many bones contain a microstructure, consisting of struts and plates, called trabecular bone. The microstructure is influenced by external loading and deteriorates when no loading is applied but can also be increased by training - similar to muscles. Consequently, countless analysis methods were developed. Commonly known application are related to medical diagnosis, for instance to find pathological changes that make a bone more susceptible to fractures. But also other disciplines such as evolutionary anthropology use these methods. The reason is, that often the only remains of extinct species are their bones. These bones can tell many stories, as the bone stores - to some extent - the daily activities in its microstructure. By analysing this microstructure, it is possible to infer the habitual physical activities of unknown individuals by using comparative samples with known behavioural patterns. Thus, we can learn about the behaviour and habitual activities of long extinct species, for example early humans.

State of the art. The microstructure of bone is typically measured by generating high resolution computed tomography (CT) images of a given bone and evaluating so-called morphometric indices (e.g. bone volume fraction or degree of anisotropy). Since bones vary in size and shape, these morphometric indices are often only evaluated at certain region of interest (ROI) in the bone. However, important information might be missed if only a small number of ROIs is used and the placement of ROIs at homologous points in different bones is challenging. Therefore, another method called holistic morphometric analysis (HMA) was developed to at least visualise different morphometric indices across the entire bone and thus allow to qualitatively compare bones on a holistic level. But no quantitative comparison was possible with this method so far.

A more direct approach to infer the habitual loading histories of an individual from the bone microstructure is used in inverse bone remodelling (IBR). Here, instead of comparing morphology to other samples, the actual loading history of the bone is computed from the microstructure. In contrast to ROI or HMA-based microstructural analysis, the method provides a quantitative and direct link between the entire set of bone morphometric parameters and its loading regime. The loading history predicted by this method was shown to be in good agreement with *in vivo* joint load data and was sensitive enough to even detect differences in locomotor modes of various primate species. However, the

method relies on the computationally expensive micro-finite element (μFE) analysis and therefore its application was limited to smaller bones and a few bone samples.

Objectives. This thesis had two major objectives: (1) To enhance the HMA method to enable quantitative inter-sample and inter-group comparison of bone morphometry and (2) To improve the computational efficiency of the IBR approach by translating the existing μFE-based IBR to homogenised FE (hFE). Consequently, both these objectives should illuminate the way for the linkage of both the morphometric analysis with biomechanical analysis of bone microstructure.

Developed methods & core results. The first objective was addressed by using statistical deformation models (SDM), to construct a canonical bone from a set of bones, onto which all bones of the set can be registered. This registration procedure allows to identify homologous regions and further to be able to compare indices measured with HMA directly between all samples. The new method, named canonical HMA or cHMA, was applied to hand bones and proximal femora of different primate species. The method could quantitatively confirm microstructural differences between species that were only seen qualitatively so far. In addition, previously unknown differences of the bone microstructure were uncovered and quantified.

For the second objective, a continuum-level optimisation function for IBR was developed and the parameters were identified using trabecular bone cubes and μFE-based IBR. The validity of the novel hFE-based IBR method was evaluated by comparing predicted loading histories of distal radius sections and femoral heads with those obtained using μFE-based IBR. Here, a good correlation between the two methods was found, with only minor differences of the predicted section forces or joint loadings. In exchange for the introduced error, the hFE-based IBR method reduced the runtime of the algorithm by several orders of magnitude.

Conclusions. This thesis offers two novel methods to analyse the bone microstructure on a holistic level, with the ability for quantitative and inter-sample and inter-group comparison. These methods can be used in the future for the inference of behaviour and habitual activities from the microstructure of bones, but can also be applied in other fields, such as medicine or basic biomedical research.

Kurzfassung

Motivation. Die meisten Knochen enthalten eine Mikrostruktur, auch trabekulärer Knochen genannt, bestehend aus kleinen knöchernen Balken und Platten. Diese Mikrostruktur kann durch externe mechanische Belastungen beeinflusst werden. Ähnlich wie bei Muskeln, baut sie etwa ab, wenn zu wenig belastet, kann sich jedoch auch durch Training aufbauen lassen. Um die Mikrostruktur zu analysieren wurden bereits unzählige Methoden entwickelt. Anwendungen sind etwa die Medizin, wo durch die Erkennung von pathologischen Veränderungen der Mikrostruktur, Knochenbrüche vermieden werden können. Allerdings sind auch andere Disziplinen außerhalb der Medizin an solchen Analysemethoden interessiert, etwa die evolutionäre Anthropologie. Denn obwohl meist nur noch die fossilen Knochen von bereits ausgestorbenen Spezies gefunden werden können, erzählen diese Knochen viele Geschichten über das Verhalten der Spezies zu Lebzeiten, da der Knochen - zu einem gewissen Grad - die Information über regelmäßige Aktivitäten in der Mikrostruktur abspeichert. Nun kann auf das Verhalten der bereits ausgestorbenen Spezies geschlossen werden, etwa über den Vergleich zu noch lebenden Arten und deren Verhalten. So können wir mehr über das Verhalten und die regelmäßigen Aktivitäten lernen, selbst wenn die Lebewesen schon lange ausgestorben sind, wie etwa bei Urzeitmenschen.

Stand der Technik. Die Mikrostruktur von Knochen wird typischerweise mit hochauflösender Computer Tomografie (CT) abgebildet. Auf diesen Bildern können dann morphometrische Kenngrößen gemessen werden, wie etwa die relative Dichte oder die Ausrichtung der trabekulären Struktur. Da Knochen in Form und Größe auch innerhalb einer Spezies variieren, werden diese Kenngrößen meist in definierten Auswerteregionen, so genannte “region of interest” (ROI), gemessen. Allerdings kann dabei Information verloren gehen, wenn etwa eine zu geringe Anzahl solcher Regionen verwendet wird. Außerdem ist die Positionierung dieser Regionen in Knochen verschiedener Individuen schwierig, da diese an homologen Punkten platziert werden müssen. Um die Auswertung zu verbessern, wurde die holistische Morphometrie Analyse (HMA) entwickelt, welche es erlaubt diese Kenngrößen über den gesamten Knochen zu visualisieren. Dies erlaubt zumindest qualitative, aber nicht quantitative, Vergleiche von mehreren Knochen auf einer holistischen Ebene.

Einen direkteren Ansatz, um regelmäßige Aktivitäten eines Individuums aus der Knochen-Mikrostruktur zu rekonstruieren, verwendet "Inverse Bone Remodelling" (IBR). Diese Methode, welche man am ehesten mit "Inversen Knochen-Umbau" übersetzen könnte, vergleicht nicht die Morphometrie der Individuen zu einander, sondern es wird die Belastungshistorie des Knochen aus der Knochen-Mikrostruktur zurückgerechnet. Im Gegensatz zur ROI basierten oder HMA Methode, erlaubt diese Methode einen direkten und quantitativen Zusammenhang zwischen der Morphometrie und den mechanischen Belastungen herzustellen. Es wurde bereits gezeigt, dass die vorhergesagte Belastungshistorie gut mit *in vivo* Messungen an der Hüfte übereinstimmt, und dass die Methode sensitiv genug ist, um Unterschiede in der Fortbewegung bei Primaten zu erkennen. Allerdings basiert diese Methode auf der rechenintensiven Mikro-Finite-Elemente (μFE) Methode, wodurch die bisherige Anwendung auf kleinere Knochen oder wenige Proben limitiert war.

Ziele. Diese Dissertation hatte zwei Hauptziele: (1) sollte die existierende HMA Methode um die Quantifizierbarkeit für den Vergleich von Individuen oder sogar Gruppen erweitert werden und (2) das rechenintensive μFE-basierte IBR Verfahren auf ein effizientes homogenisiertes FE (hFE) Verfahren übersetzt werden. Beide Ziele dienen damit auch einem weiteren, übergeordneten Ziel: Der zukünftigen Verbindung dieser beiden Methoden, um morphometrische und biomechanische Analyse der Mikrostruktur zu kombinieren.

Entwicklung der Methoden & Ergebnisse. Das erste Ziel wurde mit Hilfe eines statistischen Deformations-Modell (SDM) umgesetzt. Dies erlaubt aus einem Satz an Knochen einen kanonischen Knochen zu generieren, auf welchen dann alle Einzelknochen registriert werden. Dadurch können Homologien in einem automatischen Verfahren identifiziert werden und somit morphometrische Kenngrößen, welche mit HMA gemessen wurden, zwischen den Knochen zu quantifizieren. Die neue Methode, genannt Kanonisches-HMA (canonical HMA (cHMA)) wurde an Handknochen und an proximalen Femora von verschiedenen Primatenspezies angewendet. Mit der Methode konnten Unterschiede in der Mikrostruktur quantifiziert werden, welche bisher nur in qualitativer Form bekannt waren. Zudem konnten neue, bisher unbekannte, Unterschiede erkannt werden.

Um das zweite Ziel zu erreichen, wurde eine neue Zielfunktion für die IBR Methode entwickelt, welche auf der Kontinuums-Ebene funktioniert. Die Parameter der Zielfunktion wurden auf trabekulären Knochenwürfeln mittels μFE-basiertem IBR identifiziert. Die neue Methode wurde durch Vergleiche von μFE und hFE validiert, wobei die Belastungshistorien von distalen Radii und Femurköpfen verwendet wurden. In beiden Fällen konnte eine gute Korrelation zwischen μFE und hFE festgestellt werden, jedoch gab es kleine Unterschiede in der Vorhersage im Vergleich zu μFE. Die hFE-basierte Methode bietet jedoch um mehrere Größenordnungen schnellere Laufzeiten.

Fazit. In dieser Dissertation werden zwei neue Methoden zur Analyse der Mikrostruktur vorgestellt, welche die holistische Analyse und quantitative Vergleichbarkeit von Knochen mehrerer Individuen oder Gruppen erlauben. Diese Methoden können in der Zukunft dazu verwendet werden das Verhalten oder regelmäßige Aktivitäten aus der Mikrostruktur abzuleiten. Sie können aber auch in einer Vielzahl von anderen Feldern angewendet werden, wie etwa der Medizin oder der biomedizinischen Forschung.

Chapter 1

Introduction

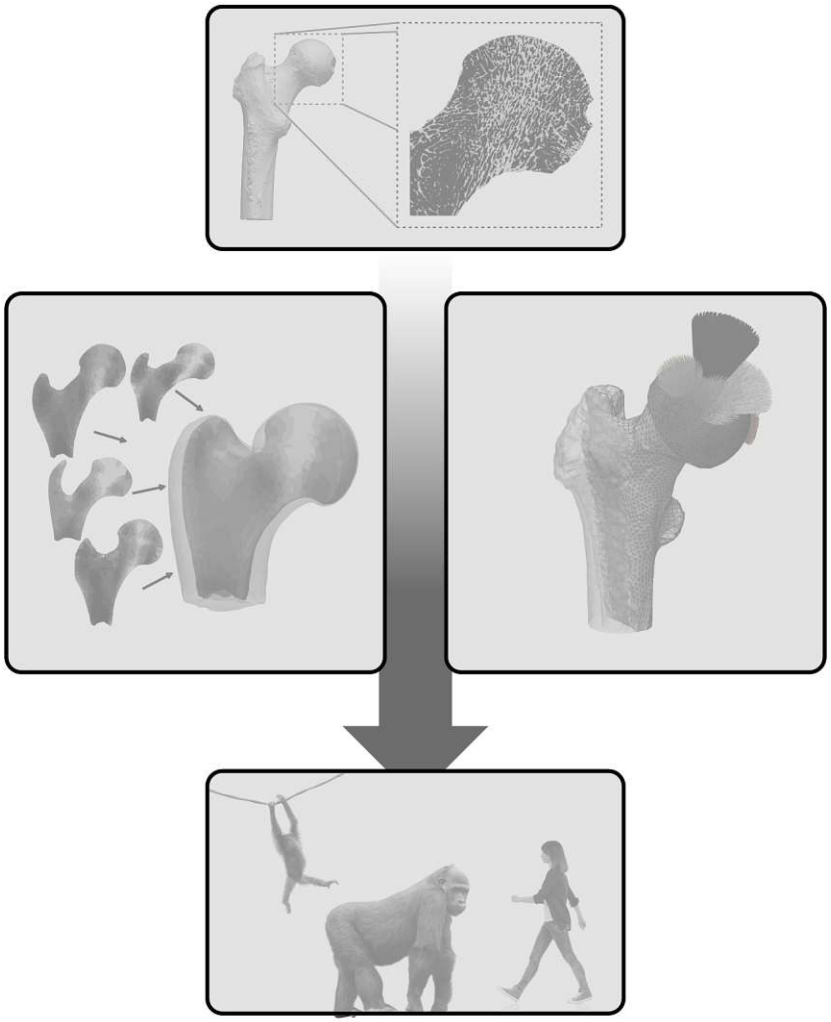

1.1 Bone Microstructure: Nature's Oldest Activity Tracker

Nearly every day fossils are found around the world. Every now and then, they turn out to be of early humans. Sometimes these findings are small sensations, as new combinations of traits are found, which were previously not known to be possible. For example, the discovery of *Homo floresiensis* [1] or *Homo naledi* [2] showed, that the human family tree is far from understood. But how can we find out where in the family tree these individuals fit in? Were these species missing links between known ancestors, adapted to niches in their environment, or simply individuals with traits beyond the known variability of the species?

The assessment of the age of the fossils is the first step to approximately pinpoint the fossil in the evolutionary timeline and determines other possible relatives from the fossil record. Finding the age, however, can be tricky [3] and the age of some fossils is still subject of scientific debate. The next question is how these fossils relate to other bones of known origin [4]. Commonly the overall shape (i.e., the anatomy) is quantified and compared to other specimens. Nowadays also elaborate analysis methods are available, such as the strontium-isotope analysis, to learn more about the diet of the creature [5] or the analysis of ancient DNA (aDNA), which can be used to actually compare genetic material [6].

Fossil age, anatomy, diet, and genetics can provide a good picture of the creature. However, it is also interesting to know which habitual physical activities the creature performed regularly during its lifetime. These habitual activities could be, for example, the preferred way of locomotion (such as quadrupedalism, climbing, or bipedalism) or if the creature regularly used tools. Habitual activities such as locomotion can, for example, explain when the human ancestors left the trees and became bipedal. These questions cannot be fully answered by already outlined methods alone. However, bones are more than their outer shape and also contain a microstructure.

Bone itself is a very interesting biological material, that has to withstand high forces during daily activities but must also be lightweight with the ability to repair itself while providing stability to the organism. Furthermore, bones change constantly and adapt to their environment to fulfil these demands [7]. As a consequence, the microstructure of the bones stores a lot of information related to habitual activities. This microstructure is more sensitive to external loading, and thus also to habitual activities, than, for example, the joint size or shape [8]. Ruff and Runestad [8] already noted, that the microstructure "*may therefore reflect what an animal was* actually *doing during its lifetime, rather than what it was* capable *of doing*". To retrieve these information, methods for bone microstructure analysis are required. As the bone microstructure can be depicted in detail without damaging the bones using high-resolution micro-CT (μCT), such imaging methods are also suited for fossils [9], as the fossils are irrecoverable and shall not be

destroyed during the process. Thus, next to the already mentioned methods, also the microstructure can be analysed to retrieve information regarding habitual activities.

Evolutionary anthropology is by far not the only field where microstructure analysis is of interest. These methods can also be used in medicine or basic biomedical research, for example, in the diagnosis of bone related diseases, such as osteoporosis [10], the monitoring of treatment [11], or the development of bone implant systems [12]. For the latter, the main focus is on gathering physiological loading conditions, which can be inferred if the habitual activities are known. These loading conditions are required, for example, in the creation of physiological, realistic models. While medical applications require methods that work *in vivo*, fossils are a pure *ex vivo* application. Nevertheless, both fields can resort to the same analysis tools. Thus, bone microstructure analysis is an important tool in many disciplines to get to the habitual physical activities and thus also the physiological loading conditions.

1.2 Motivation & Goal

Figure 1.1 shows a graphical overview of the thesis. The possible use cases for microstructure analysis and the motivation why microstructure analysis is important were already laid out in the previous section. There are many branches in the field of microstructure analysis, each containing a multitude of methods and tools. These methods and tools were already successfully applied for the described use cases, and two methods, namely holistic morphometric analysis (HMA) and inverse bone remodelling (IBR), were considered more closely for this thesis. Both these methods were already applied in evolutionary anthropology, but limitations in the methods hindered the answer of still open questions. The motivation for this thesis was to overcome these limitations and provide novel tools and ways to answer these questions in the future.

In the morphometry branch, HMA is used to qualitatively compare bones on a holistic level, that is on the level of the whole bone. This method is superior to region of interest (ROI) based methods, as the whole microstructure is evaluated and not just selected regions in the bone. A limitation of this method is, that HMA on its own does not allow for quantification of the resulting morphometric indices between samples or even groups of samples on a local level. This hindered the comparison between species, as differences between individuals could only be observed on a qualitative basis.

In the branch of biomechanics, IBR is used in combination with high-resolution micro-CT (μCT) to "extract" the loading history of the bone from the microstructure. One of the advantages of this method is, that it can be applied on bones without the need for soft-tissue information and thus is suited for the inference of the loading history of archaeological findings. IBR works by directly converting the μCT images to micro finite element (μFE) models. However, μFE models are computational expensive and are limited in the boundary conditions and material properties that can be applied. So far, μFE-based IBR was only applied to smaller portions of bones using simplified boundary conditions. Both the computational requirements and simplified loading conditions hindered the application to larger bones or complex joints so far.

The main goal of this thesis was to overcome these limitations and to add specific enhancements to both methods. The HMA method was extended to allow for quantification between samples and groups of samples by using a statistical deformation model (SDM) to construct a canonical reference bone onto which morphometric indices can be mapped and compared. The IBR method was translated from μFE to homogenised finite element (hFE) to speed up the overall runtime and allow for sophisticated boundary conditions, possible with hFE.

In the future, these newly developed methods can be applied to bones in the context of evolutionary anthropology, for example, to find out which adaptive niches certain early human species occupied, but can also be applied in other fields, such as medicine or basic biomedical research.

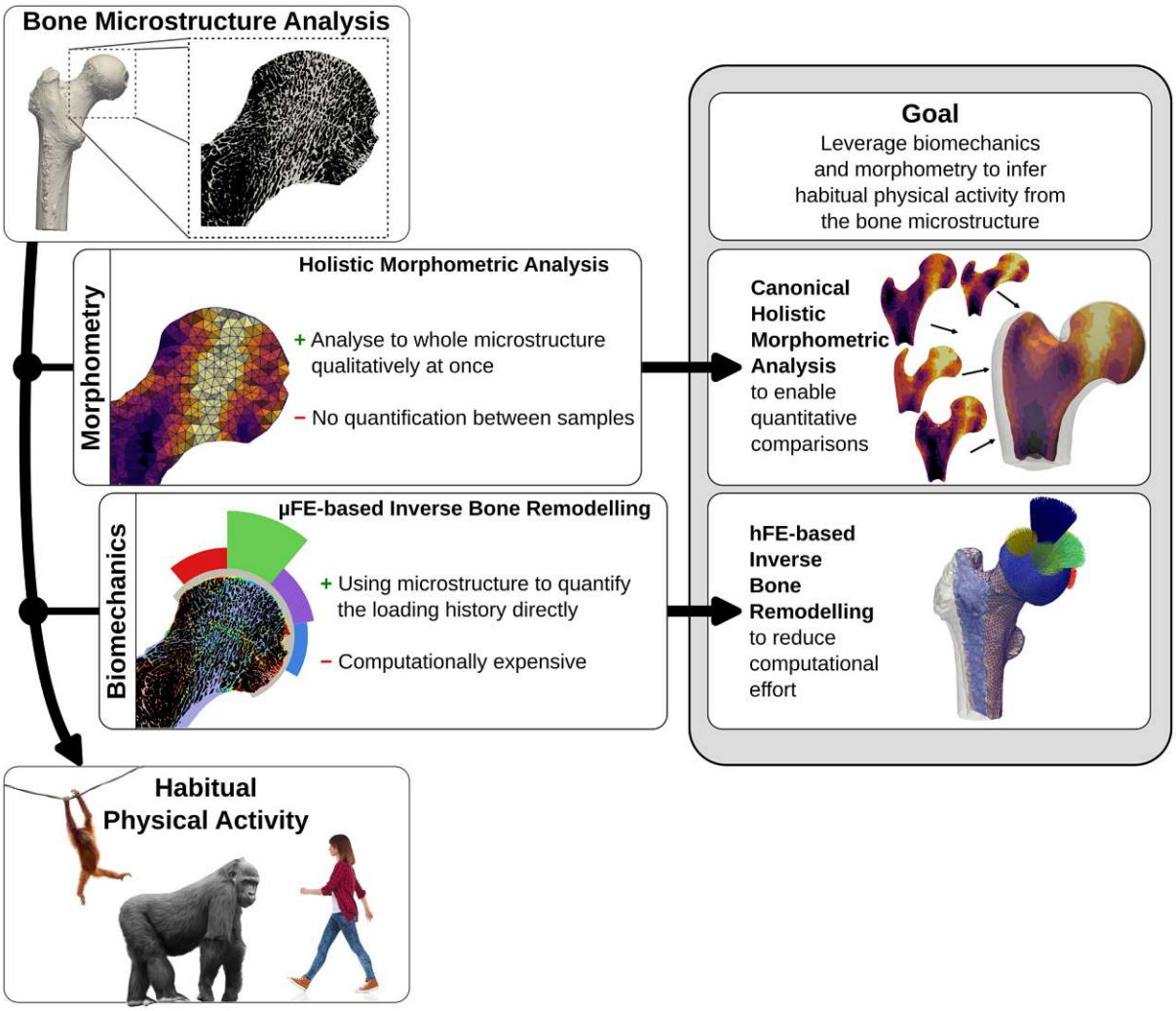

Figure 1.1: Overview of the thesis. Bone microstructure analysis for the inference of habitual physical activity, such as locomotion, can be employed using many methods. Two possibilities are morphometry analysis and biomechanical analysis. There are existing methods in each of the branches and two methods were considered in this thesis. These methods had certain limitations and two novel methods (grey box, right) were developed in this thesis: canonical holistic morphometric analysis (cHMA) and homogenised finite element (hFE)-based inverse bone remodelling (IBR). Both extend the existing methods, to overcome the limitations and work towards the goal of a combined morphometric and biomechanical analysis of bones.

1.3 Outline & Structure

The thesis is structured into an introduction, a chapter containing background information, two major chapters containing the methods and results of the thesis and a final chapter, synthesising all results.

Chapter 1 is the chapter you are currently reading and is meant to be an introductory chapter. It presents the motivation and goals of this thesis and gives some guidance how to read it. Furthermore, a list of publications is given, which were already published during the time of this thesis.

Chapter 2 covers large portions of the background for the thesis and regards the properties and function of bone, how bone changes over time and how it can adapt to new functions. It also covers state of the art methods for the analysis of bone microstructure and where these methods fail. Further, the process of inferring physiological loads from the microstructure is explained and current challenges are described. The interested reader is also referred to the books *Bone Mechanics Handbook* by Cowin [13], *Skeletal Tissue Mechanics* by Martin *et al.* [14], and *Basic and Applied Bone Biology* by Burr and Allen [15] which cover many basic information as well as advanced topics in the scope and beyond of this thesis.

Chapter 3 introduces the newly developed canonical holistic morphometric analysis (cHMA) method and explains the internal functionality and the workflow, the validation process, parameter studies, and possible methods for evaluation of the data. The method is exemplary applied to first metacarpal bones and proximal femora to quantify morphometric differences of extant primate species. In the end, an outlook is presented for further research.

Chapter 4 introduces the newly developed homogenised finite element (hFE)-based inverse bone remodelling (IBR) methods and the translation process from the tissue to continuum-level. Then, two applications for the prediction of section forces at the human distal radius and joint loads at the human proximal femur are shown and discussed. Finally, the method is used in a proof of concept study to predict joint loads in 3D on the full proximal femur of two primate species.

Chapter 5 consolidates the previous chapters and presents an outlook, how the two here developed methods can be used together in the future.

1.4 Publications

Parts of this thesis were already published in scientific literature. Chapter 3 regarding the cHMA method was partly published in publication I. Chapter 4 regarding IBR was partly published in publications II and III. A detailed description of the contributions is given in the beginning of each chapter.

I. S. Bachmann, C. J. Dunmore, M. M. Skinner, D. H. Pahr and A. Synek. 'A computational framework for canonical holistic morphometric analysis of trabecular bone'. In: *Scientific Reports* 12.1 (2022), p. 5187. DOI: 10.1038/s41598-022-09063-6

II. S. Bachmann, D. H. Pahr and A. Synek. 'A Density-Dependent Target Stimulus for Inverse Bone (Re)modeling with Homogenized Finite Element Models'. In: *Annals of Biomedical Engineering* (2022). DOI: 10.1007/s10439-022-03104-x

III. S. Bachmann, D. H. Pahr and A. Synek. 'Hip joint load prediction using inverse bone remodeling with homogenized FE models: Comparison to micro-FE and influence of material modeling strategy'. In: *Submitted to: Computer Models and Programs in Biomedicine* ()

Chapter 2

Background

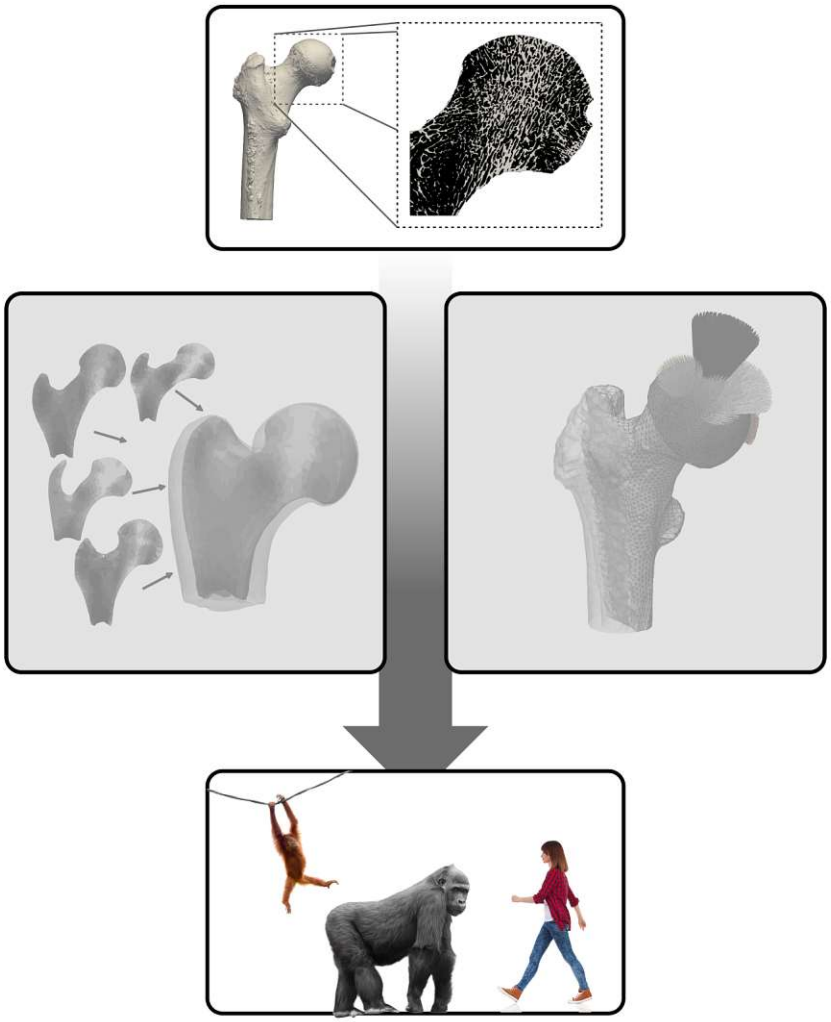

2.1 Basic Bone Biology

2.1.1 Structure and Composition

Bones are the structural building blocks of the human body. They are further used to protect organs and are also itself an organ, vital to the calcium metabolism [19]. Viewed from the outside, bones come in various shapes. Typically, they are classified based on their outer shape as long bones (*Ossa longa*), such as the femur, short bones (*Ossa brevia*), such as the carpal or tarsal bones, flat bones (*Ossa plana*), such as the ribs or scapula, air filled bones (*Ossa pneumatica*), such as the maxilla, and irregular bones (*Ossa irregularia*), such as the vertebrae [20].

Bones are attached to each other via joints. Muscles attach to the hinged structure and allow for the locomotion of the body. There are many different types of joints, with different degrees of freedom (DoF), which is important for the correct locomotion. For example, the hip joint allows rotation on a spherical surface, while the finger joints only allow for a hinged motion. Joints are not formed by a bare bone-to-bone contact, but the joint surface is covered with cartilage to decrease the friction on the joint and distribute the load. The cartilage layer is gradually merged into the bone matrix at the osteochondral interface to perform optimal load transfer from the soft cartilage layer to the stiff bone matrix [21]. Muscles attach via tendons to the bone and ligaments form connections between bones to provide further stability. The ligaments are required, as joints can typically only be loaded in compression, while the ligaments can only be loaded in tension. Both tendons and ligaments are also incorporated into the bone in a graded way at the entheses, similar to the osteochondral interface [22].

While the appearance of bones varies across the skeleton, the internal structure of bones is similar. Bones usually have a dense outer layer which is called cortical bone. On the inside, bones consist of a porous structure, called trabecular or cancellous bone. Especially in the region of joints, trabecular bone can be found. Some bones, such as the long bones, also contain hollow parts. The bone is filled with bone marrow, of which two types exists: Yellow marrow, which contains high amounts of fat and red marrow, in which new erythrocytes are formed. Bone marrow also contributes to the mechanical properties of bone, depending on the loading type [23].

Bones are built in a hierarchical manner, showing different properties at each level (Figure 2.1). Starting with the dense cortical bone: When “zooming” into the cortical bone material, an arrangement of pores can be found. There are larger pores for blood vessels, called Haversian canals, but also smaller pores forming a whole network, called canaliculi, at whose intersections small caverns lie, called lacunae. This network is also referred to as the lacuno-canalicular network (LCN). Cells called osteocytes reside in these lacunae. The Haversian canals are the centre of so called osteons, cylindrical structures that have a diameter of around $200\,\mu\mathrm{m}$ to $500\,\mu\mathrm{m}$ [24]. Each osteon itself

consists of so called lamellae and is built in a twisted plywood fashion [25]. The osteons form the main building block of cortical bone. The trabecular bone, on the other hand, consists of so called trabeculae, that have the form of rods and plates, with a diameter of $50\,\mu\mathrm{m}$ to $400\,\mu\mathrm{m}$ [26] and lengths in the range of single mm. The trabeculae themselves do not contain any Haversian canals but only the LCN. The main building blocks of trabeculae are thus not osteons but so called packets, which are visible due to their different mineralisation levels [27, 28]. These packets consists, similar to osteons, out of lamellae.

The material at the level of single trabeculae, that is in the range of $10\,\mu\mathrm{m}$ to $100\,\mu\mathrm{m}$, looks homogeneous to the eye. But when zooming into the material, it can be seen that the bone tissue is still heterogeneous and consists of even smaller building blocks. The three main building blocks of bone at the tissue-level are water, collagen, and mineral. Other composites, only accounting for a few percent of mass, complete the material mixture. The collagen fibers include hydroxyapatite (HA) crystals - a calcium containing mineral. Thus, bone can also be regarded as a nano-composite material [29] or described as “fractal-like” starting from the nano-scale [30]. The hierarchy does not stop at the nano-scale and continues down to the individual proteins. However, this thesis will focus on the morphometry and the apparent mechanical behaviour of bone only down to the micro-scale and the structures below the micro-scale are beyond the scope of this thesis. The interested reader is referred to chapter 2 of *Skeletal Tissue Mechanics* by Martin *et al.* [14] for a more elaborate overview.

Many different classifications for the hierarchical structure of bone were described in the literature. Typically, a structure with 3 to 7 or even more levels is established. Three commonly mentioned definitions are by Rho, Kuhn-Spearing and Zioupos [31], Weiner and Wagner [32], and Currey [33]. All these definitions go beyond the trabecular structure of bones, however for the purposes of this thesis, a “coarser” classification is useful. For the rest of this thesis, a slightly extended version of Currey’s definition (whole bone, meso, micro and nano-scale) is used, consisting of five levels (see also Figure 2.1):

1. *Macro-scale:* The highest level, where the whole bone is visible.
2. *Continuum-scale:* In the range of several mm, i.e., $4\,\mathrm{mm}$ to $10\,\mathrm{mm}$ range. On this level, bone is regarded as an orthotropic material [34].
3. *Meso-scale:* Between continuum and micro-scale.
4. *Micro-scale:* The sub-mm range. This size is depictable with μCT and individual trabeculae can be depicted in detail ($50\,\mu\mathrm{m}$ to $400\,\mu\mathrm{m}$ diameter [26]).
5. *Nano-scale:* Below the $\mu\mathrm{m}$ range. Pores in the bone are visible (up to $15\,\mu\mathrm{m}$ [35]).

While other classifications are centred around the biological building blocks of bone, the here given classification is centred around the methods used later-on, that heavily

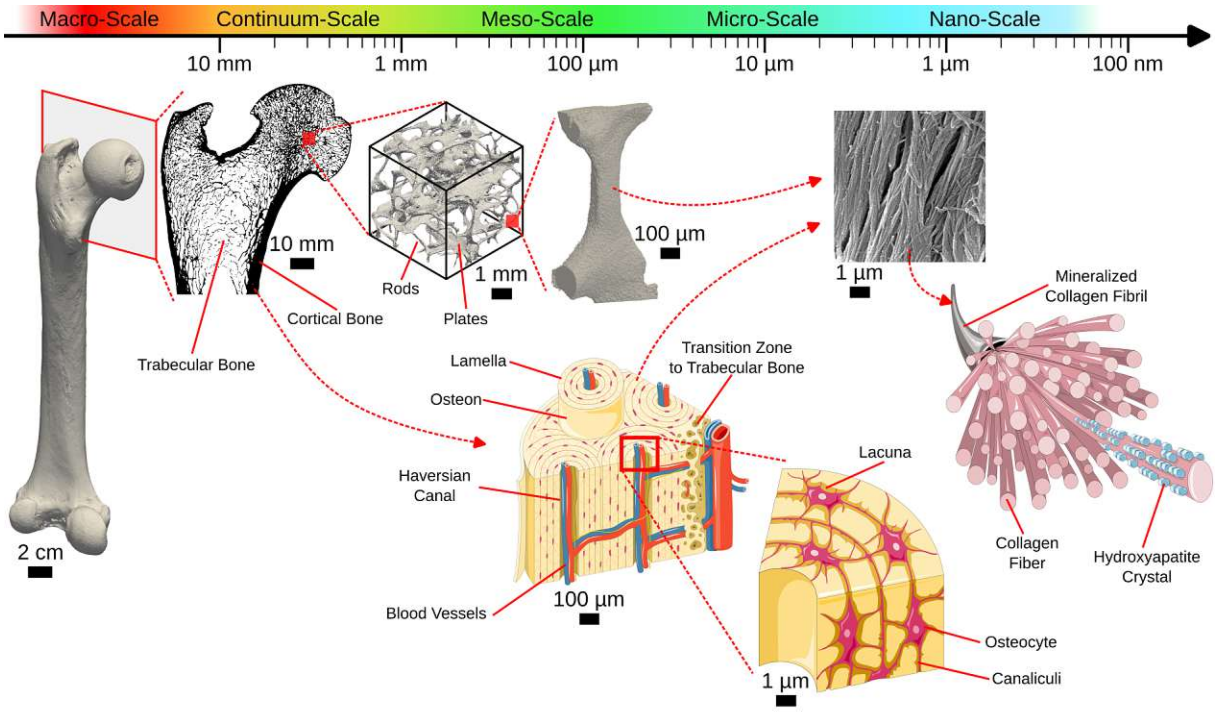

Figure 2.1: Bone shows a hierarchical structure from the macro-scale down to the nano-scale. There are no exact borders between the different scales, but a continuous transition.
This image contains Creative Commons licensed work. A detailed description can be found in the chapter “Image Credits” at the end of this thesis.

rely on the micro-scale to infer mechanical material properties on the continuum-scale. Thus, for this thesis, mainly the continuum and micro-scale are of interest.

2.1.2 (Re)modelling

Bone has to withstand dynamic loading up to several times the body weight every day [36, 37]. Microcracks and other types of damage accumulate over time and have to be repaired, before the bone would ultimately fail [38]. Unlike engineering materials, such as steel, a repair mechanism is built into the bone (Figure 2.2). Cells, called osteoblasts and osteoclasts, reside inside the bone to perform this repair. Both cells are orchestrated by the osteocytes, which are built into the bone matrix and reside in the lacunae, with their processes branching out into the canaliculi. The osteocytes can sense the microdamages in their vicinity and inform osteoblasts and osteoclasts via biochemical pathways [39]. The osteoclasts then have the task to remove old bone and the osteoblasts will afterwards build new bone matrix in a small confined area of the bone [40]. Furthermore, marcrophages remove the “debris” that the osteoclasts left behind. After the site was repaired, some of the osteoblasts stay behind and become bone lining cells, covering the newly formed bone, while other osteoblasts are built into the newly formed bone matrix to become osteocytes. This whole cycle, from bone removal to full mineralisation of the tissue, requires around 200 days [41]. In this repair-mode, both the osteoblasts

and osteoclasts work in a coordinated way and thus typically simply re-build bone tissue, without changing the net-mass. These units of coupled cells are also referred to as a bone multicellular unit (BMU) and this (coupled) repair of bone is also known as *remodelling*.

But not only do the osteocytes orchestrate the repair of broken bone, they are also able to steer the removal or the apposition of bone to some extent (Figure 2.2). Bone is removed if it is not required locally, and built-up in places where the structural integrity is in danger. The question is of course, how does the bone (i.e., the osteocytes) know where new bone matrix is required or where it can be safely removed? The osteocytes are known to be mechanosensitive cells, thus are able to monitor the mechanical environment they are in. It is currently not fully understood how the osteocytes are able to monitor the mechanical environment, nor what mechanical signals they actually "measure". However, many mechanosensitive receptors are found in osteocytes that are able to sense different stimuli [42] and thus it seems likely that the osteocytes can "feel" a multitude of mechanical signals, probably with different sensitivities. The mechanical signals are then translated into biochemical signals that can be "understood" by the osteoblasts and osteoclasts [43]. These cells are then again responsible to remove or build bone tissue, however in this case the cells do not work together as a BMU. This uncoupled response of osteoclasts and osteoblasts is also known as *modelling*, as it typically involves a net-mass change.

The terminology of the two mechanisms (remodelling and modelling) is not always used properly and often with ambiguity [44]. While both mechanisms are distinguished by the coupled or uncoupled behaviour of the cells, on a phenomenological level it is not always clear which of the two mechanisms is responsible for a change in bone. For example, if bone is getting repaired (remodelling) but after the repair less bone matrix was built-up than it was before, a before-after picture would look like modelling, i.e., a adaptation of the bone. However, this net-change in bone mass could also be attributed to age, disease, hormones, or genetics, even though the underlying process was pure remodelling. On the other hand, if bone is removed at some location and built-up at another (modelling), the total net-change is still zero - when measuring it on a macroscopic level - and thus the two modelling processes would look like remodelling. On a nano-scale, both processes can be distinguished though, due to differences in the mineralisation process [45]. However, as remodelling and modelling cannot be distinguished phenomenologically on the macroscopical level, the two terms are sometimes combined into a single one: *(re)modelling*. In this thesis, we will speak from (re)modelling to describe this phenomenological adaptation of bone over time without specifying which of the two processes was responsible for the bone mass change.

It was observed, that bone is lost if it is not appropriately loaded, for example during the microgravity of spaceflight [47], but new bone is formed if extra loads are applied, for example during weight-lifting [48]. In between these extremes the response is proportional to the mechanical stimulus the bone has to endure. This phenomenon became

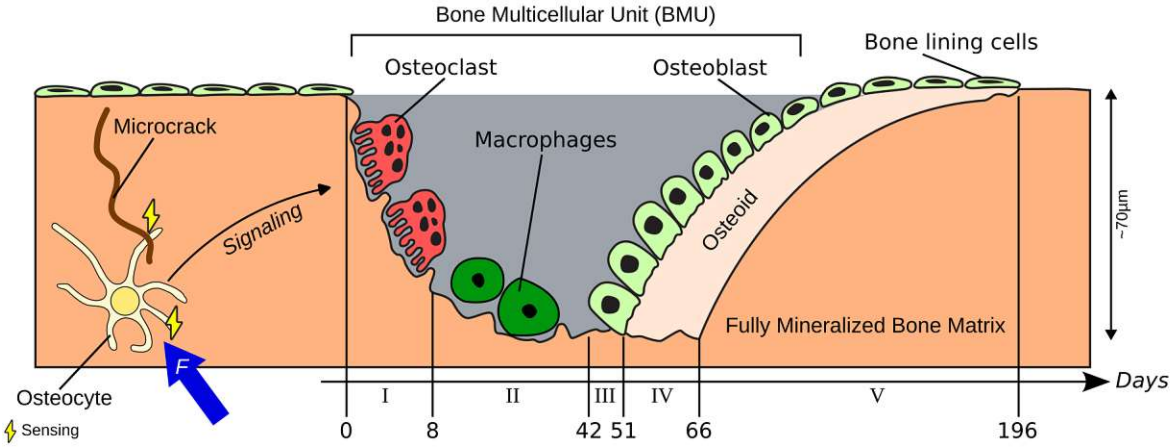

Figure 2.2: Bone remodelling and modelling. The image shows schematically both processes. The osteocytes sense damages in the bone, such as microcracks but can also sense the mechanical environment (blue arrow). The osteocytes then signals osteoclasts and osteoblasts. If both work in a coordinated way, the process is referred to as *remodelling* and they form a bone multicellular unit (BMU), while the uncoordinated removal or apposition of bone is called *modelling*. The timeline shows how long each step takes approximately, with the phases named after Eriksen *et al.* [41]: **I** osteoclastic resorption phase, **II** mononuclear cell resorption phase, **III** preosteoblastic phase, **IV** initial mineralisation lag, **V** mineralisation phase. The total depth the cells remove and rebuild is around $70\,\mu\mathrm{m}$ [41]. The interested reader is also referred to the poster of Crockett *et al.* [46], which shows the remodelling process in much more detail.

known as the "mechanostat" by Frost [49, 50], which states that bone resorption and apposition is coupled to the strain the bone has to endure. The name stems from "thermostat", a device that controls the heating in a room by measuring the temperature – similar as the bone controls its mass by measuring the mechanical signals. Frost [49] suggested, that specifically the strains in the bone tissue are the key to this control loop and that high strains induce bone apposition and low strains lead to bone resorption. Between these two extremes is a region where strains lead to no net-change, called "lazy-zone" (i.e., only normal remodelling would still be present). It was thought that this zone should exist as bone would react in a "lazy" way to incoming signals and would only start the modelling process if a threshold is exceeded (in both overloading or underloading). The existence of such a "lazy-zone" is however still debated and recent studies suggest that bone is purely load driven [51]. It is also not clear if strain is the real driving quantity, as osteocytes are known to have many receptors for different types of mechanical stimuli [42] and computer models showed, that similar structures can be formed by using a multitude of mechanical stimuli [52]. However, many different signals, measured on a macroscopic level, might induce similar signals on the level of the cells. In addition, most of the mechanical signals are strongly correlated to each other, as they are, for example, connected by Hook's law. Thus it is no wonder that different mechanical signals can lead to similar looking bone (as shown in many computer simulations), as they eventually all trigger similar responses in the bone. More recently, time-lapsed μCT images allowed to show regions in the bone of resorption or apposition

[53]. Using additionally finite element analysis (FEA) it was possible to show that the local mechanical environment indeed correlates well with resorption and apposition [51, 54, 55].

However, the mechanostat model does not work for every bone, as for example the skull bone is typically not specifically loaded but still keeps its form and shape [56]. Other bones, such as the auditory bone, have a low remodelling rate, such that the shape is not altered even by repair mechanisms [57], as shape changes may lead to detrimental effects on hearing. Thus, the regulation is also specific to each bone and mechanical stimuli are not the only source for changes in bone. For example, muscles are the "motor" to provide the mechanical signals in the bone, but may also contribute to bone (re)modelling via biochemical components [58]. Furthermore, hormones, neither produced by bone or muscles, also control processes in the bone. Probably most famous is vitamin D, a hormone controlling the calcium absorption in the bone [59]. But overdoses of vitamin D can have detrimental effects for the bone as calcium is removed from the bone leading to hypercalcemia [60], and severe cases of overdosing even may have toxic effects [61]. Thus, as Paracelcus already noted in 1538 "*The dosage alone makes it so a thing is not a poison*", the correct supply and dosage of many substances in the body is required for the correct function of bone metabolism.

2.1.3 Functional Adaptation

When looking at images of the bone microstructure, it is apparent that the trabeculae have some orientation and the density of the trabeculae is not the same in every location of the bone (Figure 2.3). Already in the 19th century, the anatomist Georg Hermann von Meyer noticed, that the trabecular structure inside the femur looks similar to drawings of the stress-trajectories of a crane, sketched by the engineer Karl Culmann [62]. Back then, it was thought that the trabeculae orient themselves according to the stress-trajectories and this relationship would become famous as "Wolff's law", formulated by Julius Wolff [63]. While the premises of Wolff were in part wrong [64], the term is still heavily used and stuck now for over a century, but is nowadays used in a more general way to describe that bone can adapt over time, based on its external loading. However, it was actually Wilhelm Roux [65], who considered this *functional adaptation* of bones, and this term describes the phenomena much better. Even though the term "Wolff's law" is very popular, we will use *functional adaptation* throughout this thesis.

In general, functional adaptation can be described as the phenomenon, that the bone microstructure, and to some extent also the overall shape of the bone, can change over time, if new functions, that are for example new habitual activities, are imposed on the bone [67]. In principle, the functional adaptation can be modelled as a biological control loop, which senses the mechanical signals and changes the bone mass locally, which eventually will lead to differences in microstructure and shape, observed especially well

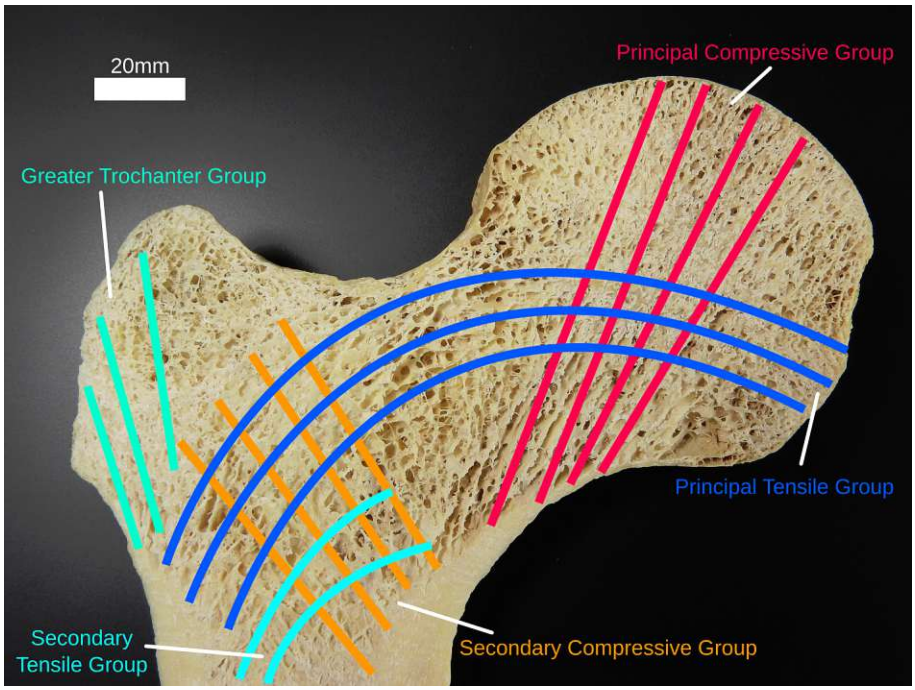

Figure 2.3: Trabecular orientation in the femoral head. The femoral head is a prime example of trabecular orientation and was also the bone Georg Hermann von Meyer studied [62]. Superimposed is the classification of the different "groups" of trabeculae, formed by their orientation according to Kerr *et al.* [66].

in related species with different modes of locomotion, for example, the primates (Figure 2.4). This functional adaptation does not work in a sense, that bone constantly adapts to each and every load, but rather a time and load averaged stimulus is responsible for the adaptation. The reason is, that over the course of a day, the bone has to endure a multitude of loads, from many different directions, in different magnitudes and frequencies. Figuratively speaking, if a person walks every day for several hours but climbs on a tree only once in a year, the bones will likely not adapt to climbing. There are also limitations on a cellular level, how much bone can be removed or built-up over time, and thus effects of functional adaptation require some time to manifest. It was found that the magnitude, frequency and number of load cycles of the load influence the adaptation [68]. That means, a low magnitude can be compensated by a high number of load cycles or *vice versa* to get to the same adaptation, however this relationship is non-linear. The frequency of the load itself also has a non-linear influence [69].

Functional adaptation was already shown in many experimental studies [72]. To name a few other recent examples, Umemura *et al.* [73] showed that there are diminishing returns in bone mass apposition, if rats were jumping a defined amount per day, and just five jumps a day would already increase the bone mass significantly. Barak, Lieberman and Hublin [74] showed that the trabecular orientation in sheep's distal tibia would change, if the sheep wore platform shoes. Wallace *et al.* [75] showed that 10 weeks of increased physical activity leads to changes in bone microstructure but would not change the shape of the entheses in turkeys. In mice, the microstructure can be

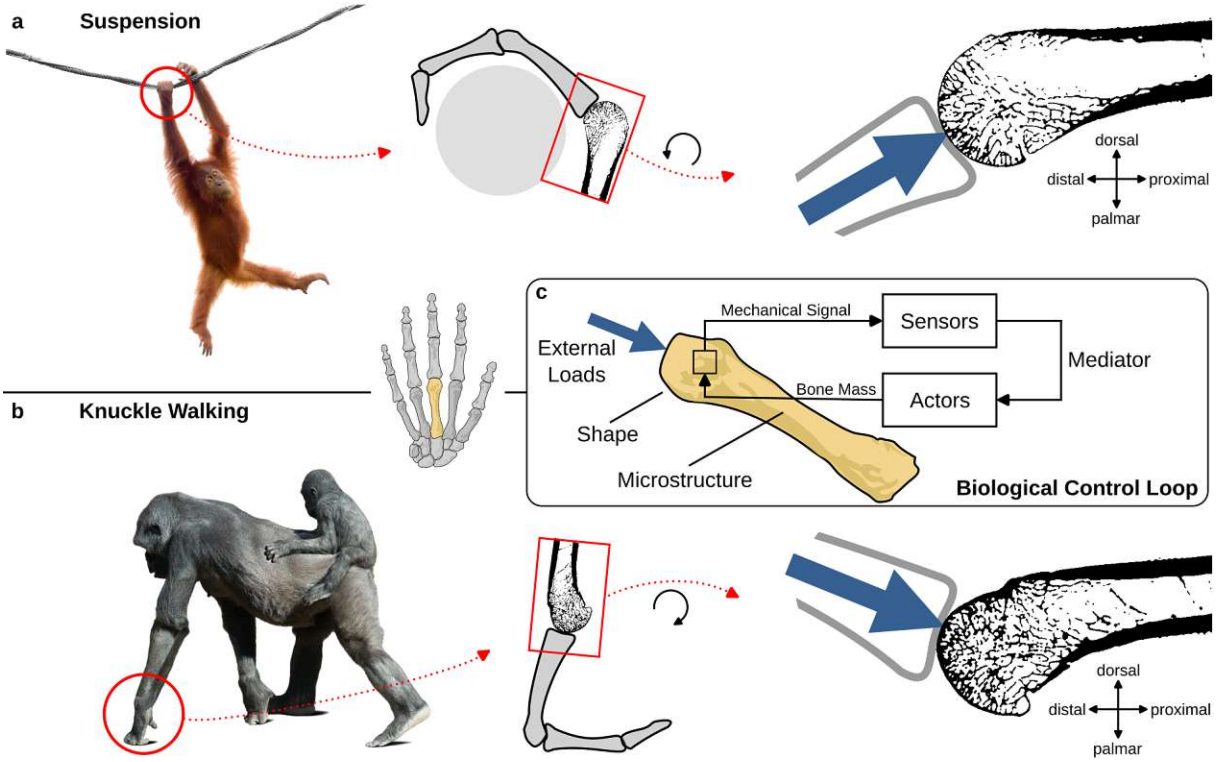

Figure 2.4: Functional adaptation of bone on the example of the third metacarpal bone [70]. Orangutans and chimpanzees employ different types of locomotion, namely suspension (Panel **a**) and knuckle-walking (Panel **b**). The different joint positions in those two locomotor-modes have an influence on the shape as well as the microstructure of the bone, as visible in the cross-section of the bone (right side). It can be noticed, that not only the overall shape is different but also the trabecular structure follows the loading direction. Orangutans show sparse trabecular bone dorsally, because the bone is loaded more often from the palmar side. Both bones are rotated from the anatomical model (red box) into the same position for a better visual interpretation. **(c)** shows a schematic control loop of functional adaptation: mechanical signals are measured (i.e., by the osteocytes), mediated to actors (i.e., osteoblasts and osteoclasts), and bone mass is changed. The control loop image was recreated from Huiskes [71].

depicted *in vivo* and thus the local loading regime can be calculated using FEA. In an experiment loading the tail of the mice, Schulte *et al.* [54] were able to correlate the mechanical stimulus with local bone (re)modelling.

2.2 Morphometry Analysis

The microstructure of bones can be influenced by many factors, such as bone related diseases, external loading, or even genetics. Therefore, there is the need to quantify bone microstructure, for example in the diagnosis of osteoporosis or the monitoring of treatments. A classic method of bone analysis is histology, where a biopsy of the bone is taken, cut sections are created and analysed under the (optical) microscope. The aim is to analyse the shape of the bone sections, i.e., to perform morphometry (from classical Greek *morphé*, which means "shape" and *metron*, which means "measurement"). Thus, this method is also called (bone-)histomorphometry [76, 77] – the measurement of the shape of bone tissue. However, histomorphometry is only a 2D method and information of the 3D bony network is lost. Furthermore, biopsies are invasive and analysis methods that can be applied *in vivo* are preferable.

In this section, modalities for the (3D) measurement of bone and methods for the evaluation of bone morphometry are presented. Then, different ways are discussed, where inside the bone the morphometry is measured, which ends in a short outline of the HMA method - used as the basis for the morphometry analysis in this thesis.

2.2.1 Modalities of Measurement

As bone consists of a mineral phase, X-rays are blocked to a higher degree in this hard-tissue than by the surrounding soft-tissues, mainly consisting of water. This creates a contrast in the X-ray images and X-ray has become the gold-standard method to analyse bones both *in vivo* and *ex vivo*. While classical 2D X-ray projections are still used as a cheap and easy way in clinical diagnosis (e.g., to diagnose fractures), dual-energy X-ray absorptiometry (DEXA) can be used to quantify the areal bone mineral density (aBMD) and is typically used in the diagnosis of osteoporosis [78]. Computed tomography (CT) can be used to depict the bone structure in 3D and different CT methods exist, which differ mainly in spatial resolution and required scan time. Using calibration phantoms and calibration equations, it is also possible to calculate BMD from the Hounsfield-units[1] of the CT directly [79], however care has to be taken to not introduce errors in the measurement protocol that skew the calculated value [80]. Clinical CT has a resolution in the range of $400\,\mu\mathrm{m}$ [81], while micro-CT (μCT) offers resolutions down to one μm [82]. However, μCT cannot be performed *in vivo* on humans, given the high radiation doses. High resolution peripheral quantitative CT (HR-pQCT) can be used for the *in vivo* measurement, as it offers lower radiation dose on the expense of a small sample volume and higher voxel size than μCT [82]. Modern synchrotron-radiation μCT (SR-μCT) can even depict structures in the sub-μm range [83], but suffer from even higher radiation

[1] Hounsfield-units (HU) are used in CT imaging to describe the absorption of the X-rays by the tissue. Per definition, air has a value of $-1000\,\mathrm{HU}$, i.e., no absorption of X-rays, and water has a value of $0\,\mathrm{HU}$. The values for hard- and soft-tissues depend on the density of the tissue.

doses than μCT and thus cannot be used for *in vivo* measurements [84]. Other methods, not using X-rays, such as quantitative ultrasound (QUS) [85] or magnetic resonance imaging (MRI) can also be used, but a constraint is the lower spatial resolution of those devices, compared to μCT. However, special MRI devices exists that offer high spatial resolution on the cost of small sample size [86]. To analyse bone on the sub-μm range, methods such as back-scattered electron microscopy can be use, which allow the measurement of the mineralisation level at the tissue-level [87]. However, while these methods offer extraordinarily high spatial resolutions, they typically only allow for a 2D analysis, or 3D surface analysis.

When it comes to measuring any morphometric quantity of bones, it is important to remember its hierarchical structure. Depending on the quantity that shall be measured, the resolution of the imaging modality, or the modality itself, can also influence the measurement (Figure 2.5). As certain quantities can only be accurately depicted below a certain resolution, measuring them on a more macroscopic level leads to averaged values over the volume. For example, while the LCN can be depicted using high-resolution SR-μCT [88], these small pores will not appear in clinical (low-resolution) CT scans. Thus, while the pore volume can be measured exactly in the high-resolution scan, it is averaged into the apparent density in the low-resolution scan. But also the modality itself can have such averaging effects, aside of the resolution. For example, methods such as plain 2D X-ray or DEXA are limited to measure only areal quantities, such as areal bone mineral density (aBMD), as the 3D image is projected into a single plane. Thus, methods are desirable that can analyse the full 3D-structure with a sufficiently high resolution, such that the tissue properties in question are properly depicted.

2.2.2 CT-based Morphometry

CT offers full 3D analysis, and although the resolution of clinically available machines is rather low, it is often sufficient for clinical diagnosis. In clinically available CT scans, only an averaged BMD measurement is possible in the volume of each voxel (typically around $0.05\,\mathrm{mm}^3$ to $0.2\,\mathrm{mm}^3$). In this case, the microstructure can only be depicted as a blurred apparent density pattern within the bone. Only if CT methods with a resolution in the μm range are used, the full depiction of the microstructure, i.e., single trabeculae, is possible. Today, this is possible even *in vivo*, at least for the peripheral skeleton, by using dedicated HR-pQCT scanners. This depiction of the microstructure offers many new possibilities, which were previously only possible using histological slices, with the advantage that the quantification can now be performed in 3D.

In the field of morphometry, a lot of indices are used, that can be measured on the bone microstructure with CT and are therefore also referred to as “CT-based morphometric indices” to distinguish them from (2D) histomorphometry [89]. A few commonly used indices and their calculations are shown in Figure 2.6. For the analysis of CT-based

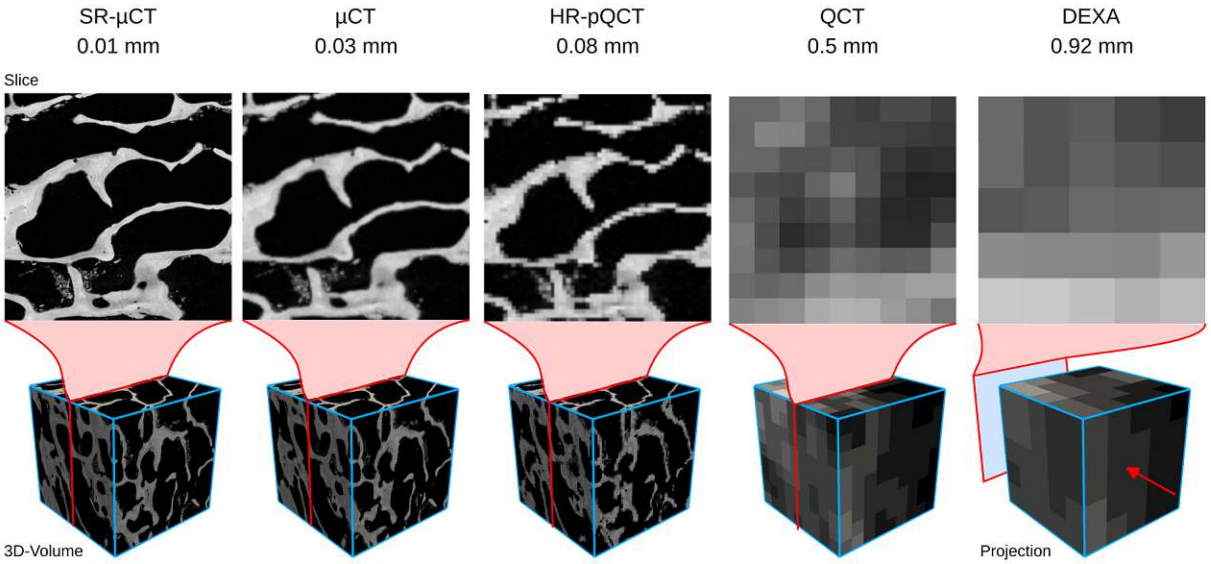

Figure 2.5: Using different imaging modalities results in different image qualities, and thus can also influence morphometric analysis in a later stage. The here shown images are created synthetically from the high-resolution SR-μCT image to simulate the effect of using different methodologies, thus the image quality is to some extent idealised. The red marker shows the position of the slice inside the 3D volume. Note, that DEXA produces only a projected 2D image and thus the shown 3D volume cannot be retrieved in reality.

morphometry, the grey-value images are often segmented into binary images, such that only two grey-values (typically zero and one) are present in the image, which divide the image into background and bone [90]. The advantage of using segmented images is, that many morphometric quantities can be evaluated easier. Furthermore, the noise in the image is effectively removed completely[2]. However, due to the so called partial volume effect (PVE) [91], the segmentation method only works for high-resolution scans, where the error due to PVE is small. For example, segmenting a QCT image, such as the one shown in Figure 2.5, would lead to high errors, as the microstructure cannot be depicted in detail anymore. Depending on the segmentation, either too many or too few voxels will be classified as bone, leading to wrong morphometric measurements.

When using segmented images, instead of BMD another quantity is typically used, called bone volume over total volume (BVTV). It gives the relative bone volume fraction as a scalar number between 0 and 1. By using a tissue mineral density (TMD) (or ash density), which is around $1.2\,\mathrm{g\,HA\,cm^{-3}}$ for human bone tissue [92], it is possible

[2]It should be noted though, that noise in the image, for example, due to the CT scanning process, can influence the segmentation algorithm and lead to over- or under-segmentation. Thus, segmentation should not be seen as a method for noise reduction in the first place and noise reduction methods typically precede the segmentation. A segmented noisy image will not be noisy anymore, but the information lost in the noise is also lost in the segmentation.

to calculate the BMD from BVTV or *vice versa*[3]. While BMD or BVTV only indicate how much bone is contained within a unit volume, there are also ways to quantify the morphology of the bone microstructure. The trabecular structure can be quantified, for example, using the trabecular thickness (Tb.Th), which describes the average thickness of the trabeculae, trabecular number (Tb.N), which describes the average number of trabeculae per unit volume, and trabecular spacing (Tb.Sp), which describes the average spacing between the trabeculae. The orientation of the trabecular structure is typically measured with the fabric tensor [94] and the scalar quantity degree of anisotropy (DA), which can be calculated from the major and minor axis lengths of the fabric ellipsoid. The bone surface area (BS) of the trabecular structure is often related to the total volume (TV) in a parameter called bone surface over total volume (BSTV), which accounts for the available surface in a unit volume. However, the calculated surface area can be highly variable due to different implementations of the underlying surface reconstruction [95]. In the last years, more advanced methods became available, for example, the classification in plates and rods [96], the inter-trabecular angle [97], network analysis of the trabecular structure [98], or analysis of local curvature [99]. Nevertheless, bone density and orientation of the trabeculae are still the most important indices measured, as they together can explain $97\,\%$ of the variability in stiffness at the continuum-level, while density alone already explains $87\,\%$ [100]. Care has to be taken when analysing and comparing bone morphometry with different software packages, as some indices can be implemented in different ways and thus also lead to different values [95].

The cortical bone can be analysed similar to the the trabecular bone and a variety of morphometric indices exists. Typical analysis of the cortex includes, but is not limited to, cortical porosity (Ct.Po), cortical area (Ct.Ar), or cortical thickness (Ct.Th). These indices are typically measured using high-resolution CT, as the small pores in the cortex have to be properly depicted [101]. However, for the course of this thesis, only trabecular morphometric indices were evaluated.

2.2.3 Regions for Evaluation

The modalities for the measurement as well as morphometric indices for bone analysis were explained in the previous sections. But an important question, not covered so far, is not only what to measure with which device, but also *where* inside the bone the measurement shall be taken. Bone is not a homogeneous piece, like for example a block of steel, but a heterogeneous and hierarchical structure. Thus, measuring the same indices at different positions inside the bone will yield different results (Figure 2.7). To circumvent

[3]Care has to be taken when density values of bone are compared. The here given value measures the mineral content only, however bone also consists of other phases, such as water and organic material. The apparent density of bone is typically given with $1\,\mathrm{g\,cm^{-3}}$ to $1.4\,\mathrm{g\,cm^{-3}}$ for trabecular bone and $1.8\,\mathrm{g\,cm^{-3}}$ to $2.0\,\mathrm{g\,cm^{-3}}$ for cortical bone [93]. But these ranges also include the porosity of the bone, thus, the actual apparent *tissue* densities are higher. There is evidence, that the trabecular tissue density is lower than that of cortical bone due to the higher turnover rate [93].

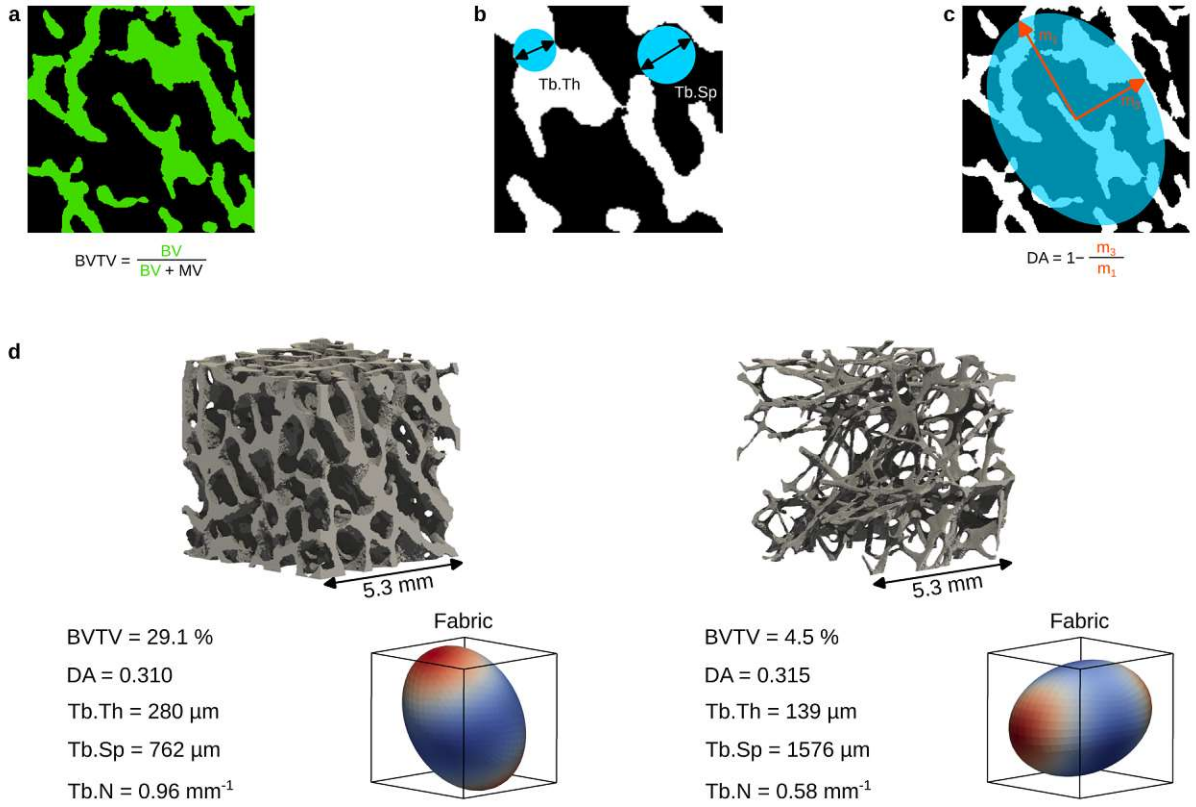

Figure 2.6: Overview of commonly used CT-based morphometric indices using schematic 2D images and exemplified evaluation on two bone cubes. The evaluation in 3D works in a similar way and values for the cubes are calculated in 3D. (**a**) Calculation of bone volume over total volume (BVTV) by using bone volume (BV) and total volume (TV) (sum of BV and marrow volume (MV)). (**b**) Trabecular thickness (Tb.Th) and trabecular spacing (Tb.Sp) can be found by measuring spherical sizes throughout the whole volume and averaging the value afterwards. (**c**) Calculation of degree of anisotropy (DA) using the fabric ellipsoid and the major and minor axes-lengths. (**d**) Evaluation of the indices on bone cubes of different density with an edge length of $5.3\,\mathrm{mm}$. While both cubes differ in their relative bone volume fraction (BVTV), the degree of anisotropy (DA) is similar. This can also be observed in the similar shaped fabric ellipsoid, which is however oriented in different directions. The difference in orientation is also apparent in the rendering of the bone cubes. The different density can also be explained in terms of the three trabecular indices trabecular thickness (Tb.Th), trabecular spacing (Tb.Sp), and trabecular number (Tb.N).

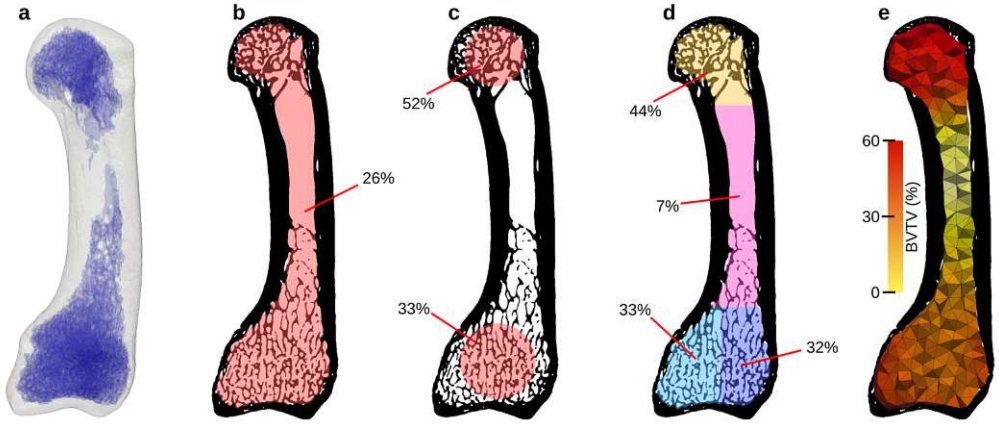

Figure 2.7: Different definitions of regions in which to evaluate trabecular morphometric indices in a bone. The numbers give the bone volume over total volume (BVTV) for the region. **(a)** μCT image of the bone, with trabecular structure highlighted in blue. **(b)** Averaging over the whole bone, which is a special case of a single ROI. **(c)** Spherical ROIs. **(d)** Sector method, a special case of multiple ROIs. **(e)** Holistic morphometric analysis (HMA) method. For easier visual interpretation (**b**)-(**e**) only show a 2D slice of the bone instead of the full volume.

this problem, a straight forward solution is to measure the morphometric index for the whole bone volume. This results in a single, although averaged, value. It is also possible to define a so called region of interest (ROI), in which the morphometric indices are evaluated. However, the question with the ROI is not only where to position it but also what size and what shape (box, spherical, arbitrary, ...) it should have. For example, if the size is varied between the voxel size and the largest possible dimension (i.e., the whole bone volume), the resulting value will either be the value of the voxel itself or the average over the whole volume. Certain morphometric indices, which measure the orientation of the trabeculae are also sensitive to the shape and also the size of the ROI [102].

Still, ROIs do not solve the problem of inhomogeneity, as differences of the microstructure can be observed even inside a single bone. Therefore, multiple ROIs, sub-sectioned ROIs or sectors (for example, in the cardinal anatomical directions) can be used to measure multiple values for each bone. This will lead to a better understanding of the heterogeneous composition, however it also creates new sources of error. The placement of the sector or ROI can be sensitive to the location it is placed. For example, while there is almost no difference between the single lower ROI in Figure 2.7c and the two sector based ROIs in Figure 2.7d, the difference is large for the upper ROI versus the sector. In this case, more empty volume of the shaft was included in the sector, leading to different results.

The concept of using multiple ROIs can be extended, until every volume in the bone is covered with at least one ROI, which eventually led to the development of the holistic morphometric analysis (HMA) method (Figure 2.7e) [103, 104]. A more detailed explanation of the HMA method is given later in chapter 3.1, and thus only a

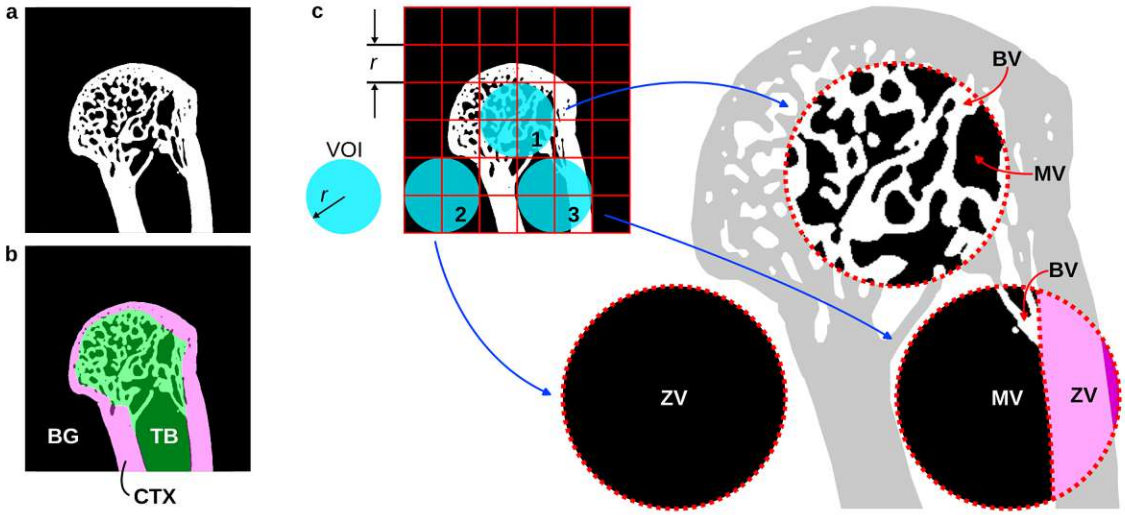

Figure 2.8: Volume of interest (VOI) based evaluation of bone, using a background grid, schematically shown for 2D images. The working principle is the same in 3D. Shown is the evaluation of trabecular morphometric indices, however, the principle is the same for cortical indices. (**a**) Original binary segmented image. (**b**) Masks, defining the trabecular volume (TB), the cortical volume (CTX), and the background (BG). (**c**) Definition of the background grid with grid distance and VOI radius r. The VOIs are centred at the vertices of the grid and three possible cases during the trabecular analysis are shown. Case **1** is a VOI fully inside the trabecular bone. Only bone volume (BV) and marrow volume (MV) have to be regarded. Total volume (TV) is calculated as the sum of BV and MV. In this case, the calculation inside the VOI is the same as for a ROI, for example, as seen in Figure 2.7c. Case **2** is a VOI fully inside the background. This VOI contains only "zero-volume" (ZV). Morphometric indices cannot be calculated in this VOI and the VOI is ignored. Case **3** shows a VOI overlapping into the cortical bone and the background. Only bone in the trabecular region is regarded here, with the same definition of BV, MV, and TV as in case 1. Both cortical bone and background are here regarded as ZV.

brief outline is presented here. HMA works on segmented and masked images and uses a regular grid onto whose vertices ROIs are placed. These ROI are here called volume of interest (VOI) to differentiate them from "real" ROIs. The masks for the segmented images are required to differentiate between trabecular volume, cortical volume, and the background of the image. Then, the morphometric indices are calculated for each of the VOI and subsequently mapped onto a volumetric mesh of the bone. The actual calculation of the morphometric indices inside the VOI works in the same way as for an ROI, but requires an additional correction step. As the VOI are placed over the whole image domain, a special "zero-volume" correction has to be applied, as shown in Figure 2.8. This correction ensures that VOIs that contain background or cortical voxels[4] get the correct morphometric indices. This step is typically not required for the ROI, as these regions are placed only inside the bone volume.

Each mesh element represents a very small ROI, but receives its value from the neighbouring eight VOIs, which examine together a much larger volume than the mesh

[4]For the morphometric analysis of cortical bone, obviously the zero-volume correction has to ensure that no background or *trabecular* voxels are regarded in the VOI.

element. However, this method has as a limitation, that these meshes can only be compared visually to each other, as there is no correspondence between the mesh elements of multiple samples. But for the analysis of single bones, where differences or patterns over the whole volume are to be analysed, or for the qualitative analysis of multiple bones, this method is superior to using multiple ROIs, as the bone is covered in an holistic way.

The interpretation and comparison of bone morphometry across multiple bones is indeed a challenging task. While HMA only allowed for a qualitative comparison, ROI based methods can be used to quantity the differences, however, as already mentioned, the placement of the ROI is crucial [105]. The placement, size and shape has to be on homologous points in order to allow for a meaningful comparison. Although techniques exist to establish homologies between bones, they are typically only performed based on the outer morphology of the bone, by selecting so called landmarks [106]. These might be condyles, areas of specific curvature or other pronounced parts of the bone. However, there are fewer of these landmarks inside the bones. The outer surface can also be used as a guide for microstructure analysis near the joints, as an ROI can simply be fitted via the joint surfaces. For example, the femoral head is spherical in shape and thus ROIs can easily be defined in a spherical coordinate system by fitting a sphere onto the joint surface [107].

2.3 Biomechanical Analysis

Biomechanics can be summarised as the application of mechanics to biological systems. It is concerned with joint and muscle forces, ground reaction forces, or mechanical properties of tissues – just to name a few key terms. A huge part of biomechanics are experiments, both *in vivo* and *in vitro*. However, there is also a rising interest in *in silico* methods [108]. Many different methods exists to analyse bones biomechanically, from overall mechanical considerations of whole bones [109] down to fluid flow in the canaliculi [110] and even lower levels, such as molecular interactions [111]. However, this section only regards biomechanical analyses of the microstructure on the micro to continuum-level.

In contrast to morphometric analysis, which only takes the geometry of the microstructure into account, the biomechanical analysis of bone also involves the mechanical environment (i.e., externally applied forces) and material properties of bone. These aspects are therefore described briefly in the following sections. Finally, the inverse bone remodelling (IBR) method will be presented, which is a biomechanical analysis method that allows to estimate the external loading history directly from the bone microstructure.

2.3.1 External Loading of Bone

Bone's microstructure is shaped by the functional adaptation to external loads. To understand how the trabecular bone is shaped, it is of importance to know how these external forces are transmitted to the bone and thus to the microstructure. From a biomechanical point of view, the joints are of interest for analysis, as these are the places where loads are transferred between bones. Also the entheses, the points where tendons or ligaments attach to the bone, are of interest, because, similar to joints, these are also regions of stress concentration due to the load transfer [112]. Measuring muscle or joint forces *in vivo* can be tricky, as inserting the required sensors in the body is invasive, yet such measurements are possible. For example joint forces can be measured using instrumented prostheses [37, 113] or by using indirect methods, such as strain gauges, which can be glued or tacked onto the bone [114]. Muscle forces cannot be measured directly today, but only indirectly by measuring the strains or forces at the tendons or ligaments [115]. Similarly, indirect methods can also be used to calculate joint loading, for example using inverse dynamics and musculoskeletal models [116]. These models are not invasive, but the exact composition of the body in terms of skeletal geometry and muscles has to be known to get proper results.

2.3.2 Material Properties of Bone

The following section focuses only on the *linear elastic* material properties, however it should be noted that bone is in general a *non-linear viscoelastic* material [117]. However, as this thesis does not employ any non-linear methods, the knowledge of these basic properties should be sufficient. The interested reader is referred to Martin *et al.* [93] for a general overview on the topic, as well as chapters 10 to 20 in Cowin [13] and the references therein for more detailed information.

Knowing the material properties of bones is important for the creation of models, for example, when working with FEA. Here, two types of models are typically used: micro finite element (μFE) models, which model the microstructure in detail, and homogenised finite element (hFE) models, where the microstructure is not modelled explicitly but replaced by an equivalent homogeneous material. For both these models, material properties are required, either on the tissue (micro) level of bone, or at the continuum-level. As already outlined in section 2.1, the main focus of this thesis lies on the micro and continuum-level, which stems exactly from the usage of both μFE and hFE. In this section it will be explained what the mechanical material properties of bone at the micro and continuum-level are, how mechanical properties on the continuum-level can be inferred from the micro level, and how these materials can be modelled in FEA.

The hierarchical structure of bones makes it challenging to find its material properties. The main issue is, that bone does not have an "intrinsic material property" that can be measured [34] and based on that property, properties of coarser (or finer) levels be calculated. Thus, measuring material properties with a specific method at a specific length-scale results in *apparent* properties valid only at that level and for that method [118].

To complicate the matter even more, bone comes in two different appearances: cortical and trabecular bone. Here, an over hundred year old question is still open, if trabecular bone can be regarded as "porous cortical bone" or if both appearances are actually different materials [119]. The smallest building block of both cortical and trabecular bone are lamellae. These approximately $5\,\mu\mathrm{m}$ thick structural building blocks [119] are actually similar in both trabecular and cortical bone, however, cortical bone seems to have a higher mineral content [93]. It is known, that the mechanical properties of this tissue are dependent mostly on collagen and mineral content [120]. Thus, both cortical and trabecular bone consists of the same materials, but their composition (i.e., mineralisation) is different and thus also their apparent material properties are different [93].

The lamellae inside an osteon (in the cortical bone) results in a transversal-isotropic material, which sometimes can also be orthotropic [93]. Trabecular bone at the tissue-level has a local orientation of the lamellae along the long axis of the trabeculae and thus trabecular bone can also be regarded as transversal-isotropic [34]. Measuring the tissue properties is challenging, due to the size of the individual building blocks and the

inhomogeneous distribution of collagen and mineral. Nevertheless, many experimental methods are nowadays available, ranging from conventional mechanical testing, over ultrasonic testing, micro- or nano-indentation methods, to micro-mechanical testing.

Measurements of both cortical and trabecular bone at the tissue-level yielded a wide range for the elastic modulus from $1\,\mathrm{GPa}$ to $26\,\mathrm{GPa}$ [119]. Using additional FEA after mechanical testing, allows for the back-calculation of the tissue modulus, which yielded values between $4\,\mathrm{GPa}$ to $14.6\,\mathrm{GPa}$ for trabecular bone [121–124]. Rietbergen and Huiskes [34] therefore noted: "*Based on the large variation in the results obtained from these studies, it has been questioned if the tissue properties of trabecular bone can be defined at all*". It seemed that advances in nano-indentation made it finally possible to measure the tissue properties reliably [125] and using such measurement resulted in very good fits between experiments and FE models, even though only isotropic material properties were used [126]. However, nano-indentation itself is limited by measurement in dry condition, as in wet conditions the indentation location cannot be found reliably [127]. Furthermore, the heterogeneity of mineralisation and anisotropy of the bone tissue itself leads to variable measurements even in small regions of the same trabeculae [127]. Similar to previous studies employing other measurement methods, a wide range of tissue moduli was found with nano-indentation, even in single specimens [127]. Recently, the mechanical testing of individual trabeculae under physiological conditions was identified as an alternative to find the tissue material properties [128]. Despite a variety of advanced methods, the range of measured elastic moduli at the tissue-level is still large ($1.2\,\mathrm{GPa}$ to $22.3\,\mathrm{GPa}$) but it is expected to become smaller in the future as more studies are conducted [129].

Even though bone at the tissue-level is anisotropic, it is often simply modelled as an isotropic material. Using only an isotropic material can be justified, as trabecular bone tissue is typically loaded in such a way that only the longitudinal modulus plays a role during loading [34]. Hence, this longitudinal modulus can be regarded as the effective isotropic modulus at the tissue-level [34]. Furthermore, the exact Poisson's ratio at the tissue-level only has a negligible role for the mechanical properties on higher levels [130] and is thus often assumed to be between 0.2 to 0.4 [127], with a typical choice being 0.3.

Gathering tissue properties of bone is actually not an easy task. But what about the continuum-level? First, it is important to understand what the term "continuum" actually means and where it begins and where it ends. The continuum-level is a rather fuzzy length scale, on which the heterogeneous microstructure can be regarded as a homogeneous macrostructure. This so called *homogenisation* makes it possible to establish a structure-property relationship and effectively reduce the number of variables required to determine mechanical properties of the microstructure. To make this homogenisation work, a "separation of scales" is required, that is, the requirement of the continuum-level to be sufficiently large, such that the microstructure can be sampled in a meaningful way

but also sufficiently small, such that gradients on the macrostructure are negligible [131]. A volume element that fulfils these conditions is also named representative volume element (RVE) [132]. As the name suggests, the volume element has to be "representative", e.g., a volume that represents a (periodic) unit-cell of the macro-material. For example, engineering materials, such as woven fibre-composites, or materials with periodic holes or structures can typically be modelled as unit-cells. However, trabecular or cortical bone volumes are very heterogeneous, that such an RVE cannot be defined, as there is simply no unit-cell [133]. Therefore, these volumes are simply named volume element (VE) in the process of trabecular bone homogenisation [133]. For trabecular bone, a rule of thumb is that at a VE should contain at least five times the trabecular spacing (Tb.Sp) of the trabecular bone [134], which corresponds to $3\,\mathrm{mm}$ to $5\,\mathrm{mm}$ for human bone [34], while others regard bone at the continuum starting only at around $5\,\mathrm{mm}$ [135]. Zysset, Goulet and Hollister [136] found $4\,\mathrm{mm}$ a "low but reasonable choice". An upper bound is typically given at around $10\,\mathrm{mm}$ [93], as on larger length-scales the heterogeneity of the trabecular bone increases. This can also be observed in Figure 2.3, as dense and sparse parts can found throughout the femoral head. For cortical bone, the same concept of an RVE or VE holds.

While at the level of the continuum one does not have to deal with fiddly bone samples, measurements at this size are still not straight forward, due to the complex structure of trabecular bone. For cortical bone, such measurements are simpler though. When using trabecular bone volumes for mechanical testing (typically cubes or cylinders), they have to be cut out of the bone for the test. This leads to several challenges during mechanical testing, of which a few shall be outlined here. Such mechanical tests can, even with perfect conditions, only identify up to nine independent material constants, thus bone has to be regarded as orthotropic, even though it is anisotropic [34]. To be able to measure the orthotropic material constants, the material axes of orthotropy has to coincide with the axes of the bone cube [34]. However, due to the heterogeneity of the trabecular structure inside such a bone volume, it is challenging to find such samples and align them properly. Furthermore, the same principle of representative volume elements applies and thus the bone volume has to be sufficiently large, which is again a challenging task, due to the heterogeneity of the trabecular bone. Lastly, the trabecular structure at the boundary is damaged during cutting which can then lead to mechanical properties different to the ones the bone sample would have *in situ* [34]. There are methods to reduce or even prevent such "end artifacts" but they typically require larger samples to be cut, which again complicates the matter for the already outlined heterogeneity of the trabecular bone [34]. Thus, while the experimental determination of mechanical properties of trabecular bone is possible at the continuum-level, only rigorous experimental design and sophisticated methods allow for a proper measurement.

As already foreshadowed, material properties can also be inferred using homogenisation methods, where a multitude of both analytical and numerical method exists [131]. The intent of these methods is to find an energetically equivalent (i.e., thermodynamically consistent) homogeneous macro-material for the inhomogeneous microstructure [131]. Parametrisation of this material in terms of constituents allows for an efficient structure-property relationship. The process of homogenisation is complex and the mathematical details cannot be outlined here for brevity. The interested reader is referred to the report by Böhm [131], which gives a general overview on the topic and provides many references to more elaborate literature.

In one of these homogenisation methods, an VE of trabecular bone is transformed into a μFE model and six canonical load cases are imposed on the bone (Figure 2.9). This method is also referred to as "computational homogenisation" of trabecular bone. Many different boundary condition types can be used, as long as they comply to the homogenisation theory. Two specific types of these boundary conditions are displacement controlled (kinematic uniform boundary condition (KUBC)) or displacement and traction controlled (periodicity compatible mixed uniform boundary condition (PMUBC)) [133]. However, the usage of such boundary conditions does not yield the *effective* material properties but only *apparent* properties, because the boundary conditions themselves influence the obtained stiffness. The apparent stiffness tensor for the material can then be efficiently calculated from the resulting stresses and strains of those six load cases. The resulting apparent stiffness tensor is in general anisotropic (21 variables), but material models typically incorporate some sort of symmetry (Figure 2.9b), such as isotropy (2 variables), cubic symmetry (3 variables), transverse-isotropy (5 variables), or orthotropy (9 variables). The anisotropic tensor can be transformed into a similar symmetrised tensor, effectively reducing the number of variables, by employing a tensor norm and minimising the error between the anisotropic and symmetrised tensor [137, 138]. Such a symmetrisation is typically performed to reduce the complexity of the model.

In a next step, a material model can be fitted, using morphometric indices as parameters for the model. At the continuum-level of trabecular bone, three main components were identified, contributing to the elastic properties: the relative density, the orientation of the trabeculae, and the mechanical properties of the tissue itself [93]. Trabecular bone can be regarded as orthotropic at the continuum-level, with the orientation of the three cardinal axes in the direction of the fabric tensor [34]. However, also more symmetry constraints can be applied, for exampling resorting to a simple isotropic material. It was found that the structure-property relationship of trabecular bone can be described using an isotropic power-law with an exponent typically in the range of two to three [34]. However, also the orthotropic material behaviour can be modelled, for example using the Zysset-Curnier model [139].

Both the isotropic power-law, as well as the orthotropic Zysset-Curnier model are based on similar equations, to get to the elastic material properties. The power-law

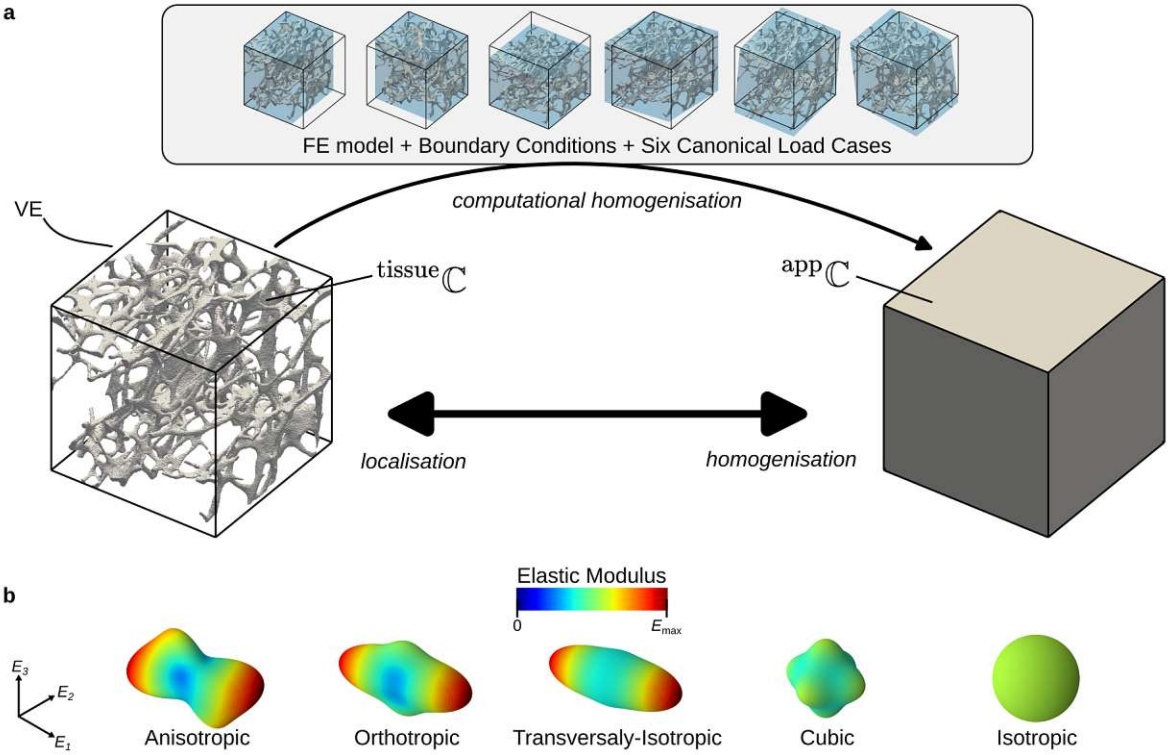

Figure 2.9: Schematic overview of computational homogenisation of trabecular bone. (**a**) A volume element (VE) in the form of trabecular bone is used to find the apparent homogeneous mechanical properties at the macro-scale. To find these properties, finite element (FE) models are generated, boundary conditions are applied (here shown are kinematic uniform boundary condition (KUBC)), and six canonical load cases are required, from which the apparent stiffness tensor ${}^{\text{app}}\mathbb{C}$ can be calculated using the tissue material properties ${}^{\text{tissue}}\mathbb{C}$. (**b**) Overview of symmetries of the stiffness tensor. Shown is the maximal elastic modulus (Young's modulus) in each direction. The symmetries can clearly be seen from the plots. Isotropy has the highest symmetries and shows a spherical modulus plot.

has three parameters: The base elastic-modulus E_0, the base Poisson's ratio ν_0, and the density exponent k. The following equation is used to get the density dependent elastic-modulus:

$$E = E_0 \, \rho^k \tag{2.1}$$

The Poisson's ratio is not adjusted by the density and simply is the base Poisson's ratio:

$$\nu = \nu_0 \tag{2.2}$$

The Zysset-Curnier model is an extension of the power-law model and uses, additionally to the density, the three eigenvalues m_i of the fabric tensor [94]. The fabric tensor has to be scaled first, such that $m_1 + m_2 + m_3 = 3$, which can be achieved by scaling the trace of the fabric tensor. An exponent l is used to scale these eigenvalues, additionally to the density-exponent k. The model consists of five parameters: E_0, ν_0, k, l, and the base shear-modulus G_0 and yields three independent elastic-moduli (Eq. (2.3)), as well as three independent shear-moduli (Eq. (2.4)), and three independent Poisson's ratios (Eq. (2.5)).

$$E_i = E_0 \, \rho^k \, m_i^{2l} \tag{2.3}$$

$$G_{ij} = G_0 \, \rho^k \, (m_i m_j)^l \tag{2.4}$$

$$\nu_{ij} = \nu_0 \left(\frac{m_j}{m_i} \right)^l \tag{2.5}$$

In the case of an material with all eigenvalues equal to 1, the model only yields three independent constants, as $E_i = E_0 \, \rho^k$, $G_{ij} = G_0 \, \rho^k$, and $\nu_{ij} = \nu_0$, and is thus cubic-symmetric. It further reduces to the isotropic power-law model (Eq. (2.1)), if Eq. (2.6) is fulfilled for E_0, G_0, and ν_0.

$$\nu_0 = \frac{E_0}{2 \, G_0} - 1 \tag{2.6}$$

2.3.3 Inverse Bone Remodelling

It was already outlined, that bone can adapt to new functions using (re)modelling. As functional adaptation is partially driven by external mechanical signals, it is thus natural to incorporate biomechanical analysis into the analysis of bone's microstructure. The joints and entheses are in the focus of the analysis, as each activity has its unique set of joint postures and muscle activation patterns. Subsequently, these external biomechanical factors will manifest in the microstructure. The bone microstructure can therefore also be used to infer information of external loading.

While so called forward (re)modelling simulations can be used to predict the properties of the bone microstructure for a defined loading, inverse bone remodelling (IBR) tries to invert this process and predicts the (daily averaged) loading that led to a given

density distribution (i.e., the bone microstructure). As the name denotes, it is a inverse problem, that comes with certain limitations [140]. In general, such inverse problems do not have unique solutions, except for simple 1D cases [141]. The reason is, that the number of variables quickly gets larger than the number of available equations and thus no unique solution can be found anymore. It is obvious, that multiple combinations of forces can indeed lead to the same resultant force that drives the (re)modelling and without further knowledge, it is not possible to uniquely determine the real set of forces, if only the resultant force or any arbitrary set of forces with the same resultant force is known. However, by restricting the model to a set of possible load cases will decrease or even remove this ambiguity. While analytical solutions are not available, solutions can still be found numerically by using optimisation procedures.

The first such IBR models were created by Fischer, Jacobs and Carter [142]. They used 2D hFE models and an optimisation criterion, based on the remodelling theory by Beaupré, Orr and Carter [143]. These models follow the mechanostat, and assume that the tissue requires a certain daily target stimulus to stay in homeostasis. If the target stimulus is not reached, bone would be resorbed and a level higher than the homeostatic value would lead to bone apposition. If it is assumed that a bone is in homeostasis (i.e., there is no functional adaptation at the moment of measurement), it is then possible to identify this homeostatic loading condition by finding a loading that loads the bone homogeneously with the target stimulus. That means, that the inverse problem can be written as an optimisation problem, minimising the difference to this target stimulus. The model of Fischer, Jacobs and Carter [142] uses effective stress as the target stimulus. As the model uses homogenised elements, the effective stress is translated to a tissue-level stress in the model. A couple of years later, Christen *et al.* [144] implemented IBR with μFE and a similar optimisation criterion (Figure 2.10). As the element size of μFE is already at the tissue-level, no conversion from continuum to tissue-level is necessary and SED was used instead of effective stress. At about the same time, a different method was developed using artificial neural networks (ANNs) [145, 146]. Here, many forward remodelling simulations are used to train an ANN to predict the load cases based on the density distributions. These models also used hFE models of bones in 2D, but also 3D variants exists [147]. Yet another method is the “reverse trajectorial approach”, which uses principal stress trajectories [148–150]. The principal stress trajectories, computed using FEA, are compared to the orientation of the trabecular bone and the load cases are identified where principal stress trajectories and orientation show the highest agreement. These models incorporated also musculoskeletal models in combination with FEA. A variation of this method only uses the principal orientation of the trabeculae without the need for FEA [151] and these “structural signals” could be used to infer hip loading conditions from fossils [152]. Using time-lapsed μCT images, it is also possible to derive the (re)modelling state (formation, resorption, quiescence) of

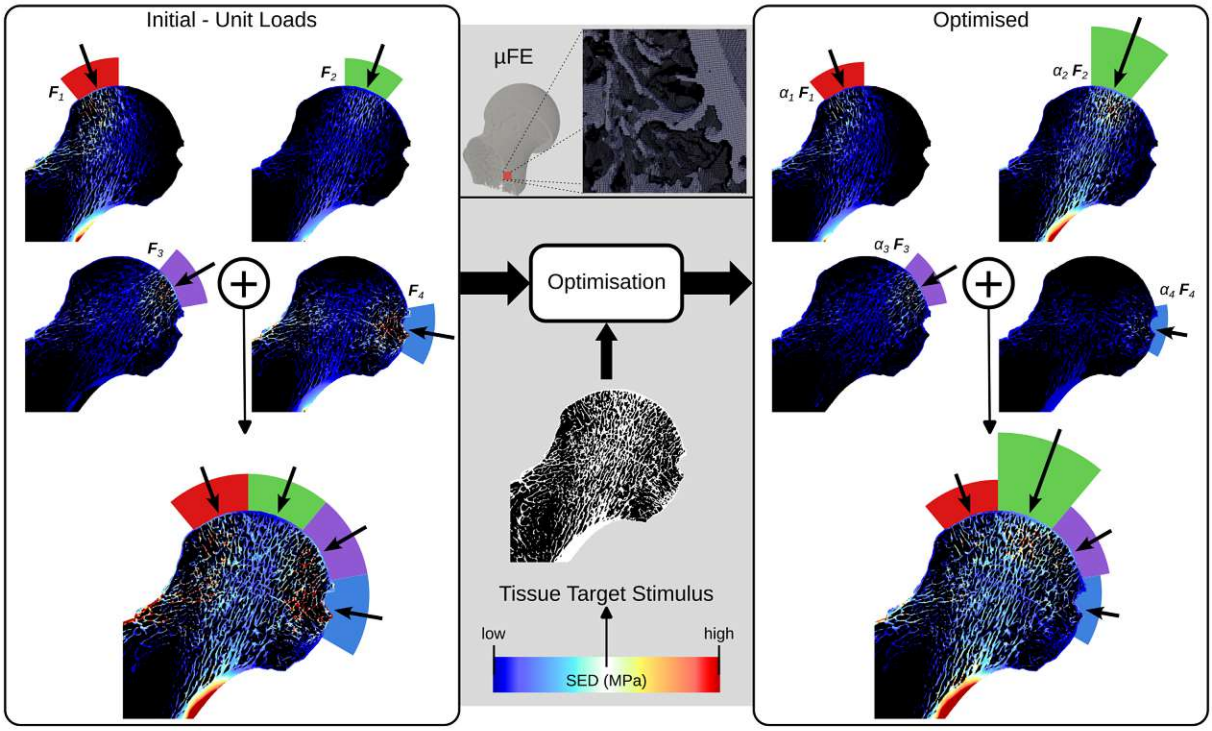

Figure 2.10: Inverse bone remodelling (IBR). A schematic overview of the process according to the μFE-based method of Christen *et al.* [144], shown for the femoral head by Synek *et al.* [70]. Unit load cases $\boldsymbol{F}_1$ to $\boldsymbol{F}_4$ are applied on a μFE model of a bone. Then, for each load case a mechanical quantity, in this case strain energy density (SED), is evaluated and fed into an optimisation function. The optimisation function scales the load cases such, that the difference of the sum of all load cases and the tissue target stimulus is minimal. This then yields scaling factors α_1 to α_4 for the unit loads.

a volume of bone and use this information in an enhanced IBR method of the Christen *et al.* [144] model [153].

All these models have in common, that loading scenarios that were not part of the initial set of load cases (unit loads) can not be found. This means, that the IBR method can only find scaling factors for load cases it knows *a priori* and due to the underlying functional adaptation law, it is only able to identify the time and load-averaged loading. It is also not possible to pinpoint a single activity with the IBR method, but merely the overall *loading history*. The information regarding single activities is simply not stored in the bone microstructure. This behaviour was also shown experimentally using trabecular bone cubes [154]. When bone cubes with an artificial structure were used, that were optimally oriented for a single load case, IBR could find this loading with very low residuals towards the target stimulus, while for real bones, these residuals were always higher, even though the cubes showed a visible orientation of the trabeculae. This indicates, that real bone is adapted to a multitude of loads, i.e., the time and load-averaged loading history, but also other, non-mechanical signals influence the bone adaptation [154].

Out of all the recently developed IBR methods, the μFE-based method by Christen *et al.* [144] is the easiest to apply, as μCT images of bones can directly be converted into μFE models. Furthermore, the elegance of this model lies in its simple optimisation criterion, defined on the tissue-level of bone. But this simplified optimisation criterion and easy image processing comes with the price of high computational effort for solving the μFE models and is limited to simple boundary conditions, due to the "voxellated" surface of the models [155].

On the other side of the spectrum are hFE-based models, such as the IBR method by Fischer, Jacobs and Carter [142]. hFE requires some extra modelling effort but offers faster solving times and the possibility to use a wide variety of boundary conditions, already part of many FE-solvers available today. While the modelling effort can be negligible, with the employment of automatic meshing tools [156], also the optimisation criterion itself requires an adaptation, as the (re)modelling theory (e.g., the "mechanostat") is defined on the tissue-level and not at the continuum-level, employed in hFE. The law used by Fischer, Jacobs and Carter [142] is based on analyses of porous media [157, 158] and is used to convert the effective stress at the continuum-level to an effective stress on the tissue-level using a power-law of the element's density. This power-law stems from the relationship of ultimate strength of trabecular bone on the two levels.

The ANN models, which also employ hFE, circumvent this issue, as the density distributions, required for model training, can be generated with any existing validated forward (re)modelling law. Thus no connection between tissue and continuum target stimulus is required in the IBR model *per se*, but inherently requires homogenised material properties for the forward (re)modelling models. It should also be noted, that these models can only predict the phenomenological response and do not provide a direct mechanical reason for the choice of the optimal load cases. While it is in principle possible to compute the local mechanical stimuli for the found optimal load case using FEA, this extra step is not required for the other IBR implementations (by Fischer, Jacobs and Carter [142] or Christen *et al.* [144]), as FEA is already the basis for their predictions.

So far, only a few studies investigated how well hFE or μFE-based IBR models can actually predict the loading history by comparing it to actual *in vivo* loading data. Moreover, studies comparing μFE and hFE models are still scarce.

2.4 Infer Habitual Physical Activity from Bone Microstructure

We have seen that bones are constantly changing and adapting, due to (re)modelling. As (re)modelling is partially driven by the (outer) mechanical loading of the bones, new habitual physical activies are also "learned" by the bones. Therefore, functional adaptation is of interest in evolutionary anthropology, as the knowledge, which habitual activities a living being engaged in during its lifetime are important to understand the evolution and are also of interest to understand what long extinct species were capable of [72].

While certain changes of bones are driven by genetics (genotype) and thus can show slow but general trends, functional adaptation can also show adaptation, that happened only during the lifetime (phenotype) [159]. However, also a phenotypic adaptation can lead to genotypic adaptation, by natural selection over a long period [159]. To overcome the ambiguity of the term *functional adaptation*, Main, Simons and Lee [159] used two more specific terms, namely *plasticity adaptation* and *evolutionary adaptation*, to highlight the short-term and reversible adaptation and the long-term, macroevolutionary adaptation. For example, while humans show a general difference in morphology in their arms compared to orangutans, due to evolutionary adaptation over millions of years, a professional tennis player will show a plasticity adaptation of its arms, due to more frequent tennis playing in comparison to other humans [160]. This differentiation in terminology between the two types of functional adaptation is, however, not important for the course of the thesis. While the here developed methods can be applied for both types, care has to be taken though that plasticity adaptations are not confounded with evolutionary adaptations and *vice versa*. Thus, it is good to keep this differentiation at the back of one's mind.

One advantage of the analysis of bone microstructure is that trabecular bone has a higher turnover rate compared to the denser cortical bone and thus, entheses (which are part of the cortical bone) [75] or the overall shape of the bone changes slower than that of trabecular bone [9]. Furthermore, certain features of bones are also bound by other factors, for example, the geometry of a joint is bound by its function and thus a change in geometry of the joint will typically occur much slower than a microstructural adaptation. Functional adaptation is not regulated systemically but only locally [161]. Thus, changes of the microstructure only occur in the loaded bones, but not at other locations of the skeleton, distant from the external stimulus. But bone microstructure does not change only due to functional adaptation, but there are also other influencing factors, for example, nutrition [162], chronic inflammation [163], kidney-related disorders [164], age [165, 166], hormonal changes due to menopause [167], ontogenesis [168], genetics [169], or other (lifestyle) factors [165]. Furthermore, not every habitual activity will be stored in the bone, as the *time and load averaged* stimulus drives the

functional adaptation. As a final limitation, a functional adaptation once made, might be reverted or replaced if the habitual activity is suspended for a prolonged time or replaced by another. However, a recent study found a chronic manifestation of some of the functional adaptations imprinted in the bone during an acute phase of loading in a murine model and thus it is plausible, that some functional adaptations are even stored in a "structural memory" over a long time [170]. Still, the bone microstructure is best used for the inference of recent, or even lifelong activities, that lasted at least several years before imaging the bones or in case of fossils, in the years before death.

Given all these limitations and imponderables, it might sound as if microstructure analysis is actually too limited and other methods to infer habitual activities are better suited. But microstructure analysis is only a single tool in the methodological toolbox (Figure 2.11), and experiments have to be conducted as well, to verify findings [171]. Both biomechanical or morphometric analyses can be thought of as puzzle pieces between many different methods, such as the analysis of associated findings during archaeology (tools, footprints, flora, or fauna) [172], novel methods such as aDNA analysis [6], or the analysis of diet using strontium-isotope analysis [5]. Finally, for extinct species, where only the fossilised bones are found, the alternatives, for example, musculoskeletal models or *in vivo* measurements, are limited. Thus, microstructure analysis offers an important source of information, especially if combined with other methods [9].

But how can one finally infer the habitual activity of extinct species based on microstructure analysis? A commonly used method is comparison to extant species. Activities can be observed in those extant species, correlated to their bone microstructure, and subsequently compared to the microstructure of the extinct individuals. For the analysis of humans and its ancestors, the extant hominids[5] are used as a comparative set (for example see [173]). Not only our closest ancestors, bonobos, chimpanzees, orangutans, and gorillas are used, but also monkeys are often included in such comparisons (for example see [174]). However, these primates are not "frozen ancestors", but have developed on their own over the last million years [175]. And thus also the comparison between samples of the fossil record of the hominids yields valuable information. Also direct approaches, such as IBR can be used and were successfully applied for the reconstruction of habitual activity [70, 148–150, 176–178].

Inferring habitual activity is not only a task for anthropologist and the investigation on fossilised bones. Also in medicine, such methods can be useful, for example, to estimate physiological loading conditions directly from CT images. Use cases are, for example, proper modelling or the diagnosis of bone-related diseases as well as monitoring of bone healing after fracture or implantation. However, in clinical use cases, the focus is on the

[5]The hominids, or hominidae, are a taxonomic family that include the great apes and humans. These include the extant genera *Pongo* (orangutan), *Pan* (bonobos and chimpanzees), *Gorilla* (gorillas), and *Homo* (humans). However also extinct genera, such as *Australopithecus* or *Paranthropus*, relatives of the current living ones are counted in this taxonomic family.

Figure 2.11: Inferring habitual physical activity from bones is a multidisciplinary task, where the microstructure and biomechanical analysis are just puzzle pieces. The whole fossil record as well as comparative sample sets of recent species are required. Furthermore, all archaeological findings such as tools, footprints, flora, fauna, fire-usage, and more might be incorporated into the inference. Experiments might be conducted to verify findings and recent methods such as ancient DNA (aDNA) can enhance the understanding even more.
This image contains Creative Commons licensed work. A detailed description can be found in the chapter “Image Credits” at the end of this thesis.

inference of loading conditions from *in vivo* data. This complicates the methodology, because high resolution imaging is often not available, or limited to peripheral bones. Therefore, morphometric analysis and μFE-based IBR methods are often only available for these peripheral bones. Nevertheless, technical advances in medical imaging allow for higher resolution even *in vivo* at any position in the body, for example by using photon-counting CT [179], and methods such as IBR were initially developed with only clinical QCT resolutions available, although only applied in simple 2D models so far [180].

Chapter 3

Canonical Holistic Morphometric Analysis

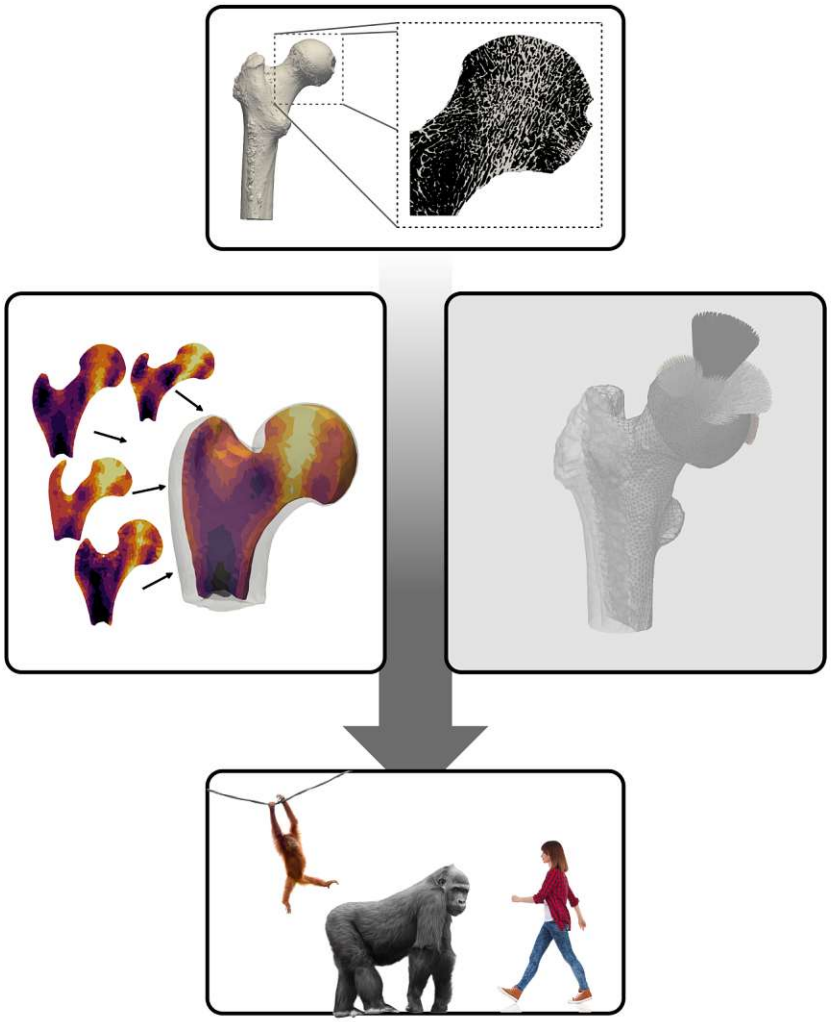

As described in the background chapter (section 2.2.3), one of the most sophisticated methods, for the analysis of trabecular bone microstructure is the holistic morphometric analysis (HMA) method. However, a limitation of this method was, that these comparisons could not be done quantitatively. In this chapter, an enhanced version of the HMA method, called canonical HMA, or cHMA, will be presented that enables also quantitative comparison of bone morphometry in homologous regions. This chapter is divided into three sections: In section 3.1, the development and validation of the method is outlined, section 3.2 gives some examples for methods of evaluation, which are possible with the novel cHMA method. Finally, section 3.3 covers in more detail some limitations of the method and directions for future research, which were only briefly laid out in the discussion of sections 3.1 and 3.2. The essential background information are repeated briefly in the beginning of sections 3.1 and 3.2, while more detailed information were already presented in chapter 2.

3.1 Method Development and Validation

3.1.1 Related Publication and Declaration of Contributions

This section is based on the publication

> S. Bachmann, C. J. Dunmore, M. M. Skinner, D. H. Pahr and A. Synek. 'A computational framework for canonical holistic morphometric analysis of trabecular bone'. In: *Scientific Reports* 12.1 (2022), p. 5187. DOI: 10.1038/s41598-022-09063-6

Author contributions: **Sebastian Bachmann**: Conceptualisation, Methodology, Software, Validation, Formal analysis, Investigation, Writing - Original Draft, Writing - Review & Editing, Visualisation. **Christopher J. Dunmore**: Conceptualisation, Formal Analysis, Resources, Data Curation, Writing - Review & Editing. **Matthew M. Skinner**: Conceptualisation, Resources, Writing - Review & Editing, Project administration, Funding acquisition. **Dieter H. Pahr**: Conceptualisation, Methodology, Writing - Review & Editing, Supervision. **Alexander Synek**: Conceptualisation, Methodology, Writing - Review & Editing, Supervision.

Acknowledgements: This project has received funding from the European Research Council (ERC) under the European Union's Horizon 2020 research and innovation program (Grant agreement No. 819960).

The authors are grateful to: Jean-Jacques Hublin (Collège de France, Paris), Christophe Boesch and Uta Schwarz (MPI-EVA, Leipzig), Emmanuel Gilissen and Wim Welden (Royal Museum for Central Africa, Tervuren), Maria Teschler-Nicola and Ronald Muehl (Natural History Museum, Vienna), Jacopo Moggi-Cecchi and Silvia Bortoluzzi (University of Florence, Florence), and Birgit Großkopf (Johann-Friedrich-Blumenbach Institut für Zoologie und Anthropologie der Georg-August-Universität Göttingen, Göttingen), Inbal Livne (Powell-Cotton Museum, Birchington) and Nicole Edmison (Smithsonian Institution National Museum of Natural History NMNH, Washington D.C.), for access to specimens in their care. For technical assistance we would also like to thank Habiba Chirchir (Marshall University, Huntingdon), Patrick Schoenfeld and David Plotzki (MPI-EVA, Leipzig).

3.1.2 Introduction

Living bone can functionally adapt [72] to loads it experiences and thus reflects, to some extent, the behaviour of individuals over their lifetime. This functional adaptation, caused by modelling and remodelling of bone [40], has been experimentally demonstrated in external shape change [72, 181], the thickening of cortical bone [72, 182],

entheseal shape change on the cortical bone surface [183, 184], and change in the architecture of trabecular bone [74, 185], or a combination of these phenomena. Unlike cortical bone, trabecular architecture is usually completely internal, concentrated in the epiphyses of long bones, and far more porous at the mesoscale [33]. As a result of these and many other differences, trabecular bone reacts to experienced loads differently than cortical bone, and thus records different information about these loads. Inference of function from trabecular bone architecture is complicated by genetic, ontogenetic [168], and systemic [186] factors that also influence bone form. However, numerous studies have found trabecular architectures that reflect assumed habitually and significantly loaded joint postures [103, 187–198], regardless of whether this load is gravitational, muscular, or a combination of both [199, 200]. Thus, analysis of trabecular architecture provides additional information that can be combined with studies of internal and external cortical bone morphology, to provide a more holistic understanding of how bone reflects behaviour. We can use the bone morphology of recent species, with observable behaviours, to infer behaviour patterns of extinct species [9]. Therefore, methods to evaluate the trabecular morphologies of different species and compare them, offer an important tool to help answer evolutionary biological or anthropological questions.

Many different protocols exist to quantify the inner, trabecular structure of bone. These range from quantitative computed tomography (QCT) with a coarse resolution in the range of half a millimetre to high resolution techniques such as micro-computed tomography (μCT) with resolutions in the micrometre range. Using QCT it is possible to get estimates of bone-mineral density or bone volume fraction (BVTV), however other morphometric quantities can only be assessed at a high resolution, which is able to depict the trabecular structure in detail. μCT allows for the imaging of the complete trabecular structure, and a variety of CT-based morphometric quantities exist to describe the bony network [89]. Two parameters, namely BVTV and local anisotropy, measured via a fabric tensor, are of special interest. BVTV alone accounts for approximately $87\,\%$ and both values together for $97\,\%$ of the trabecular stiffness, which is a proxy for the mechanical properties of the bone [100].

Morphometric quantities can be measured for the whole trabecular volume, which yields a single value which can be compared between samples. However, the trabecular structure can be very heterogeneous - for example at the proximal femur - and thus it is not possible to gather precise differences using summary statistics on this multi-modal distribution. Therefore, a common approach is the use of regions of interest (ROI), where a subsection of the trabecular volume is selected for the investigation. One or multiple, spherical, cubic or arbitrarily shaped ROIs can be used. However, the placement of the ROI inside the bone at a homologous, i.e., anatomically equivalent, location is crucial when comparing different individuals and can be challenging in species with disparate morphology [105]. To ameliorate such problems, multiple ROIs [201, 202] or sectors [203–206], or the combination of both [207] can be used.

Another method that avoids many of these issues, is holistic morphometric analysis (HMA) [103, 104]. HMA can map the morphometric quantities continuously over the whole trabecular volume onto volume meshes, which can then be visualised and compared qualitatively between different samples without ROI selection. It was successfully applied to a variety of bones, including carpals, metacarpals and phalanges [103, 191–194, 206], proximal femora [195–197], distal femora [198], distal tibiae [195], proximal humeri [195], distal radii [187], and first metatarsals [188]. However, HMA is not yet able to compare the site-specific morphometry, below the sector level, for different individuals quantitatively in homologous regions [9, 189, 190].

The HMA method was already successfully applied in combination with other methods. For example a sector-based analysis [189, 206] can be employed, but, as with other sector methods, requires *a-priori* geometric division of the trabecular structure. Trabecular mapping [208] offers another way, where morphometric quantities are measured below the cortical bone and mapped onto the periosteal surface. A similar approach was applied to map HMA morphometric quantities to the endosteal surface of metacarpals [193, 194]. However, both of these approaches are necessarily limited to analyse the edge of the trabecular network. Volumetric sliding semi-landmarks [209] and coherent point drift [210] allow for volumetric quantitative comparisons between samples using HMA [190].

The principle in these methods is to find a canonical representation, either a surface or volume, on which all samples can be mapped, measured and finally compared. A volumetric canonical bone can also be created using statistical deformation models (SDM) [211]. The individual bones can then be registered onto the canonical bone and isotopological meshes can be created using mesh-morphing [212]. The advantage of the SDM approach is that it is landmark-free, and thus requires no extra annotation of the data. However, currently SDM methods have only been applied to QCT data, whereas μCT data is required in order to evaluate CT-based morphometric quantities. Furthermore, SDM approaches have, so far, only been used to create canonical models in a single species, which often have less inter-subject variation in bone shape.

As the SDM is typically used to register bones of similar shape and texture, that are bones of a single species, the question arose if the SDM is actually capable of registering bones with dissimilar shape and texture. To systematically test the performance of the SDM, synthetic data can be used in the registration procedure [213, 214]. The synthetic data is required to have full control over the parameters and be able to create the canonical bone analytically as a baseline for the tests.

The goals of this study were (1) to investigate whenever it is possible to use SDM to construct a canonical bone using synthetic and real μCT images of different species and (2) to identify model parameters and investigate the robustness of the SDM using a set of first metacarpal bones of various primate species.

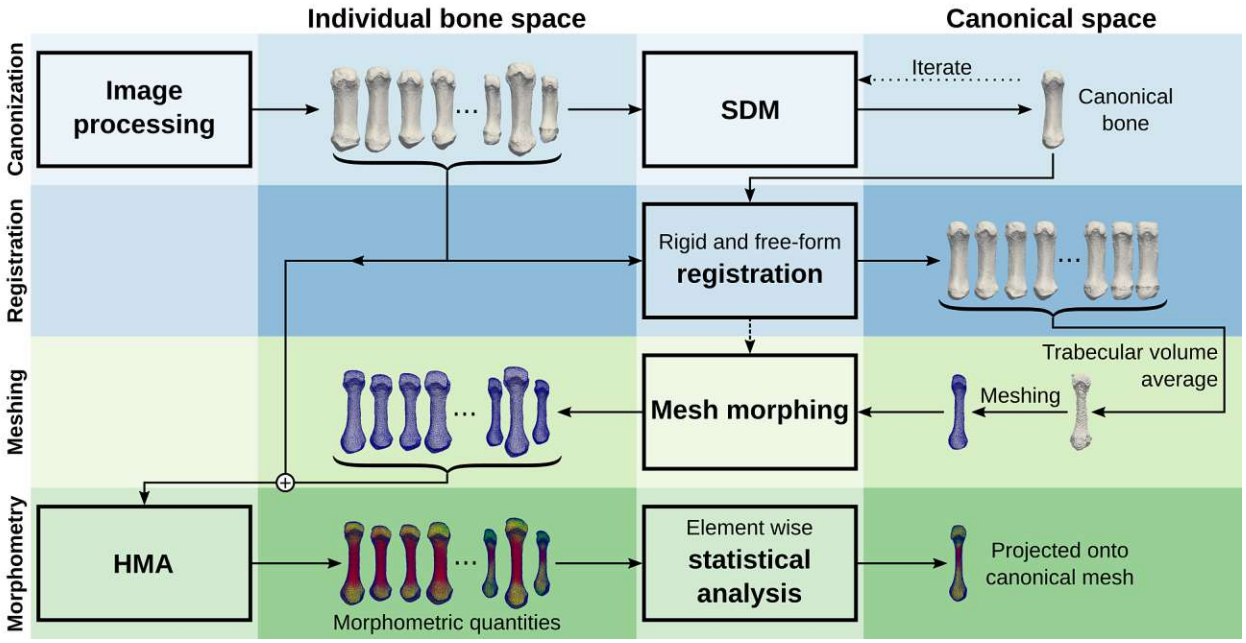

Figure 3.1: Graphical summary. Each block describes a separate step in the workflow, which runs from top to bottom. The four main steps are the creation of the canonical bone, the registration of all individual images, the meshing part, and finally the evaluation of the morphometric quantities and statistical analysis.

3.1.3 Methods

Outline

The cHMA method extends the established HMA workflow and combines it with several other methods. A graphical summary can be seen in Figure 3.1. It works by creating a canonical reference onto which different HMA results can be mapped and thus directly compared. The first stage of the workflow is to create a canonical bone image by using a statistical deformation model (SDM). In the next stage, all individual bone images are registered onto the canonical bone image, yielding transformations that map each bone volume onto the canonical bone image. The trabecular volume within all individual bone images is transformed into the canonical space, averaged, and meshed using a tetrahedral mesher, which is then referred to as the canonical mesh. Isotopological meshes are created by morphing the canonical mesh back into each individual bone space. The HMA method can then be applied using the original bone images and these individual meshes, which possess homologous elements across the sample. In a further step, the mapped morphometric quantities can be statistically compared at each element across the samples. If required, results of HMA or the statistical analysis can be mapped back onto the canonical mesh and evaluated further.

Holistic Morphometric Analysis

The established HMA method is the basis for the new cHMA workflow and is described in detail by Gross *et al.* [104] and Tsegai *et al.* [103]. It is a general extension of the FE material mapping algorithm by Pahr and Zysset [215]. Therefore only a brief outline shall be given here; the workflow is shown graphically in Figure 3.2. HMA can map a wide variety of morphometric quantities of bones [89] from both trabecular and cortical volumes onto finite element meshes. Binary segmented μCT images, depicting the microstructure of the bone, are used as the input for HMA. The first step of the process is to separate the trabecular volume from the whole volume using the "fill" method [156]. This method creates two image masks for the bone: a cortical and a trabecular mask. Separate masks are required to measure morphometric quantities unique to either the cortical or the trabecular bone. Then a volumetric mesh is created for the cortical and the trabecular volume, respectively. In the next step a regular grid, the so called background grid, is created and morphometric quantities are evaluated in a spherical volume of interest (VOI) centred at each grid vertex. The VOI act as region of interest (ROI), similar to classical morphometric approaches, but are named differently to avoid confusion when sub-regions of the bone are evaluated and additional "real" ROIs are used. The spheres have the same radius as the spacing of the grid, thus the sampling spheres overlap. Typically, $2.5\,\mathrm{mm}$ grid spacing and $5\,\mathrm{mm}$ sphere diameter are used due to the underlying homogenisation theory [133, 215]. To cope with VOIs overlapping the bone volume, a "zero-volume correction" is applied. The background (i.e., voxels which are neither labelled as trabecular or cortical bone) is ignored in the VOI and only the trabecular or cortical volume inside the VOI is regarded for the evaluation. This correction got its name as the background counts as "zero volume" in the evaluation. In the last step, the measured values at the background grid vertices are interpolated trilinearly at the centroids of the mesh elements. For certain morphometric quantities, such as degree of anisotropy, the sphere diameter has a lower bound, while other quantities, such as bone volume fraction, can in theory use smaller sphere diameters too [216]. Larger VOI diameters are also possible, resulting in a more averaged but also faster mapping. However, too large diameters result in very high averaging, and thus also a smoothing of density gradients in the resulting image.

Statistical Deformation Models

The statistical deformation model (SDM) was originally developed by Rueckert, Frangi and Schnabel [217] and the process shall be repeated here briefly. The main idea of the SDM is, that the variability in medical images, for example, of different patients, can be described using the average deformations of all images. Such a deformation is created by using an image transform $\boldsymbol{T}$, for example, a B-spline transform in the case of SDM [218]. Such B-spline transforms can be used to deform the image locally, and are therefore also

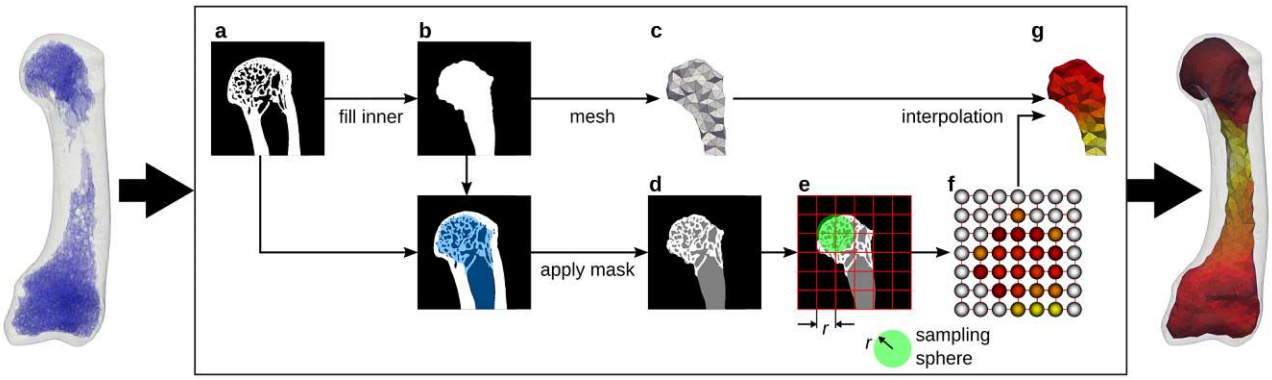

Figure 3.2: Mapping of morphometric quantities of trabecular bone onto finite-element meshes using the HMA method. The schematic overview shows the required image processing steps for a 2D slice, although the principle is similarly in 3D. (**a**) Original segmented μCT image. (**b**) Trabecular mask. (**c**) Mesh generated from trabecular mask. (**d**) Masked trabecular volume . (**e**) Evaluation of morphometric quantity using background grid with grid distance r and sampling sphere with radius r. (**f**) Evaluated quantity at the background grid vertices (spheres not to scale). (**g**) Linear interpolated quantity on the mesh.

referred to as "free-form deformations". The mathematical background of such B-spline transformations is presented here briefly and the here given formulation follows Rueckert and Aljabar [218]. The B-spline transform works by employing a 3D cubic B-spline function, that is parameterised using a control point grid Φ with $n_x \times n_y \times n_z$ $(n_x, n_y, n_z \geq 4)$ grid points, whose vertices (the vectors to these vertices) are denoted $\phi_{i,j,k}$ and are uniformly spaced with distance δ. A non-uniform spacing is also possible by scaling to a uniform spacing. The B-spline function is defined on the domain of an image volume $\Omega = \{\boldsymbol{p} = [x, y, z]^T \,|\, 0 \leq x < X, 0 \leq y < Y, 0 \leq z < Z\}$ with X, Y, Z being the dimensions of the image and $\boldsymbol{p}$ being any valid point in the image domain. The B-spline function can then be written as:

$$\boldsymbol{T}_{\text{bspline}}(\boldsymbol{p}) = \sum_{l=0}^{3} \sum_{m=0}^{3} \sum_{n=0}^{3} B_l(u)\, B_m(v)\, B_n(w)\, \phi_{i+l,j+m,k+n} \tag{3.1}$$

where $i = \lfloor \frac{x}{\delta} \rfloor - 1, j = \lfloor \frac{y}{\delta} \rfloor - 1, k = \lfloor \frac{z}{\delta} \rfloor - 1, u = \frac{x}{\delta} - \lfloor \frac{x}{\delta} \rfloor, v = \frac{y}{\delta} - \lfloor \frac{y}{\delta} \rfloor, w = \frac{z}{\delta} - \lfloor \frac{z}{\delta} \rfloor$. Here, i, j, k give the index of the control point grid[1] and $u, v, w \in [0, 1)$ are the fractional parts of the coordinate. B_l represents the l-th basis function of the B-spline, which can be calculated using a recursive equation. For the cubic B-spline, there are four such basis

[1]The keen reader has probably noticed that i, j, k can become -1. The definition of the control point grid is such, that this point exists, i.e., $-1 \leq i < n_x, i \in \mathbf{Z}$ and likewise for the other indices.

functions:

$$\begin{aligned} B_0(t) &= \frac{-t^3 + 3t^2 - 3t + 1}{6} \\ B_1(t) &= \frac{3t^3 - 6t^2 + 4}{6} \\ B_2(t) &= \frac{-3t^3 + 3t^2 + 3t + 1}{6} \\ B_3(t) &= \frac{t^3}{6} \end{aligned} \tag{3.2}$$

where $t \in [0, 1]$. These basis functions can also be thought of as weighting functions for the control points and have the property that the sum of all basis functions is equal to 1, for every t.

When all control points are at their initial position (i.e., form a regular grid), the transformation produces no deformation. Only if the control points are moved in space by a vector $\boldsymbol{u}_{i,j,k}$, a deformation can be described, i.e., for every point $\boldsymbol{p}$ of the input image, a new point $\boldsymbol{p}'$ is calculated using $\boldsymbol{p}' = \boldsymbol{T}_{\text{bspline}}(\boldsymbol{p}, \Phi')$ using the displaced control points ${\phi'}_{i,j,k} = \phi_{i,j,k} + \boldsymbol{u}_{i,j,k}$. Thus, the B-spline transform calculates the interpolation of the displacement field, based on the control point grid positions of the B-spline function.

A set of n images can now be registered onto a reference image using such B-spline transforms and their respective control point displacements for each image l, given by ${}^{l}\boldsymbol{u}_{i,j,k}$, can be retrieved. Then, the average control point displacement at the control point index i, j, k for the n images can be calculated as:

$$\bar{\boldsymbol{u}}_{i,j,k} = \frac{1}{n} \sum_{l=1}^{n} {}^{l}\boldsymbol{u}_{i,j,k} \tag{3.3}$$

This then gives the average displacement of the images, by creating a new B-spline transform with the average control point set $\bar{\phi}_{i,j,k} = \phi_{i,j,k} + \bar{\boldsymbol{u}}_{i,j,k}$.

As the B-spline transformation can only impose a local deformation, another transformation is required to impose global transformation, such as translation, rotation, scaling, or shear of the whole image. Several transformations models, using different degrees of freedom (DoF), are available for this purpose and can be stacked in the registration pipeline. To also impose the overall mean global transformation, the average of the global transformation has to be calculated accordingly.

In general, a B-spline of n-th order requires at least $n+1$ grid points. For example, the here used cubic B-spline requires at least four control points. However, the control point grid is typically not fully enclosed by the image domain but control points are placed outside the image domain. Furthermore, it is a convention to define the B-spline in terms of a numbers of mesh patches over the image domain[2]. The number of mesh patches over the image domain is then equal to $m_x \times m_y \times m_z = (n_x - n) \times (n_y - n) \times (n_z - n)$.

[2]See for example the description of the BSplineTransform from the ITK software package at `https://itk.org/Doxygen/html/classitk_1_1BSplineTransform.html#details`, accessed 30.12.2022.

For this thesis, the notation of mesh patches is used, as it is closely related to the used software packages.

Canonical Bone

The here developed method was created similar to the one presented by Steiner, Synek and Pahr [219] and operates on masked images of bones, where one image (the mask) describes the label of each voxel (bone or background) while the other image contains the actual grey-value. These can be the same images as required for the HMA workflow. All images are registered onto a randomly chosen reference image using a similarity transform. This type of transform allows only for translation, rotation and isotropic scaling. All similarity transformations are averaged by taking the arithmetic mean of the translation and scaling as well as averaging the rotation by quaternion averaging [220]. The centre of rotation is fixed in all transformations. The inverse of the averaged transformation is then applied to the reference image, to scale, rotate and translate the reference image into an average position. In the next step all images are registered onto the aligned reference image. First, a similarity transform is again used, then a free-form deformation is applied using a cubic B-spline transformation. When all images are registered, the transformed images and the B-spline control point grid displacements are averaged. The resulting average B-spline transformation is then inverted and applied to the averaged image, yielding the new reference image. The steps of registering and averaging can be iterated several times, until the model has converged. Diminishingly qualitative changes in the canonical bone shape indicate the convergence of the model, while the surface distance between two consecutive iterations can be used for quantification. The last reference image is then used as the canonical bone image for the further steps.

Adaptations to the original workflow for QCT images are required for μCT images because the runtime of the registration is proportional to the image size and hence registration of μCT images can become impractical. Therefore, a resizing step was added to rescale the images to a resolution similar to that of QCT by increasing the voxel size by an isotropic factor. Rescaling the images before registration reduces the number of voxels and because the resulting transformations from the registration are smooth over the whole image domain, they can be applied to the original high-resolution images that accurately depict trabecular architecture as well [221]. The process of registration including the rescaling process is shown schematically in Figure 3.3. However, the rescaling of the images also influences the registration quality, as with increasing scale factors, details are lost. Another parameter which influences the registration quality but also the overall runtime is the B-spline control grid spacing. A lower grid spacing can be used to register local features better at the expense of higher runtime. Therefore, optimal values for these two parameters have to be identified which allow for a feasible runtime with adequate registration quality.

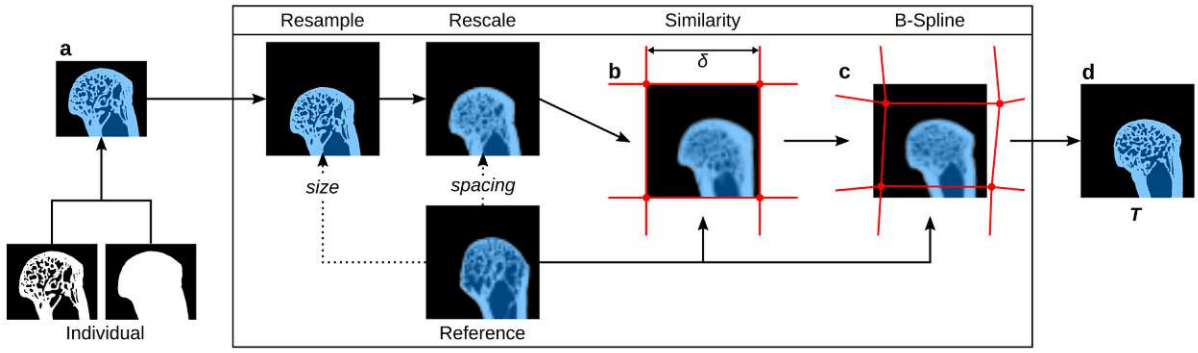

Figure 3.3: Schematic overview of a single registration run in 2D, which is in principle similar to the real registration in 3D. (**a**) Original binary segmented μCT image and mask are combined into masked image. This image is then resampled to the same size and rescaled to match the voxel spacing of the reference. (**b**) Image after similarity transform using the reference image and undeformed B-spline control point grid with grid spacing δ. Only grid nodes in the vicinity of the image domain are shown. (**c**) Image after B-spline transformation with deformed control point grid. (**d**) Transformed original image using the transformation $\boldsymbol{T}$ gained from the two registration steps.

Negative normalised cross correlation was used for both similarity and B-spline registration as cost-function for the optimisation. A conjugate gradient line search optimiser was used for the similarity and a L-BFGS-B optimiser [222] for the B-spline registration. All other parameters were used as described by Steiner, Synek and Pahr [219].

Mesh morphing

After the canonical bone image is created, each image is registered onto the canonical bone image. This yields transformations that are used to morph a canonical mesh, generated on the canonical bone, onto each individual bone. The canonical mesh is created on the inner mask of the canonical bone, i.e., the trabecular volume. There are two options how this inner mask can be created. Either the “fill” method [156] is applied on the generated canonical bone, or the inner masks of the individual samples are transformed into the canonical space and averaged, similar to the averaging of the canonical bone itself. Here, the latter method was used, by transforming the inner bones, creating the average image of all individual images, and applying a threshold of 0.5 to produce a valid binary mask. Then, the canonical mesh can be created on the averaged inner mask, as described for the HMA method.

Using the canonical mesh and the transformations from the canonical space into the individual space, the individual meshes can be generated by mesh morphing. In this step, only the vertices of the meshes are moved in space, without altering their connectivity. Thus, isotopological meshes are created, that is, the topology of the meshes does not change. However, in this process the elements might get distorted, which can, in the extreme cases, lead to degraded elements. The degradation of the elements can be checked using various mesh metrics, which detect different types of degradation [223]. Because

isotopological meshes are a requirement for the cHMA workflow, common strategies to repair degraded elements after morphing, such as local or global remeshing, can not be applied. Therefore, excessive mesh degradation has to be avoided in the first place. Hence, the registration procedure should yield transformations, which add minimal mesh distortion during the morphing step.

Element-wise Statistical Analysis

After HMA has mapped the quantities onto the meshes, the values of the corresponding elements can be collected and evaluated using statistical methods. It is possible to employ both comparisons between individuals or create groups for the statistical analysis. Using statistical tests, it is then possible to identify regions in the bone that are significantly different between individuals or groups. However, care has to be taken when employing this element-wise statistical analysis, because one issue with the direct comparison is the inflation of the so called α-error (Type-I error). Typically, the α-level is set to $5\,\%$, which translates roughly for a $5\,\%$ chance to have a false-positive. However, as many thousand statistical tests are performed in the element-wise comparison, the absolute number of false-positives can get very high. Or if thought the other way around: If just 100 elements are compared, there will be around 5 elements showing a false significant difference. Therefore, this so called α-inflation has to be corrected for, a method also known as family-wise error-rate (FWER) control [224].

A straight forward and simple way is to use the Bonferroni-correction. The chosen α-value is corrected by dividing it by the number of tests performed: $\alpha' = \alpha n^{-1}$. However, this method is very conservative and if thousands of tests are performed, the resulting α-value will become extremely small - so small that with the number of elements used in cHMA, typically not a single test will produce a significant result, but only if the differences are extraordinarily large. This means in statistical terms, that while the type-I error is reduced, the type-II error is increased, and thus the statistical tests will show many false-negatives. Of course, such a rigorous approach can be applied, but the aim of such an element-wise analysis is to find also subtle differences between samples, which are effectively eliminated when a too stringent correction is applied.

Another method for FWER control employs permutation tests [224]. This method is not as conservative as the Bonferroni-correction but requires more computational effort for the correction of the α-value. Without going into detail of the process, which can be looked-up in Nichols and Hayasaka [224], the main idea is to calculate a new critical value for the statistical test by estimating the so called maximum statistic and choosing the critical value as the $(1-\alpha)$-quantile of the maximum statistic. In the permutation method, the maximum statistic can be found empirically: The distribution of values over all elements including their labels (the group that has to be compared in the statistical test) is collected. Then the labels are permuted, and the statistical test is performed on the new data for all elements. The maximum statistical-test value over all elements

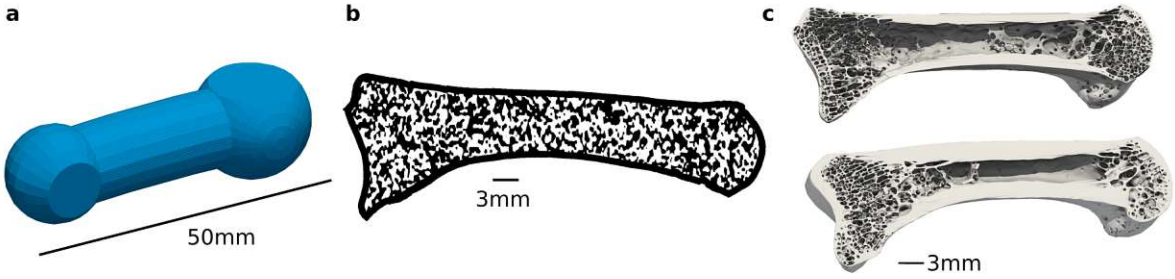

Figure 3.4: Synthetic test bone images. (**a**) Parameterised shape. (**b**) Synthetic trabecular bone. (**c**) Two real first metacarpals for comparison.

is then stored and the permutation repeated several thousand times. Depending on the statistical test used, this procedure can take a long time. Permutation tests can be implemented with any statistical test, thus also non-parametric ones, which makes them a versatile albeit slow tool.

Yet another method for the control of the α-error is random field theory (RFT), which offers a faster, parametric approach than permutation tests [225, 226]. However, RFT implementation for irregular tetrahedral meshes is challenging, and the requirements for the use of RFT might not be met by the data [224]. Moreover, RFT currently does not support the use of non-parametric tests, which could be used instead of, for example, the often employed t-tests for data not fulfilling the normality assumption.

Synthetic Bones

The first validation assessed the capabilities of the SDM to produce a canonical shape using synthetic bone samples, which should resemble parameterisable first metacarpal bones of various primate species (Figure 3.4a). 30 randomly created shape-parameterised synthetic bones were created for this experiment. The shapes used six parameters, which were selected similar to the variability seen in real bones (Figure 3.5, Table 3.1). Additionally, an isotropic scaling factor was used to increase the variability further and also test the similarity transform, preceding the B-spline transform. These bones consisted only of a dense shell with an empty shaft, to reduce any bias introduced by the texture, i.e., the trabecular microstructure. The images were created by specifying a range of values, from b_{lower} to b_{upper}, for each parameter, that determined ± 3 standard deviations of a normal distribution (i.e., $99.73\,\%$ of the fictitious population) and then drawing 30 random values from each of these distributions. Using this method, a baseline image can be created using all the *a priori* means (defined as $(b_{\text{upper}} - b_{\text{lower}}) \,/\, 2$) as the parameters. The synthetic bones were generated in OpenSCAD[3], exported as STL, and converted into voxel images using an STL to voxel converter[4] using a target voxel size of $0.03\,\text{mm}$.

[3] `https://openscad.org`
[4] `https://github.com/reox/stl-to-voxel`

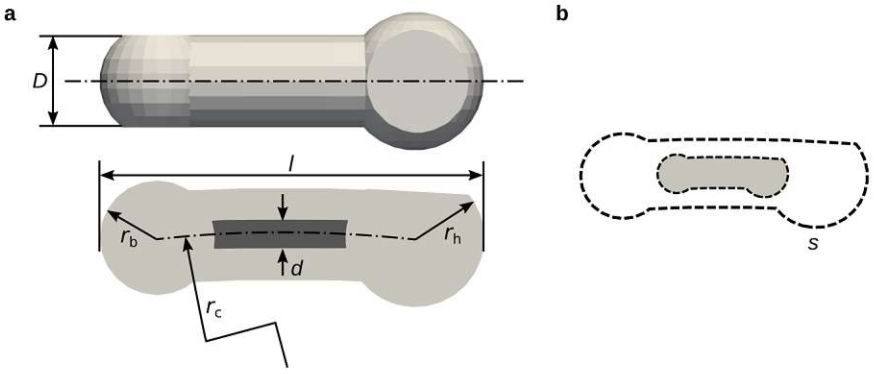

Figure 3.5: Parametric bone. (**a**) Top view and cross section. The parameters are: D the outer shaft diameter, d the inner shaft diameter, l the overall length, r_b the radius of the base, r_h the radius of the head, and r_c the radius of the curvature. The angle of the curvature is calculated such, that the overall length is met. The flat spots are added, such that the bone has a defined "head" and "base". (**b**) Isotropic scaling with factor s is applied after the bone is created.

Table 3.1: Synthetic Bone Parameters

Parameter	b_{lower} to b_{upper}	Description
D	$10\,\text{mm}$ to $14\,\text{mm}$	Outer shaft diameter
d	$2\,\text{mm}$ to $6\,\text{mm}$	Inner shaft diameter
r_b	$7\,\text{mm}$ to $8\,\text{mm}$	Base radius
r_h	$8\,\text{mm}$ to $10\,\text{mm}$	Head radius
r_c	$200\,\text{mm}$ to $400\,\text{mm}$	Radius of curvature
l	$40\,\text{mm}$ to $60\,\text{mm}$	Total length
s	$80\,\%$ to $120\,\%$	Isotropic scaling

Finally, the canonical image was created using the SDM and compared to the baseline image.

As a second test, 30 synthetic bones with the same shape but random texture were used to assess the behaviour of the SDM on registering different textures (Figure 3.4b). An outer mask of an existing metacarpal bone was eroded to produce an offset mask (inner mask) of the same shape. This erosion creates a "cortex" with constant thickness. This inner mask was then filled with blocks of random values, to which a Gaussian blur was applied. A thresholding step yielded a binary image with a random trabecular-like structure. In this test, the hypothesis was that the canonical bone will have the same shape as the input bone and is not locally deformed by the random texture. Hence, the outer mask acted as a baseline to compare the created canonical bone to. To qualitatively compare the created canonical bone, an averaged image of all 30 images was created.

In both tests, two comparisons were made: One comparison between the created canonical bone and the registered images and one comparing the canonical bone to the baseline. The first comparison shows how well each image was registered onto the canonical bone, while the second test describes how well the *a priori* shape was replicated by the SDM. For both comparisons two image based metrics were used [227]. First, the

Hausdorff distance was calculated, giving a worst-case surface distance measure. Second, the Dice coefficient was calculated to give an overall measure of the overlap of the two images. Canonical and baseline images were aligned by centroid in order to compare them. The Hausdorff distance should be as small as possible, while the Dice coefficient should be as close to 1 as possible.

Parameter Study using Mc1

The registration method can be controlled by a set of parameters, which influence certain steps during the registration process. The cHMA workflow should allow analyses of high resolution (μCT) scans in a reasonable amount of time, capture sufficient detail in the anatomical structure, but should avoid overfitting during the registration and local distortions, which would deteriorate the quality of the morphed meshes later in the cHMA workflow.

To identify parameters suitable for morphometric analysis of μCT images from bones of different species, a sample of thirty μCT images of first metacarpals (Mc1) was used from a previous study [193]. The set contained ten samples each of *Homo sapiens*, *Pan paniscus*, and *Pan troglodytes verus*, respectively. The images had different voxel sizes ranging from $0.023\,\mathrm{mm}$ to $0.031\,\mathrm{mm}$ due to the usage of different scanners. Therefore, all images were resampled to an isotropic voxel size of $0.03\,\mathrm{mm}$ and a total image size of $674\times681\times1779$ voxels during the registration procedure. All images were already segmented and masked from the previous study [193]. Images from the left hand were mirrored to match the right side.

Two main parameters were varied in order to identify a suitable parameter set: (1) Image rescaling factor and (2) B-spline control grid spacing. The previously presented model by Steiner, Synek and Pahr [219], developed for the proximal femur, used a grid spacing of $21\,\mathrm{mm}\times15\,\mathrm{mm}\times37\,\mathrm{mm}$ with an isotropic voxel size of $0.6\,\mathrm{mm}$. Therefore, two different rescaling factors of 10 and 20 were tested, resulting in a voxel size of $0.3\,\mathrm{mm}$ and $0.6\,\mathrm{mm}$ respectively and the grid spacing was varied with 4, 6, 10, 20 and $30\,\mathrm{mm}$ distance. As the grid spacing is not the same in the three cardinal directions, the given spacings resulted in a grid of $5\times5\times13$, $3\times3\times9$, $2\times2\times5$, $1\times1\times3$, and $1\times1\times2$ control points. A total of 10 different parameter runs were evaluated.

The full SDM workflow using two iterations, registration and mesh morphing was applied for each parameter run. Tetrahedral meshes were created using a characteristic edge length of $1\,\mathrm{mm}$ for all elements. The result was judged based on both image registration metrics and mesh distortion metrics as well as visual inspections of the registered images and morphed meshes. The overall runtime of the SDM workflow was measured for each parameter run. Image metrics, namely Dice coefficient, mean surface distance (MSD) and Hausdorff distance, were calculated between the transformed images and the canonical bone [227]. A brief graphical explanation of these image metrics is shown in Figure 3.6. Mesh metrics, namely tet-collapse [228] and volume-skew [229] were

calculated for the canonical and individual meshes. Briefly, tet-collapse measures the ratio of height and face area and is zero for a fully collapse tetrahedron and one for an optimal tetrahedron. Volume-skew measures the deviation in volume from an equilateral tetrahedron and is one for a degenerated tetrahedron and zero if the tetrahedron is equilateral. The final parameter set was selected by choosing the parameter set with the highest image metrics but lowest mesh degradation.

Robustness

To evaluate robustness of the cHMA method, three different tests were performed:

1. The convergence behaviour of the SDM was investigated,
2. the influence of the starting images was evaluated and
3. a tenfold cross-validation was performed.

All tests were performed using the chosen parameter set from the parameter identification and the metacarpal bone sample as described in the previous sections.

In order to identify the number of iterations needed in the SDM, a model was created using a total of ten iterations, saving the results of intermediate iterations. The intermediate images were compared using the same image metrics as used for the parameter identification using the image of the final iteration as the reference.

The bias towards the starting image was tested by generating a canonical bone with two iterations but choosing a different random starting image for each run. The canonical image of the parameter identification served as the reference and image metrics were calculated using nine additional starting configurations.

Finally, a tenfold cross-validation was performed, i.e., leaving out three samples per run for the canonical bone creation. The same starting image was used, except for the run where this image was excluded, to get comparable results without the influence of the starting image. Again, two iterations were used in the SDM and the final canonical bone was compared using the image metrics to the canonical bone of the parameter identification.

Hard- and Software

The whole registration and SDM framework was implemented in SimpleITK 2.0 [230] using Python 3.7 (Python Software Foundation, `https://www.python.org`). Meshing was done using CGAL 4.11 [231] in Medtool. Visualisations were created in ParaView 5.9 (Kitware, `https://www.paraview.org`). Statistical analysis was done with SciPy 1.2.3 [232] in Medtool 4.5 (Dr. Pahr Ingenieurs e.U., `http://www.medtool.at`). All the registrations were run on a Dual Intel(R) Xeon(R) Gold 6144 @ 3.50GHz using 16 cores in parallel.

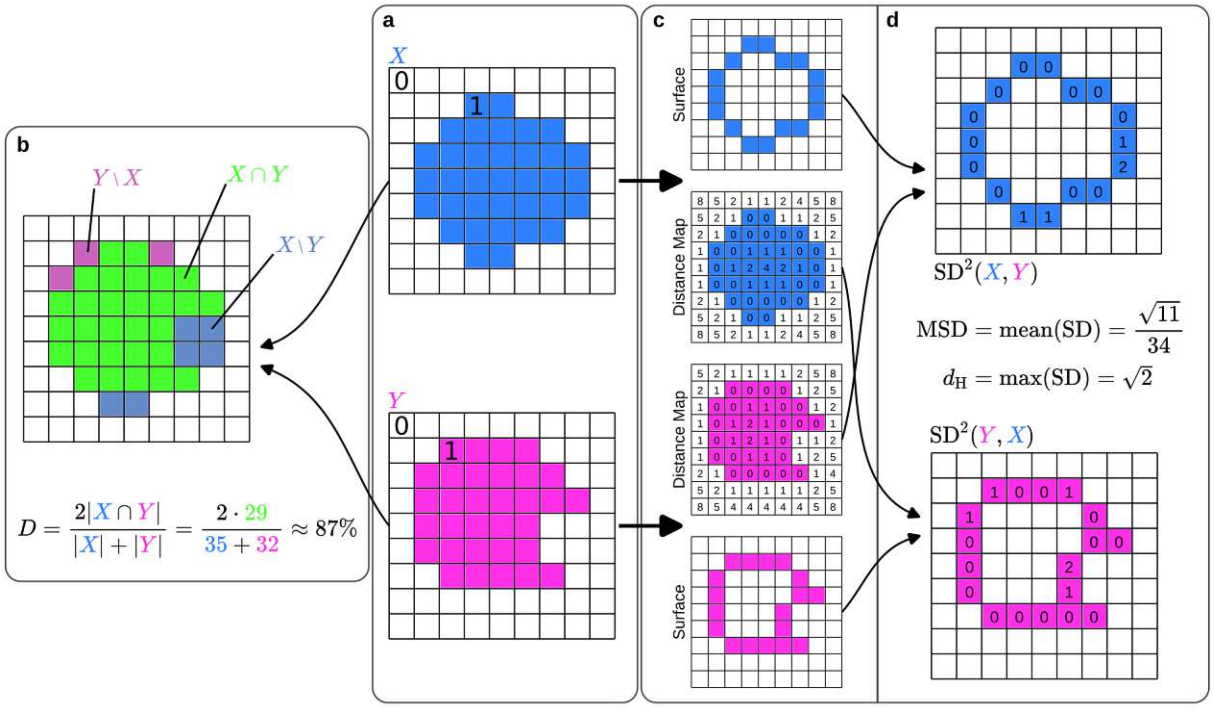

Figure 3.6: Schematic overview of the used image metrics and their calculation for discrete 2D images. In principle, the calculation works in the same way for 3D images. (**a**) Binary input images X and Y, resembling the shapes. (**b**) The Dice coefficient $D \in [0, 1]$ is a similarity measure, that can be applied on images to measure the overlap of two shapes. It is easily calculated for binary images by the fraction of twice the number of intersecting pixels $2|X \cap Y|$ of the two overlaid shapes, and the total number of pixels inside the two shapes $|X| + |Y|$. (**c**) To calculate the surface distances, the surface (i.e., contour in 2D) of the shape is extracted as well as a distance map. Here, the squared distance maps are used, because the squared distances are always integer numbers and thus easier to handle. Furthermore, squared values are always positive, yielding also only positive surface distances. Signed versions are available as well, for example, to measure on which side the two surface lie. Only the absolute surface distances are used in this thesis though. (**d**) The actual calculation of the surface distance from image X to image Y, denoted as $\text{SD}(X, Y)$, uses the surface of image X and the distance map of image Y and yields a vector with a distance for each surface pixel. SD^2 denotes the squared surface distance. As only pixels that are on the surface of X are used in the calculation, the resulting distances are indeed the surface distances between the images. To calculate the mean surface distance (MSD), the distances from both X to Y and from Y to X have to be calculated first. Then, the mean of the two combined surface distance vectors is calculated. This definition of the MSD is sometimes also referred to as symmetric mean surface distance, as the distances in both directions are used. In this instance, MSD is around 0.1. The Hausdorff-distance d_{H} is calculated as the maximal surface distance of all surface pixels, and is in this example around 1.4.

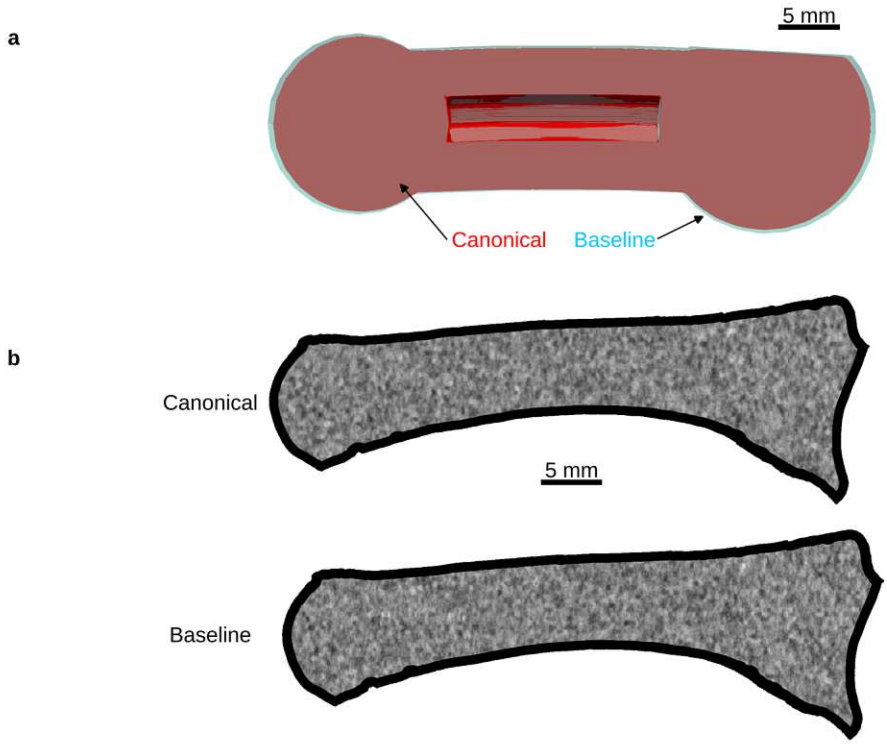

Figure 3.7: Cut sections of the synthetic canonical bones. (**a**) Synthetic shape test. In red is the created canonical bone, overlaid with the baseline in blue. Both images were aligned by their centroids. (**b**) Synthetic texture test. The cortical bone is clearly visible and sharply separated. The trabecular bone shows an averaged pattern. Only small qualitative differences in the trabecular pattern are visible between the canonical bone and the baseline.

3.1.4 Results

Synthetic Bones

Cut sections of the created canonical bones can be seen in Figure 3.7. The resulting distance measures of individual images to the canonical image after the model creation are given in Table 3.2. In both the shape and texture test cases, the mean Dice coefficients were close to one, and mean Hausdorff distances were smaller than a single voxel during registration ($0.3\,\mathrm{mm}$). Qualitatively, the overall baseline shape was well reproduced by the canonical image in both test cases. Compared to the baseline image, the canonical shape was slightly smaller in the synthetic shape test, noticeable by the larger Hausdorff distance ($0.554\,\mathrm{mm}$). In the test with same shape but different texture, almost no change in the outer shape was observed and the cortex was still sharply separated towards the inner structure. The inner structure showed as a random, grey texture due to the averaging of the synthetic binary structure, similarly to the created baseline image.

Parameter Study

All ten parameter runs produced canonical bones and all bones were successfully registered onto it. Image and mesh metrics were calculated for each parameter run and the runtime for canonical bone creation and registration was tracked (Figure 3.8). For larger B-spline grid spacings and higher rescaling factors, the runtime was lower than for small grid spacings and lower rescaling factors. The fastest run took $171\,\mathrm{min}$, while the slowest run took $1270\,\mathrm{min}$. Image metrics got better for lower grid spacings and lower rescaling factors, while mesh metrics got worse on average.

The mesh metrics showed a steep deterioration for grid spacings smaller than $20\,\mathrm{mm}$, while the image metrics changed more gradually over the full range of tested spacings. As a result of this drastic change in mesh metrics, a $20\,\mathrm{mm}$ grid spacing was considered as the smallest possible grid spacing, without large mesh distortions. Single meshes had areas of distorted elements, apparent in the visual inspection, for grid spacings $10\,\mathrm{mm}$ and lower, while no distortions could be observed at $20\,\mathrm{mm}$ spacing or higher. The runtimes for $20\,\mathrm{mm}$ grid spacing were $330\,\mathrm{min}$ for $10\times$ rescaling and $173\,\mathrm{min}$ for $20\times$ rescaling. Despite longer runtimes, $10\times$ rescaling was chosen as it had considerably better MSD on average ($-10\,\%$) with similar Hausdorff distance ($+1.9\,\%$).

Robustness

Using the identified parameters, a canonical bone was created using up to ten iterations. Qualitatively, no substantial change was visible for two or more iterations, suggesting that the model had converged (Figure 3.9). Rigid body motion of the bone was observed, which resulted in a higher surface distance between two successive iterations than anticipated. The MSD between the final and penultimate iteration was $0.027\,\mathrm{mm} \pm 0.026\,\mathrm{mm}$ with a Dice coefficient of 0.99. Two iterations were used for all further studies, as there was no visible change except for minor rigid body motion.

Qualitative inspection of the canonical bone with a different start image showed no considerable changes in bone shape but differences in bone size, translation and rotation (Figure 3.9). The canonical bone size, ranged from $39\,\mathrm{mm}$ to $41.3\,\mathrm{mm}$ with a mean of $40.6\,\mathrm{mm}$ in the longitudinal axis. These size differences were also apparent in the MSD,

Table 3.2: Metrics for synthetic data experiments. Values are given as mean±std for the canonical bone versus all registered images and only the single value for the canonical bone versus the baseline image.

	Canonical vs.	Hausdorff (mm)		Dice (-)		Runtime (min)
Shape	Images	0.2664	±0.106	0.992	±0.003	566
	Baseline	0.5540		0.953		
Texture	Images	0.0451	±0.006	0.999	±0.0003	431
	Baseline	0.0603		0.995		

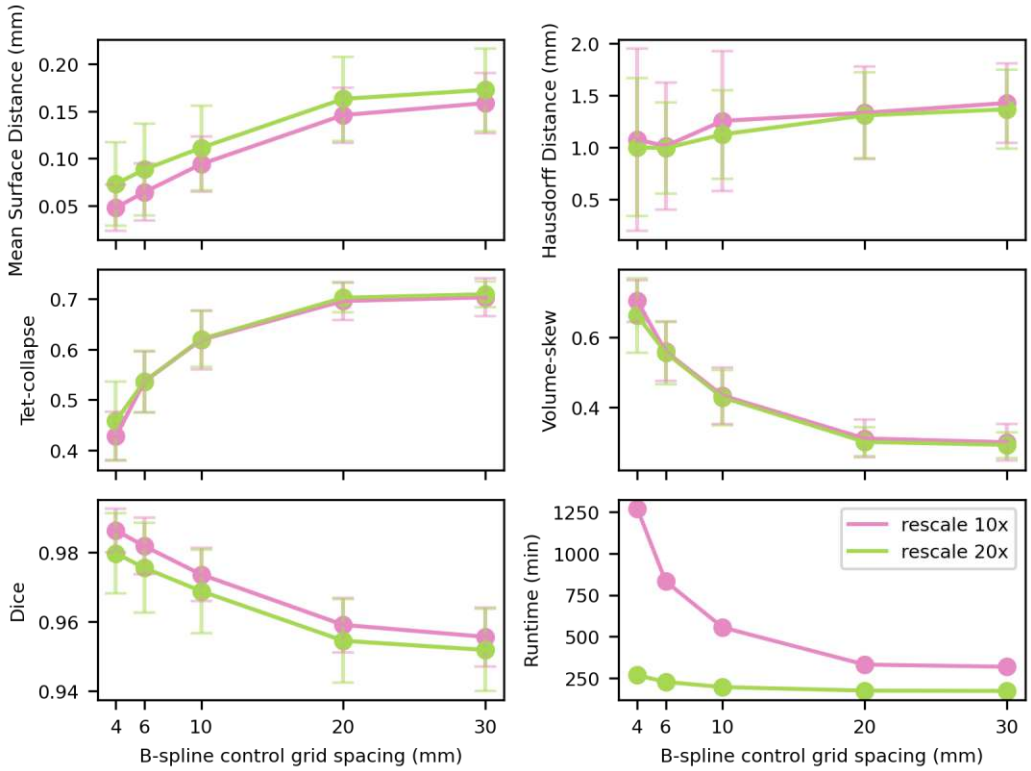

Figure 3.8: Average image and mesh metrics as well as runtime for the parameter identification studies. Each plot shows a single metric, split up for the two tested rescaling factors. The bars show the standard deviation. Runtimes are given for the canonical bone creation using 16 CPUs in parallel.

which was $0.43\,\mathrm{mm}$ on average and ranged from $0.17\,\mathrm{mm}$ to $0.67\,\mathrm{mm}$. Dice coefficient was 0.87 on average, ranging from 0.83 to 0.95.

All except one canonical bone in the cross-validation study were qualitatively similar in shape. This one canonical bone used a different starting image and thus resulted in a different sized bone, which is in line with the start image bias described above. MSD was $0.09\,\mathrm{mm}$ on average with values ranging from $0.04\,\mathrm{mm}$ to $0.34\,\mathrm{mm}$ and Dice coefficient was 0.97 on average, ranging from 0.91 to 0.99.

3.1.5 Discussion

The cHMA workflow shows the applicability of statistical deformation models (SDMs) to μCT data of different species, using a lower resolution image for the registration and the original, high-resolution image, which can in the next step directly be used for the morphometric analysis with HMA. The tests on synthetic bones showed that the SDM produces shapes that are similar to *a priori* shapes and the method is robust against outliers. Furthermore, the parameter study showed which parameters can be adjusted and how large the computational costs are in dependency of the parameters.

A similar method was recently presented by DeMars *et al.* [190]. The method is similar to the approach shown here, as HMA is also used to evaluate morphometric quantities. However, the meshes are created on the individual bones first and then correspondence is established using a coherent point drift algorithm. That means that meshes are created for all bones separately, while the here presented workflow uses isotopological meshes without the need of interpolation of values onto the canonical point cloud. Another similar workflow was presented by Taghizadeh *et al.* [233]. A canonical bone is constructed and meshed, however the individual meshes are then used to build a statistical model of shape, BVTV and anisotropy rather than doing element-wise statistical analysis. Another similar approach was used by Marangalou *et al.* [234]. However, in their method, a mesh-morphing approach with landmarks was used and not an SDM. All these three models were so far only applied to human bones. In contrast to other existing methods, the cHMA method was tested on bones of different species and provides a high level of automation. For instance, no landmarks need to be defined to run the model and μCT data can directly be fed into the workflow.

There are certain limitations with the validation tests and the synthetic data used. The used shapes and textures represent real bones only approximately. The synthetic shapes are missing local features, like surface unevenness, or smaller and bigger pores, that are present in real bones. Only the overall surface distance was evaluated, but no extra check for homologous regions at the surface or inside was performed. The random texture in the synthetic texture images does not represent a trabecular structure, as it is random and not ordered. However, as the metrics that are used for the registration do not incorporate local correlations and simply compare voxel by voxel, it should not

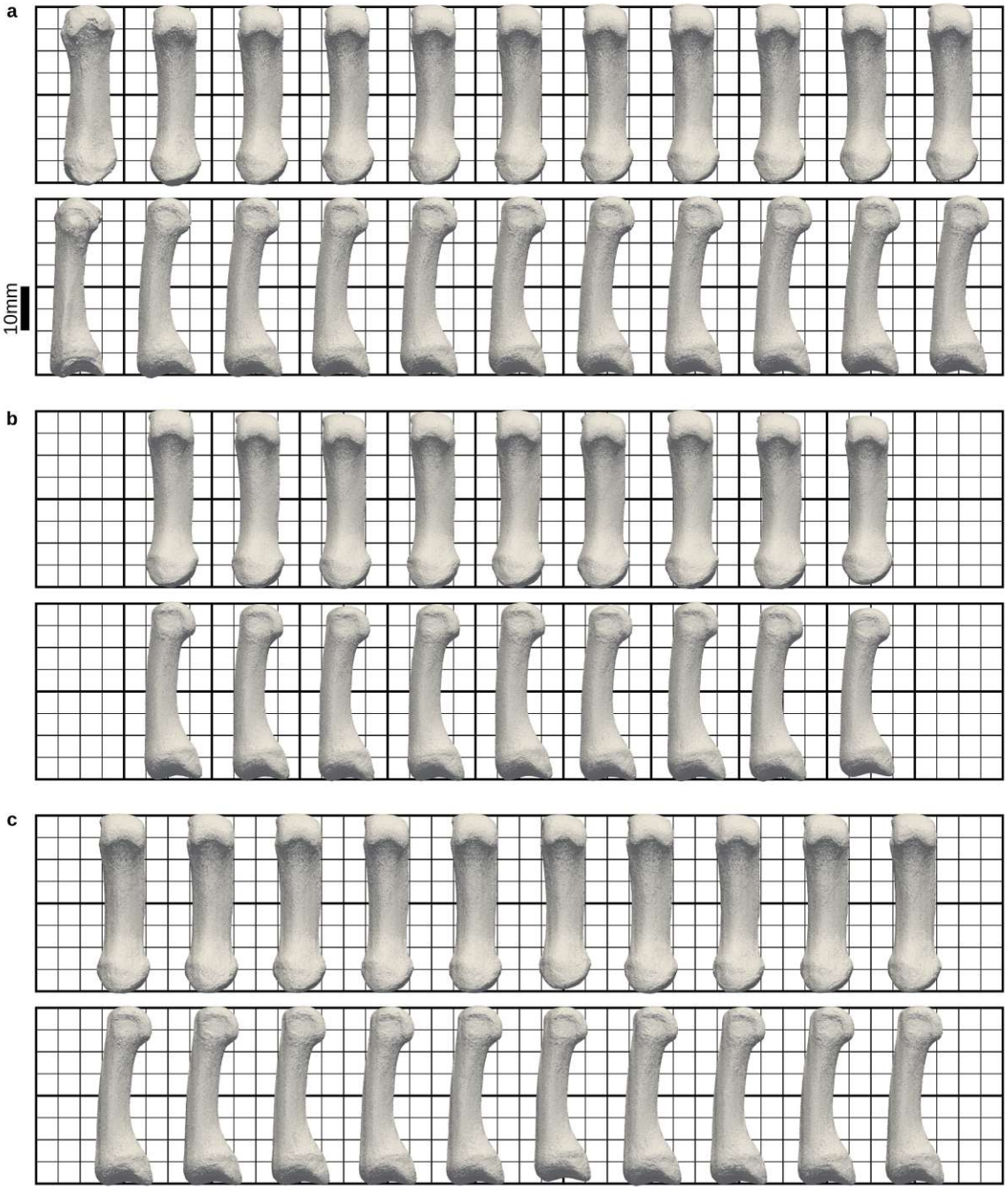

Figure 3.9: Overview over all robustness studies. (**a**) Ten iteration test. The first image is the initially chosen start image. (**b**) For the start image bias test, differences in longitudinal height can be seen. (**c**) Tenfold cross-validation. The sixth image had another start image than the other images.

matter if the texture is random or structured. For other types of metrics, other types of synthetic bone images might be used instead.

Despite the high level of automation, the cHMA workflow still requires a number of parameters to be set manually. Some of these parameters were identified by using parameter studies, while others were obtained from literature [219]. The parameter identification procedure highlighted the need to find a balance between capturing anatomical details and maintaining high quality meshes. Here, the parameters were identified by subjective criteria, i.e., minimal distortion in the meshes, maximal overlap of images, and visual inspection of the resulting meshes. A more objective measure would be beneficial in the future, however due to the lack of a gold-standard, it was not possible to select the parameters based on absolute measures. The parameter study only reflected a sub-set of all parameters. Many other parameters were already taken from literature [219] but a dedicated study might even find better parameter sets.

Although the method was generally robust, a marginal start image bias was observed that resulted in different location, rotation and scale of the canonical bone. This bias can be explained by the use of the similarity transform. The similarity transformation did not always produce images which would overlap in a true anatomical homologous position. For example, a rotation might also minimise the metric in the same way as scaling would do. To enforce a better initial alignment of the bones, anatomical landmarks could be used, similar to shape models. However, landmarking requires extra manual work and introduces new errors into the model. But the method is able to perform the initial alignment step with a minimal set of, for example, three to four, landmarks to roughly align the bone before the free-form registration. Thus, the extra effort is kept to a minimum with the potential benefit of a better registration. Another option would be the use of a different metric or tweaking the optimiser to find a better starting position.

To conclude, cHMA offers a novel approach to construct a canonical reference bone for the quantitative comparison of morphometry across the boundaries of species. The required parameters for the creation of the canonical bone were identified in this chapter using first metacarpal bones. The whole method is built like a framework, to easily enable future adaptations, extensions, or the usage of other bones.

3.2 Methods of Evaluation

3.2.1 Related Publication and Declaration of Contributions

This section is based on the publication

> S. Bachmann, C. J. Dunmore, M. M. Skinner, D. H. Pahr and A. Synek. 'A computational framework for canonical holistic morphometric analysis of trabecular bone'. In: *Scientific Reports* 12.1 (2022), p. 5187. DOI: 10.1038/s41598-022-09063-6

Author contributions: **Sebastian Bachmann**: Conceptualisation, Methodology, Software, Validation, Formal analysis, Investigation, Writing - Original Draft, Writing - Review & Editing, Visualisation. **Christopher J. Dunmore**: Conceptualisation, Formal Analysis, Resources, Data Curation, Writing - Review & Editing. **Matthew M. Skinner**: Conceptualisation, Resources, Writing - Review & Editing, Project administration, Funding acquisition. **Dieter H. Pahr**: Conceptualisation, Methodology, Writing - Review & Editing, Supervision. **Alexander Synek**: Conceptualisation, Methodology, Writing - Review & Editing, Supervision.

Acknowledgements: This project has received funding from the European Research Council (ERC) under the European Union's Horizon 2020 research and innovation program (Grant agreement No. 819960).

The authors are grateful to: Jean-Jacques Hublin (Collège de France, Paris), Christophe Boesch and Uta Schwarz (MPI-EVA, Leipzig), Emmanuel Gilissen and Wim Welden (Royal Museum for Central Africa, Tervuren), Maria Teschler-Nicola and Ronald Muehl (Natural History Museum, Vienna), Jacopo Moggi-Cecchi and Silvia Bortoluzzi (University of Florence, Florence), and Birgit Großkopf (Johann-Friedrich-Blumenbach Institut für Zoologie und Anthropologie der Georg-August-Universität Göttingen, Göttingen), Inbal Livne (Powell-Cotton Museum, Birchington) and Nicole Edmison (Smithsonian Institution National Museum of Natural History NMNH, Washington D.C.), for access to specimens in their care. For technical assistance we would also like to thank Habiba Chirchir (Marshall University, Huntingdon), Patrick Schoenfeld and David Plotzki (MPI-EVA, Leipzig).

3.2.2 Introduction

The new cHMA method was developed and validated in chapter 3.1. In the next step, the cHMA method is applied to two sets of bones where morphological similarities and differences between species have been well documented in the past. This gives the opportunity to verify that these morphological details are found also with cHMA. In

addition to the visualisation techniques, known from HMA, cHMA also allows to apply uni- and multivariate statistic methods to gather further insights. First, a non-exhaustive list of methods for evaluation is presented in this section which is then applied to two sample sets of bones.

The first bone sample set consists of first metacarpal bones from a previous study by Dunmore *et al.* [193]. The bones of the hand are of interest, as many interactions with the environment are made with the hands, and thus functional adaptation is likely to occur in those bones close to "substrate reaction forces", i.e., bones most distally in the skeleton [9]. Furthermore, different primate species show distinct locomotion methods that involve frequent and forceful hand use. Gorillas (*Gorilla gorilla*), bonobos (*Pan paniscus*), and chimpanzees (*Pan troglodytes*) employ the so called "knuckle walking", as they use their hands in quadrupedalism [235, 236]. Orangutans (*Pongo sp.*) live in trees and employ suspension [237, 238]. Humans (*Homo sapiens*) use their hands in various ways, for example to use tools or manipulate small objects. In the previous study, Dunmore *et al.* [193] used the HMA method [103, 104] as well as 3D geometric morphometrics (3D GM) [209] and trabecular mapping [208] for the analysis of the trabecular structure. Specifically, BVTV and DA were evaluated. To overcome the issue of systematic differences in BVTV between species [186], it was normalised by the mean BVTV of each sample to form relative bone volume over total volume (rBVTV). The trabecular mapping technique was only employed near the joint surfaces, on which the semilandmarks for 3D GM were defined. Thus, the evaluation was restricted to the head and base of the first metacarpal. Species specific density patterns were found in both the head and base, consistent with the habitual abduction of the thumb in humans ("pad-to-pad" grip) and the habitual adduction of the thumb in nonhuman great apes during precision and power grips.

The second bone sample set consists of proximal femora from a previous study by Georgiou *et al.* [196, 197]. The femur is the largest bone in the human body and is of importance for the locomotion. As different types of locomotion (bipedalism, quadrupedalism, climbing) require different flexion/extension angles of the hip joint, differences in locomotion should also be visible in the trabecular structure of the femoral head. In the previous study, Georgiou *et al.* [196] analysed the femoral heads using HMA and found characteristic density patterns consistent with the locomotor mode, distinguishing humans and the nonhuman greater apes. In a second study, Georgiou *et al.* [197] used a thresholding technique, applied to the HMA results to identify and visualise that the femoral head exhibit characteristic "pillar structures", which might stem from the different joint loading regimes.

The overall goal of this study was to reproduce the findings by Dunmore *et al.* [193] on the first metacarpal bones and by Georgiou *et al.* [196, 197] on the femoral heads of various primate species. To reduce the computational effort, the original sample sets used in these studies were reduced, to use only 10 samples of three species each. The species

were chosen such that two species should show similar morphometric indices to each other, while one species should show a different structure. The required registration parameters for the first metacarpals were already identified in a previous step (see section 3.1). Thus, a secondary goal was to investigate if these parameters can directly be used for the larger proximal femora.

3.2.3 Methods

In order to reproduce the results by Dunmore *et al.* [193] and Georgiou *et al.* [196, 197], cHMA offers a wide variety for the quantitative comparison of morphometric indices. A selection of those methods will be outlined here briefly.

Group-Wise Statistics

The most straight forward method to quantitatively compare morphometric indices across various samples using cHMA is to calculate statistical quantities, such as mean or standard deviation, for groups of samples for all elements in the mesh. In the simplest case, that might just be the full set of images, the SDM was trained on, but any subgroup of the sample set can be used as well. Typically, morphometric quantities are mapped using HMA on the morphed meshes. Then it is possible to simply calculate element-wise statistics using all meshes in the group. Care has to be taken only if the measured quantity depends on the volume of the element in the morphed mesh. However, all quantities currently available within the HMA-framework can be averaged without adjusting for the volume, as the quantities are measured at the centroid of the mesh elements and are valid only for that point.

When groups of samples are available, differences between them can be calculated as well. On the two distributions, statistical tests, such as t-tests can be performed. Care has to be taken with multiple testing, as described in section 3.1.3. Furthermore, other statistical tests (parametric and non-parametric ones) can be used as well and also other statistical methods can be useful, such as calculating the effect size (for example Cohen's d [239]).

Mesh Sub-Sections

As morphometric quantities such as BVTV may have systematic differences not only between species but even inside a single bone, it may be required to restrict the evaluation to a sub-region. A useful byproduct of the canonical mesh is, that such sub-regions can be easily defined on the canonical mesh and transferred to the other meshes with ease. When evaluating larger bones, such as the proximal femur, this method can be applied to crop-out only a smaller region, such as the femoral head, and evaluate the morphometric indices only in that region.

Principal Component Analysis

Patterns in data can be invisible to the observer, because they are only apparent in higher dimensions and are hidden by the shear number of variables. However, there are methods that can be used in such cases, to either reduce the number of dimensions or to find the principal pattern inside the data. One such method is principal component analysis (PCA) [240], where the idea is to find the variables in the high-dimensional space, that explain most of the variability in the data. In its essence, PCA is similar to linear regression analysis but in n-dimensional space, and can be efficiently implemented using the eigenvectors and eigenvalues of the covariance-matrix.

The PCA method can be directly applied on the morphometric indices, mapped on the HMA meshes. In this case, the n elements in the mesh are regarded as variables, containing each k measurements, i.e., k is the number of samples. Then, the PCA model is created and the components sorted by the explained variance. To visualise clusters of samples, the highest principal components can be plotted. Typically, this can be done in a 2D scatter plot, if the explained variance of the first two components is high enough. Otherwise, more components might be added at the expense of perceptibility of the clusters in the higher-dimensional space, or multiple 2D plots can be created to compare pairs of components.

There are several rules of thumb (see for the example the introduction in Shaukat, Rao and Khan [241]) how to apply the PCA method. These rules usually don't give specific numbers but only vague ranges. For example, that $k \gg n$ and that there shall be a "larger number" of k in general - usually over 100. These rules are usually not met for the application in cHMA (and other quantitative methods evaluating morphometry in multiple ROIs), as the number of mesh elements n is usually much larger than the number of samples k. Thus, care has to be taken, to not over-interpret the results, especially with very low number of samples. Furthermore, the total explained variance should be checked carefully, as maybe more than two components are required to explain a reasonable amount of variance. Even if these rule of thumb are not met for PCA, the resulting insights can be useful in an exploratory data analysis. Found patterns should be thoroughly analysed in a next step though, for example, using statistical tests.

Modes of the SDM

While PCA models can be created from morphometric quantities for all mesh elements, they can also be created for the B-spline coefficients inside the SDM. In cHMA, the SDM is actually not used to it's full potential. The reason is, that only the mean bone shape is of interest, and the variability is neglected in the creation of the canonical bone. However, for interpreting the variability of the sample set, PCA can be used to find the variability in shape, as seen by the original SDM implementation of Rueckert, Frangi and Schnabel [217]. To get this variability, a PCA model is created from the B-spline coefficients of

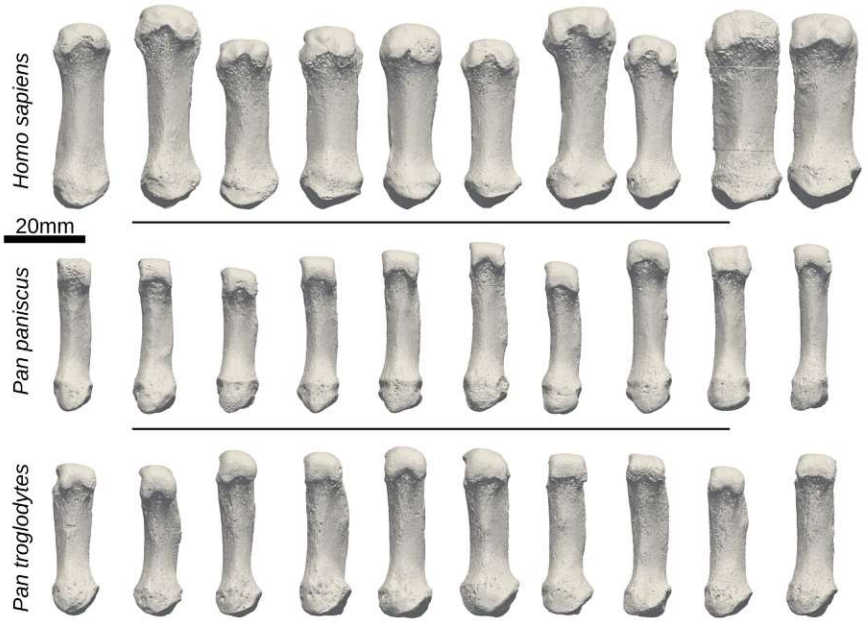

Figure 3.10: Overview of the first metacarpal sample set in a frontal view.

the SDM. Next, a new shape can be created by taking the mean deformation (i.e., the mean coefficients) and adding to them a scaled version of any or a combination of the eigenvectors. Each of the eigenvectors is commonly referred to as a "mode". The mean bone image can then be transformed using this scaled transformation.

Sample sets

First Metacarpals. The first set of bones contains 30 first metacarpals (Mc1), 10 each of three different primate species, namely *Homo sapiens*, *Pan paniscus*, and *Pan troglodytes*. All images were acquired from a previous study [193]. The images had different voxel sizes ranging from $0.023\,\mathrm{mm}$ to $0.031\,\mathrm{mm}$ due to the usage of different scanners. Therefore, all images were resampled to an isotropic voxel size of $0.03\,\mathrm{mm}$ and a total image size of $674\times681\times1779$ voxels during the registration procedure. All images were already segmented and masked from the previous study [193]. Images from the left hand were mirrored to match the right side. A rendering of all bones can be seen in Figure 3.10

The findings from a previous study on the same data set should be replicated [193]. Specifically, Dunmore *et al.* [193] reported higher relative BVTV (rBVTV) in the radiopalmar aspects of the head and base in *Homo* compared to the great apes. These results were based on qualitative interpretation of the volumetric distribution of trabecular morphometry, while quantitative assessment was limited to subcortical bone below the joint surfaces.

To test if cHMA can replicate and quantify these results for the entire volume, the workflow was run with the parameters as identified in section 3.1. The canonical bone was created using two iterations in the SDM and the mesh was created using a charac-

teristic element side length of $1\,\mathrm{mm}$ and morphed onto all bones. A background grid of $2.5\,\mathrm{mm}$ was used in the HMA process, with a sampling sphere diameter of $5\,\mathrm{mm}$. BVTV was evaluated for all samples with HMA and rBVTV was calculated by normalising each sample's BVTV by its mean BVTV. This step was necessary to compensate for systematic differences between taxa and allowed for the analysis of bone volume distribution while controlling for magnitude [189, 194].

Element-wise statistical tests were performed on the resulting rBVTV values mapped onto the isotopological meshes. Pairwise independent samples t-tests were used, followed by permutation tests for FWER control [224], yielding a new t-value threshold for significance. The significance level was set to $\alpha = 0.05$. Moreover, principal component analysis (PCA) was calculated on the mesh elements to identify common and distinct rBVTV patterns among species. Finally, also the variation of the whole data set was assessed by evaluating the modes of the SDM using PCA. All values are given as mean ± standard deviation, if not denoted otherwise.

Proximal Femur. A second case study was performed in order to check whether the results of a study on a larger bone, not part of the parameter identification procedure, can also be replicated. Thirty proximal femora, cut below the lesser trochanter, from a previous study were used [196, 197]. The set contained ten samples of *Homo sapiens*, *Gorilla gorilla*, and *Pan troglodytes*, respectively. All images were already segmented and masked similar to the first metacarpals. A rendering of all bones can be seen in Figure 3.11.

Georgiou *et al.* [196] found similar BVTV patterns for *Pan* and *Gorilla* while *Homo* showed a different pattern, lacking an anterior concentration in the femoral head. Moreover, the species specific pillar structures inside the femoral head, likely stemming from postural differences between the species, should be investigated further [197]. These findings were so far only described qualitatively.

Overall, the same settings as for the metacarpal sample set were used for both SDM and HMA. Only the image rescaling and mesh element size were adapted to reduce the runtime as a result of the larger bone size. Original voxel sizes ranged from $0.05\,\mathrm{mm}$ to $0.07\,\mathrm{mm}$ and were all resampled to an isotropic voxel size of $0.06\,\mathrm{mm}$, leading to an image size of $1247\times1836\times1916$ voxels during the registration. The B-spline grid setting resulted in $4\times5\times6$ grid points over the image domain and $10\times$ rescaling resulted in a voxel size of $0.6\,\mathrm{mm}$ during registration. Meshes for HMA were created using a characteristic edge length of $3\,\mathrm{mm}$ to account for the larger size of the bones compared to the metacarpals [104]. Statistical analysis on the first metacarpal bones was performed in analogy to the case study on the first metacarpal bones. However, in addition to the full bone analysis, the head region was cropped and analysed separately to be consistent with Georgiou *et al.* [196, 197]. This included thresholding the rBVTV distribution of the femoral head

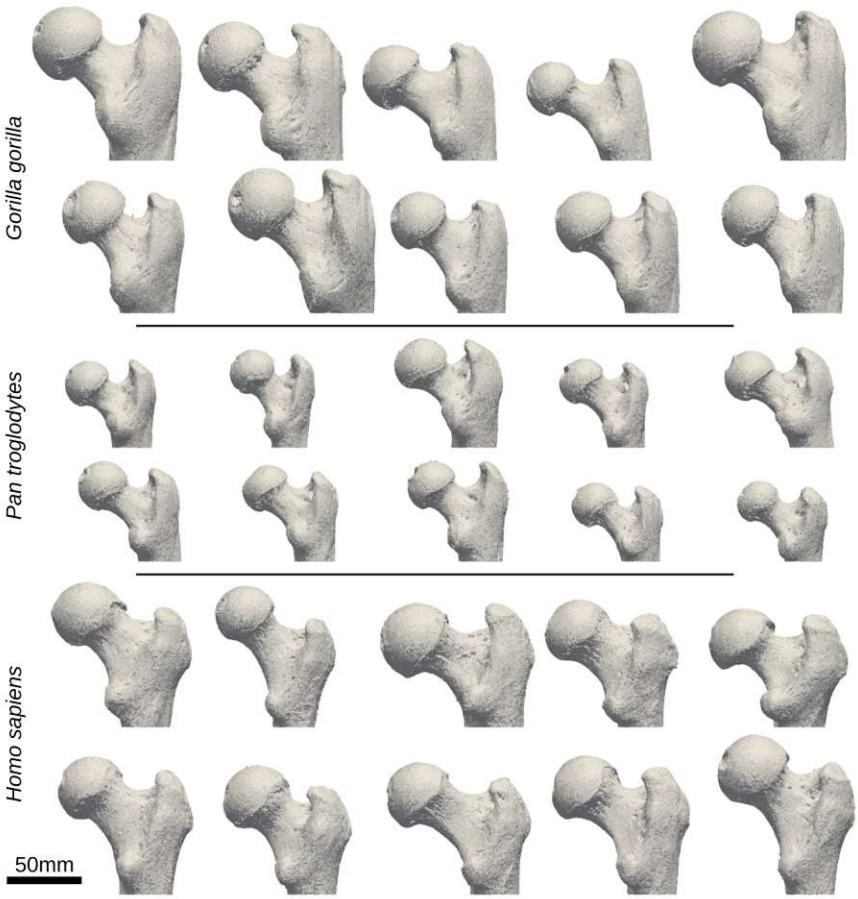

Figure 3.11: Overview of the proximal femur sample set in a frontal view.

at the 80-percentile to qualitatively identify the presence of the previously observed pillar structures.

Hard- and Software

The whole registration and SDM framework was implemented in SimpleITK 2.0 [230] using Python 3.7 (Python Software Foundation, `https://www.python.org`). All other steps were performed directly in Medtool 4.5 (Dr. Pahr Ingenieurs e.U., `http://www.medtool.at`). Meshing was done using CGAL 4.11 [231] in Medtool. Visualisations were created in ParaView 5.9 (Kitware, `https://www.paraview.org`). Statistical analysis was done with SciPy 1.2.3 [232] in Medtool.

All registration regarding the first metacarpal were run on a Dual Intel(R) Xeon(R) Gold 6144 @ 3.50GHz using 16 cores in parallel. All registration regarding the proximal femur were run on a Dual Intel(R) Xeon(R) E5-2697 v3 @ 2.60GHz using 28 cores in parallel.

3.2.4 Results

First metacarpal

All images were successfully registered onto the canonical bone. The Dice coefficient was 0.96 ± 0.008, Hausdorff distance $1.33\,\mathrm{mm} \pm 0.443\,\mathrm{mm}$ and mean surface distance (MSD) $0.146\,\mathrm{mm} \pm 0.03\,\mathrm{mm}$. The canonical mesh consisted of $10\,880$ linear tetrahedral elements. Volume-skew for the canonical mesh was 0.49 ± 0.216 and tet-collapse 0.59 ± 0.153. After mesh morphing, the volume-skew was 0.52 on average, ranging from 0.49 to 0.62 and tet-collapse was 0.56 on average, ranging from 0.5 to 0.58.

Relative BVTV (rBVTV) was evaluated for all samples and group-wise comparisons between the species were done element wise. Mean rBVTV distributions for each species and thresholded canonical meshes for the three pairwise comparisons can be seen in Figure 3.12. *Pan paniscus* and *Pan troglodytes verus* had similar rBVTV distributions, which can be seen in the low number of significantly different elements after FWER control. However, both species significantly differed in comparison to *Homo*, which showed higher densities in the radio-palmar region in the base. A smaller area of significant difference in the radio-palmar aspect of the head can be seen in comparison to *Pan paniscus*. These results are in line with the previous study, however there are also differences found which were not visible in the previous study due to the limited focus on trabecular distribution immediately below the subchondral region. *Homo* showed a region of lower density in the proximal shaft region above the base, in comparison to *Pan*. There was also a smaller region of higher density in *Homo* in the disto-radial region at the shaft. In the PCA plot (Figure 3.16a) of the first two principal components of rBVTV, *Homo*

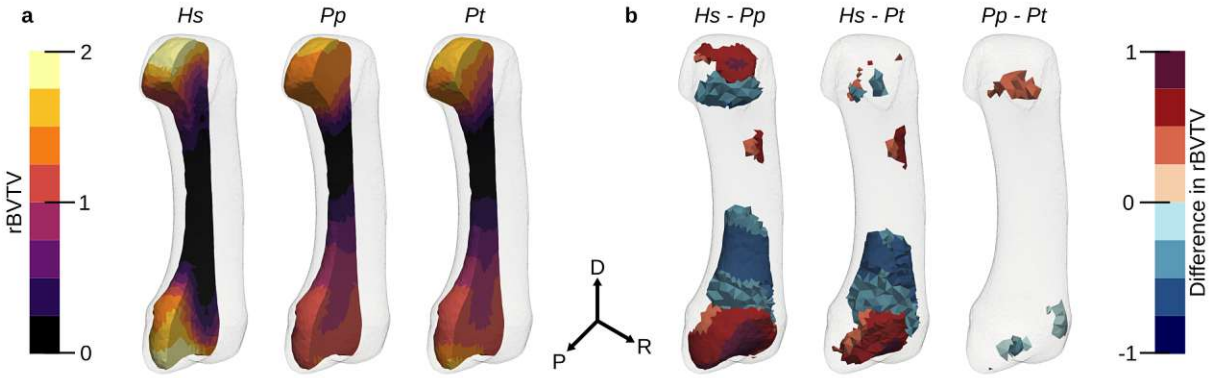

Figure 3.12: Average rBVTV and thresholded elements after family-wise error-rate (FWER) control. (**a**) Average rBVTV per species cut along the sagittal plane. From left to right: *Hs*: *Homo sapiens*, *Pp*: *Pan paniscus*, *Pt*: *Pan troglodytes*. (**b**) Statistically significant groupwise differences, thresholded at critical level for $\alpha = 0.05$ after FWER-control. Color gives the difference in rBVTV per species. For each pairwise comparison, a positive value (red) indicates that the first species has higher rBVTV while a negative value (blue) indicates that the second species has a higher rBVTV.
D: Distal, P: palmar, R: radial.

separated well from *Pan* via the first component. The first component accounted for $65.9\,\%$ of the total variance, and the second component for $8.9\,\%$.

Figure 3.13 shows the variability in shape for the first metacarpal, scaled by ± 3 standard deviations, i.e., capturing around $99.7\,\%$ of the variability for each mode. The first mode captured the width and thickness of the bone, while the second mode was only responsible for subtle width changes.

Proximal femur

The canonical bone was successfully created and all femora were registered onto the canonical bone. The canonical mesh contained $13\,075$ linear tetrahedral elements. Volume-skew for the canonical mesh was 0.25 ± 0.147 and tet-collapse 0.74 ± 0.12. After the mesh-morphing, volume-skew was 0.46 on average, ranging from 0.35 to 0.56 and tet-collapse was 0.6 on average, ranging from 0.53 to 0.67. The Dice coefficient of the images after registration was 0.98 ± 0.005 and Hausdorff distance was $6.48\,\mathrm{mm} \pm 4.022\,\mathrm{mm}$, while the MSD was $0.246\,\mathrm{mm} \pm 0.11\,\mathrm{mm}$.

The same HMA workflow was applied as for the first metacarpal bone. No clear pattern was visible in the univariate statistics for the full proximal femur (Figure 3.14) after family-wise error-rate (FWER) control. Therefore, the elements in the head region were analysed separately. The head region, which consisted of 5140 elements, was extracted from the full mesh and rBVTV was calculated for this region separately. Less than 70 elements showed significant differences after FWER-control in each pairwise comparison. The 80-percentile threshold of the rBVTV distribution of the mean mesh of each species showed a pillar structure inside the femoral head (Figure 3.15). This pillar structure

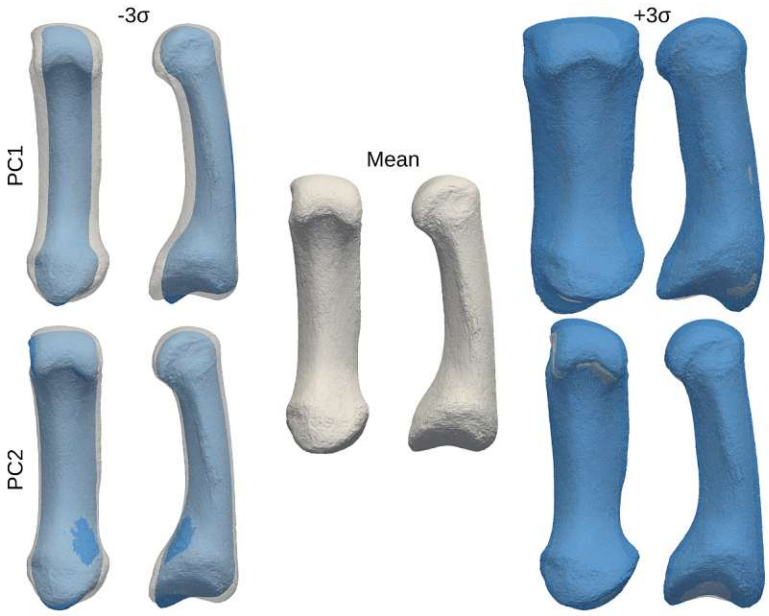

Figure 3.13: PCA shape modes for the first metacarpal bone in a frontal and sagittal view. Shown are $\pm 3\sigma$ of the first two principal components in blue of the shape deviation and the mean of the shape in white, measured from the B-spline coefficients of the SDM. The first component explained $33.9\,\%$ and the second component $20.1\,\%$ of the variance.

could be found in all three species and distally bifurcated into two pillars ending at the posterior and anterior aspects articular surface. The posterior pillar was present in all three species and extended anteriorly at the trabecular surface in only *Homo*. *Gorilla* and *Pan* exhibited an anterior pillar deep in the trabecular structure, which reached the trabecular surface in only *Gorilla*. The PCA plot (Figure 3.16b) for rBVTV in the head region showed a good separation of *Homo* versus *Gorilla* and *Pan*. However, the first principal component only accounted for $23.5\,\%$ and the second for $12.6\,\%$.

3.2.5 Discussion

It was possible to run the full workflow on both metacarpal as well as femoral bones using the identified parameters. Except for the canonical mesh size and resampled voxel size during registration, the parameters identified from metacarpals (i.e., B-spline grid spacing) could also be used for femoral bones. Even though the effective voxel size during registration was larger in the femora study ($0.6\,\mathrm{mm}$) than for the metacarpals ($0.3\,\mathrm{mm}$) to reduce the runtime, the registration performance was still acceptable, i.e., high Dice coefficient, low MSD, but larger Hausdorff distance than for the metacarpals. In both case studies, known differences between species could be found and quantified, and new, previously unreported differences in the trabecular bone could be observed.

These novel significant differences in the first metacarpals were located in the trabecular bone, farther away from the cortical surface, which was previously not analysed. For the metacarpal bones, the spatial extent of differences at the base between *Homo*

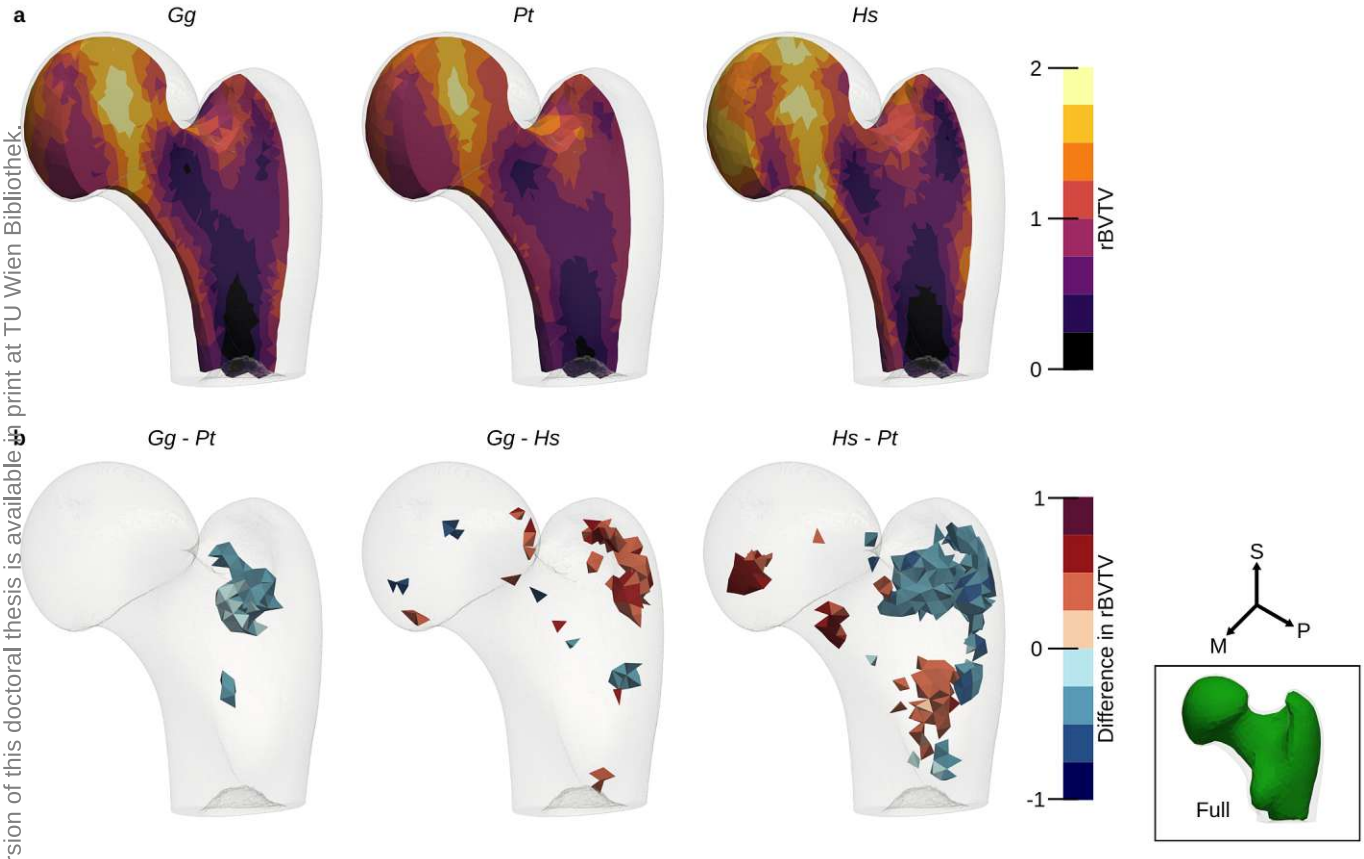

Figure 3.14: (**a**) Mean rBVTV distribution and (**b**) statistical analysis after family-wise error-rate (FWER) control of the proximal femur. From left to right: *Gg*: *Gorilla gorilla*, *Pt*: *Pan troglodytes*, *Hs*: *Homo sapiens*. S: superior, M: medial, P: posterior.

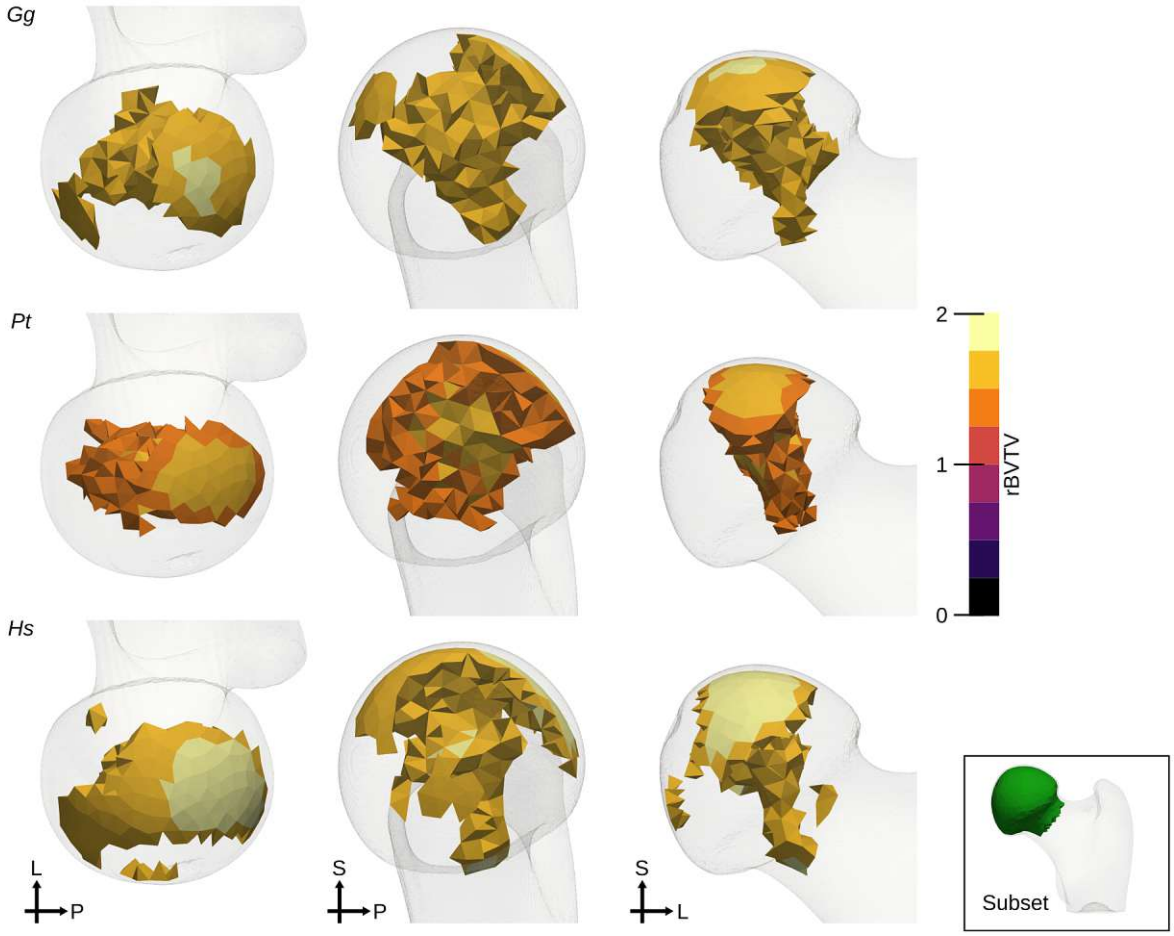

Figure 3.15: Thresholded femoral heads. rBVTV after thresholding at 80-percentile of each distribution in the femoral head only, shown here in three different views per species. From top to bottom: *Gg*: *Gorilla gorilla*, *Pt*: *Pan troglodytes*, *Hs*: *Homo sapiens*. L: lateral, S: superior, P: posterior.

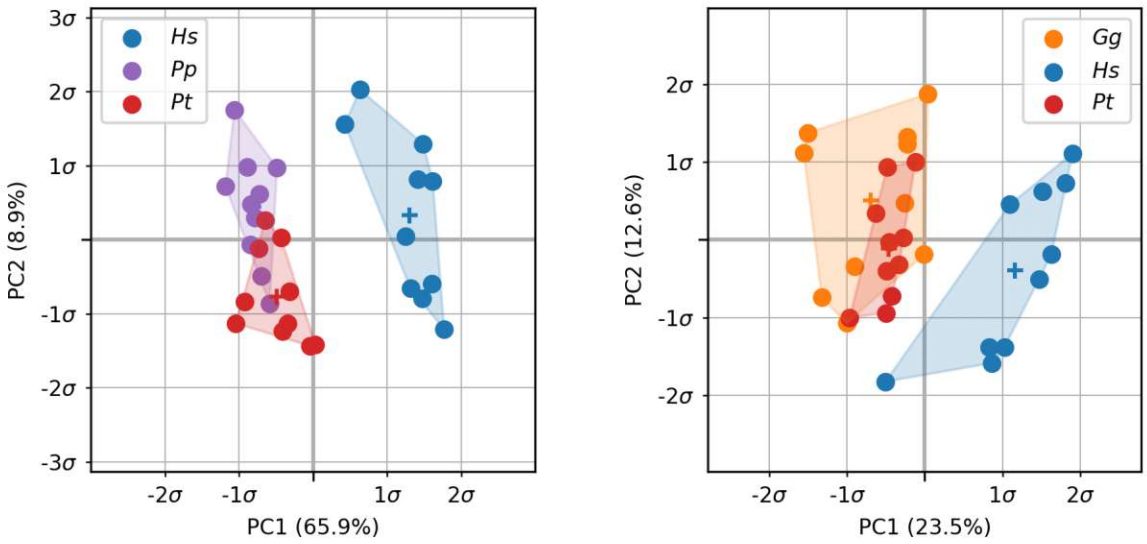

(a) First Metacarpal **(b)** Femoral Head

Figure 3.16: relative bone volume over total volume (rBVTV) PCA plots. The plot shows the first two components in the principal component space for rBVTV. **(a)** plot for the full first metacarpal (See Figure 3.12 for rBVTV plot). **(b)** plot for the femoral head (See Figure 3.15 for rBVTV plot). *Gg*: *Gorilla gorilla*, *Hs*: *Homo sapiens*, *Pp*: *Pan paniscus*, *Pt*: *Pan troglodytes*.

and *Pan* could be observed, including the density differences in the medullary cavity. Density patterns for the femoral head were consistent with previous results [196, 197]. However, there was no significant difference in the full proximal femur or the femoral head using univariate statistics and the pillar structure was not as prominent in the averaged images as it was shown to be in individuals. Only multivariate statistics, using PCA, on the cropped femoral head demonstrated the previously seen difference between the species. These findings suggest that the pillar structure might be more variable between individuals and thus is not found in the averaged images. Hence, element-wise comparisons are not able to pick up the signal because the variance for this small sample set is too high.

The PCA modes of the SDM were used to visualise the main variability in shape of the data set. While these SDM modes only reflect the shape variation, the variation in texture, i.e., microstructure, could also be visualised. However, this requires certain adaptations in the SDM workflow, as the average texture has to be calculated as well. This would lead to a so called statistical deformation and texture model (SDTM) [219, 242, 243], an extension of the SDM. To extend such SDTM models even further, any morphometric indices, other than density information, can be added in the PCA [233].

The here shown methods of evaluation only represent a subset of possibilities that can be employed using the cHMA method. As the whole method is build like a framework, it is possible to use different evaluation method or even combine it with other existing methods, depending on the scientific question. Furthermore, the here shown evaluations

were only performed on rBVTV, but the method works similarly for other morphometric indices.

3.3 Outlook

3.3.1 Mesh Deformation and Registration Quality

One of the major concerns with the application of cHMA is the tradeoff between mesh degradation and image registration quality. Using a very fine B-spline grid spacing and enough iterations in the optimiser, it is possible to achieve almost perfect registration in terms of Dice coefficient or surface distance. However, locally the registered images get largely distorted, which is especially apparent in the morphed meshes. Here, inverted (self-intersecting) elements, or elements that collapsed into planes or points can be observed. While for the application of cHMA such degraded meshes are *per se* not a problem, FEA can not be used with such degraded meshes. However, also in cHMA the mesh quality is of importance, because it is questionable if homologies are established between two bones when portions of one bone are squished into a very small region.

To regularise the registration, a relatively coarse B-spline grid was chosen ($20\,\mathrm{mm}$). The effect of using different B-spline grid distances can be seen in Figure 3.17. Using a coarse grid spacing leads to a more global deformation, while a small grid spacing increases the level of local deformation that can be covered by the B-spline. Another relatively easy solution is to restrict the displacement of B-spline grid nodes during the registration. The reason is, that the image deformation is directly influenced by the B-spline grid deformation. Optimisers with bounds can be used for such purposes. However, a crucial question is, how large the restriction of the displacement can be, until a critical deformation is reached. A lower bound is the criterion of diffeomorphic transformation, which means that the transformation can be inverted. B-spline transformations are not necessarily diffeomorphic, but criterions for a B-spline transform to be diffeomorphic can be given in terms of maximal grid displacements [244]. For a cubic 3D B-spline transformation, the sufficient condition is that the displacement magnitude at each grid point in all three directions is less than $\delta/2.4794$, where δ is the grid spacing. Unfortunately, these values are conservative and restricting the displacements to such a value typically results in insufficiently registered images, also noted in literature [218]. In preliminary studies using the proximal femur image set, it was found that for a $20\,\mathrm{mm}$ grid spacing, a $15\,\mathrm{mm}$ restriction on the node displacements results in approximately the same mesh deformations and registration metrics as the unconstrained registration. But restrictions using the criterion for diffeomorphism [244] only allowed a displacement of just $8\,\mathrm{mm}$, which led to insufficient registration of the bones. However, also other methods exists such as stacking of multiple B-spline transformations, to ensure diffeomorphism but still increasing the registration performance [218]. But using a stack of B-spline transformations cannot be used in the SDM without prior modification of the algorithm. Only in the final registration stage, other types of transformations can easily be applied.

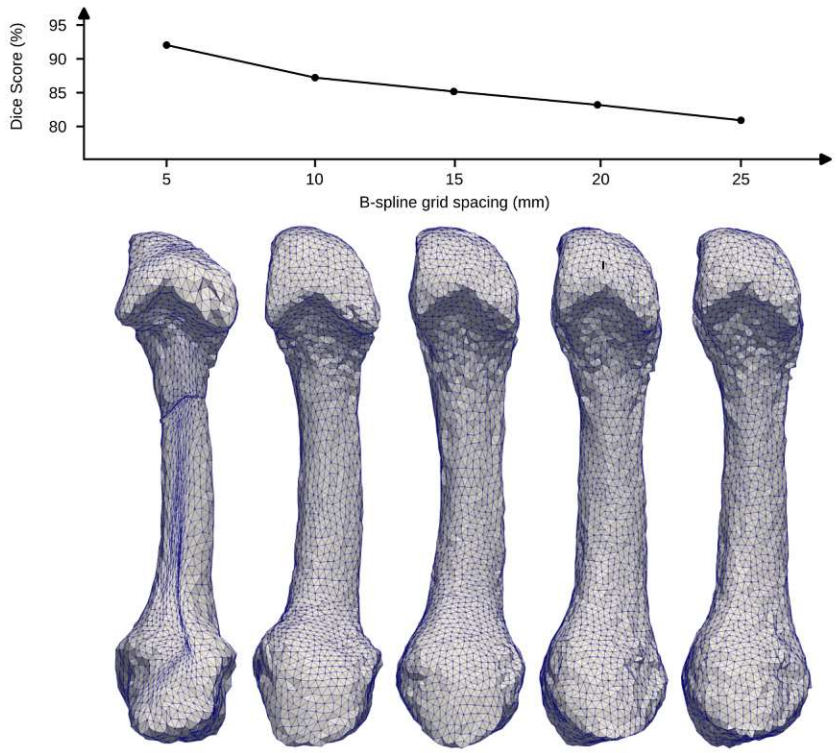

Figure 3.17: Mesh deformation and B-spline grid spacing. The plot on top gives the Dice score. Using a lower grid spacing, leads to a higher Dice score and thus better image registration, however visible mesh degradation is apparent in the $5\,\mathrm{mm}$ grid spacing.

While a multitude of methods exists for the regularisation of the B-spline transformation, each of them has to be thoroughly tested for the specific use case. Some of these methods offer a simple implementation, but then restrict the transformation too much to give useful results for multi-species registration. Others require extensive changes to the existing algorithm, while promising excellent result. Thus, a task for the future is to find methods, that fulfil the triad mesh degradation, image registration quality, and implementation easiness.

3.3.2 Finding Homologies

A number of validations was performed for the cHMA method. However, it was not directly possible to quantify how well homologous regions are identified. A relatively straight forward method for this investigation is to manually define homologous regions in the original image set, for example, using landmarks. Then the images are registered onto each other and the landmarks are transferred onto the canonical bone. The position of the landmarks on the canonical bone can then be investigated. Ideally, landmarks of homologous points are exactly in the same position on the canonical bone as well. However, the identification of homologous points is not straight forward, especially if multiple species are involved. For example, gorillas, and partially also other knuckle walking species, have a characteristic feature on their metacarpal bones, known as dorsal

metacarpal ridge (DMR) [245]. This DMR is missing in other non-knuckle-walking species, and thus the question is how such structures can be related to other species. Furthermore, while landmarks on the surface of the bone can be identified via anatomical descriptions, such landmarks are sparse on the inside of the bone. But as the cHMA method allows for the registration of the whole bone volume, also the assessment of the accuracy on the inside would be required. So far, a conclusive data set for the evaluation of such landmarks is missing.

Thus, several experiments can be conducted to elucidate this question. One could be the aforementioned comparison between manually annotated (anatomical) landmarks and the same landmarks projected on a canonical bone. This would answer the question if such homologous points are implicitly identified by cHMA, given the limitations of manual landmarking as described above. Another test could be to compare the cHMA method with the recently developed "Phenotypic PointCloud Analysis" [190, 246]. It uses a different registration method based on the coherent point drift algorithm and thus could get information how similar the volumetric correspondence is, compared to cHMA.

3.3.3 Fossils and Incomplete Data

The here shown examples of the application of cHMA were solely on perfectly preserved bones of extant species. However, a goal is to use the method also for fossils, which are often not found in perfect condition (Figure 3.18). The morphometric analysis of fossils can be challenging [247] as taphonomic changes of the bones can influence the measured morphometric indices, even after a relatively short time [248]. Cracks in the bones will also influence morphometric quantities, such as trabecular orientation [249]. During the fossilisation, the organic bone phase also crystallises, or other materials are included in the bone. These effects can be localised but also global and will influence the measurement of BMD significantly, if not corrected for. Special μCT method such as neutron μCT (n-μCT) can be used to get better images, even from fossilised bone, but such devices are not readily available [250]. Finally, many fossils only exists in fragments, which can be an issue during the registration of the images.

All these taphonomic damages makes it hard to register images of fossils. Systematic differences, for example of higher mineralisation due to fossilisation, can influence certain image similarity metrics, used in the image registration. This can be avoided by selecting a robust registration metric. Problems can also occur at cracks or inclusions, as such regions might be "over-registered" in the registration, i.e., large deformations are imposed to move or even remove such regions from the resulting image. Again, selecting robust registration metrics can help in such situations, but also the regularisation of the transformations used in the registration. Lastly, including fragmentary images in the creation of the canonical bone might skew the canonical bone too much. A straight

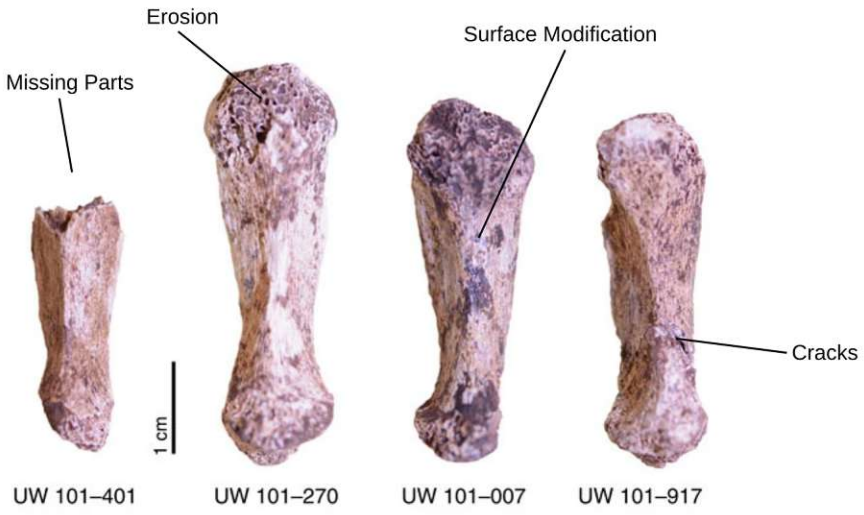

Figure 3.18: A variety of taphonomic damages on the example of the first metacarpal fossils [251] of *Homo naledi* [2]. This example shows just a subset of taphonomic damages.
This image contains Creative Commons licensed work. A detailed description can be found in the chapter "Image Credits" at the end of this thesis.

forward solution is to create the canonical bone on a set of ideal bones first and then only register the fossils later-on. This has the disadvantage that the fossils are not included in the canonical bone and thus also the PCA analysis of the SDM is hindered, but it offers a much cleaner workflow and the possibility to use specific registration parameters for such special bones.

Similar to fragmentary fossils, subsections of bones might be used, as already described for the proximal femur sample set. Here, the intention is to reduce the computational effort in the creation of the canonical bone as well as the registration of the samples. For femora, where the shaft is actually hollow, no trabecular information can be seen below the minor trochanter and thus, the samples were cropped at this position. However, including samples with different cut heights introduces another source of variability, that can impose problems in the registration. It was noticed, that in some samples the mesh degradation in the distal region of the femur was increased, presumably due to the different heights. Here, also regularisation can help, as it can restrict too high deformations. However, also the option to remove regions of high degradation from the mesh in a later stage is possible, and was successfully demonstrated for the proximal femur, by focusing the analysis on the femoral head.

The SDM inside cHMA can be employed for many more tasks. If the texture (i.e., the density distribution) is also incorporated to form a statistical deformation and texture model (SDTM), it is for example possible to use such a model to reconstruct shape and texture of missing data or even reconstruct 3D images from 2D images [252]. Such a method can also be used to reconstruct taphonomically damaged bones [253]. However, such methods rely on the collected variation in the sample set for the reconstruction of features of a single bone. For fossils however, it is questionable if a representative sample

set can be found, for the imputation of missing data. Furthermore, if regions of the bone are reconstructed from such a sample set, the inference from the bone microstructure is strongly biased by the information of the SDTM. Nevertheless, such methods offer the possibilities to create smooth meshes, even from damaged bones and the application can also be limited to fill-in smaller cracks or voids instead of reconstructing large portitions of bones.

Another option to register fragments of bones onto a canonical bone is to use a landmark based registration, for the initial alignment of the data (similarity transform). The correct alignment of the images is necessary, as the B-spline transform does not include affine transformations, such as rotation or translation. Thus, if fragmentary bones are badly aligned, also the resulting B-spline transform will give bad results. Even with a minimal number of landmarks, it is possible to pre-align the bones. For example, if the overall size, rotation and position of the bone can definitely be defined using landmarks, it is actually a faster and more robust way instead of using a similarity transform with an image-based registration metric. However, landmarking requires extra manual work and certain problems with landmarking were already discussed in the former section.

3.3.4 Using the Morphed Meshes for FEA

The meshes generated by the cHMA method have the advantage to be isotopological. While the here generated meshes only were used as an easy way to establish a relationship between the samples over the whole volume, other methods, such as FEA, also require meshes. While FEA does not require isotopological meshes *per se*, it can be helpful to have them in order to compare different samples to each other. Steiner, Synek and Pahr [254] already demonstrated, that a combination of SDM and FEA is possible and also other studies used mesh morphing (with or without an SDM) as a tool to quickly generate new FEA meshes from a given template [212, 255–259]. Typically, these mesh morphing studies were performed on single species though, i.e., humans. However, it is not yet known if the element quality is still good enough, when multi-species samples are used, as the variability might be larger and thus also the deformations get larger, which leads to more degraded elements. Therefore, future studies should investigate how well such multi-species meshes can be used for the application of FEA, i.e., how the degradation of the meshes can kept to a minimum while preserving the flexibility of the mesh-morphing. This research question also incorporate the other here mentioned questions, for example, how the whole registration method can be regularised and thus degradation of the meshes effectively reduced.

Chapter 4

hFE-based Inverse Bone Remodelling

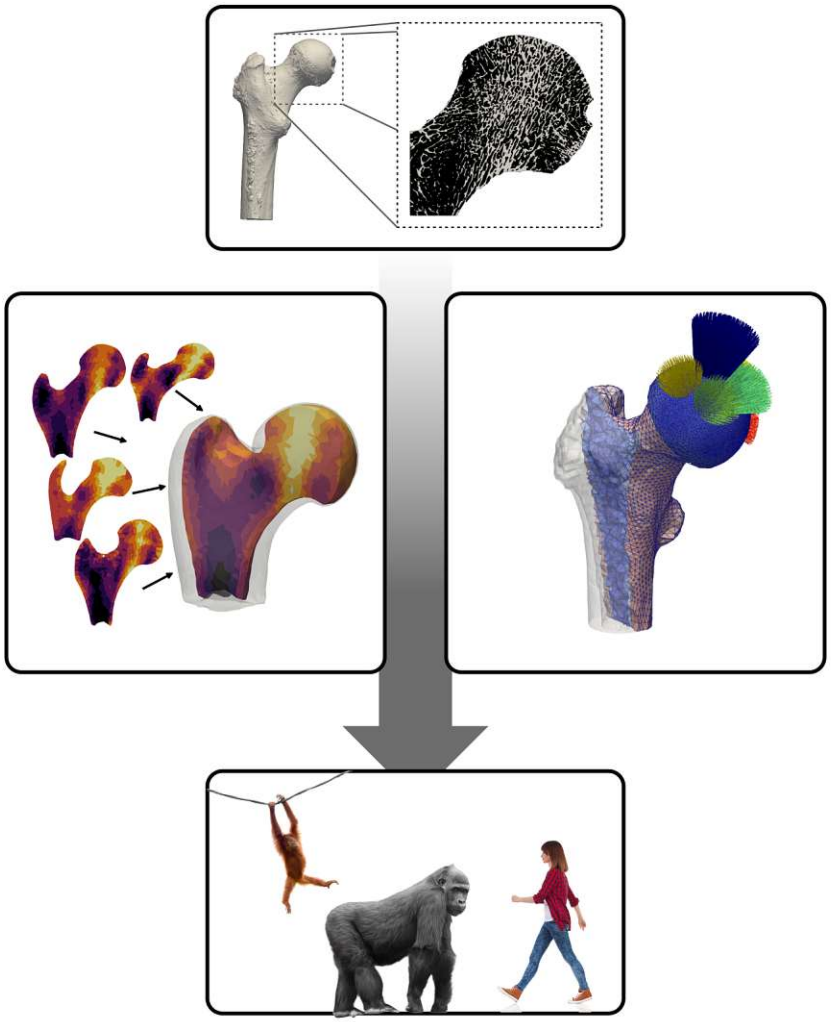

This chapter will present enhancements made to the inverse bone remodelling (IBR) method. As described in the background chapter (section 2.3.3), a major limitation of the IBR method is that it relies on μFE models, which are computationally expensive. In this chapter, the path to overcome this limitation, by using hFE instead of μFE models, is outlined and the enhanced IBR method is applied to two bones of the human skeleton. Specifically, this chapter is divided into four sections. The translation from μFE-based to hFE-based IBR and implementation details are explained in section 4.1. In the following two sections, the translated method is applied to the distal radius (section 4.2) and the femoral head (section 4.3) and compared to results from the original μFE-based IBR algorithm. In section 4.4 an outlook is given by first presenting a proof of concept study, which was previously not computationally feasible with the μFE-based method. Then two specific limitations are discussed and possible future studies are outlined. Essential background information is briefly repeated in the introduction of the sections 4.1, 4.2, and 4.3, while more detailed information can be found in chapter 2.

4.1 Translating Tissue to Continuum-Level

4.1.1 Related Publication and Declaration of Contributions

This section is based on the publication

> S. Bachmann, D. H. Pahr and A. Synek. 'A Density-Dependent Target Stimulus for Inverse Bone (Re)modeling with Homogenized Finite Element Models'. In: *Annals of Biomedical Engineering* (2022). DOI: 10.1007/s10439-022-03104-x

Author contributions: **Sebastian Bachmann**: Conceptualisation, Methodology, Software, Validation, Formal analysis, Investigation, Writing - Original Draft, Writing - Review & Editing, Visualisation. **Dieter H. Pahr**: Conceptualisation, Methodology, Writing - Review & Editing, Supervision. **Alexander Synek**: Conceptualisation, Methodology, Writing - Review & Editing, Supervision.

Acknowledgements: This project has received funding from the European Research Council (ERC) under the European Union's Horizon 2020 research and innovation program (Grant agreement No. 819960).

4.1.2 Introduction

Finite element (FE) models of bone can be used for many applications, for example, to predict fracture risk or to optimise operative planning in orthopaedic surgery [260]. While it is relatively easy to create such models using generic geometry and boundary conditions, real bones are diverse in their shape, inner microstructure, and *in vivo* loading conditions. Hence, using patient-specific geometry, material, and boundary conditions is required to enhance the precision of those models [261]. While there was a significant advancement in capturing patient-specific geometries and bone material models that account for microstructure, including physiological *in vivo* loading is still challenging. Physiological loading conditions can be measured *in vivo* using invasive technologies such as implanted strain gauges [114] or instrumented endo-prostheses [37, 262]. While instrumented endo-prostheses can measure the joint loading accurately, they are not used in healthy patients. Non-invasive options are musculoskeletal models [116] which, however, require exact modelling of the muscles and bones of the patient.

Another approach to estimate physiological loading is to use the information stored in the microstructure of the bones. Bone undergoes constant repair and is also able to adapt to regular external loading. Two mechanisms, known as remodelling and modelling, are responsible for changing the bone [40]. While remodelling is determined by a coupled local bone resorption and formation, no such coupling can be observed during

modelling. Often both modes cannot be discriminated, and the phenomenological response is then referred to as (re)modelling. Among other factors such as metabolism, it is driven by mechanosensitive cells [42] inside the bone. Therefore, mechanical quantities can be measured inside the bone and used as a proxy for the (re)modelling response. One method that uses this relationship is inverse bone (re)modelling (IBR) [142, 144]. Contrary to forward (re)modelling models, where the resulting microstructure is of interest when a particular load is applied, IBR can be used to find the loading that led to a given microstructure. Briefly, one possibility is to use FE models to impose a set of unit loads on the bone to measure the response in local mechanical quantities such as stress or strain energy density (SED). Then, the magnitude, direction, or superposition of these unit loads is varied until a nearly homogeneous loading state is reached, which is assumed to be close to a physiological loading in terms of the measured variable.

The first IBR algorithms were developed by Fischer, Jacobs and Carter [142]. They used 2D FE models to predict joint loads and muscle forces at the proximal femur [180, 263, 264], to differentiate between coxa valga and vara [176], to predict relative bone loads at the distal radius and ulna [265], and to relate bone density to locomotor mode or activity [177, 266]. While Fischer, Jacobs and Carter [142] used relatively low-resolution quantitative-CT ($\sim 0.8\,\mathrm{mm}$ resolution) for measuring bone density, 2D homogenised FE (hFE) models and stress as the target stimulus, Christen *et al.* [144] used micro-computed tomography (μCT) images, which depict the microstructure of bones in more detail, in 3D with SED as the target stimulus. Despite its simplicity, 3D IBR using μFE models was successfully applied to estimate physiological loading conditions for mouse vertebrae [144], mouse femora [267], human tibia [51], human vertebrae [268], predicting the reaction forces at the distal radius [269], and differentiate between species with different locomotor modes, using the hip [178] or finger bones [70]. While μFE-based IBR can be used to predict physiological loads on smaller bones (e.g., of mice or segments of bones), application to large bones (e.g., entire femur) is not a viable option due to high computational demands and resulting runtimes. Further, realistic boundary conditions, e.g., including articular contact, can only be modelled with high effort in μFE models [155] but contact boundary conditions are readily available in most FE solvers when smooth meshes are used. Thus, only simplified boundary conditions are typically used in μFE, for example by using embedding materials [269] or fully bonded articulated bones [270]. Furthermore, due to the higher runtimes on large bones, also the number of load cases is limited in μFE-based IBR [271]. Replacing the μFE models with hFE models would allow efficient IBR with realistic boundary conditions. However, so far, hFE-based IBR was limited to 2D models [142, 176, 177, 180, 263–266]. In addition, no comparison between μFE- and hFE-based IBR has been performed so far.

The goal of this study was to translate the established IBR method for μFE by Christen *et al.* [144] to hFE so that in the future physiological loading can also be estimated for larger bones with more realistic boundary conditions and lower computational demands.

This translation from the tissue-level SED optimisation to the continuum-level was performed using a large set of trabecular bone cubes.

4.1.3 Methods

The original formulation of the μFE-based IBR algorithm by Christen *et al.* [144] shall be repeated here briefly. A set of N_{LC} unit loads is applied to the bone. Each of the load cases can act m_i times per day, however for the reconstruction of the loading history using unit loads, this value can be set to 1 [271]. Then, unit load scaling factors α_i are found, such that the squared difference of local SED $U(x)$ and a tissue-level target stimulus $\tilde{U}$ is minimised. These scaling factors are identified in an optimisation procedure, using a residual function $r(s_i)$ of SED scaling factors $s_i = \alpha_i^2 / N_{\mathrm{LC}}$. As SED is used, which cannot be negative, the optimisation is subjected to only positive real numbers for s_i and can be written as:

$$\min_{s_i \in \mathbb{R}_0^+} r(s_i) = \int \left(\tilde{U} - \sum_{i=1}^{N_{\mathrm{LC}}} s_i \, U_i(x) \right)^2 dV \tag{4.1}$$

However, the tissue-level target stimulus cannot be used for homogenised FE analysis, as elements are at the continuum-level. Elastic constants of porous media can be related to the density using a power-law [157] to form a relationship between tissue and continuum-level. Therefore, the tissue-level stimulus $\tilde{U}$ can be replaced by a continuum-level stimulus $\tilde{U}_{\mathrm{hom}}$, which is a function of local relative density ρ:

$$\tilde{U}_{\mathrm{hom}} = \tilde{U}_0 \, \rho(x)^d \tag{4.2}$$

To ensure compatibility at $\rho = 1$, $\tilde{U}_0$ is set to $\tilde{U}$. Inserting Eq. (4.2) into Eq. (4.1) gives:

$$\min_{s_i \in \mathbb{R}_0^+} r(s_i) = \int \left(\tilde{U}_0 \, \rho(x)^d - \sum_{i=1}^{N_{\mathrm{LC}}} s_i \, U_i(x) \right)^2 dV \tag{4.3}$$

Note that the proposed continuum stimulus is therefore isotropic, although trabecular bone elasticity is orthotropic at the continuum-level [34]. Contrary to μFE, where all elements have the same volume, hFE meshes usually contain differently sized elements, and thus, the volume cannot be neglected in the equation. Eq. (4.3) has to be rewritten in a discrete form to be used for FEA and can further be transformed into a matrix equation to be directly solved by using a non-negative least squares solver [272].

The SED is measured at the integration points of each of the N_{IP} integration points of the FE mesh, for all of the N_{LC} unit load cases. The volume of each integration point V_j has to be calculated and the density of each integration point ρ_j is already known from the material homogenisation. Substituting the integral with a finite sum gives:

$$\min_{s_i \in \mathbb{R}_0^+} r(s_i) = \sum_{j=1}^{N_{\mathrm{IP}}} \left(\tilde{U}_0 \, \rho_j^d - \sum_{i=1}^{N_{\mathrm{LC}}} s_i \, U_{j,i} \right)^2 V_j \tag{4.4}$$

This function can be transformed into a matrix form $r(\boldsymbol{x}) = ||\boldsymbol{A}\boldsymbol{x} - \boldsymbol{b}||$, in order to be solved efficiently. To write the matrix equations efficiently $\mathbf{1}_m = (1, \ldots, 1)^T$ defines a column vector of shape $m \times 1$ filled with ones of arbitrary length. Further, $[\boldsymbol{A} \circ \boldsymbol{B}]_{ij} = [\boldsymbol{A}]_{ij}[\boldsymbol{B}]_{ij}$ is the Hadamard product of two matrices of equal size and $\boldsymbol{a} \otimes \boldsymbol{b} = C_{ij} = a_i b_j$ is the dyadic product of two vectors of equal size.

The SED values of all N_{IP} integration points of the FE mesh for the N_{LC} unit load cases are stored in a matrix $\boldsymbol{U}$ of shape $N_{\mathrm{IP}} \times N_{\mathrm{LC}}$, the integration point volumes in a vector $\boldsymbol{V}$ of shape $N_{\mathrm{IP}} \times 1$, and the relative densities for each integration point in a vector $\boldsymbol{\rho}$ of shape $N_{\mathrm{IP}} \times 1$. Then, the optimisation using the scaling vector $\boldsymbol{s}$ of shape $N_{\mathrm{LC}} \times 1$, can be written in matrix form as:

$$\min_{\boldsymbol{s} \in \{\mathbb{R}_0^+\}^{N_{\mathrm{LC}}}} r(\boldsymbol{s}) = ||\boldsymbol{U}'\boldsymbol{s} - \tilde{\boldsymbol{U}}|| \tag{4.5}$$

Where $\boldsymbol{U}'$ is the volume corrected matrix of SED, defined as $\boldsymbol{U}' = \boldsymbol{U} \circ \left(\sqrt{\boldsymbol{V}} \otimes \mathbf{1}_{N_{\mathrm{LC}}} \right)$ and $\tilde{\boldsymbol{U}}$ is the target stimulus vector, defined as $\tilde{\boldsymbol{U}} = \tilde{U}_0 \, \boldsymbol{\rho}^d \circ \sqrt{\boldsymbol{V}}$. The same equation can still be used for μFE. The volume and density are constants in μFE and can therefore be set to an arbitrary value or simply to 1 without having an effect on the result.

The next step is to identify the exponent d from the power-law relationship of Eq. (4.2). Here, a bottom-up approach was chosen, to identify this value on bone cubes, similar to those used to infer apparent material properties. The idea is, that if the optimal loading state of the bone cube is found using μFE-based IBR, the macroscopic SED will correspond to the homogeneous target stimulus. Six canonical load cases can be applied to the bone cube, for example using kinematic uniform boundary condition (KUBC) [133] or periodicity compatible mixed uniform boundary condition (PMUBC) [133]. As homogenisation with different boundary conditions lead to different stiffness tensors of the bone cubes [273], differences in the optimal SED are also to be expected. Using the six canonical load cases, it is possible to describe any strain state of the bone cube at the macroscopic level, thus the hypothesis is, that the optimal strain state can be found if these six load cases are optimised. Then the optimised macroscopic SED $\langle U_{\mathrm{opt}} \rangle$, equivalent to the homogeneous target stimulus, can be calculated from the volume averaged stresses $\langle \boldsymbol{\sigma}_i \rangle$ and *a-priori* volume averaged strains $\langle \boldsymbol{\varepsilon}_i \rangle$ using:

$$\langle U_{\mathrm{opt}} \rangle = \frac{1}{2} \sum_{i=1}^{6} s_i \, \langle \boldsymbol{\sigma}_i \rangle : \langle \boldsymbol{\varepsilon}_i \rangle \tag{4.6}$$

When bone cubes with different densities are available, the relationship of resulting homogeneous target stimulus and density can be fitted (Figure 4.1). Two sets of trabec-

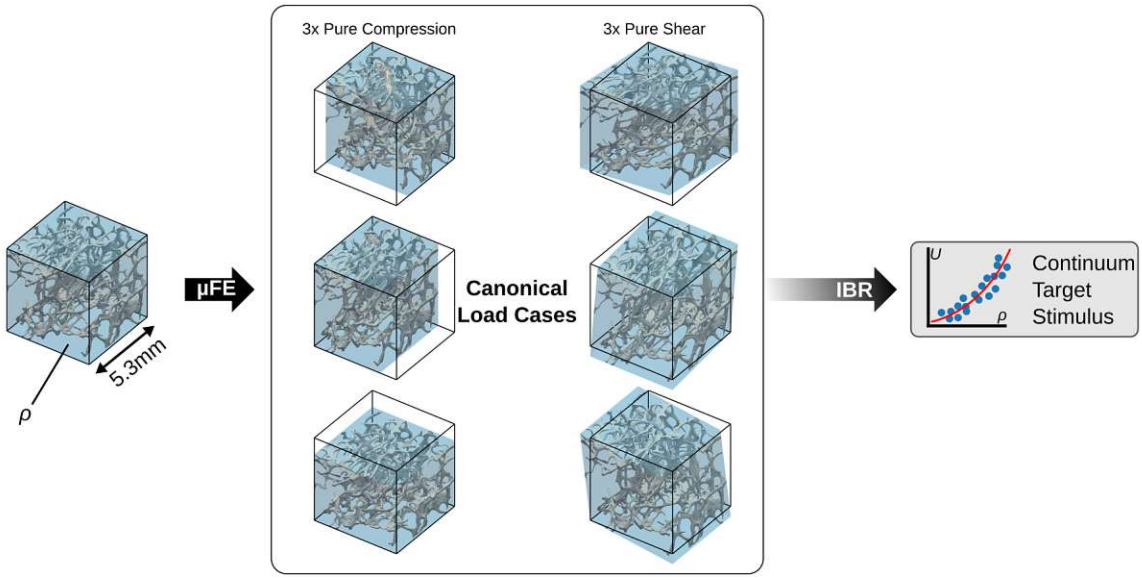

Figure 4.1: Fitting the continuum target stimulus using trabecular bone cubes. Six canonical load cases (three pure compression, three pure shear; Here shown exemplary for KUBC) are used to load the trabecular bone cubes. Then, the load cases are used in IBR and the optimised macroscopic SED is calculated. Finally, the continuum target stimulus can be fitted using the relative density ρ of the bone cubes.

ular bone cubes were used to fit the target stimulus with different types of boundary conditions. First, a set of 701 trabecular bone cubes from three different bones (proximal femur, distal radius, and vertebrae) was used from a previous study, in which the apparent stiffness properties of these cubes were identified using KUBC [274]. The same cubes were used to identify the exponent d for the continuum-level target stimulus of IBR, by applying the six canonical load cases using KUBC. Second, a set of 168 femoral trabecular cubes was used, which were aligned by their axes of orthotropy [275]. This alignment was necessary to use PMUBC. Subsequently, the six canonical load cases were applied for using PMUBC.

To evaluate the results of the optimisation, the coefficient of variation (CV) was calculated before and after the optimisation, which is a measure of the homogeneity of the SED distribution [144]. The CV is calculated from the tissue-level SED distribution obtained with uniform scaling of the six canonical load cases ($s_i = 1$) and optimally scaled load cases. Then, Cohen's d [239] was calculated and t-tests were performed to evaluate the effect of the optimisation.

Soft- and Hardware

All statistical analyses were performed using scipy [232] 1.7.2 and Python 3.7.4 (Python Software Foundation, `https://www.python.org`). The hFE meshing and the material mapping were performed using medtool 4.5 (Dr. Pahr Ingenieurs e.U., Pfaffstätten, Austria, `http://www.medtool.at`). The μFE models were solved in ParOSol [276]. All analyses were performed on a dual AMD EPYC 7452 system.

4.1.4 Results

Bone Cubes: KUBC

The μFE-based IBR on the bone cubes could significantly reduce the coefficient of variation (CV) of the tissue-level SED on average from $78.8\,\%$ to $74.2\,\%$ ($p < 0.001$; Cohen's $d = 0.263$; Figure 4.2b). The optimised continuum stimulus followed a power-law with an exponent of 1.19 and a high coefficient of determination ($R^2 = 99.7\,\%$; Figure 4.2a).

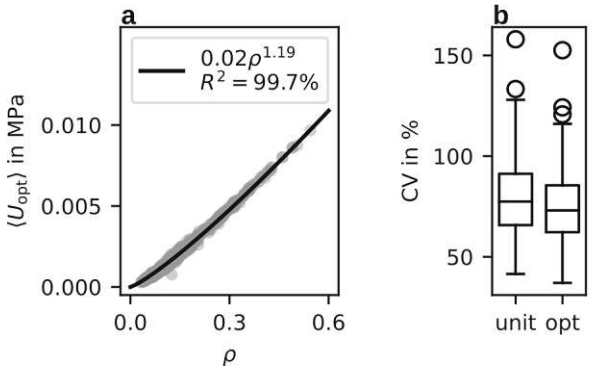

Figure 4.2: (**a**) Fitted power-law on the optimised continuum stimulus for the bone cubes using KUBC. (**b**) Coefficient of variation (CV) for the SED distribution of the bone cubes before (unit) and after optimisation (opt).

Bone Cubes: PMUBC

On the sample set of 168 bone cubes, a slightly higher exponent was found (1.297), with a similarly good fit ($R^2 = 98.7\,\%$; Figure 4.3a). The mean CV was significantly reduced from $84.5\,\%$ to $79.4\,\%$ ($p < 0.001$; Cohen's $d = 0.31$; Figure 4.3b).

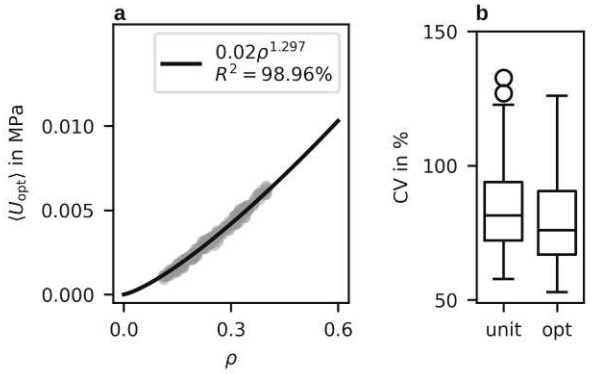

Figure 4.3: (**a**) Fitted power-law on the optimised continuum stimulus for the bone cubes using PMUBC. (**b**) Coefficient of variation (CV) for the SED distribution of the bone cubes before (unit) and after optimisation (opt).

4.1.5 Discussion

The tissue-level optimisation function of Christen *et al.* [144] was translated to a continuum-level optimisation function using a power-law, connecting both levels using the relative density. The required exponent of the power-law was identified in a bottom-up approach for two sets of unit load cases (KUBC and PMUBC).

The here found exponents for the relation between tissue and continuum-level were 1.19 (for KUBC) and 1.297 (for PMUBC) and thus both lower than in the similar model of Fischer, Jacobs and Carter [142], where an exponent of 2 was used. This relationship was found in experiments regarding bone strength [157] and analytical models of porous structures [158]. However, no comparison to other methods or validation of this assumption has been made so far in the context of IBR. One explanation for this difference in value might be, that the exponent was fitted on a dataset, using the accumulated macroscopic SED as a target value, instead of resorting to proxy values such as bone strength. Thus, while bone strength might scale well with an exponent of 2, the accumulated SED might not.

This discrepancy in exponent can also stem from the boundary conditions used for the bone cubes. Both types cannot perfectly reflect the true physiological loading state, as KUBC tends to be too stiff and PMUBC too soft. Thus, a bone cube loaded with a physiological boundary condition might yield a different optimised orientation, for example, when using an *in situ* boundary conditions [273]. This stiffening or softening behaviour of the boundary conditions was also observed in the resulting exponent. The softer PMUBC yielded a higher exponent, thus giving more weight on the density to give the same SED. Thus, the exponent found for PMUBC was closer to the "theoretical value" of 2 used by Fischer, Jacobs and Carter [142], compared to the results obtained by KUBC. This might indicate that PMUBC are closer to a physiological loading than KUBC and thus generally better suited for the task of identifiying the required parameters. On the other hand, if the true exponent of the power-law lies between the ones obtained from KUBC and PMUBC, similar to the apparent stiffness, both values would give lower and upper bounds with the effective value in between.

In this study, only the exponent of the power-law was determined using parameter fitting, whereas U_0 was assumed to be consistent with the tissue-level target stimulus. To reassure that the found exponent value is not influenced by the fixed tissue target stimulus, the same curve fitting procedure was repeated with an unconstrained U_0. Here, similar values for the exponent were found (1.215 for KUBC and 1.369 for PMUBC) with only slightly different U_0 ($0.0208\,\mathrm{MPa}$ for KUBC and $0.0219\,\mathrm{MPa}$ for PMUBC). This is not surprising, as a homogeneous bone cube with $100\,\%$ density should have exactly the tissue target stimulus as macroscopic SED after the optimisation.

There are also other factors that can influence the found exponent of the power-law connect tissue to continuum-level target SED. The trabecular bone cubes only consisted of cubes with a maximum density of around $60\,\%$ for the KUBC data set and around

$40\,\%$ for the PMUBC data set. This means, that high-density cubes were not in the set, which could lead to inaccuracies in the prediction for cortical or near-cortical bone, with high density. For hFE-models that separate the cortical bone from the trabecular volume ("smooth models" [156]), not many elements in the trabecular volume have high densities and elements in the cortex are typically near a BVTV of $100\,\%$. However, for voxel-based FE models, where no separation between cortex and trabecular volume can be made [216], such high volume fractions are possible.

One limitation of this study was that KUBC and PMUBC-derived power-law exponents were found using different data sets. To check whether the used bone cube data set would influence the exponent, the smaller set of bone cubes by Panyasantisuk *et al.* [275] used for the PMUBC-based fit was also evaluated with KUBC. Here, the exponent was 1.161 (1.168 without constraining U_0) which is close to the value of 1.19 found by using the larger bone cube set from Gross, Pahr and Zysset [274], and thus again lower than in PMUBC ($d = 1.297$), suggesting that the low exponent is not dependent on the bone cubes used.

To fit the continuum target stimulus on the bone cubes, the same IBR optimisation function was used, which assumes that the daily stimulus is additive and based on SED. This method was necessary, as in the continuum version of the IBR method, each element will be optimised with the same additive objective function. However, this averaged quantity behaves differently than a true linear superposition of stresses and strains, necessary to describe a strain state on the bone cube. Thus, while the optimisation function is consistent for both continuum and tissue-level, a superposition of the tensorial quantities to yield the optimised macroscopic SED will certainly give a different exponent as well.

Although a good fit was achieved when fitting the continuum target stimulus on the bone cubes, the used tissue stimulus function is still highly simplified as it only accounts for an accumulative and time-averaged stimulus of bone. While it showed the ability to predict physiological loading conditions using μFE methods on a variety of bones [51, 70, 144, 178, 267–269, 271], other formulations can be used as well. Fischer, Jacobs and Carter [142] used continuum-level effective stress, scaled to the tissue-level, while the here employed method scales the stimulus to the continuum-level and directly uses SED. Other possibilities to describe the stimulus function can be obtained by switching from a scalar to a higher-order quantity. For very small isotropic elements, as they are used in μFE, a more elaborate optimisation criterion might be superfluous, whereas hFE might benefit from including more information as bone is known to be orthotropic and loaded in a multiaxial way at this scale [34]. For instance, the optimal loading stimulus could include the orientation of principal stresses or the ratio of minimum and maximum principal stresses. Thus, future work could also test the viability of using different vectorial or tensorial quantities.

Such an objective function was recently presented by Schenk and Zysset [277], which used the strain tensor directly and hydrostatic strain as the target stimulus. This formulation of IBR used continuum elements directly and also connected the volume fraction dependency using a power-law. The exponent for the volume fraction dependency was identified with 0.008 and is thus much smaller as the here found values. This exponent results in relatively low sensitivity to the density of each element (e.g., for elements above $10\,\%$ BVTV, the tissue-level stimulus is already scaled by a factor of 0.98).

An entirely different 3D hFE IBR approach was used by Campoli, Weinans and Zadpoor [145] and Garijo *et al.* [147]. They used forward remodelling models to train artificial neural networks (ANN) many different loading patterns that could then be used to predict the loading pattern in a given bone. While these models were able to work on larger bones, such as the proximal femur [145, 147] or the proximal tibia [278], they are only phenomenological, require highly time-consuming re-training for new load cases, and also individualised training for each bone. Also, the choice of the forward remodelling algorithm will influence the result, similar to the choice of the target stimulus in the here used model.

The here presented continuum target stimulus extends the previously presented μFE-based IBR method such that it can also be applied using hFE models. The presented stimulus is still consistent with the original formulation, such that μFE and hFE models can be used with the same optimisation function and the results could be directly compared. Parameters of this target stimulus could be fitted in a bottom-up approach on the same trabecular bone cubes, as required for the homogenisation of the material properties for the hFE. The here found exponents for the model were robust against variations in fitting parameters (using different set of bone cubes; constraining U_0) but different boundary conditions (KUBC or PMUBC) yielded different results. While the here presented continuum target stimulus only uses the relative density of the elements, more elaborate functions can be used to relate more material properties, such as trabecular orientation, from the continuum to the tissue-level. Necessary parameters for more elaborate optimisation functions can be identified analogous to the power-law function presented in this study. Thus, this method can be used as a framework for further developments.

4.2 Section Forces: Distal Radius

4.2.1 Related Publication and Declaration of Contributions

This section is based on the publication

> S. Bachmann, D. H. Pahr and A. Synek. 'A Density-Dependent Target Stimulus for Inverse Bone (Re)modeling with Homogenized Finite Element Models'. In: *Annals of Biomedical Engineering* (2022). DOI: 10.1007/s10439-022-03104-x

Author contributions: **Sebastian Bachmann**: Conceptualisation, Methodology, Software, Validation, Formal analysis, Investigation, Writing - Original Draft, Writing - Review & Editing, Visualisation. **Dieter H. Pahr**: Conceptualisation, Methodology, Writing - Review & Editing, Supervision. **Alexander Synek**: Conceptualisation, Methodology, Writing - Review & Editing, Supervision.

Acknowledgements: This project has received funding from the European Research Council (ERC) under the European Union's Horizon 2020 research and innovation program (Grant agreement No. 819960).

4.2.2 Introduction

Now that a continuum translation of the tissue target stimulus was available, it should be applied to a practical example and put to the test. The distal radius was identified as the first test case. There are several key points, why the distal radius is of interest. The distal radius is prone to fractures [279], and thus many researchers investigated the healing process [280] as well as implant systems for the fixation of such fractures [281]. However, also from an evolutionary point of view, the hand and surrounding joints are of interest, as the wrist joint has changed over the course of evolution in the primates [282, 283]. Nowadays, radiographic scans of the distal radius are also used for the diagnosis of osteoporosis [284], due to its easy accessibility. In addition, its microstructure can be depicted *in vivo* using HR-pQCT [82]. Thus, results of this study would already indicate if such models would work in pre-clinical (using HR-pQCT) or even clinical studies (using QCT). Furthermore, the distal radius has a relatively simple geometry, roughly in the form of a elliptic cylinder (or cone, depending on the height of the scanned region), which aids in the automatic meshing of the bones.

Typically a $9\,\mathrm{mm}$ or $18\,\mathrm{mm}$ high section below the articular surface of the distal radius is imaged using HR-pQCT [285], and μFE models of the distal radius typically only use those sections [286]. From the μCT or HR-pQCT images, also smooth hFE models can be created [287]. As the cortex and the trabecular bone can be depicted in high detail,

it is possible to separate them in the hFE model as well. For lower resolution data, for example from a clinical QCT, a voxel model can be created, using each of the QCT voxels as a single hexahedral element [288], but the same models can also be created from μCT data [216, 289]. Only a few hFE models included the full joint region, instead of using sections, but the boundary conditions in the joint are often still simplified [290].

There are already several studies that investigated physiological loading of the distal radius by using μFE-based IBR [153, 269, 291]. These models used distal radius sections and forces and moments were modelled using displacements and rotations. These studies showed, to some extent, equivocal results, as different loading histories were predicted. While the predicted forces were found in the same magnitude range but different distributions of the components, the predicted moments would differ by a factor of 10. However, differences in the loading histories can also be explained by the usage of a soft connector layer for the displacements, which was used by some studies [269, 291] while others applied the displacements directly [153].

To validate the results from IBR, experimental data is required. However, experimental data for loading of the wrist joint and the radius is scarce. Loads from the hand are transferred via the hand-bones into the radius. Depending on the extension/flexion angle of the wrist, a certain amount of the axial load is shared with the ulna, however the radius always transfers the majority of the load ($>70\,\%$) in any extension/flexion position [292]. As the axial loading component of the distal radius is typically larger than the radial or dorsal loading component (i.e., shear forces) during active wrist motion [293], it is predicted, that IBR will identify the axial direction as the dominant loading in its loading history.

The main objective of this study was to test the continuum target stimulus for IBR, as developed in section 4.1, on μCT sections of the distal radius for the prediction of the loading history and compare the results to μFE-based IBR. As a secondary objective, the difference of the predictions with hFE models of varying complexity should be analysed.

4.2.3 Methods

Outline

A graphical overview of the study is given in Figure 4.4. The continuum target stimulus parameters were already identified in section 4.1.4 using the KUBC data set from Gross, Pahr and Zysset [274]. A set of distal radii was used to create μFE and three types of hFE models. IBR was applied using three canonical displacement boundary conditions to evaluate the optimised reaction force. The results of the hFE-based IBR were then compared to the results of μFE-based IBR.

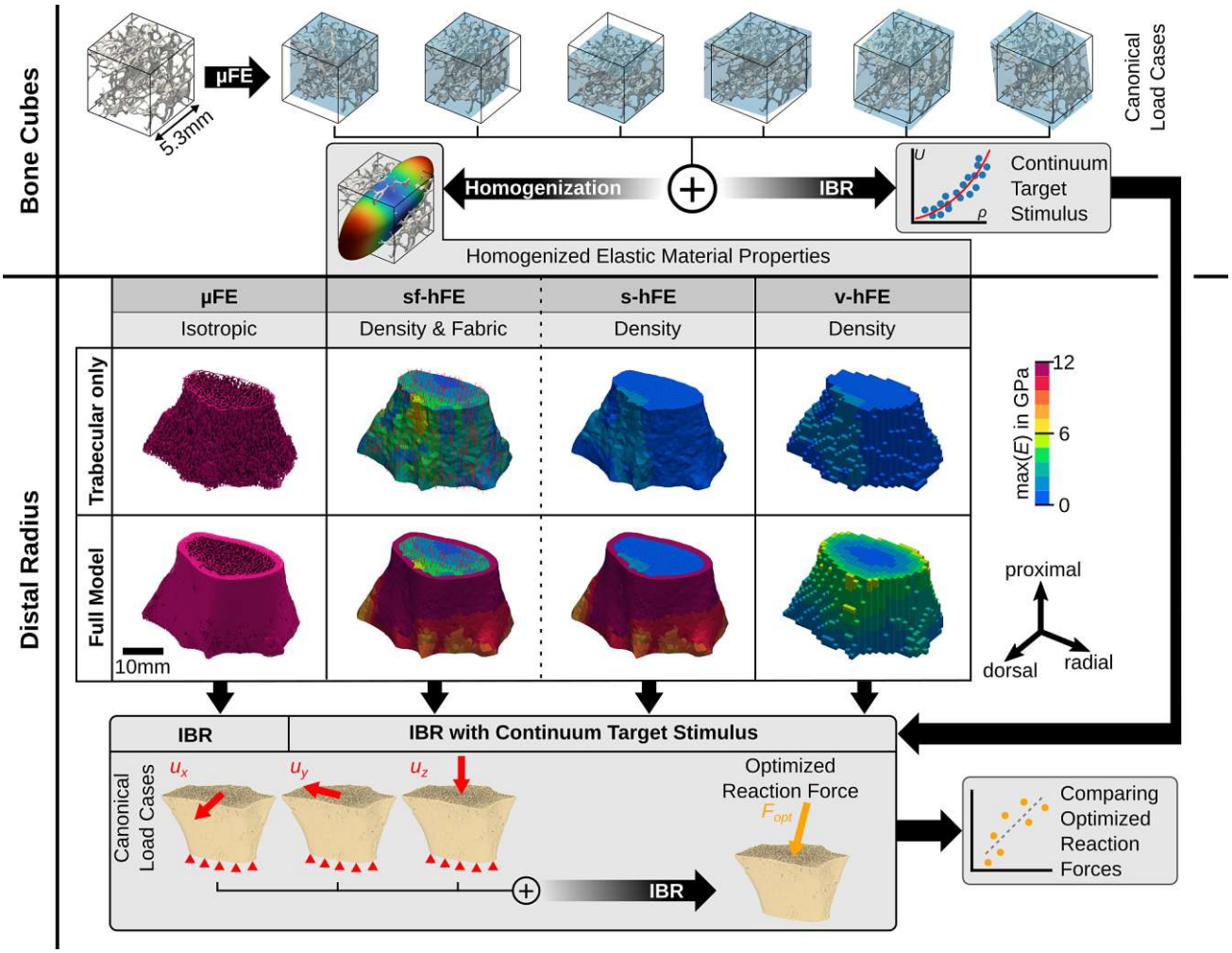

Figure 4.4: Schematic overview of the distal radius study, which is split into two parts. In the first part, the continuum target stimulus is identified on trabecular bone cubes (see section 4.1). This stimulus is required for the homogenised inverse bone remodelling (IBR) and applied in the second part, where μFE and hFE models are compared to each other in their ability to predict optimised reaction forces.

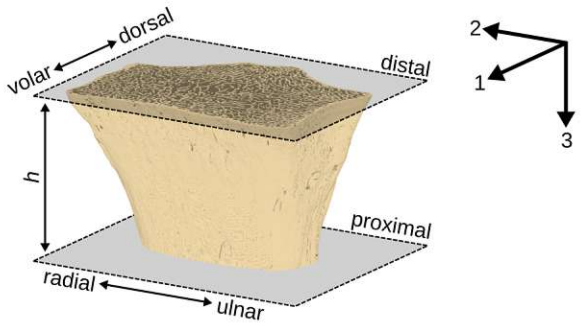

Figure 4.5: Alignment of the distal radii segments in the image frame. The average height h of the radii was $19.22\,\mathrm{mm}$. The bones were aligned such that the volar surface was parallel to the 2-axis of the image, and the axial direction was parallel to the 3-axis. Volar, radial, and proximal corresponded to the positive 1, 2, and 3-direction, respectively. The boundary conditions of the FE model were applied to the nodes of the proximal and distal faces of the bone, which were coplanar with the shown planes.

Sample Processing

A μCT-image set of 21 distal radius sections from a previous study [216, 294] was used to test the new continuum-level target stimulus for IBR. No new scans or experiments were conducted on the specimens for this study. The image resolution was $32.8\,\mu\mathrm{m}$, with an average section height of $19.22\,\mathrm{mm}$. The anatomical axes of the bones were aligned to the image coordinate system to retrieve comparable results (Figure 4.5). The axial direction was already aligned during scanning to the 3-axis. The volar surface was manually aligned along the 2-axis.

Finite Element Modelling

Two sets of models were created to investigate if the cortex added any bias in the IBR. The first set contained only the trabecular bone without the cortex, while the second set included both trabecular bone as well as the cortex. As homogenised material properties were only identified on trabecular bone samples, the goal of this reduced model was to find out if the homogenisation of trabecular bone yields the same results as μFE, without the influence of the dense cortex.

The μFE models were created similar to the bone cubes described in section 4.1, using a direct voxel to linear hexahedral element conversion and a linear, isotropic material with $E = 12\,\mathrm{GPa}$ and $\nu = 0.3$. Two model types were created: one including the cortex (full model) and one without the cortex (trabecular-only). Three load cases (compression in 3-direction, shear in 23 and 13 plane) were applied by imposing a displacement of $0.01\,\mathrm{mm}$ magnitude on the nodes of the distal plane in the respective direction. All nodes at the proximal plane were fixed in all three directions. The reaction force $\boldsymbol{F}_i$ at the distal plane was calculated for each load case.

Table 4.1: KUBC based base material model parameters used in the distal radius study.

	E_0 in MPa	G_0 in MPa	ν_0	k	l
Trabecular (Density & Fabric) [274]	10 320.4	3470.7	0.2278	1.62	1.1
Trabecular (Density) [274]	8812.8	-	0.2462	1.63	-
Cortical (Density)	12 000.0	-	0.3000	1.63	-

Three different homogenised FE models were created from the radii sections using two different meshing methods and two different material mappings (see Figure 4.4). Likewise, as in μFE, each model was created with and without the cortex. Smooth FE models [156] (s-hFE and sf-hFE) were created similar to a previous study [295] using quadratic tetrahedral elements for the trabecular bone and quadratic wedge elements for the cortical bone. Both had an element edge length of around $1\,\mathrm{mm}$. Homogenised voxel FE models (v-hFE) were created similar to a previous study [216], using a regular grid of quadratic hexahedral elements with an element edge length of around $1\,\mathrm{mm}$. The same boundary conditions as for the μFE models were applied.

Homogenised Material Properties

An hFE material mapping algorithm [215] (Sampling sphere diameter $5\,\mathrm{mm}$, background grid distance $2.5\,\mathrm{mm}$) was used to map either a power-law-based density-dependent material or a Zysset-Curnier type [139] material, which is dependent on local fabric and density. Equations of all material models are given in section 4.2.3. Elastic material constants for trabecular bone based on homogenisation with KUBC were already identified in a previous study by Gross, Pahr and Zysset [274] using the same bone cubes as for the identification of the continuum target stimulus. KUBC were selected as it was assumed that these boundary conditions best resemble the applied loading of the distal radius section. The density-dependent material properties for the cortical bone were the same material properties as used for the density-dependent trabecular material but scaled to $E = 12\,\mathrm{GPa}$ and used a Poisson's ratio of $\nu = 0.3$. These adaptations were required to ensure compatibility with the μFE material properties. The used base material constants are given in Table 4.1. Trabecular bone material properties of the smooth hFE models were mapped using local density only (s-hFE) or using density and fabric (sf-hFE). Cortical bone in both smooth models was modelled using the power-law-based density-dependent material. In the voxel hFE models (v-hFE), material properties were mapped using only density for both trabecular and cortical bone.

Inverse Bone Remodelling

Inverse bone (re)modelling, including the previously identified exponent d (Eq. (4.2)) for the continuum target stimulus, was applied to all radius sections and all four model

types with and without cortex. The exponent $d = 1.19$ was acquired from the bone cube set of Gross, Pahr and Zysset [274] using KUBC as canonical load cases and the tissue target stimulus U_0 was set to $0.02\,\mathrm{MPa}$ [144]. A non-negative least squares solver (`scipy.optimize.nnls` [232]) was used for the optimisation. The resulting optimal scaling factors α_i were used to scale the three reaction forces $\boldsymbol{F}_i$. First, unit scaled force $\boldsymbol{F}_{\mathrm{unit}} = \sum_{i=1}^{3} \boldsymbol{F}_i$ were calculated and, second, the optimised reaction forces were calculated as $\boldsymbol{F}_{\mathrm{opt}} = \sum_{i=1}^{3} \alpha_i \boldsymbol{F}_i$ to allow for a comparison of reaction forces before and after optimisation.

Statistical Evaluation

The hFE models were compared to the μFE models by linear regression of $\boldsymbol{F}_{\mathrm{unit}}$ and $\boldsymbol{F}_{\mathrm{opt}}$ respectively. The coefficient of determination and Lin's concordance correlation coefficient (CCC) [296] were calculated for each regression. Further, the magnitude of the optimised force was evaluated as well as the off-axis angle θ from the 3-axis, calculated as:

$$\theta = \cos^{-1}\left((0,0,1)^T \cdot \hat{\boldsymbol{F}}_{\mathrm{opt}}\right) \tag{4.7}$$

This angle gives a measure of the ratio between the magnitude of axial loading and shear loading, irrespective of the components.

Two scores were defined to compare the similarity between μFE and hFE in terms of predicted force angle and magnitude. An angle score for the two vectors $\boldsymbol{a}$ and $\boldsymbol{b}$ is defined as:

$$S_a(\boldsymbol{a}, \boldsymbol{b}) = 1 - \frac{\cos^{-1}(\hat{\boldsymbol{a}} \cdot \hat{\boldsymbol{b}})}{\pi} \tag{4.8}$$

Here, $\hat{\boldsymbol{a}} = \boldsymbol{a}/||\boldsymbol{a}||$ denotes the unit vector of $\boldsymbol{a}$. A magnitude score is defined as:

$$S_m(\boldsymbol{a}, \boldsymbol{b}) = 1 - \sqrt{\frac{(||\boldsymbol{a}|| - ||\boldsymbol{b}||)^2}{||\boldsymbol{a}||^2 + ||\boldsymbol{b}||^2}} \tag{4.9}$$

Both scores are one if the two vectors are equal and zero if the two vectors are dissimilar. The angle and magnitude scores were evaluated for both the unit force $\boldsymbol{F}_{\mathrm{unit}}$ and the optimised force $\boldsymbol{F}_{\mathrm{opt}}$, using in both cases the μFE-based IBR results as the reference vector.

Soft- and Hardware

All statistical analyses were performed using scipy [232] 1.7.2 and Python 3.7.4 (Python Software Foundation, `https://www.python.org`). The hFE meshing and the material mapping were performed using medtool 4.5 (Dr. Pahr Ingenieurs e.U., Pfaffstätten, Austria, `http://www.medtool.at`). The μFE models were solved in ParOSol [276], and all hFE models were solved in Abaqus 2022 (Dassault Systèmes, Vélizy-Villacoublay, France). All analyses were performed on a dual AMD EPYC 7452 system.

Table 4.2: Regression coefficients for trabecular-only model: Unit reaction forces

		Slope	Intercept in N	R^2 in %	CCC in %
sf-hFE	$F_{\text{unit},1}$	1.37	0.426	99.22	87.61
	$F_{\text{unit},2}$	1.38	1.53	97.91	82.46
	$F_{\text{unit},3}$	1.42	12.7	98.61	82.16
s-hFE	$F_{\text{unit},1}$	0.661	0.154	98.65	87.03
	$F_{\text{unit},2}$	0.864	0.872	98.45	98.17
	$F_{\text{unit},3}$	0.574	5.63	99.06	77.72
v-hFE	$F_{\text{unit},1}$	0.629	0.115	98.40	83.71
	$F_{\text{unit},2}$	0.837	0.708	98.83	97.96
	$F_{\text{unit},3}$	0.558	4.54	99.06	75.23

4.2.4 Results

Distal Radius: Trabecular Bone Only

The μFE models had on average 104 million degrees of freedom (DoF) and took on average $63.8\,\text{min}$ to solve using 27 CPUs in parallel. The sf-hFE and s-hFE models had on average $89\,800$ DoF and took on average $46.8\,\text{s}$ and $47.5\,\text{s}$ to solve, respectively. The v-hFE models had on average $74\,283$ DoF and took on average $19.3\,\text{s}$ to solve. All hFE models used 4 CPUs in parallel.

The predicted reaction forces $\boldsymbol{F}_{\text{unit}}$ before optimisation (Figure 4.6 a-c) differed between hFE and μFE for models of the radii without cortical shell. While both v-hFE and s-hFE underestimated the reaction forces, sf-hFE overestimated them. However, all hFE models had a good correlation of reaction forces with μFE, with R^2 over $98\,\%$ and good agreement in CCC with over $75\,\%$ for all reaction force components (Table 4.2).

After optimisation (Figure 4.6 d-f), μFE-based IBR identified the force component in the 3-direction (normal force) as the dominant load direction. Forces in 3-direction were $312\,\text{N}$ on average, while shear components were much smaller with $6.2\,\text{N}$ (1-direction) and $20.7\,\text{N}$ (2-direction) on average. As a result, the off-axis angle was small, with an average of $7°$ (Figure 4.7b). hFE-based IBR was able to identify the dominant load direction, but shear forces did not agree well with μFE-based IBR. As shear forces could not be captured by the hFE models, only the correlation of the force in the 3-direction was high, with R^2 over $94\,\%$ and CCC over $75\,\%$ (Table 4.3). Both smooth hFE models showed a better similarity in angle, while v-hFE and s-hFE had a higher similarity in magnitude than sf-hFE (Figure 4.7c).

Distal Radius: Full Models

The μFE models had on average 198 million DoF and took on average $83\,\text{min}$ to solve (on 27 CPUs), while sf-hFE and s-hFE had $107\,624$ DoF and took on average $67.8\,\text{s}$ and

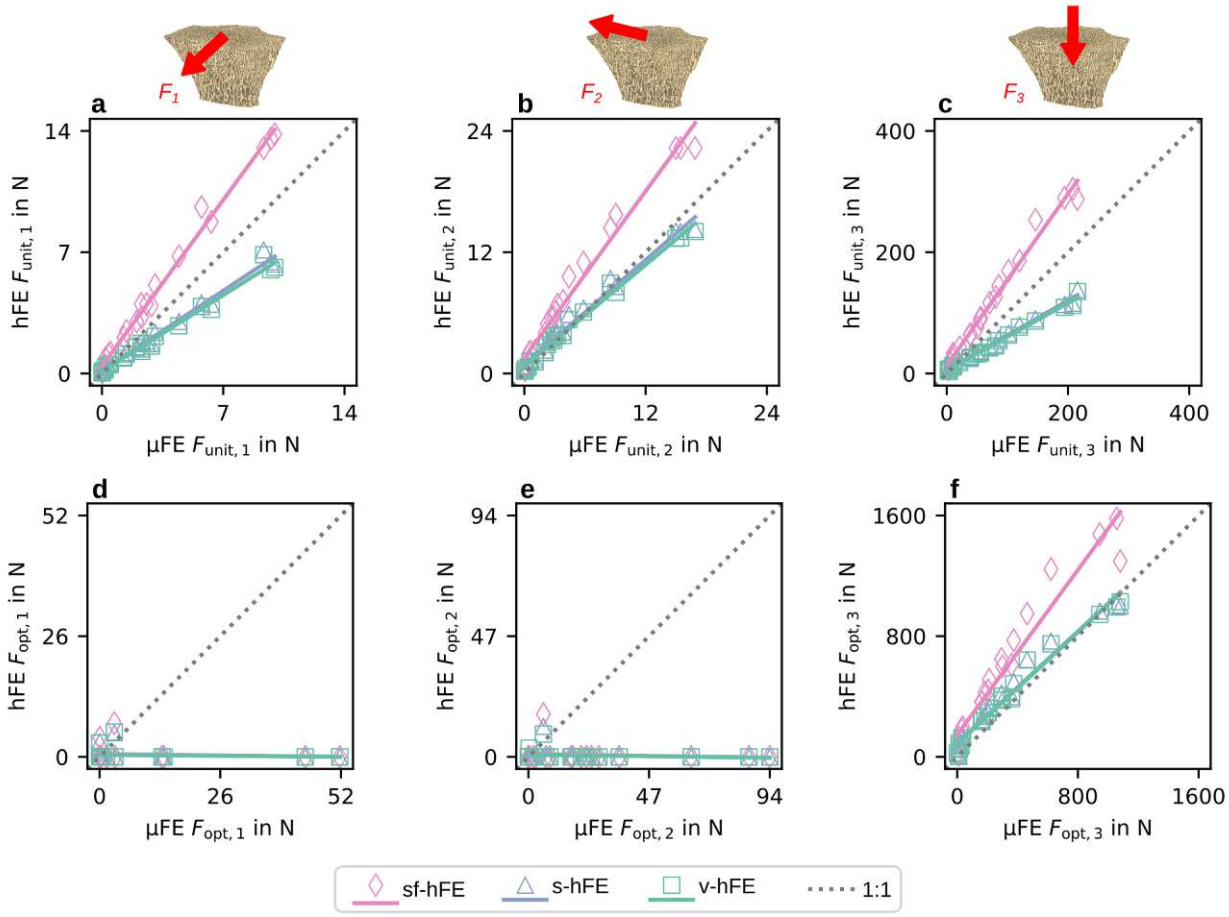

Figure 4.6: Trabecular-only model: **(a-c)** hFE over μFE unit scaled reaction force components. (**d-f)** Optimised reaction force components

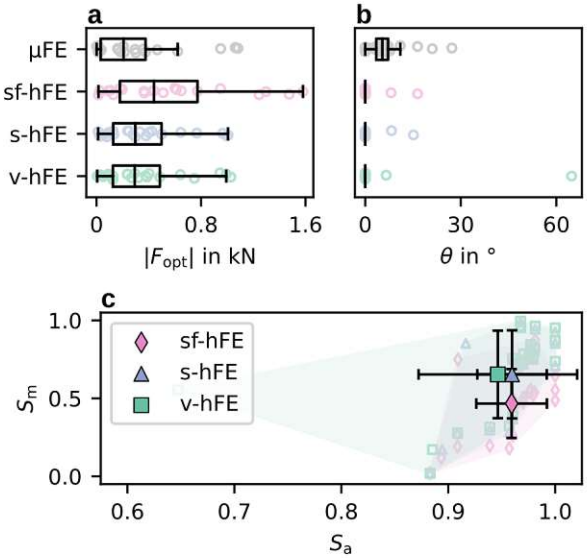

Figure 4.7: Trabecular-only model: **(a)** Optimised force magnitude and **(b)** angular difference towards the 3-axis for **(c)** angle (S_a) and magnitude similarity score (S_m). The marker gives the mean value, with the standard deviation as error bars.

Table 4.3: Regression coefficients for trabecular-only model: Optimised reaction forces

		Slope	Intercept in N	R^2 in %	CCC in %
sf-hFE	$F_{\mathrm{opt},1}$	-0.0114	0.614	0.86	-1.94
	$F_{\mathrm{opt},2}$	-0.0158	1.12	1.48	-2.04
	$F_{\mathrm{opt},3}$	1.37	146	94.02	76.12
s-hFE	$F_{\mathrm{opt},1}$	$-0.008\,62$	0.456	0.92	-1.46
	$F_{\mathrm{opt},2}$	-0.0113	0.799	1.48	-1.45
	$F_{\mathrm{opt},3}$	0.924	92.3	96.87	96.08
v-hFE	$F_{\mathrm{opt},1}$	$-0.008\,42$	0.453	0.86	-1.43
	$F_{\mathrm{opt},2}$	-0.0129	0.853	3.14	-1.67
	$F_{\mathrm{opt},3}$	0.926	84.8	97.26	96.68

$54.4\,\mathrm{s}$ to solve (on 4 CPUs). v-hFE had on average $88\,386$ DoF and took on average $24\,\mathrm{s}$ to solve.

Similar to the models without cortex, reaction forces before optimisation ($\boldsymbol{F}_{\mathrm{unit}}$) correlated well between hFE and μFE models but showed over or underestimation (Figure 4.8a-c). While sf-hFE had higher unit reaction forces on average, both s-hFE and v-hFE underestimated the reaction force. All hFE models correlated well with μFE, with R^2 over $98\,\%$. CCC was over $97\,\%$ for both smooth hFE models, except for the 3-direction in s-hFE and all components for v-hFE (Table 4.4). Contrary to the radius without cortex, v-hFE and s-hFE showed different reaction forces.

After optimisation (Figure 4.8d-f), μFE-based IBR showed results in agreement with the radius without cortex, but the overall load magnitudes were higher. Forces in 3-direction were dominant with an average of $1735.8\,\mathrm{N}$, and shear forces were one order of magnitude lower with averages of $268.2\,\mathrm{N}$ and $428.5\,\mathrm{N}$ for the 1- and 2-direction, respectively. The average off-axis angle was $17°$ (Figure 4.9b). hFE-based IBR also identified the 3-direction as dominant. In contrast to the radius without cortex, almost all hFE models also predicted shear forces in agreement with μFE-based IBR. While the magnitude of the optimised reaction force showed a similar pattern as for the models without cortex, the angle of the optimised reaction force was best predicted by sf-hFE (Figure 4.9c). All models showed a high correlation for the optimised force ($R^2 > 81\,\%$, CCC $> 84\,\%$) except for the 1-direction component in sf-hFE and the 1 and 2-direction for v-hFE (Table 4.5).

4.2.5 Discussion

This study presents the application of a new method for homogenised inverse bone (re)modelling (IBR) on the basis of previously described μFE-based IBR to predict physiological *in vivo* loading for bones. While all hFE models were able to predict the magnitude of the optimised reaction force with a good to high coefficient of determination relative to the μFE-based IBR, the angular accuracy varied between the different

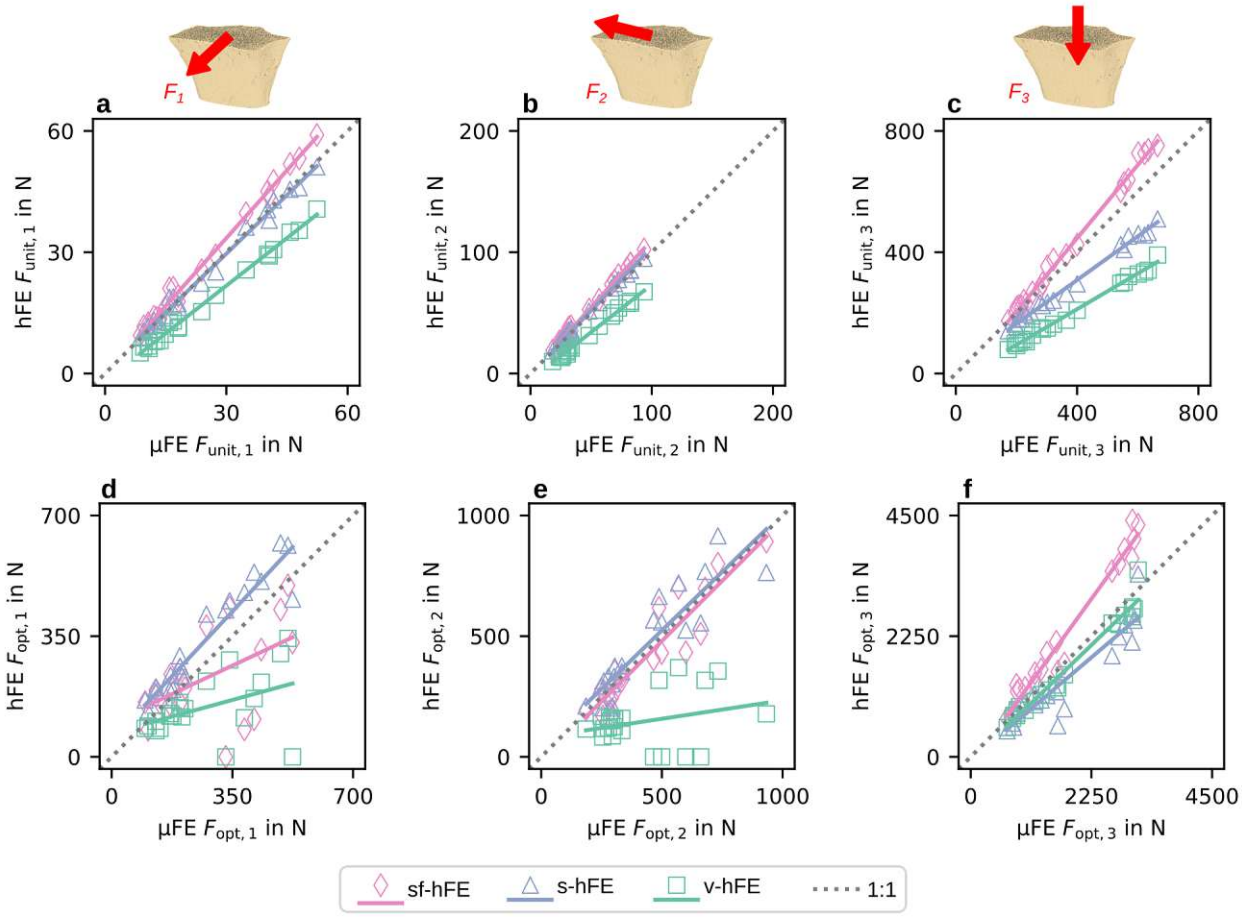

Figure 4.8: Full model: **(a-c)** Unit scaled reaction force components. **(d-f)** Optimised reaction force components for the full model.

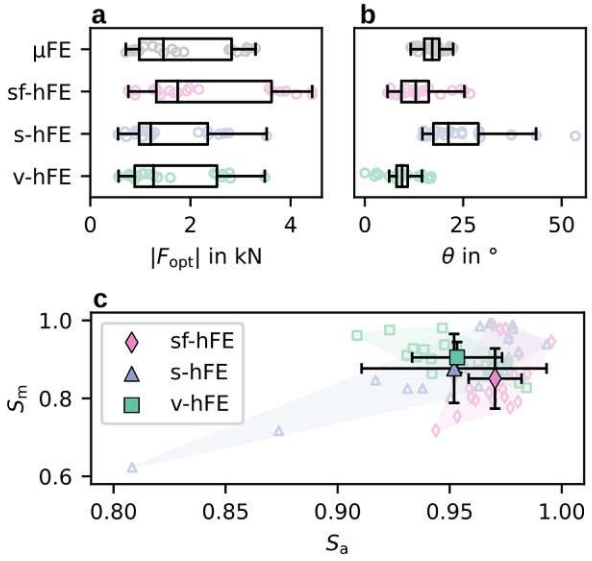

Figure 4.9: Full model: **(a)** Optimised reaction force magnitude and **(b)** angle towards the z-axis for the full model. **(c)** Angle (S_a) and magnitude score (S_m) for the full model. sf-hFE shows the smallest deviation and the highest similarity in angle, while s-hFE and v-hFE show better similarity in magnitude. The marker gives the mean value, with the standard deviation as error bars.

Table 4.4: Regression coefficients for full model: Unit reaction forces

		Slope	Intercept in N	R^2 in %	CCC in %
sf-hFE	$F_{\text{unit},1}$	1.12	−0.047	99.32	97.28
	$F_{\text{unit},2}$	1.11	−1.08	99.73	97.93
	$F_{\text{unit},3}$	1.21	−36.3	99.43	95.66
s-hFE	$F_{\text{unit},1}$	0.967	0.641	98.99	99.45
	$F_{\text{unit},2}$	1.04	−0.175	99.64	99.46
	$F_{\text{unit},3}$	0.72	20.3	99.03	81.39
v-hFE	$F_{\text{unit},1}$	0.786	−1.86	99.38	83.98
	$F_{\text{unit},2}$	0.785	−5.21	99.52	77.39
	$F_{\text{unit},3}$	0.588	−23.1	99.35	48.34

Table 4.5: Regression coefficients for full model: Optimised Reaction forces

		Slope	Intercept in N	R^2 in %	CCC in %
sf-hFE	$F_{\text{opt},1}$	0.471	99.9	26.80	49.05
	$F_{\text{opt},2}$	0.999	−19.5	86.54	92.34
	$F_{\text{opt},3}$	1.39	−176	96.83	84.12
s-hFE	$F_{\text{opt},1}$	1.07	46.6	91.24	86.23
	$F_{\text{opt},2}$	0.97	38.8	81.32	89.20
	$F_{\text{opt},3}$	0.852	−62.8	85.82	86.25
v-hFE	$F_{\text{opt},1}$	0.274	69.1	19.29	24.76
	$F_{\text{opt},2}$	0.152	81.8	7.38	8.97
	$F_{\text{opt},3}$	0.963	−83.1	96.94	97.08

types of hFE models. Inclusion of the cortex had the highest influence on the model accuracy, while differences in material mapping or different meshing methods had less influence.

Using the computationally efficient (70 to 200 times faster than μFE) hFE-based IBR method presented in this study allowed the prediction of physiological loading of 21 distal radius samples with a high correlation to μFE based IBR if fabric and cortex is included in the model. While the correlation was high, the hFE models overestimated (sf-hFE) or underestimated (s-hFE, v-hFE) the unit reaction forces and subsequently also the optimally scaled reaction forces. This discrepancy was larger for the models that used only trabecular bone than it was for the full models, with the exception of v-hFE, which showed a higher deviation from μFE in the full model. There might be several reasons for these differences. First, the boundary conditions used to find the apparent stiffness can influence the homogenised elastic material properties. KUBC is known to overestimate the apparent stiffness [273]. Other boundary condition types, such as PMUBC [133], could be tested instead. Second, the homogenisation was done based on trabecular bone cubes with a maximum relative density of 60 %. Thus, for models that include elements with a higher density, the apparent properties might not match. This could be the case for v-hFE, where the cortex is averaged with the trabecular volume. Due to the high density-gradient between trabecular and cortical volume, smooth models (which model a sharp boundary between the volumes) work better in this respect. Different material mappings, which include a tissue function [216], could be applied in such cases. Last, micro-structural effects of low-density volumes can lead to a different result at the continuum-level. Several radii had low-density regions (<10 % relative density) in the proximal region. Such effects are mitigated when the cortex is included.

The physiological reaction forces of the full distal radius section predicted by both hFE and μFE-based IBR were in a plausible region. The predicted off-axis force angle was similar to the one found by Smith, Werner and Harley [293] for the pushup load case *ex vivo*, but the predicted force magnitude was higher on average (1811 N for μFE with cortex) than estimated from that experiment (663 N). However, this magnitude is still in a physiological region estimated with up to 2410 N for power grip exercise [297]. A few other studies also used IBR to predict distal radius loading. Walle *et al.* [153] predicted physiological section forces using μFE-based IBR on a clinical μFE model of distal radius sections and found a similar pattern of optimised reaction force components, with smaller shear components (140 N and 280 N) than normal force (420 N). Conversely, Christen *et al.* [269], using the same algorithm, found results different from estimates in literature [293, 297] and the results of this study. Specifically, Christen *et al.* [269]. found high amounts of shear forces (45 N to 465 N) and relatively low normal forces (1 N to 235 N). However, different boundary conditions, by the addition of a soft connector layer, were applied to the models. Furthermore, also rotational load cases were added to predict moments, which was not the case in this study. Such load cases were not

added in this study, as only μFE and hFE-based IBR were compared to each other and evaluating the moments is not strictly necessary [291].

Differences between IBR-predicted and physiological load magnitudes could also be the result of the chosen target stimulus value. While the predicted load magnitude is influenced directly by the tissue target stimulus, the load angle (i.e., the ratio of force components) remains unaffected [271]. In this study, a tissue target stimulus of $0.02\,\mathrm{MPa}$ was used [144]. The value originates from the assumption that bone has to experience $2000\,\mu\epsilon$ to $3000\,\mu\epsilon$ of peak strain every day [298] in order to maintain its mass, which can be converted to an SED when the material properties are known. For the herein used material properties, an effective strain for the current tissue stimulus is $1826\,\mu\epsilon$ and is thus in a realistic region for *in vivo* strains [299]. Without additional information on the physiological range of strains, the tissue stimulus must be chosen arbitrarily or calibrated from *in vivo* data. For example, Christen *et al.* [51] found a value of around $0.01\,\mathrm{MPa}$ (equivalent to $1715\,\mu\epsilon$ with the therein used material properties) for homeostasis at the distal tibia.

This study has some limitations. The hFE models were, so far, only tested on the distal radius sections. This location is characterised by relatively homogeneous trabecular bone predominately loaded in axial compression. In proximity to joints loaded in a multi-directional way, such as the proximal or distal femur, the hFE-based IBR might deviate more from μFE-based IBR. The continuum stimulus was identified on bone cubes loaded with KUBC, which were also used to identify the homogenised elastic material properties for the hFE models. Other boundary conditions might lead to different exponents in the continuum stimulus as well as to other elastic material properties. The here used target stimulus is a scalar quantity, which ignores other information at the continuum-level, such as the orientation of the microstructure. Further, the inclusion of mechanobiological factors, such as metabolism or genetics, in the model might also increase the predictive power of IBR in general. The simplified theory of IBR assumes that the microstructure can fully be explained by mechanical stimuli alone, which holds true only for artificial bone structures [144]. In general, bone is however influenced by many different factors such as genetics and metabolism [271]. Recent publications also incorporated mechanoregulation theory [153] into the target stimulus but required time-lapsed CT to identify remodelling sites in the bone, which is not always available. Only three load cases were applied to the radius sections for simplicity of the models. As these load cases can only predict the reaction force, three rotational load cases should be added for the prediction of moments, to predict physiological loading conditions more accurately.

Despite these limitations, this study could show that μFE-based IBR can be translated to hFE to provide a faster way of predicting physiological loadings from bones. hFE-based IBR was tested on distal radius sections using different kinds of meshing and material mappings. Both μFE and hFE showed a good agreement in terms of predicted load angle

if the cortical bone was included in the model and further improved if the bone's anisotropy is added. The predicted loads correlated well, but systematic differences between μFE and hFE due to the homogenisation of the microstructure were observed. Smooth hFE models, including the cortex, showed the best agreement with μFE results. Overall, μFE-based IBR still provides a robust way to infer physiological loading conditions from the bone microstructure, but hFE models offer a computationally more efficient alternative with the ability to model more realistic boundary conditions and more complex load cases.

4.3 Joint Loading: Femoral Head

4.3.1 Related Publication and Declaration of Contributions

This section is based on the publication

> S. Bachmann, D. H. Pahr and A. Synek. 'Hip joint load prediction using inverse bone remodeling with homogenized FE models: Comparison to micro-FE and influence of material modeling strategy'. In: *Submitted to: Computer Models and Programs in Biomedicine* ()

Author contributions: **Sebastian Bachmann**: Conceptualisation, Methodology, Software, Validation, Formal analysis, Investigation, Writing - Original Draft, Writing - Review & Editing, Visualisation. **Dieter H. Pahr**: Conceptualisation, Methodology, Writing - Review & Editing, Supervision. **Alexander Synek**: Conceptualisation, Methodology, Writing - Review & Editing, Supervision.

Acknowledgements: This project has received funding from the European Research Council (ERC) under the European Union's Horizon 2020 research and innovation program (Grant agreement No. 819960).

4.3.2 Introduction

The hFE-based IBR method was applied to the distal radius in the previous section. The distal radius is a bone with relatively simple geometry, homogeneous microstructure, and simple loading condition, as the bone experiences almost exclusively axial compression in a physiological scenario [293]. A study investigating the predictive power on bones with a more diverse loading regime and heterogeneous microstructure is still missing. Furthermore, only section forces have been estimated so far, while the ultimate goal would be to estimate the joint loading.

To fill this gap, hFE-based IBR could be applied to the proximal femur to predict hip joint loading. In contrast to the distal radius, the proximal femur microstructure is heterogeneous, with differently oriented trabeculae, and the outer bone geometry is more complex. Also, *in vivo* measurements, for example, using instrumented prostheses [37], are available; thus, the results of IBR can be checked for plausibility. Furthermore, the proximal femur was already analysed using IBR methods, for example using 2D hFE models [176, 177, 180, 264] and 3D μFE models [178, 271]. From a clinical point of view, the proximal femur is of interest because it poses a high fracture risk, especially in elderly people [300], and is thus also a common bone to evaluate fracture risk on [301]. Lastly, the femur is the longest and most massive bone in the human body and is thus a good test case for the computational efficiency of the hFE-based IBR method.

The primary objective of this study was to apply the previously developed hFE-based IBR algorithm to the proximal femur and assess its performance. Specifically, it should be tested if the results by Synek and Pahr [271], achieved by μFE-based IBR, can be reproduced by hFE-based IBR. A secondary objective was to assess how simple the hFE models can be to still get results in good agreement with μFE-based IBR. This information is also important if image data with lower image quality or spatial resolution, such as QCT or MRI, should be used in the future as the basis of hFE-based IBR.

4.3.3 Methods

Outline

A graphical overview of the study is given in Figure 4.10. First, μCT images were processed, and μFE and hFE models were created from the same CT images. While μFE only used a single isotropic material for the entire bone, different material models were used in hFE. Unit load cases were applied in four directions in the frontal plane. After solving the FE models, optimal loading was determined using IBR. The peak and mean force of each model were then calculated, and all models were compared with respect to μFE, which acted as the baseline.

Finite Element Model Meshes and Boundary Conditions

A set of 19 images of proximal femora was used from a previous study [271, 302]. No additional experiments or scans were performed on the specimens. The images were originally scanned in a μCT scanner with $30.3\,\mu\mathrm{m}$ voxel size but were resampled to $60.6\,\mu\mathrm{m}$ voxel size to reduce computational costs. This resolution was shown to still be sufficient for μFE based IBR [291]. The femur was rotated into a head-centred coordinate system, and the head region was cropped from the femur, as described previously [271] (Figure 4.10a). Following Synek and Pahr [271], a voxel-based cartilage layer was added, $2.2\,\mathrm{mm}$ larger than the radius of the head. The head radius was found by fitting a sphere to the femoral head. Additionally, trabecular and cortical volumes were identified using the “fill” method [156] of medtool (Version 4.6, Dr. Pahr Ingenieurs e.U., Pfaffstätten, Austria) and labelled in the images.

μFE meshes were generated in analogy to [271] by direct conversion of each voxel belonging to bone or cartilage to a hexahedral element. Smooth FE meshes were created using the “bone mesher” [156] of medtool and a custom cartilage mesh generator implemented with gmsh [303]. In brief, the “bone mesher” algorithm generates a tetrahedral volumetric mesh of the trabecular region and uses a thickness map of the cortex to create a thin, closed cortical layer using wedge elements [156]. The algorithm starts with a coarse surface mesh of the outer cortical volume, which is refined several times with a subsequent morphing step of the nodes onto the cortical surface [156]. This refinement

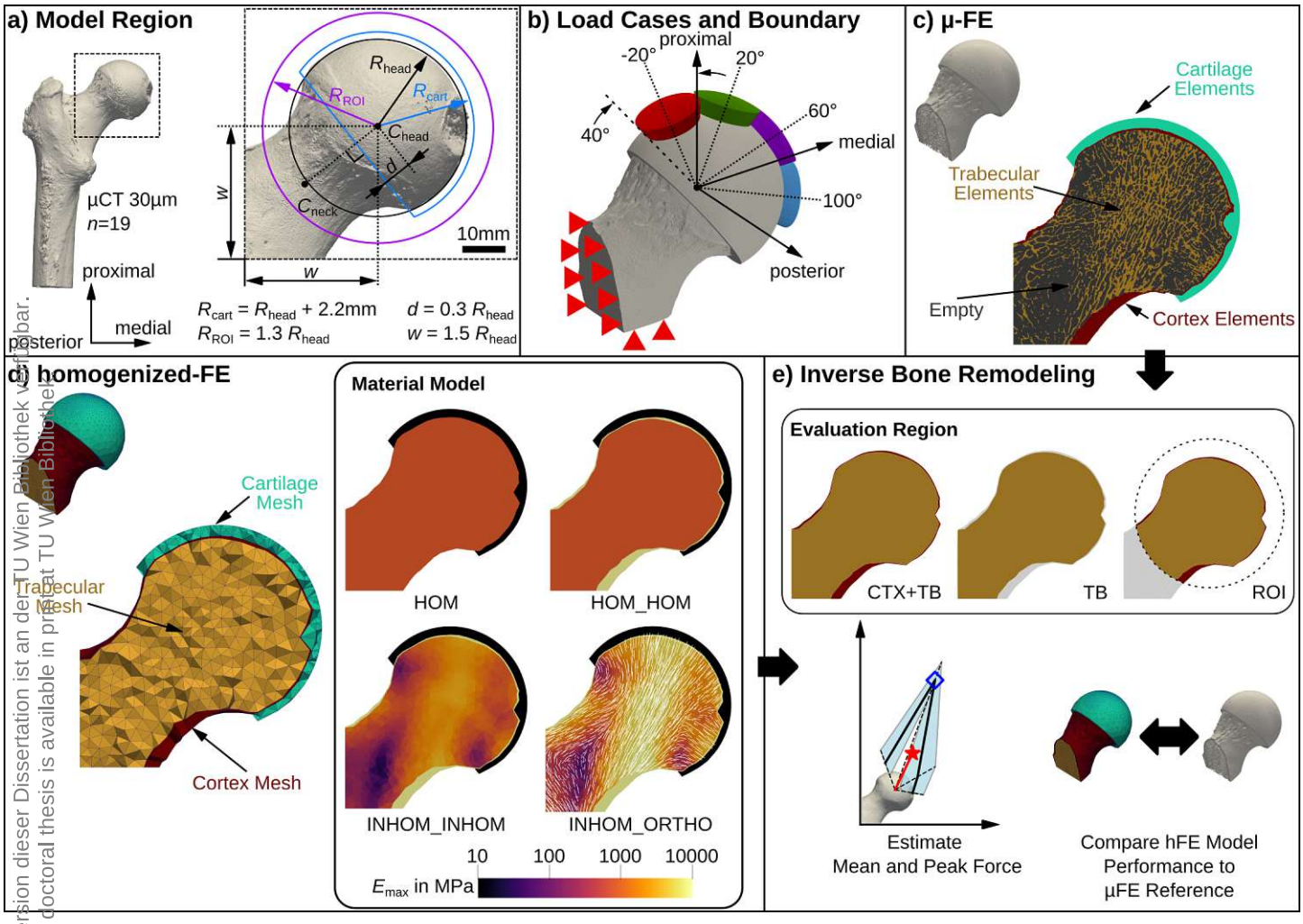

Figure 4.10: Graphical overview of the study. (**a**) Shows the selected region for the femoral head model, the anatomical landmarks and used sizes for the cartilage and region of interest (ROI). (**b**) Overview of the four applied load cases and their location on the surface of the cartilage. (**c**) μFE model showing different regions inside the model. The "empty" regions are not actually modelled. (**d**) Overview of homogenised-FE (hFE) model and the four different material models used. HOM: cortex and trabecular bone use the same homogeneous material. HOM_HOM: cortex and trabecular bone use a different but homogeneous material. INHOM_INHOM: both cortex and trabecular bone are modelled with two density-dependent inhomogeneous materials. INHOM_ORTHO: the cortex uses an inhomogeneous material law while the trabecular bone uses an inhomogeneous orthotropic material law. (**e**) Inverse Bone Remodelling (IBR). Shown are the evaluation regions schematically. CTX+TB: both cortical and trabecular bone were used in the optimisation. TB: only trabecular bone was used. ROI: cortical and trabecular bone inside a sphere (see definition of ROI in **a**) were used. With IBR, the mean and peak force was estimated and the different hFE models were compared to the reference, which was μFE.

allows to control the element size for the cortical elements. The volumetric trabecular and cortical meshes are finally created, using the refined cortical surface mesh. For this study, a coarse mesh with approximately $10\,\mathrm{mm}$ side length of the triangles was used and two refinement steps were applied. The resulting mesh had a maximum element size of $2.5\,\mathrm{mm}$ for the trabecular elements and approximately $2.5\,\mathrm{mm}$ side length of the triangular basis of the cortex wedge elements. The cartilage layer was constructed using the same parameters as in μFE but used an additional refined loading area using a maximal element size of $1\,\mathrm{mm}$. The cortical bone used 2$^{\mathrm{nd}}$ order wedge elements (C3D15), while the trabecular bone and the cartilage were meshed using 2$^{\mathrm{nd}}$ order tetrahedrons (C3D10).

Force boundary conditions were applied in $40°$ spherical cap areas on the cartilage layer [271] (Figure 4.10b). For μFE, a normal force vector, acting in the head centre, was constructed, and the force was evenly distributed among all nodes in the contact area. For hFE, a pressure acting on the contact surface area was applied to model the same force magnitude and direction as in μFE. The two cut surfaces at the neck were pinned in all three directions. Four load cases were applied using $-20°$, $20°$, $60°$, and $100°$, all in the frontal plane, with a unit force magnitude of F_u=1 kN per load case.

To validate that the used boundary conditions in μFE and hFE give the same results, models of a single femoral head were created using a even finer mesh resolution in hFE than used in the study. Three refinement steps were used, resulting in a mesh size of around $1.25\,\mathrm{mm}$, to reduce the influence of differences in volume in the cortex, caused by smoothing of pores and other high-curvature regions by the meshing algorithm. The model was completely filled with an isotropic homogeneous material and the force (μFE) and pressure (hFE) boundary conditions were applied for the $20°$ load case. The reaction force at the neck boundary was calculated for both models, to compare the error using the different loadings. The resulting magnitude was $1000.1\,\mathrm{N}$ for μFE and $996.4\,\mathrm{N}$ for hFE. Then, the displacement field of the two models was compared on each node of the hFE mesh by searching for the nearest node in the μFE mesh. A corresponding μFE node was found on average in $0.029\,\mathrm{mm} \pm 0.009\,\mathrm{mm}$ distance and the displacement field differed on average by a magnitude of $0.012\,\mathrm{mm} \pm 0.006\,\mathrm{mm}$ with an average displacement magnitude of $0.239\,\mathrm{mm} \pm 0.135\,\mathrm{mm}$ for μFE and $0.233\,\mathrm{mm} \pm 0.135\,\mathrm{mm}$ for hFE. The main difference between the two meshes was the underestimation of volume in the neck region in the hFE mesh due to large pores in the cortex, thus giving a softer model with slightly larger displacements in the head. Given that the actual reaction force magnitude only differed by less than $1\,\%$ and the displacement differences can be explained by the lower hFE mesh volume, the boundary conditions were assumed to be comparable.

Material Models

An isotropic tissue material was used for the bone in the μFE models using $E = 12\,\mathrm{GPa}$ and a Poisson's ratio of $\nu = 0.3$ [17, 274]. The cartilage was modelled with $E = 10\,\mathrm{MPa}$ and $\nu = 0.3$ [271].

hFE models were created using different material mappings for the trabecular and cortical bone regions, two models with homogeneous (density-independent) and two with inhomogeneous (density-dependent) finite element material properties (Figure 4.10d, Table 4.6). The simplest model (HOM) used the same isotropic and homogeneous material for both cortex and trabecular bone. The next model (HOM_HOM) used two different isotropic homogeneous materials for the cortex and trabecular bone. The two most advanced models used a density-dependent inhomogeneous cortex with either a density-dependent inhomogeneous trabecular bone (INHOM_INHOM) or a density and fabric-dependent orthotropic trabecular bone (INHOM_ORTHO).

Homogenised base material properties were taken from Panyasantisuk *et al.* [275], who used FE-based homogenisation with periodicity compatible mixed uniform boundary condition (PMUBC). These values were scaled to match the $12\,\mathrm{GPa}$ μFE material. Two different types of material mapping models, an inhomogeneous, density-dependent material and an orthotropic, density and fabric dependent material (Zysset-Curnier material model [139]) were considered. Equations of all material models are given in section 4.2.3. Homogeneous material properties of the HOM and HOM_HOM models were calculated by using the average density and inserting it into an inhomogeneous material mapping law. For the HOM model, the average density ($31.9\,\%$) of the entire modelled region was used and inserted in the "INHOM (tb)" law (Table 1) and yielded an elastic modulus of $E = 1107.61\,\mathrm{MPa}$. For HOM_HOM, the average density for trabecular ($25.7\,\%$) and cortical bone ($97.3\,\%$) was evaluated separately and yielded elastic moduli of $E = 720.26\,\mathrm{MPa}$ using the "INHOM (tb)" law and $E = 11\,360.75\,\mathrm{MPa}$ by using the "INHOM (ctx)" law, respectively. The inhomogeneous cortex model used the same inhomogeneous model as the trabecular bone but a tissue modulus of $E_0 = 12\,\mathrm{GPa}$ and Poisson's ratio $\nu = 0.3$ was used, such that it matches μFE at $100\,\%$ bone density. The cartilage was modelled using $E = 10\,\mathrm{MPa}$ and $\nu = 0.3$, same as in μFE [271]. To map the inhomogeneous isotropic and orthotropic material to the meshes, a material mapping algorithm [215] in medtool was used (Sampling sphere diameter: $5\,\mathrm{mm}$, background grid distance: $2.5\,\mathrm{mm}$) using the segmented high-resolution image data, computing local density and fabric and using the corresponding material mapping law to get the element-wise elastic material properties.

Mesh Convergence

To test the dependency of element size in the hFE models, different mesh densities were created and the INHOM_ORTHO model was applied for 17 of the 19 femora. Two models

Table 4.6: Elastic base material properties. See section 4.2.3 for details of the material models. tb: trabecular; ctx: cortex.

	E_0 in MPa	μ_0 in MPa	ν_0	k	l
ORTHO (tb) [275]	13 757.76	4136.17	0.2228	2.01	1.20
INHOM (tb) [275]	10 904.96	-	0.2526	2.00	-
INHOM (ctx)	12 000.00	-	0.3000	2.00	-

were removed because the cartilage mesh generation failed for the coarsest mesh. The volume weighted mean SED was calculated for each of the models and standardised by the results of the finest model. Figure 4.11 gives the mean SED for the $20°$ load case, the total runtime of each model and bone volume (trabecular and cortical volume, not including the cartilage layer). The name of each model is the number of cortical refinement steps, the number of wedge elements over the cortex thickness and the maximal element size for the trabecular bone. Finally, the model $2/1/2.5$ (2 refinement steps, 1 element over the cortex, $2.5\,\mathrm{mm}$ maximal element size) was selected, as the deviation of mean SED from the finest model was on average below $5\,\%$ and it had runtimes one order of magnitude lower than the next finer model. The volumes of the hFE meshes with the selected meshing parameters were compared to the voxel-based volume of μFE, to ensure that both models are not biased because of different volumes. The hFE meshes had $0.5\,\%$ to $1.1\,\%$ less volume than μFE, due to the smoothing of the mesh surfaces in hFE.

Inverse Bone Remodelling

Details of the continuum-level IBR were already presented in chapter 4.1.3. The PMUBC based continuum target stimulus was used (See chapter 4.1.4), with $d = 1.297$ and U_0 set to $0.02\,\mathrm{MPa}$. It was assumed that PMUBC better resemble the loading situation in the femur compared to KUBC.

IBR was then performed on three sets of elements. First, the full FE models were used, including both cortical and trabecular bone [271]. Second, only the trabecular elements were considered in the optimisation to avoid bias from the cortical elements [70]. Third, a region of interest (ROI) was cropped from the head, using a spherical region with a radius of $1.3\,R_{\mathrm{head}}$ (see Figure 4.10a), following the hypothesis that most of the information regarding the joint load direction is “stored” in the head region and not the neck. For the ROI evaluation, both trabecular and cortical bone was used in the optimisation.

Evaluation of Models

The computational performance was measured as total CPU-time for the solving of the FE models. To compare the overall performance between μFE and hFE, the loading

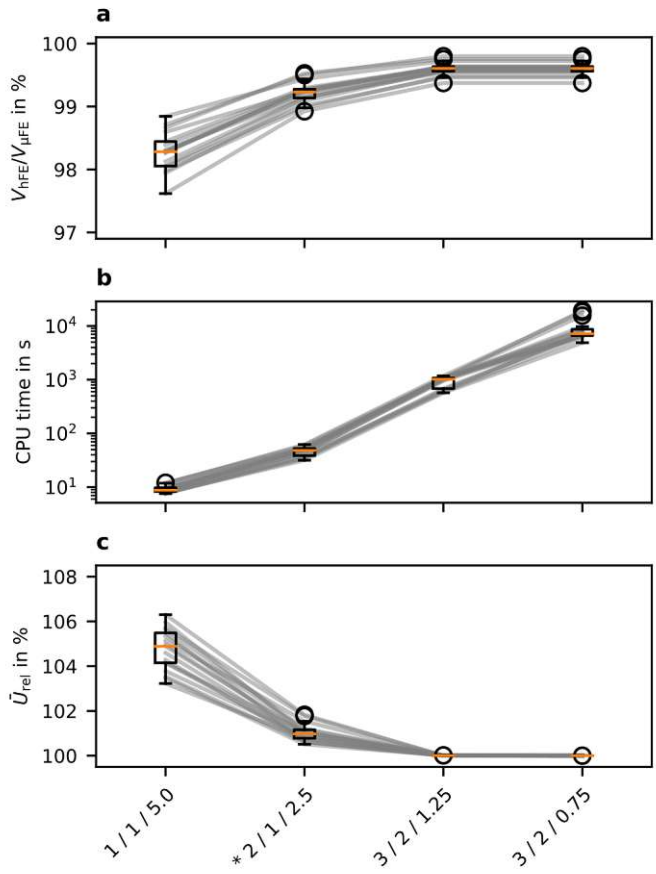

Figure 4.11: Mesh convergence study. **(a)** Change in volume, relative to the true volume measured in the μCT image. **(b)** total CPU time for solving the model (all four load cases). **(c)** change of mean SED $\bar{U}$, relative to the finest model (3 / 2 / 0.75) for the $20°$ load case.
The model marked with an asterisk (*) was finally selected for this study.

Table 4.7: Average total CPU time required for solving all load cases of the FE models. HOM, HOM_HOM, INHOM_INHOM, and INHOM_ORTHO denote the hFE models with different material modelling strategies.

	Mean	SD	Min	Max
μFE	499.9h	387.2h	185.8h	1841.7h
INHOM_ORTHO	47.0s	8.1s	32.3s	63.4s
INHOM_INHOM	49.2s	8.1s	35.6s	63.0s
HOM_HOM	22.3s	4.6s	14.9s	31.3s
HOM	23.3s	4.3s	16.7s	31.1s

history was visualised. The loading history is represented by set of scaled load cases $\alpha_i \boldsymbol{F}_i$ [271]. As each of the load cases has the same unit load magnitude F_u, the loading history can also be written as a vector of the scaling factors: $F_u[\alpha_1, \alpha_2, \alpha_3, \alpha_4]^T$. To quantify the error between hFE-based IBR and μFE-based IBR, the root mean squared error (RMSE) between the loading history vectors was evaluated. For further interpretation of the predicted forces, the peak and mean force were calculated from the loading history. The peak force $\boldsymbol{F}_{\text{peak}} = \alpha_i \boldsymbol{F}_i$ was defined as the force with the highest scaling factor α_i and the mean force was calculated as $\boldsymbol{F}_{\text{mean}} = 1/4 \sum_{i=1}^{4} \alpha_i \boldsymbol{F}_i$. The magnitude $|\boldsymbol{F}|$ and angle ϕ were calculated for both peak and mean force vectors to analyse them separately. To have an error measure relative to the peak force, the RMSE was standardised by the respective μFE peak force magnitude.

Hard- and Software

All μFE models were solved in ParOSol [276] on a dual Intel(R) Xeon(R) Gold 6144 using 16 processes in parallel. The hFE models were solved in Abaqus V6R2022 (Dassault Systèmes, Vélizy-Villacoublay, France) on an Intel(R) Xeon(R) CPU E3-1231 v3 using four processes in parallel. IBR, pre- and post-processing was performed in Python 3.7.4 (Python Software Foundation, https://www.python.org), scipy 1.7.2 [232] and medtool 4.6 (Dr. Pahr Ingenieurs e.U., Pfaffstätten, Austria, http://www.medtool.at).

4.3.4 Results

Computational Performance

The overall FE solving time, measured as total CPU-time, was reduced by almost 5 orders of magnitude using hFE instead of μFE models from an average of $500\,\text{h}$ to under $60\,\text{s}$ (Table 4.7). The homogeneous hFE models (HOM and HOM_HOM) were solved approximately twice as fast as inhomogeneous/orthotropic hFE models. Number of degrees of freedom ranged from 354 million to 598 million in μFE, and from 110 thousand to 177 thousand in hFE.

Loading History

The optimally scaled forces obtained from IBR were influenced by the type of material model used. In general, more information in the model (density, fabric) led to a better agreement with the μFE results (Figure 4.12). The pattern of the individual loading history (α_1 to α_4) were strongly dependent on the material model. While INHOM_ORTHO and INHOM_INHOM showed a similar pattern to μFE, HOM_HOM and HOM showed a different pattern (Figure 4.12). In HOM, the $20°$ and $60°$ load cases were scaled strongly and in HOM_HOM almost a uniform load distribution was predicted between the four load cases. A detailed plot comparing all four scaling factors is shown in Figure 4.14.

The RMSE of the loading history (Figure 4.13) quantitatively confirmed the trend that more information in the model (density, fabric) improved the prediction. INHOM_ORTHO and INHOM_INHOM gave the lowest errors, indicating the best agreement with the μFE results. Using different evaluation regions showed a similar trend between the different models, but INHOM_ORTHO and INHOM_INHOM achieved overall lower errors when the trabecular evaluation region was used.

While different hFE material models resulted in large differences in the predicted loading histories, the evaluation region of the IBR model only led to minor differences (Figure 4.12 and Figure 4.13). Using trabecular or ROI evaluation regions led to a more similar pattern between μFE-based IBR and hFE-based IBR with the INHOM_INHOM and INHOM_ORTHO models. Specifically, the $60°$ load case was downscaled and $-20°$ and $20°$ load cases were upscaled when using trabecular or ROI region instead of the full evaluation region.

Peak and Mean Force

Averaged peak and mean forces are shown in Figure 4.12, while Figure 4.15 presents magnitudes and angles separately.

The magnitude of the mean force was in a similar range to μFE for INHOM_INHOM, overestimated for INHOM_ORTHO, and underestimated for both HOM and HOM_HOM (Figure 4.15a). The angle of the mean force was consistently tilted towards the $60°$ load case using hFE-based IBR (Figure 4.15b). This was particularly pronounced in the HOM model, where the mean force pointed almost entirely in the $60°$ load case direction.

The peak force magnitude was systematically underestimated by hFE-based IBR in the HOM, HOM_HOM, and INHOM_INHOM models, whereas good agreement with μFE-based IBR was found using INHOM_ORTHO model (Figure 4.15c). The predicted peak force angle was correctly identified in almost all samples using the HOM_HOM, INHOM_INHOM, and INHOM_ORTHO models, but not for the HOM models. An exception was the HOM_HOM model for the trabecular evaluation region, where a peak force angle of $100°$ was predicted in all samples (Figure 4.15d).

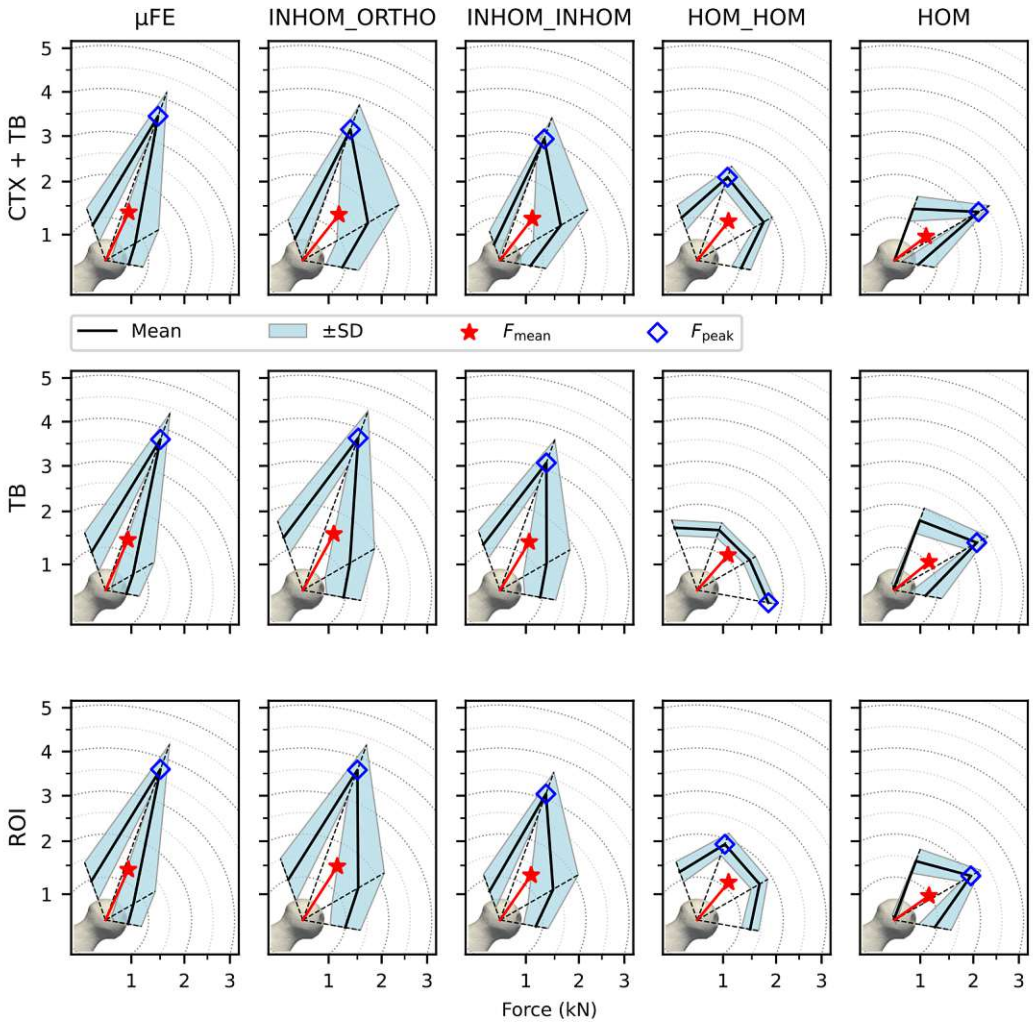

Figure 4.12: Predicted loading history (mean ± standard deviation), mean force, and peak forces for the different material models (one per column) and different optimisation regions (one per row).

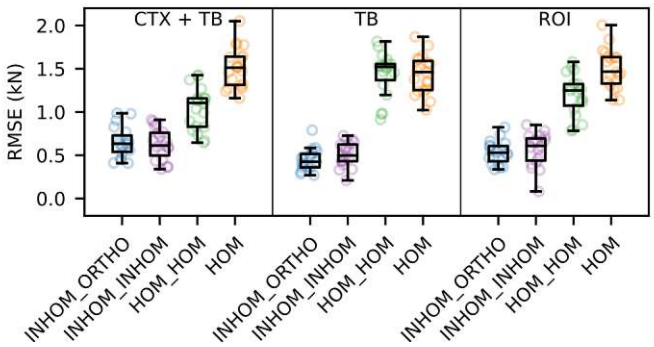

Figure 4.13: Root mean squared error (RMSE) of the loading history vector ($F_u[\alpha_1, \alpha_2, \alpha_3, \alpha_4]^T$) between μFE and the respective hFE model for each evaluation region.

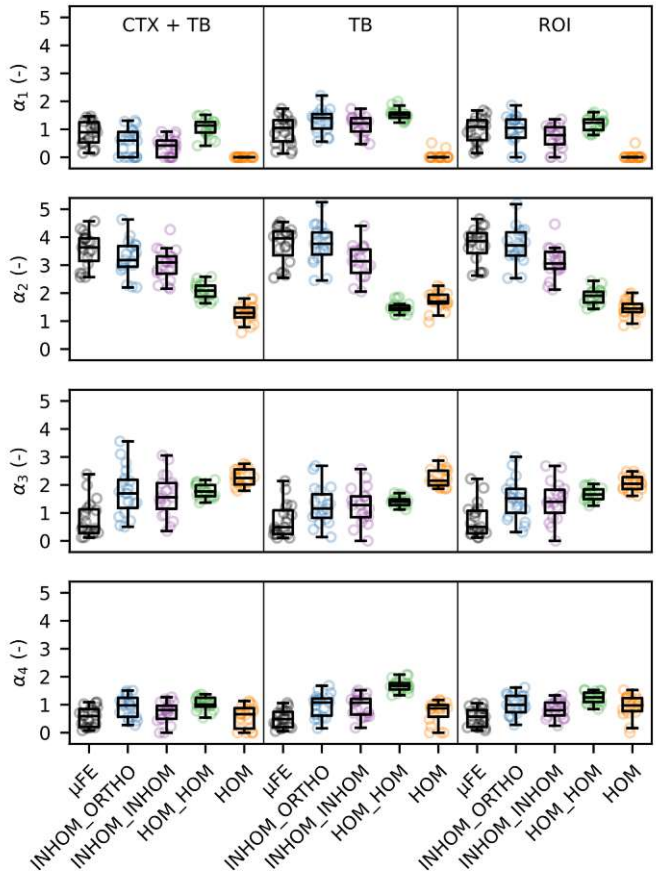

Figure 4.14: Distribution of individual scaling factors for the different material models and optimiser regions.

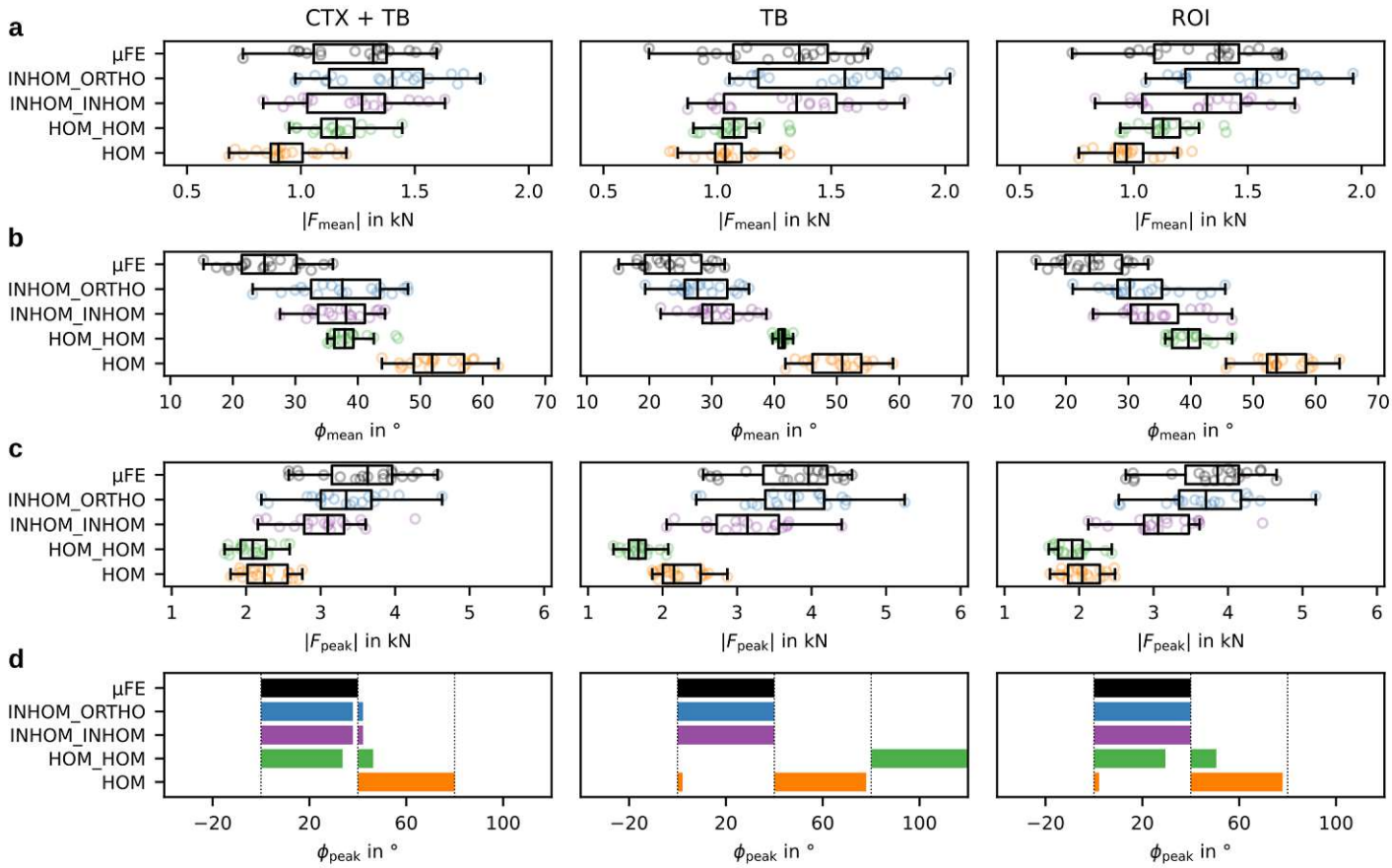

Figure 4.15: Overview of predicted peak and mean force magnitudes and directions with different material models and different evaluation regions. Three evaluation regions CTX+TB, TB, ROI versus different force measures. **(a)** Mean force magnitude. **(b)** Mean force angle. **(c)** Peak force magnitude. **(d)** Peak force angle. The bar for each of the four discrete angles gives the percentage of models predicting that angle as peak. For instance, the HOM_HOM model for the TB evaluation region predicted $100\,\%$ of the samples to be $100°$ but $74\,\%$ to be $20°$ and $16\,\%$ to be $60°$ for the ROI evaluation region.

Standardising the RMSE by the peak force magnitude revealed the generally observed trend again (Table 4.8): Adding more information to the model gave a lower value on average and INHOM_ORTHO was the best model for all optimisation regions.

The resulting peak and mean forces were less affected by the optimisation region than the loading history. A notable difference, however, was the erroneous peak force direction for the HOM_HOM models and the trabecular evaluation region in all 19 samples, which was predicted correctly for 16 samples using the entire evaluation region and 14 samples using the ROI evaluation region.

4.3.5 Discussion

This study showed that hFE-based IBR can be used to predict both the mean and peak hip joint forces at the femoral head. With the best hFE models, hFE-based IBR predictions were in good agreement with μFE-based IBR and offered a huge computational

Table 4.8: RMSE of the loading history divided by μFE peak force for all models and evaluation regions. Values are given in percent as mean ± standard deviation. CTX+TB: full evaluation region. TB: only trabecular bone considered in evaluation. ROI: region of interest for evaluation.

	CTX + TB		TB		ROI	
INHOM_ORTHO	18.49	±4.32	12.08	±2.97	14.16	±2.45
INHOM_INHOM	17.54	±3.87	13.62	±2.58	14.91	±4.08
HOM_HOM	29.08	±4.73	38.83	±5.98	32.27	±4.44
HOM	42.95	±5.81	39.03	±6.56	40.81	±5.54

speed gain due to the lower number of elements. Using an inhomogeneous rather than homogeneous trabecular bone material model had the highest influence on the predicted values, whereas the evaluation region of the IBR algorithm only had a minor influence on the results.

Using different types of material models gave a clear indication of the primary information of the bone structure used in the IBR algorithm. The fully homogeneous model (HOM) represents the "purely geometrical" information. Using the HOM models, IBR led to a strong overestimation of the load in the direction of the femoral neck, which is the stiffest direction if the cortical thickness and bone density distribution are neglected. When the distinction between cortical and trabecular bone was added in the HOM_HOM model, the influence of the geometry decreased and resulted in the prediction of almost uniform loading of the femoral head. As soon as inhomogeneous bone material was used in the hFE models, either with or without orthotropy, the IBR predictions came close to the predictions of μFE. A reason could be the principal compressive group, which only appears in the inhomogeneous models and could be responsible for the higher scaling of the $20°$ load case in comparison to the HOM and HOM_HOM models. In this case, the orthotropic material scales the stiffnesses in the principal direction of the compressive group even higher and thus gives an even better prediction than the inhomogeneous material. However, the $60°$ and $100°$ load cases were consistently scaled higher using hFE when compared to μFE. One reason might be a too stiff trabecular material behaviour resulting from the material mapping, which computed the bone densities based on several sampling spheres with a diameter of $5\,\mathrm{mm}$. This might lead to the inability to resolve small low-density regions or steep density gradients, such as behind the fovea capitis.

The bias of hFE-based IBR due to material models also influenced the agreement of the mean and peak force with μFE-based IBR. While the mean force magnitude was least influenced by the kind of hFE model, the mean force angle was strongly influenced due to the higher scaled $60°$ and $100°$ load cases. On the other hand, the peak force angle was correctly predicted for most models and evaluation regions (over $73\,\%$ for HOM_HOM, except for TB region; over $94\,\%$ for INHOM_INHOM and INHOM_ORTHO, independent of region), but the peak magnitude varied largely. The mean force magnitude is a more

robust measure, as it averages all scaling factors, while the peak force only uses a single scale factor [271]. Conversely, the peak angle is more robust than the mean angle, as the proportions of the scaling factors to each other influence the mean angle while the maximum scale factor is found reliably, if at least inhomogeneous material is used.

Using different evaluation regions in IBR led to no drastic change in the joint force predictions, except for the HOM_HOM model. In this case, the predicted peak force angle changed when the trabecular evaluation region was used. μFE-based predictions were generally less influenced by the evaluation region than hFE-based predictions. Thus, selecting a region for the optimisation might be more important in hFE than in μFE, to filter for example, very high SEDs in regions where the boundary conditions are applied.

These results suggest that for the application of hFE-based IBR in the future, at least inhomogeneous material properties are required. Only modelling the pure geometry or cortical and trabecular volumes separately increases the error in the prediction 2 to 3 times. Further, models that did not include material inhomogeneity (HOM, HOM_HOM) were not able to predict the peak angle in a robust manner. The added orthotropy only influenced the results slightly in this study. However, the here used optimisation criterion does not use the orthotropy information and a different optimisation function could yield better results together with the orthotropic model. While there is an additional gain in speed when using homogeneous models (HOM and HOM_HOM) instead of inhomogeneous models (INHOM_INHOM and INHOM_ORTHO), the speed gain between different hFE models was marginal (30 versus 60 CPU seconds) when compared to the gain of hFE versus μFE in general (500 CPU hours). Given the high gain in computational speed and minor drawbacks in terms of accuracy, this study suggests that hFE-based IBR might also be suitable for load predictions using clinical imaging technology. In future studies, inhomogeneous models could be created from clinical CT scans [177, 180], as μCT-based FE models deliver comparable results to models based on clinical CT scans in terms of the bone strength prediction [304]. However, the results of IBR with hFE models created from clinical CT scans remain to be evaluated in detail.

This study has some limitations. Only simplified boundary conditions were used, as circular contact patches with resultant forces only in the frontal plane were used. However, in reality peak force components are also acting in the sagittal and transversal plane in the hip [37], which cannot be identified with the current set of load cases. The restriction of load cases was necessary to enable a comparison of the results between hFE and μFE-based IBR with feasible runtimes. Also, the pinning of the cut-planes at the neck is a simplification of the physiological boundary. Further, a contact boundary condition might also give more realistic stress distributions [305] and thus also more realistic results in IBR. In addition, only the femoral head was considered for IBR, but muscle forces on the proximal femur might influence the result. Muscle forces were so far only modelled in 2D representations of the proximal femur in IBR [176, 177, 180, 264] and in 3D using neural network based IBR [147]. However, the effect of muscle forces on

IBR is not yet known and might be negligible, as the stress distribution of the head is not influenced by adding muscle forces [306]. Thus, further studies are required to elucidate the effect of different boundary conditions on IBR. Finally, the continuum target stimulus of the IBR algorithm used here only contains density information. Orientation of the material could be added in the future to further improve the joint load predictions.

To conclude, hFE-based IBR was in good agreement to μFE but with much lower runtime. The accuracy of the predictions depended on the used material models and at least inhomogeneous material properties were required to get to similar results to μFE-based IBR. The evaluation region used for optimisation only had minor influence on the result. These results indicate that *in vivo* load prediction using IBR based on clinical CT data may be feasible in the future.

4.4 Outlook

4.4.1 Using 3D Load Cases and Larger Bones

To show the capabilities of the newly developed hFE-based IBR method, an additional proof of concept study was performed. This study should showcase the new possibilities, by using a larger portion of the proximal femur, previously analysed (Section 4.3) and applying more load cases. Furthermore, also non-human bone should be used, to highlight the potential use in evolutionary anthropology.

Two femora were used, one sample of *Homo sapiens* from a previous study [271, 302] and one sample of *Gorilla gorilla* from a previous study [197, 307]. The *Homo* femur was available with a spatial resolution of $90\,\mu\mathrm{m}$ (resampled from a $30\,\mu\mathrm{m}$ scan) and only the proximal part was scanned until the mid-shaft. The *Gorilla* femur had a spatial resolution of $60\,\mu\mathrm{m}$ and the proximal region down to below the lesser trochanter was available. To align the *Gorilla* femur in the required coordinate system, a lower resolution scan of the whole femur (scan resolution $125\,\mu\mathrm{m}$) was used and the high-resolution scan registered onto the aligned image.

The shaft was aligned, according to Synek and Pahr [271] and the head size and neck-head axis was fitted manually in Paraview 5.9 (Kitware, `https://www.paraview.org`). 12 load cases were applied: 4 in the frontal plane (the same as in section 4.3), and 4 each anterior and posterior (Figure 4.16 top). The meshes were created in the same manner as described in section 4.3 and the INHOM_ORTHO material mapping was applied. hFE-based IBR was performed, always using the ROI method for evaluation, as described in section 4.3.

To check whether these "full" models produce similar results than the "head-only" models shown in section 4.3, such a head-only model was created also for the bone of *Homo* using all 12 load cases. The main difference between those two models were generally higher load scaling factors in the head-only model ($11\,\%$ to $80\,\%$ higher) compared to the full model. However, a similar loading history pattern, i.e., the same non-zero load cases, was predicted in both the full and the head-only model, except for L4, which was zero for the full model but 1.4 for the head-only model.

Finally, both the full models of *Homo* and *Gorilla* were compared to each other. The resulting predicted loading of the *Homo* and *Gorilla* sample are shown in Figure 4.16 and load scaling factors are given in Table 4.9. When comparing the load cases between *Homo* and *Gorilla*, it is apparent, that *Gorilla* has overall higher scaling factors. Furthermore, load case L4 is very high, in comparison to *Homo*. Striking is also the difference in the load cases L6, L7, and L11. It can further be noticed, that in both species the sum of load cases are higher on the anterior side (L5 to L8) than on the posterior side (L9 to L12) (See also Table 4.9). This higher anterior force matches the measured anterior peak-force from the OrthoLoad data (HIGH100 Forces) [37].

Table 4.9: 3D Load case comparison. The table gives the load scaling factors α_1 to α_{12} for the 12 load cases.

	L1	L2	L3	L4	L5	L6	L7	L8	L9	L10	L11	L12
Homo sapiens	0.0	4.8	2.5	0.0	0.0	1.7	2.3	0.0	0.0	1.8	0.8	0.0
Gorilla gorilla	0.0	5.3	3.4	4.0	0.0	3.4	4.7	0.0	0.0	1.9	2.0	0.0

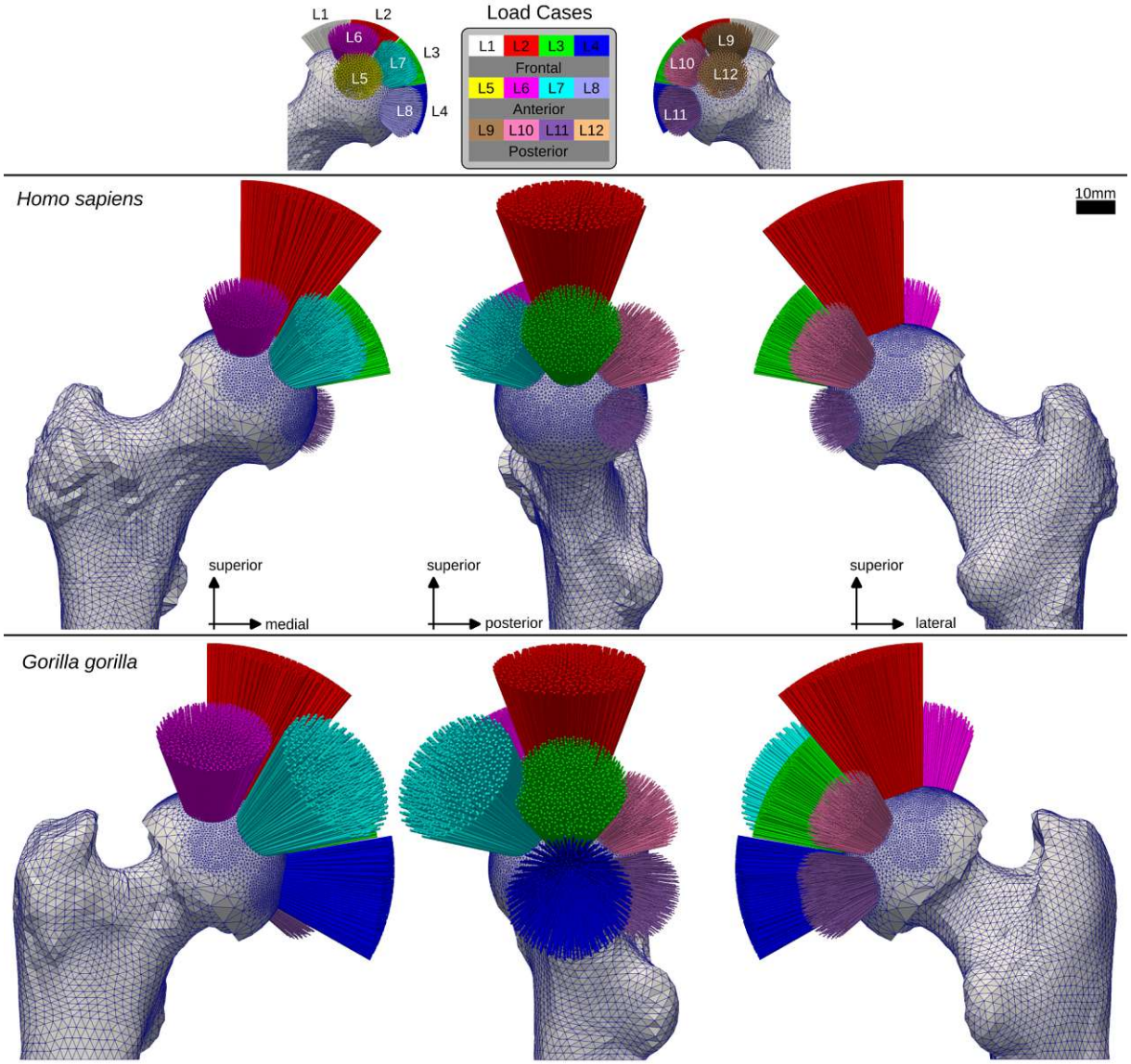

Figure 4.16: Resulting 3D Loading for the *Homo sapiens* and *Gorilla gorilla* sample.

Despite the preliminary nature of this study, the predicted load cases that are found with hFE-based IBR are plausible for both *Homo* and *Gorilla*. Of course, there are several limitations in this proof of concept. The anatomical alignment might not be comparable between the two species, because it is based on the shaft alignment and the head-to-neck angle [271]. These anatomical landmarks were harder to find in *Gorilla* than in *Homo*, due to the different morphology. It is also unclear if systematic differences between the species [186] have an influence on the continuum target stimulus and thus different exponents are required for each species. Such systematic differences could, for example, explain the generally higher scaling in *Gorilla*. The same identification of the continuum target stimulus exponent can be performed on bone cubes of other species, to check whenever similar exponents are found.

Acknowledgements. The author is grateful to I. Livne for access to the *Gorilla* sample of the Powell-Cotton Museum, Birchington-on-Sea, UK; K. Smithson (University of Cambridge) for microXCT scanning at Necsa, Wits, Cambridge; and M. Cazenave for providing the images of *Gorilla* for this study.

4.4.2 More Realistic Load Cases

So far, the hFE-based IBR was only applied to replicate the results obtained with μFE-based IBR. However, hFE also allows to use more, and especially also more realistic load cases, such as load transfer at a joint by simulating contacting articular surfaces. Including more realistic load cases might also help to answer question e.g. raised by Georgiou *et al.* [197] about the relation of resultant load and pressure distribution at the hip joint. There, it was hypothesised, that the pressure distribution in the hip joint is not equally distributed anteriorly and posteriorly, but the posterior side shows a higher pressure, due to a smaller contact area and thus would increase the BVTV in this region, despite the anterior loading peak during locomotion [197]. To answer this question, actual contact boundary conditions, which model the full hip joint would be superior to the spherical cap boundary condition that is used right now [177]. However, some changes to the here presented method are required, as physiological correct contact patches cannot be modelled as unit-load cases anymore. Sliding the contact patch over the surface would result in overlapping load case zones, which creates equivocal results in the optimisation [271]. But an analysis of the probability of certain load cases, i.e., their "goodness", may still be possible using an adapted workflow. Thus, eventually two modes of the IBR method could be used in the future: one mode that estimates the (time and load averaged) loading history by predicting the optimal combination of unit-loads and another mode where the "goodness" of a single load case is computed, e.g., based on the resulting load homogeneity within the bone. In the latter, the "goodness" of many

load cases could be determined independently from each other and overlapping load cases would not compromise the optimisation algorithm.

4.4.3 Sensitivity

An open question is, how sensitive of the hFE-based IBR method is in the prediction of the loading history. A high sensitivity is desirable, to detect even subtle differences in habitual activity. It was shown the method is sensitive enough to identify differences in habitual activity when using μFE [70, 178] or 2D hFE [177] but a similar study is still missing for the 3D hFE approach, as developed in this thesis. But such a sensitivity analysis is not only interesting for evolutionary anthropology, but also in medicine. Here, the sensitivity of the method could be assessed by using time-lapsed CT images. Several interesting questions are, for example, how the predicted loading history develops during fracture healing or how it changes due to treatment or other interventions. Yet another interesting approach to test the sensitivity would be the application of longitudinal data to evaluate age-related changes. Here, patterns of changes in habitual activity over the life-course should be visible.

Chapter 5

Synthesis

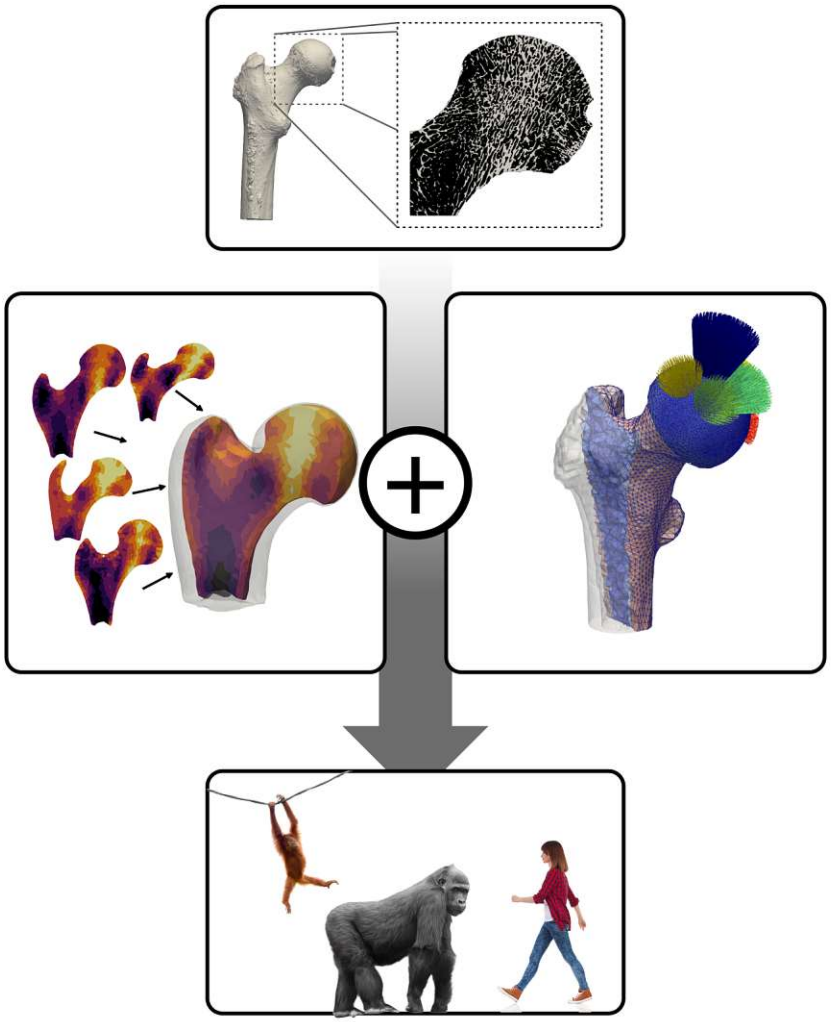

5.1 Conclusions

Within the overarching theme of inferring habitual physical activity from the bone microstructure, the goal of this thesis was to enhance morphometrical and biomechanical tools for bone microstructure analysis. This goal was reached by the fulfilment of two main objectives. The first objective in the branch of morphometric analysis was to enhance the holistic morphometric analysis (HMA) method to allow for quantification of differences between samples, missing in the method so far. The new canonical holistic morphometric analysis (cHMA) method extends HMA with a framework for the creation of a canonical bone using a statistical deformation model (SDM) as well as element-wise statistical analysis between individuals or groups of samples of the resulting morphometric indices, mapped onto finite element (FE) meshes. The second objective in the branch of biomechanical analysis was to speed up the inverse bone remodelling (IBR) method, as it was currently based on computationally expensive micro finite element (μFE) models. This objective was tackled by translating the μFE-based method to homogenised finite element (hFE), to speed up the FE-models and allow for sophisticated boundary conditions using smooth meshes in the future. This translation was performed in a bottom-up approach, by using trabecular bone cubes as the basis for the translation from tissue to continuum-level.

Specifically, the following core results were found for the morphometric analysis using the cHMA method:

- *Statistical deformation model (SDM) can be used to generate canonical bones of different species.* Previously, this method was applied only for single species. In this thesis, it was shown that it is possible to create canonical bone shapes of multiple primate species. The creation of the canonical bone was shown to be robust and converged after a few iterations.

- *The SDM can directly be used on the same μCT images as required for HMA.* Using the same images in the whole workflow simplifies the applicability of the model. The SDM was used only for relatively coarse QCT images before, but μCT images can be used by resampling them in the registration pipeline.

- *The cHMA method allows for the quantification of differences between species.* Known differences, only observed qualitatively so far, were quantified, and new differences could be revealed with this new method on a comparative sample set of primate hand and leg bones.

- *The cHMA method is built as a framework for future adaptations.* The method itself can be adapted and changed in many places and is not limited to the evaluation of morphometric indices. Many more methods require meshes and such methods can directly be intertwined with cHMA.

In the branch of biomechanical analysis and specifically the IBR method, the following core results were found:

- *A bottom-up approach can be used to find the continuum target stimulus for inverse bone remodelling (IBR).* A large set of trabecular bone cubes allowed the parameter identification of the new continuum-level target stimulus, used in the optimisation. While in this thesis only a simple density-dependent criterion was used, other criteria could be developed using the same methodology, extending it for example by the orientation of the bone structure.

- *The hFE-based IBR with a density-dependent continuum-level target stimulus led to good agreement with μFE-based IBR on the distal radius and femoral head.* For both the distal radius sections as well as the femoral head, the predicted loading history was in good agreement compared to the computationally expensive μFE. However, the level of agreement depends on the hFE model complexity and in general, more information in the model led to a better prediction.

- *Inhomogeneous material properties are required in the hFE models to predict the joint loading.* Modelling only the geometry of the bones was not sufficient to predict joint loading, which also shows, that the bone microstructure itself contains a lot of information about the activity, not "stored" in the geometry of the bone.

- *The cortical bone contains important information for the prediction of the loading history.* The predictions get worse, when omitting the cortical bone, either by fully removing it from the model or modelling it with the same homogeneous material properties as trabecular bone. This shows that cortical bone is indeed important to correctly load the trabecular bone in the FEA. However, the cortical bone might be omitted in the optimisation procedure without losing information.

- *The new hFE-based IBR method can be used to predict the loading history of large bones with high computational efficiency.* Previously, the computational requirements for μFE-based IBR were too high to work for larger bones, such as the proximal femur or a full femur. Using the hFE models, such large bone structures can be solved within minutes, even with several unit load cases.

Given these results, both methods offer unique features for the inference of habitual physical activity from the bone microstructure. Questions that could be answered with the aid of these methods are, for example, "*How do different species differ in morphometry throughout the whole bone?*" or "*How does the loading history of complex joints, such as the knee, look like?*". Both methods can not only be used independently, but also in a complementary manner. Morphological analysis can be followed by loading history analysis, to connect biomechanics and morphometry analysis. This connection between the two branches will be the next big leap towards the ultimate goal of a fully holistic biomechanical and morphometrical analysis of bone's microstructure.

5.2 Outlook

Specific tasks for further research on the herein presented methods were already discussed in section 3.3 and section 4.4. To briefly recapitulate them, the cHMA method has to be extended in the registration process to allow for the correct registration of fossils, where the main problem are missing parts of the bone. Furthermore, the mesh morphing process has to be refined to allow for the morphing of FE meshes with low element degradation, in the quest to allow FEA directly on the morphed meshes. This can especially be an issue if bones from different species are used. In the hFE-based IBR, boundary conditions such as contact shall be implemented, with the now available smooth meshes.

There is also the goal to combine both methods into a fully holistic method that is able to use *both* morphometry and biomechanics. There are already many intersection points, for example, both methods require a mesh and the material mapping approach used in hFE is in its core the same than the one used in HMA. A combination of cHMA and hFE-based IBR is indeed possible in many ways. In the simplest case, results of IBR can be mapped from individuals to a canonical bone, which can aid the interpretation of the results. Using the group means from cHMA it is possible to run IBR on the averaged bones of many individuals. Such an analysis could also be used to check whenever the shape or the morphometry is responsible for a seen loading pattern. For example, it would be possible to morph the geometry of the bone over a range of species but keep the morphometry constant [308].

If both methods are used in symbiosis, it would be possible to correlate (bio)mechanical indices with morphometric ones, to answer questions why a certain microstructure is present in the bone or in which load cases (i.e., habitual activity) it is actually used. Such an analysis can be very valuable, for example in the case of the femoral head, where certain patterns of trabecular bone were observed, but would not intuitively fit to the expected peak load directions. Using IBR here could illuminate why the trabecular bone is shaped in a certain way. Another example is the first metacarpal bone, where the cHMA method showed an increased level of trabecular bone in the medullary cavity of *Pan*. Here, the biomechanical purpose of this trabecular bone could be analysed with IBR. Thus, in both cases a combined analysis could answer why bone mass is present in certain but unexpected locations.

List of References

[1] P. Brown, T. Sutikna, M. J. Morwood, R. P. Soejono, Jatmiko, E. W. Saptomo and R. A. Due. 'A new small-bodied hominin from the Late Pleistocene of Flores, Indonesia'. In: *Nature* 431.7012 (2004), pp. 1055–1061. DOI: 10.1038/nature02999.

[2] L. R. Berger, J. Hawks, D. J. de Ruiter, S. E. Churchill, P. Schmid, L. K. Delezene, T. L. Kivell, H. M. Garvin, S. A. Williams, J. M. DeSilva, M. M. Skinner, C. M. Musiba, N. Cameron, T. W. Holliday, W. Harcourt-Smith, R. R. Ackermann, M. Bastir, B. Bogin, D. Bolter, J. Brophy, Z. D. Cofran, K. A. Congdon, A. S. Deane, M. Dembo, M. Drapeau, M. C. Elliott, E. M. Feuerriegel, D. Garcia-Martinez, D. J. Green, A. Gurtov, J. D. Irish, A. Kruger, M. F. Laird, D. Marchi, M. R. Meyer, S. Nalla, E. W. Negash, C. M. Orr, D. Radovcic, L. Schroeder, J. E. Scott, Z. Throckmorton, M. W. Tocheri, C. VanSickle, C. S. Walker, P. Wei and B. Zipfel. 'Homo naledi, a new species of the genus Homo from the Dinaledi Chamber, South Africa'. In: *eLife* 4 (2015). DOI: 10.7554/elife.09560.

[3] R. Grün. 'Direct dating of human fossils'. In: *American Journal of Physical Anthropology* 131.S43 (2006), pp. 2–48. DOI: 10.1002/ajpa.20516.

[4] A. Mounier. 'Anatomy, Evolution of Human'. In: *The International Encyclopedia of Anthropology*. John Wiley & Sons, Ltd, 2018, pp. 1–14. DOI: 10.1002/9781118924396.wbiea1765.

[5] J. Montgomery. 'Passports from the past: Investigating human dispersals using strontium isotope analysis of tooth enamel'. In: *Annals of Human Biology* 37.3 (2010), pp. 325–346. DOI: 10.3109/03014461003649297.

[6] S. Pääbo. 'Ancient DNA'. In: *Scientific American* 269.5 (1993), pp. 86–92.

[7] R. Huiskes. 'If bone is the answer, then what is the question?' In: *Journal of Anatomy* 197.2 (2000), pp. 145–156. DOI: 10.1046/j.1469-7580.2000.19720145.x.

[8] C. B. Ruff and J. A. Runestad. 'Primate Limb Bone Structural Adaptations'. In: *Annual Review of Anthropology* 21.1 (1992), pp. 407–433. DOI: 10.1146/annurev.an.21.100192.002203.

[9] T. L. Kivell. 'A review of trabecular bone functional adaptation: what have we learned from trabecular analyses in extant hominoids and what can we apply to fossils?' In: *Journal of Anatomy* 228.4 (2016), pp. 569–594. DOI: 10.1111/joa.12446.

[10] M. Ito. 'Recent progress in bone imaging for osteoporosis research'. In: *Journal of Bone and Mineral Metabolism* 29.2 (2011), pp. 131–140. DOI: 10.1007/s00774-010-0258-0.

[11] R. Chapurlat. 'In vivo evaluation of bone microstructure in humans: Clinically useful?' In: *BoneKEy Reports* 5 (2016), p. 813. DOI: 10.1038/bonekey.2016.40.

[12] J. A. Steiner, S. J. Ferguson and G. H. van Lenthe. 'Computational analysis of primary implant stability in trabecular bone'. In: *Journal of Biomechanics*. In Memory of Rik Huiskes 48.5 (2015), pp. 807–815. DOI: 10.1016/j.jbiomech.2014.12.008.

[13] S. C. Cowin. *Bone Mechanics Handbook*. Ed. by S. C. Cowin. Second Edition. CRC Press, 2001. DOI: 10.1201/b14263.

[14] R. B. Martin, D. B. Burr, N. A. Sharkey and D. P. Fyhrie. *Skeletal Tissue Mechanics*. 2nd ed. Springer Nature, 2015. DOI: 10.1007/978-1-4939-3002-9.

[15] D. B. Burr and M. R. Allen, eds. *Basic and Applied Bone Biology*. Elsevier, 2019. DOI: 10.1016/c2016-0-03781-6.

[16] S. Bachmann, C. J. Dunmore, M. M. Skinner, D. H. Pahr and A. Synek. 'A computational framework for canonical holistic morphometric analysis of trabecular bone'. In: *Scientific Reports* 12.1 (2022), p. 5187. DOI: 10.1038/s41598-022-09063-6.

[17] S. Bachmann, D. H. Pahr and A. Synek. 'A Density-Dependent Target Stimulus for Inverse Bone (Re)modeling with Homogenized Finite Element Models'. In: *Annals of Biomedical Engineering* (2022). DOI: 10.1007/s10439-022-03104-x.

[18] S. Bachmann, D. H. Pahr and A. Synek. 'Hip joint load prediction using inverse bone remodeling with homogenized FE models: Comparison to micro-FE and influence of material modeling strategy'. In: *Submitted to: Computer Models and Programs in Biomedicine* ().

[19] M. Peacock. 'Calcium Metabolism in Health and Disease'. In: *Clinical Journal of the American Society of Nephrology* 5.Supplement 1 (2010), S23–S30. DOI: 10.2215/cjn.05910809.

[20] A. J. Waldeyer. *Waldeyer Anatomie des Menschen*. Ed. by J. Fanghänel, F. Pera, F. Anderhuber and R. Nitsch. 18th ed. De Gruyter, 2009.

[21] A. Di Luca, C. Van Blitterswijk and L. Moroni. 'The osteochondral interface as a gradient tissue: From development to the fabrication of gradient scaffolds for regenerative medicine'. In: *Birth Defects Research Part C: Embryo Today: Reviews* 105.1 (2015), pp. 34–52. DOI: 10.1002/bdrc.21092.

[22] M. Benjamin, H. Toumi, J. R. Ralphs, G. Bydder, T. M. Best and S. Milz. 'Where tendons and ligaments meet bone: attachment sites ('entheses') in relation to exercise and/or mechanical load'. In: *Journal of Anatomy* 208.4 (2006), pp. 471–490. DOI: 10.1111/j.1469-7580.2006.00540.x.

[23] F. Wang, F. Metzner, G. Osterhoff, L. Zheng and S. Schleifenbaum. 'The role of bone marrow on the mechanical properties of trabecular bone: a systematic review'. In: *BioMedical Engineering OnLine* 21.1 (2022), p. 80. DOI: 10.1186/s12938-022-01051-1.

[24] P. Fratzl and R. Weinkamer. 'Nature's hierarchical materials'. In: *Progress in Materials Science* 52.8 (2007), pp. 1263–1334. DOI: 10.1016/j.pmatsci.2007.06.001.

[25] M.-M. Giraud-Guille. 'Plywood structures in nature'. In: *Current Opinion in Solid State and Materials Science* 3.3 (1998), pp. 221–227. DOI: 10.1016/S1359-0286(98)80094-6.

[26] B. Clarke. 'Normal Bone Anatomy and Physiology'. In: *Clinical Journal of the American Society of Nephrology : CJASN* 3.Suppl 3 (2008), S131–S139. DOI: 10.2215/CJN.04151206.

[27] P. Roschger, E. P. Paschalis, P. Fratzl and K. Klaushofer. 'Bone mineralization density distribution in health and disease'. In: *Bone* 42.3 (2008), pp. 456–466. DOI: 10.1016/j.bone.2007.10.021.

[28] L. J. Smith, J. P. Schirer and N. L. Fazzalari. 'The role of mineral content in determining the micromechanical properties of discrete trabecular bone remodeling packets'. In: *Journal of Biomechanics* 43.16 (2010), pp. 3144–3149. DOI: 10.1016/j.jbiomech.2010.07.038.

[29] B. Ji and H. Gao. 'Mechanical properties of nanostructure of biological materials'. In: *Journal of the Mechanics and Physics of Solids* 52.9 (2004), pp. 1963–1990. DOI: 10.1016/j.jmps.2004.03.006.

[30] N. Reznikov, M. Bilton, L. Lari, M. M. Stevens and R. Kröger. 'Fractal-like hierarchical organization of bone begins at the nanoscale'. In: *Science* 360.6388 (2018), eaao2189. DOI: 10.1126/science.aao2189.

[31] J.-Y. Rho, L. Kuhn-Spearing and P. Zioupos. 'Mechanical properties and the hierarchical structure of bone'. In: *Medical Engineering & Physics* 20.2 (1998), pp. 92–102. DOI: 10.1016/s1350-4533(98)00007-1.

[32] S. Weiner and H. D. Wagner. 'THE MATERIAL BONE: Structure-Mechanical Function Relations'. In: *Annual Review of Materials Science* 28.1 (1998), pp. 271–298. DOI: 10.1146/annurev.matsci.28.1.271.

[33] J. D. Currey. 'The structure and mechanics of bone'. In: *Journal of Materials Science* 47.1 (2011), pp. 41–54. DOI: 10.1007/s10853-011-5914-9.

[34] B. van Rietbergen and R. Huiskes. 'Elastic Constants of Cancellous Bone'. In: *Bone Mechanics Handbook*. Ed. by C. C. Cowin. 2nd. Bone Mechanics Handbook. CRC Press LLC, 2001. Chap. 15.

[35] P. Milovanovic, Z. Vukovic, D. Antonijevic, D. Djonic, V. Zivkovic, S. Nikolic and M. Djuric. 'Porotic paradox: distribution of cortical bone pore sizes at nano- and micro-levels in healthy vs. fragile human bone'. In: *Journal of Materials Science: Materials in Medicine* 28.5 (2017). DOI: 10.1007/s10856-017-5878-7.

[36] J. Nilsson and A. Thorstensson. 'Ground reaction forces at different speeds of human walking and running'. In: *Acta Physiologica Scandinavica* 136.2 (1989), pp. 217–227. DOI: 10.1111/j.1748-1716.1989.tb08655.x.

[37] G. Bergmann, A. Bender, J. Dymke, G. Duda and P. Damm. 'Standardized Loads Acting in Hip Implants'. In: *PLOS ONE* 11.5 (2016). Ed. by M. A. Pérez, e0155612. DOI: 10.1371/journal.pone.0155612.

[38] Z. Seref-Ferlengez, O. D. Kennedy and M. B. Schaffler. 'Bone microdamage, remodeling and bone fragility: how much damage is too much damage?' In: *BoneKEy Reports* 4 (2015), p. 644. DOI: 10.1038/bonekey.2015.11.

[39] S. Goldring. 'The osteocyte: Key player in regulating bone turnover'. In: *RMD Open* 1 (2015). DOI: 10.1136/rmdopen-2015-000049.

[40] E. Seeman. 'Bone Modeling and Remodeling'. In: *Critical Reviews in Eukaryotic Gene Expression* 19.3 (2009), pp. 219–233. DOI: 10.1615/critreveukargeneexpr.v19.i3.40.

[41] E. F. Eriksen, H. J. G. Gundersen, F. Melsen and L. Mosekilde. 'Reconstruction of the formative site in iliac trabecular bone in 20 normal individuals employing a kinetic model for matrix and mineral apposition'. In: *Metabolic Bone Disease and Related Research* 5.5 (1984), pp. 243–252. DOI: 10.1016/0221-8747(84)90066-3.

[42] L. Wang, X. You, L. Zhang, C. Zhang and W. Zou. 'Mechanical regulation of bone remodeling'. In: *Bone Research* 10.1 (2022). DOI: 10.1038/s41413-022-00190-4.

[43] Y. Uda, E. Azab, N. Sun, C. Shi and P. D. Pajevic. 'Osteocyte Mechanobiology'. In: *Current Osteoporosis Reports* 15.4 (2017), pp. 318–325. DOI: 10.1007/s11914-017-0373-0.

[44] M. M. Barak. 'Bone modeling or bone remodeling: That is the question'. In: *American Journal of Physical Anthropology* (2019). DOI: 10.1002/ajpa.23966.

[45] A. Roschger, W. Wagermaier, S. Gamsjaeger, N. Hassler, I. Schmidt, S. Blouin, A. Berzlanovich, G. M. Gruber, R. Weinkamer, P. Roschger, E. P. Paschalis, K. Klaushofer and P. Fratzl. 'Newly formed and remodeled human bone exhibits differences in the mineralization process'. In: *Acta Biomaterialia* (2020). DOI: 10.1016/j.actbio.2020.01.004.

[46] J. C. Crockett, M. J. Rogers, F. P. Coxon, L. J. Hocking and M. H. Helfrich. 'Bone remodelling at a glance'. In: *Journal of Cell Science* 124.7 (2011), pp. 991–998. DOI: 10.1242/jcs.063032.

[47] D. Grimm, J. Grosse, M. Wehland, V. Mann, J. E. Reseland, A. Sundaresan and T. J. Corydon. 'The impact of microgravity on bone in humans'. In: *Bone* 87 (2016), pp. 44–56. DOI: 10.1016/j.bone.2015.12.057.

[48] P. D. Chilibeck, D. G. Sale and C. E. Webber. 'Exercise and Bone Mineral Density'. In: *Sports Medicine* 19.2 (1995), pp. 103–122. DOI: 10.2165/00007256-199519020-00003.

[49] H. M. Frost. 'Bone "mass" and the "mechanostat": a proposal'. In: *The Anatomical Record* 219.1 (1987), pp. 1–9. DOI: 10.1002/ar.1092190104.

[50] H. M. Frost. 'Bone's mechanostat: A 2003 update'. In: *The Anatomical Record* 275A.2 (2003), pp. 1081–1101. DOI: 10.1002/ar.a.10119.

[51] P. Christen, K. Ito, R. Ellouz, S. Boutroy, E. Sornay-Rendu, R. D. Chapurlat and B. van Rietbergen. 'Bone remodelling in humans is load-driven but not lazy'. In: *Nature Communications* 5 (2014), p. 4855. DOI: 10.1038/ncomms5855.

[52] R. Ruimerman, B. van Rietbergen, P. Hilbers and R. Huiskes. 'The Effects of Trabecular-Bone Loading Variables on the Surface Signaling Potential for Bone Remodeling and Adaptation'. In: *Annals of Biomedical Engineering* 33.1 (2005), pp. 71–78. DOI: 10.1007/s10439-005-8964-9.

[53] A. Birkhold, H. Razi, R. Weinkamer, G. Duda, S. Checa and B. Willie. 'Monitoring in vivo (re)modeling: A computational approach using 4D microCT data to quantify bone surface movements'. In: *Bone* 75 (2015), pp. 210–221. DOI: 10.1016/j.bone.2015.02.027.

[54] F. Schulte, D. Ruffoni, F. Lambers, D. Christen, D. Webster, G. Kuhn and R. Müller. 'Local Mechanical Stimuli Regulate Bone Formation and Resorption in Mice at the Tissue Level'. In: *PloS one* 8 (2013), e62172. DOI: 10.1371/journal.pone.0062172.

[55] A. C. Scheuren, P. Vallaster, G. A. Kuhn, G. R. Paul, A. Malhotra, Y. Kameo and R. Müller. 'Mechano-Regulation of Trabecular Bone Adaptation Is Controlled by the Local in vivo Environment and Logarithmically Dependent on Loading Frequency'. In: *Frontiers in Bioengineering and Biotechnology* 8 (2020). DOI: 10.3389/fbioe.2020.566346.

[56] L. Lanyon. 'Functional strain in bone tissue as an objective, and controlling stimulus for adaptive bone remodelling'. In: *Journal of Biomechanics* 20.11-12 (1987), pp. 1083–1093. DOI: 10.1016/0021-9290(87)90026-1.

[57] T. Frisch, M. S. Sørensen, S. Overgaard, M. Lind and P. Bretlau. 'Volume-Referent Bone Turnover Estimated From the Interlabel Area Fraction After Sequential Labeling'. In: *Bone* 22.6 (1998), pp. 677–682. DOI: 10.1016/S8756-3282(98)00050-7.

[58] M. Brotto and L. Bonewald. 'Bone and muscle: Interactions beyond mechanical'. In: *Bone* 80 (2015), pp. 109–114. DOI: 10.1016/j.bone.2015.02.010.

[59] A. G. Turner, P. H. Anderson and H. A. Morris. 'Vitamin D and bone health'. In: *Scandinavian Journal of Clinical and Laboratory Investigation* 72.sup243 (2012), pp. 65–72. DOI: 10.3109/00365513.2012.681963.

[60] P. J. Tebben, R. J. Singh and R. Kumar. 'Vitamin D-Mediated Hypercalcemia: Mechanisms, Diagnosis, and Treatment'. In: *Endocrine Reviews* 37.5 (2016), pp. 521–547. DOI: 10.1210/er.2016-1070.

[61] P. Kaur, S. K. Mishra and A. Mithal. 'Vitamin D toxicity resulting from overzealous correction of vitamin D deficiency'. In: *Clinical Endocrinology* 83.3 (2015), pp. 327–331. DOI: 10.1111/cen.12836.

[62] G. H. von Meyer. 'Die Architektur der Spongiosa'. In: *Archisfur Anatomie, Physiologie und wissenschaftliche Medizin, Reichert und DuBois-Reymonds Archiv* 34 (1867), pp. 615–628.

[63] J. Wolff. 'Das Gesetz der Transformation der Knochen'. In: *Verlag von August Hirschwald* (1892).

[64] S. C. Cowin. 'The False Premise in Wolff's Law'. In: *Bone Mechanics Handbook, Second Edition*. Ed. by S. C. Cowin. CRC Press LLC, 2001. Chap. 30, pp. 30-1 –30-15.

[65] W. Roux. 'Anpassungslehre, Histomechanik und Histochemie'. In: *Virchows Archiv für Pathologische Anatomie und Physiologie und für Klinische Medizin* 209.2 (1912), pp. 168–209. DOI: 10.1007/bf01991758.

[66] R. Kerr, D. Resnick, D. J. Sartoris, S. Kursunoglu, C. Pineda, P. Haghighi, G. Greenway and J. Guerra. 'Computerized tomography of proximal femoral trabecular patterns'. In: *Journal of Orthopaedic Research* 4.1 (1986), pp. 45–56. DOI: 10.1002/jor.1100040106.

[67] P. Pivonka, A. Park and M. R. Forwood. 'Functional Adaptation of Bone: The Mechanostat and Beyond'. In: *Multiscale Mechanobiology of Bone Remodeling and Adaptation*. Springer International Publishing, 2017, pp. 1–60. DOI: 10.1007/978-3-319-58845-2_1.

[68] C. H. Turner. 'Three rules for bone adaptation to mechanical stimuli'. In: *Bone* 23.5 (1998), pp. 399–407. DOI: 10.1016/s8756-3282(98)00118-5.

[69] J. Rittweger. 'Vibration as an exercise modality: how it may work, and what its potential might be'. In: *European Journal of Applied Physiology* 108.5 (2009), pp. 877–904. DOI: 10.1007/s00421-009-1303-3.

[70] A. Synek, C. J. Dunmore, T. L. Kivell, M. M. Skinner and D. H. Pahr. 'Inverse remodelling algorithm identifies habitual manual activities of primates based on metacarpal bone architecture'. In: *Biomechanics and Modeling in Mechanobiology* 18.2 (2018), pp. 399–410. DOI: 10.1007/s10237-018-1091-y.

[71] R. Huiskes. 'Simulation of Self-Organization and Functional Adaptation in Bone'. In: *Hefte zur Zeitschrift Der Unfallchirurg* 261 (1997), pp. 299–320.

[72] C. Ruff, B. Holt and E. Trinkaus. 'Who's afraid of the big bad Wolff?: "Wolff's law" and bone functional adaptation'. In: *American Journal of Physical Anthropology* 129.4 (2006), pp. 484–498. DOI: 10.1002/ajpa.20371.

[73] Y. Umemura, T. Ishiko, T. Yamauchi, M. Kurono and S. Mashiko. 'Five Jumps per Day Increase Bone Mass and Breaking Force in Rats'. In: *Journal of Bone and Mineral Research* 12.9 (1997), pp. 1480–1485. DOI: 10.1359/jbmr.1997.12.9.1480.

[74] M. M. Barak, D. E. Lieberman and J.-J. Hublin. 'A Wolff in sheep's clothing: Trabecular bone adaptation in response to changes in joint loading orientation'. In: *Bone* 49.6 (2011), pp. 1141–1151. DOI: 10.1016/j.bone.2011.08.020.

[75] I. J. Wallace, J. M. Winchester, A. Su, D. M. Boyer and N. Konow. 'Physical activity alters limb bone structure but not entheseal morphology'. In: *Journal of Human Evolution* 107 (2017), pp. 14–18. DOI: 10.1016/j.jhevol.2017.02.001.

[76] A. M. Parfitt, M. K. Drezner, F. H. Glorieux, J. A. Kanis, H. Malluche, P. J. Meunier, S. M. Ott and R. R. Recker. 'Bone histomorphometry: Standardization of nomenclature, symbols, and units: Report of the asbmr histomorphometry nomenclature committee'. In: *Journal of Bone and Mineral Research* 2.6 (1987), pp. 595–610. DOI: 10.1002/jbmr.5650020617.

[77] D. W. Dempster, J. E. Compston, M. K. Drezner, F. H. Glorieux, J. A. Kanis, H. Malluche, P. J. Meunier, S. M. Ott, R. R. Recker and A. M. Parfitt. 'Standardized nomenclature, symbols, and units for bone histomorphometry: A 2012 update of the report of the ASBMR Histomorphometry Nomenclature Committee'. In: *Journal of Bone and Mineral Research* 28.1 (2012), pp. 2–17. DOI: 10.1002/jbmr.1805.

[78] G. M. Blake and I. Fogelman. 'The role of DXA bone density scans in the diagnosis and treatment of osteoporosis'. In: *Postgraduate Medical Journal* 83.982 (2007), pp. 509–517. DOI: 10.1136/pgmj.2007.057505.

[79] K. Engelke. 'Quantitative Computed Tomography—Current Status and New Developments'. In: *Journal of Clinical Densitometry*. Osteoporosis Fracture Risk Assessment 20.3 (2017), pp. 309–321. DOI: 10.1016/j.jocd.2017.06.017.

[80] C. L. Brunnquell, C. Winsor, H. L. Aaltonen and S. Telfer. 'Sources of error in bone mineral density estimates from quantitative CT'. In: *European Journal of Radiology* 144 (2021), p. 110001. DOI: 10.1016/j.ejrad.2021.110001.

[81] I. Guha, B. Klintström, E. Klintström, X. Zhang, Ö. Smedby, R. Moreno and P. K. Saha. 'A comparative study of trabecular bone micro-structural measurements using different CT modalities'. In: *Physics in Medicine and Biology* 65.23 (2020), p. 235029. DOI: 10.1088/1361-6560/abc367.

[82] A. J. Burghardt, T. M. Link and S. Majumdar. 'High-resolution Computed Tomography for Clinical Imaging of Bone Microarchitecture'. In: *Clinical Orthopaedics and Related Research* 469.8 (2011), pp. 2179–2193. DOI: 10.1007/s11999-010-1766-x.

[83] F. Peyrin. 'Investigation of bone with synchrotron radiation imaging: from micro to nano'. In: *Osteoporosis International* 20.6 (2009), pp. 1057–1063. DOI: 10.1007/s00198-009-0855-8.

[84] S. Ma, O. Boughton, A. Karunaratne, A. Jin, J. Cobb, U. Hansen and R. Abel. 'Synchrotron Imaging Assessment of Bone Quality'. In: *Clinical Reviews in Bone and Mineral Metabolism* 14.3 (2016), pp. 150–160. DOI: 10.1007/s12018-016-9223-3.

[85] K. Raum, Q. Grimal, P. Varga, R. Barkmann, C. C. Glüer and P. Laugier. 'Ultrasound to Assess Bone Quality'. In: *Current Osteoporosis Reports* 12.2 (2014), pp. 154–162. DOI: 10.1007/s11914-014-0205-4.

[86] N. Iita, S. Handa, S. Tomiha and K. Kose. 'Development of a compact MRI system for measuring the trabecular bone microstructure of the finger'. In: *Magnetic Resonance in Medicine* 57.2 (2007), pp. 272–277. DOI: 10.1002/mrm.21130.

[87] P. Roschger, H. S. Gupta, A. Berzlanovich, G. Ittner, D. W. Dempster, P. Fratzl, F. Cosman, M. Parisien, R. Lindsay, J. W. Nieves and K. Klaushofer. 'Constant mineralization density distribution in cancellous human bone'. In: *Bone* 32.3 (2003), pp. 316–323. DOI: 10.1016/s8756-3282(02)00973-0.

[88] Y. Carter, C. D. L. Thomas, J. G. Clement and D. M. L. Cooper. 'Femoral osteocyte lacunar density, volume and morphology in women across the lifespan'. In: *Journal of Structural Biology* 183.3 (2013), pp. 519–526. DOI: 10.1016/j.jsb.2013.07.004.

[89] M. L. Bouxsein, S. K. Boyd, B. A. Christiansen, R. E. Guldberg, K. J. Jepsen and R. Müller. 'Guidelines for assessment of bone microstructure in rodents using micro–computed tomography'. In: *Journal of Bone and Mineral Research* 25.7 (2010), pp. 1468–1486. DOI: 10.1002/jbmr.141.

[90] J. Rogowska. 'Overview and Fundamentals of Medical Image Segmentation'. In: *Handbook of Medical Image Processing and Analysis*. Elsevier, 1999, pp. 73–90. DOI: 10.1016/b978-012373904-9.50013-1.

[91] D. Laidlaw, G. E. Marai, K. W. Fleischer and A. H. Barr. 'Partial Volume Segmentation and Boundary Distance Estimation with Voxel Histograms'. In: *Handbook of Medical Image Processing and Analysis*. Elsevier, 2009, pp. 223–243. DOI: 10.1016/b978-012373904-9.50021-0.

[92] S. Tassani, C. Öhman, F. Baruffaldi, M. Baleani and M. Viceconti. 'Volume to density relation in adult human bone tissue'. In: *Journal of Biomechanics* 44.1 (2011), pp. 103–108. DOI: 10.1016/j.jbiomech.2010.08.032.

[93] R. B. Martin, D. B. Burr, N. A. Sharkey and D. P. Fyhrie. 'Mechanical Properties of Bone'. In: *Skeletal Tissue Mechanics*. Springer New York, 2015, pp. 355–422. DOI: 10.1007/978-1-4939-3002-9_7.

[94] T. P. Harrigan and R. W. Mann. 'Characterization of microstructural anisotropy in orthotropic materials using a second rank tensor'. In: *Journal of Materials Science* 19.3 (1984), pp. 761–767. DOI: 10.1007/bf00540446.

[95] L. Steiner, A. Synek and D. H. Pahr. 'Comparison of different microCT-based morphology assessment tools using human trabecular bone'. In: *Bone Reports* (2020), p. 100261. DOI: 10.1016/j.bonr.2020.100261.

[96] M. Stauber and R. Müller. 'Volumetric spatial decomposition of trabecular bone into rods and plates - A new method for local bone morphometry'. In: *Bone* 38.4 (2006), pp. 475–484. DOI: 10.1016/j.bone.2005.09.019.

[97] N. Reznikov, H. Chase, Y. Ben Zvi, V. Tarle, M. Singer, V. Brumfeld, R. Shahar and S. Weiner. 'Inter-trabecular angle: A parameter of trabecular bone architecture in the human proximal femur that reveals underlying topological motifs'. In: *Acta Biomaterialia* 44 (2016), pp. 65–72. DOI: 10.1016/j.actbio.2016.08.040.

[98] A. Mondal, C. Nguyen, X. Ma, A. E. Elbanna and J. M. Carlson. 'Network models for characterization of trabecular bone'. In: *Physical Review E* 99.4 (2019), p. 042406. DOI: 10.1103/physreve.99.042406.

[99] S. J. P. Callens, D. C. Tourolle né Betts, R. Müller and A. A. Zadpoor. 'The local and global geometry of trabecular bone'. In: *Acta Biomaterialia* (2021). DOI: 10.1016/j.actbio.2021.06.013.

[100] G. Maquer, S. N. Musy, J. Wandel, T. Gross and P. K. Zysset. 'Bone Volume Fraction and Fabric Anisotropy Are Better Determinants of Trabecular Bone Stiffness Than Other Morphological Variables'. In: *Journal of Bone and Mineral Research* 30.6 (2015), pp. 1000–1008. DOI: 10.1002/jbmr.2437.

[101] A. J. Burghardt, H. R. Buie, A. Laib, S. Majumdar and S. K. Boyd. 'Reproducibility of direct quantitative measures of cortical bone microarchitecture of the distal radius and tibia by HR-pQCT'. In: *Bone* 47.3 (2010), pp. 519–528. DOI: 10.1016/j.bone.2010.05.034.

[102] M. Vafaeefar, K. M. Moerman, M. Kavousi and T. J. Vaughan. 'A morphological, topological and mechanical investigation of gyroid, spinodoid and dual-lattice algorithms as structural models of trabecular bone'. In: *Journal of the Mechanical Behavior of Biomedical Materials* 138 (2023), p. 105584. DOI: 10.1016/j.jmbbm.2022.105584.

[103] Z. J. Tsegai, T. L. Kivell, T. Gross, N. H. Nguyen, D. H. Pahr, J. B. Smaers and M. M. Skinner. 'Trabecular Bone Structure Correlates with Hand Posture and Use in Hominoids'. In: *PLoS ONE* 8.11 (2013). Ed. by L. Bondioli, e78781. DOI: 10.1371/journal.pone.0078781.

[104] T. Gross, T. L. Kivell, M. M. Skinner, N. Nguyen and D. H. Pahr. 'A CT-image-based framework for the holistic analysis of cortical and trabecular bone morphology'. In: *Palaeontologia Electronica* (2014). DOI: 10.26879/438.

[105] T. L. Kivell, M. M. Skinner, R. Lazenby and J.-J. Hublin. 'Methodological considerations for analyzing trabecular architecture: an example from the primate hand'. In: *Journal of Anatomy* 218.2 (2011), pp. 209–225. DOI: 10.1111/j.1469-7580.2010.01314.x.

[106] F. L. Bookstein. *Morphometric Tools for Landmark Data*. Cambridge University Press, 1992. DOI: 10.1017/cbo9780511573064.

[107] M. Ryan, L. Barnett, J. Rochester, J. M. Wilkinson and E. Dall'Ara. 'A new approach to comprehensively evaluate the morphological properties of the human femoral head: example of application to osteoarthritic joint'. In: *Scientific Reports* 10.1 (2020), p. 5538. DOI: 10.1038/s41598-020-62614-7.

[108] M. Viceconti, A. Henney and E. Morley-Fletcher. 'In silico clinical trials: how computer simulation will transform the biomedical industry'. In: *International Journal of Clinical Trials* 3.2 (2016), p. 37. DOI: 10.18203/2349-3259.ijct20161408.

[109] F. Pauwels. *Biomechanics of the Locomotor Apparatus*. Springer, 1980. 532 pp.

[110] Y. Kameo and T. Adachi. 'Interstitial fluid flow in canaliculi as a mechanical stimulus for cancellous bone remodeling: in silico validation'. In: *Biomechanics and Modeling in Mechanobiology* 13.4 (2013), pp. 851–860. DOI: 10.1007/s10237-013-0539-3.

[111] A. K. Nair, A. Gautieri, S.-W. Chang and M. J. Buehler. 'Molecular mechanics of mineralized collagen fibrils in bone'. In: *Nature Communications* 4.1 (2013), p. 1724. DOI: 10.1038/ncomms2720.

[112] H. M. Shaw and M. Benjamin. 'Structure–function relationships of entheses in relation to mechanical load and exercise'. In: *Scandinavian Journal of Medicine & Science in Sports* 17.4 (2007), pp. 303–315. DOI: 10.1111/j.1600-0838.2007.00689.x.

[113] G. Bergmann, F. Graichen, A. Rohlmann, A. Bender, B. Heinlein, G. N. Duda, M. O. Heller and M. M. Morlock. 'Realistic loads for testing hip implants'. In: *Bio-Medical Materials and Engineering* 20.2 (2010), pp. 65–75. DOI: 10.3233/BME-2010-0616.

[114] R. A. Nazer, J. Lanovaz, C. Kawalilak, J. D. Johnston and S. Kontulainen. 'Direct in vivo strain measurements in human bone—A systematic literature review'. In: *Journal of Biomechanics* 45.1 (2012), pp. 27–40. DOI: 10.1016/j.jbiomech.2011.08.004.

[115] B. C. Fleming and B. D. Beynnon. 'In Vivo Measurement of Ligament/Tendon Strains and Forces: A Review'. In: *Annals of Biomedical Engineering* 32.3 (2004), pp. 318–328. DOI: 10.1023/B:ABME.0000017542.75080.86.

[116] A. Erdemir, S. McLean, W. Herzog and A. van den Bogert. 'Model-based estimation of muscle forces exerted during movements'. In: *Clinical Biomechanics* 22.2 (2007), pp. 131–154. DOI: 10.1016/j.clinbiomech.2006.09.005.

[117] J. H. McElhaney. 'Dynamic response of bone and muscle tissue'. In: *Journal of Applied Physiology* 21.4 (1966), pp. 1231–1236. DOI: 10.1152/jappl.1966.21.4.1231.

[118] K. Choi, J. L. Kuhn, M. J. Ciarelli and S. A. Goldstein. 'The elastic moduli of human subchondral, trabecular, and cortical bone tissue and the size-dependency of cortical bone modulus'. In: *Journal of Biomechanics* 23.11 (1990), pp. 1103–1113. DOI: 10.1016/0021-9290(90)90003-L.

[119] E. X. Guo. 'Mechanical Properties of Cortical Bone and Cancellous Bone Tissue'. In: *Bone Mechanics Handbook*. Ed. by S. C. Cowin. CRC Press, 2001. Chap. 10.

[120] R. B. Martin and D. L. Boardman. 'The effects of collagen fiber orientation, porosity, density, and mineralization on bovine cortical bone bending properties'. In: *Journal of Biomechanics* 26.9 (1993), pp. 1047–1054. DOI: 10.1016/s0021-9290(05)80004-1.

[121] B. van Rietbergen, H. Weinans, R. Huiskes and A. Odgaard. 'A new method to determine trabecular bone elastic properties and loading using micromechanical finite-element models'. In: *Journal of Biomechanics* 28.1 (1995), pp. 69–81. DOI: 10.1016/0021-9290(95)80008-5.

[122] B. van Rietbergen, J. Kabel, A. Odgaard and R. Huiskes. 'Determination of Trabecular Bone Tissue Elastic Properties by Comparison of Experimental and Finite Element Results'. In: *Material Identification Using Mixed Numerical Experimental Methods*. Ed. by H. Sol and C. W. J. Oomens. Dordrecht: Springer Netherlands, 1997, pp. 183–192. DOI: 10.1007/978-94-009-1471-1_19.

[123] A. J. Ladd, J. H. Kinney, D. L. Haupt and S. A. Goldstein. 'Finite-element modeling of trabecular bone: comparison with mechanical testing and determination of tissue modulus'. In: *Journal of Orthopaedic Research: Official Publication of the Orthopaedic Research Society* 16.5 (1998), pp. 622–628. DOI: 10.1002/jor.1100160516.

[124] J. Kabel, B. van Rietbergen, M. Dalstra, A. Odgaard and R. Huiskes. 'The role of an effective isotropic tissue modulus in the elastic properties of cancellous bone'. In: *Journal of Biomechanics* 32.7 (1999), pp. 673–680. DOI: 10.1016/s0021-9290(99)00045-7.

[125] P. K. Zysset. 'Indentation of bone tissue: a short review'. In: *Osteoporosis International* 20.6 (2009), pp. 1049–1055. DOI: 10.1007/s00198-009-0854-9.

[126] Y. Chevalier, D. Pahr, H. Allmer, M. Charlebois and P. Zysset. 'Validation of a voxel-based FE method for prediction of the uniaxial apparent modulus of human trabecular bone using macroscopic mechanical tests and nanoindentation'. In: *Journal of Biomechanics* 40.15 (2007), pp. 3333–3340. DOI: 10.1016/j.jbiomech.2007.05.004.

[127] C. J. Collins, O. G. Andriotis, V. Nedelkovski, M. Frank, O. L. Katsamenis and P. J. Thurner. 'Bone Micro- and Nanomechanics'. In: *Encyclopedia of Biomedical Engineering*. Elsevier, 2019, pp. 22–44. DOI: 10.1016/b978-0-12-801238-3.99937-9.

[128] M. Frank, A. G. Reisinger, D. H. Pahr and P. J. Thurner. 'Effects of Osteoporosis on Bone Morphometry and Material Properties of Individual Human Trabeculae in the Femoral Head'. In: *JBMR Plus* 5.6 (2021), e10503. DOI: 10.1002/jbm4.10503.

[129] D. Wu, P. Isaksson, S. J. Ferguson and C. Persson. 'Young's modulus of trabecular bone at the tissue level: A review'. In: *Acta Biomaterialia* 78 (2018), pp. 1–12. DOI: 10.1016/j.actbio.2018.08.001.

[130] A. J. Ladd and J. H. Kinney. 'Numerical errors and uncertainties in finite-element modeling of trabecular bone'. In: *Journal of Biomechanics* 31.10 (1998), pp. 941–945. DOI: 10.1016/s0021-9290(98)00108-0.

[131] H. J. Böhm. *A short introduction to basic aspects of continuum micromechanics*. Tech. rep. 206. Institute for Lightweight Design and Structural Biomechanics, TU Wien, 2022. eprint: https://www.ilsb.tuwien.ac.at/links/downloads/ilsbrep206.pdf.

[132] R. Hill. 'Elastic properties of reinforced solids: Some theoretical principles'. In: *Journal of Mechanics Physics of Solids* 11 (1963). ADS Bibcode: 1963JMPSo..11..357H, pp. 357–372. DOI: 10.1016/0022-5096(63)90036-X.

[133] D. H. Pahr and P. K. Zysset. 'Influence of boundary conditions on computed apparent elastic properties of cancellous bone'. In: *Biomechanics and Modeling in Mechanobiology* 7.6 (2007), pp. 463–476. DOI: 10.1007/s10237-007-0109-7.

[134] T. P. Harrigan, M. Jasty, R. W. Mann and W. H. Harris. 'Limitations of the continuum assumption in cancellous bone'. In: *Journal of Biomechanics* 21.4 (1988), pp. 269–275. DOI: 10.1016/0021-9290(88)90257-6.

[135] T. D. Brown and A. B. Ferguson. 'Mechanical Property Distributions in the Cancellous Bone of the Human Proximal Femur'. In: *Acta Orthopaedica Scandinavica* 51.1-6 (1980), pp. 429–437. DOI: 10.3109/17453678008990819.

[136] P. K. Zysset, R. W. Goulet and S. J. Hollister. 'A Global Relationship Between Trabecular Bone Morphology and Homogenized Elastic Properties'. In: *Journal of Biomechanical Engineering* 120.5 (1998), pp. 640–646. DOI: 10.1115/1.2834756.

[137] B. van Rietbergen, A. Odgaard, J. Kabel and R. Huiskes. 'Direct mechanics assessment of elastic symmetries and properties of trabecular bone architecture'. In: *Journal of Biomechanics* 29.12 (1996), pp. 1653–1657. DOI: 10.1016/s0021-9290(96)80021-2.

[138] A. Norris. 'The isotropic material closest to a given anisotropic material'. In: *Journal of Mechanics of Materials and Structures* 1.2 (2006), pp. 223–238. DOI: 10.2140/jomms.2006.1.223.

[139] P. K. Zysset and A. Curnier. 'An alternative model for anisotropic elasticity based on fabric tensors'. In: *Mechanics of Materials* 21.4 (1995), pp. 243–250. DOI: 10.1016/0167-6636(95)00018-6.

[140] M. Wang, D. Dutta, K. Kim and J. C. Brigham. 'A computationally efficient approach for inverse material characterization combining Gappy POD with direct inversion'. In: *Computer Methods in Applied Mechanics and Engineering* 286 (2015), pp. 373–393. DOI: 10.1016/j.cma.2015.01.001.

[141] B. Ebbecke. *Knochenwachstum endlich verständlich*. 2003.

[142] K. J. Fischer, C. R. Jacobs and D. R. Carter. 'Computational method for determination of bone and joint loads using bone density distributions'. In: *Journal of Biomechanics* 28.9 (1995), pp. 1127–1135. DOI: 10.1016/0021-9290(94)00182-4.

[143] G. S. Beaupré, T. E. Orr and D. R. Carter. 'An approach for time-dependent bone modeling and remodeling-theoretical development'. In: *Journal of Orthopaedic Research* 8.5 (1990), pp. 651–661. DOI: 10.1002/jor.1100080506.

[144] P. Christen, B. van Rietbergen, F. M. Lambers, R. Müller and K. Ito. 'Bone morphology allows estimation of loading history in a murine model of bone adaptation'. In: *Biomechanics and Modeling in Mechanobiology* 11.3-4 (2011), pp. 483–492. DOI: 10.1007/s10237-011-0327-x.

[145] G. Campoli, H. Weinans and A. A. Zadpoor. 'Computational load estimation of the femur'. In: *Journal of the Mechanical Behavior of Biomedical Materials* 10 (2012), pp. 108–119. DOI: 10.1016/j.jmbbm.2012.02.011.

[146] A. A. Zadpoor, G. Campoli and H. Weinans. 'Neural network prediction of load from the morphology of trabecular bone'. In: *Applied Mathematical Modelling* 37.7 (2013), pp. 5260–5276. DOI: 10.1016/j.apm.2012.10.049.

[147] N. Garijo, J. Martínez, J. M. García-Aznar and M. A. Pérez. 'Computational evaluation of different numerical tools for the prediction of proximal femur loads from bone morphology'. In: *Computer Methods in Applied Mechanics and Engineering* 268 (2014), pp. 437–450. DOI: 10.1016/j.cma.2013.10.005.

[148] P. J. Bishop, S. A. Hocknull, C. J. Clemente, J. R. Hutchinson, A. A. Farke, B. R. Beck, R. S. Barrett and D. G. Lloyd. 'Cancellous bone and theropod dinosaur locomotion. Part I—an examination of cancellous bone architecture in the hindlimb bones of theropods'. In: *PeerJ* 6 (2018), e5778. DOI: 10.7717/peerj.5778.

[149] P. J. Bishop, S. A. Hocknull, C. J. Clemente, J. R. Hutchinson, R. S. Barrett and D. G. Lloyd. 'Cancellous bone and theropod dinosaur locomotion. Part II—a new approach to inferring posture and locomotor biomechanics in extinct tetrapod vertebrates'. In: *PeerJ* 6 (2018), e5779. DOI: 10.7717/peerj.5779.

[150] P. J. Bishop, S. A. Hocknull, C. J. Clemente, J. R. Hutchinson, A. A. Farke, R. S. Barrett and D. G. Lloyd. 'Cancellous bone and theropod dinosaur locomotion. Part III—Inferring posture and locomotor biomechanics in extinct theropods, and its evolution on the line to birds'. In: *PeerJ* 6 (2018), e5777. DOI: 10.7717/peerj.5777.

[151] M. M. Barak, E. Sherratt and D. E. Lieberman. 'Using principal trabecular orientation to differentiate joint loading orientation in the 3rd metacarpal heads of humans and chimpanzees'. In: *Journal of Human Evolution* 113 (2017), pp. 173–182. DOI: 10.1016/j.jhevol.2017.08.018.

[152] M. Cazenave, A. Oettlé, T. R. Pickering, J. L. Heaton, M. Nakatsukasa, J. Francis Thackeray, J. Hoffman and R. Macchiarelli. 'Trabecular organization of the proximal femur in Paranthropus robustus: Implications for the assessment of its hip joint loading conditions'. In: *Journal of Human Evolution* 153 (2021), p. 102964. DOI: 10.1016/j.jhevol.2021.102964.

[153] M. Walle, F. Marques, N. Ohs, M. Blauth, R. Müller and C. Collins. 'Bone Mechanoregulation Allows Subject-Specific Load Estimation Based on Time-Lapsed Micro-CT and HR-pQCT in Vivo'. In: *Frontiers in Bioengineering and Biotechnology* 9 (2021). DOI: 10.3389/fbioe.2021.677985.

[154] P. Christen, K. Ito, A. A. dos Santos, R. Müller and B. van Rietbergen. 'Validation of a bone loading estimation algorithm for patient-specific bone remodelling simulations'. In: *Journal of Biomechanics* 46.5 (2013), pp. 941–948. DOI: 10.1016/j.jbiomech.2012.12.012.

[155] P. Bhattacharya, D. Betts and G. H. van Lenthe. 'A novel contact interaction formulation for voxel-based micro-finite-element models of bone'. In: *International Journal for Numerical Methods in Engineering* 115.4 (2018), pp. 411–426. DOI: 10.1002/nme.5810.

[156] D. H. Pahr and P. K. Zysset. 'From high-resolution CT data to finite element models: development of an integrated modular framework'. In: *Computer Methods in Biomechanics and Biomedical Engineering* 12.1 (2009), pp. 45–57. DOI: 10.1080/10255840802144105.

[157] D. Carter and W. Hayes. 'The compressive behavior of bone as a two-phase porous structure'. In: *The Journal of Bone & Joint Surgery* 59.7 (1977), pp. 954–962. DOI: 10.2106/00004623-197759070-00021.

[158] L. J. Gibson. 'The mechanical behaviour of cancellous bone'. In: *Journal of Biomechanics* 18.5 (1985), pp. 317–328. DOI: 10.1016/0021-9290(85)90287-8.

[159] R. P. Main, E. L. R. Simons and A. H. Lee. 'Interpreting Mechanical Function in Extant and Fossil Long Bones'. In: *Vertebrate Skeletal Histology and Paleohistology*. Ed. by V. de Buffrénil, A. J. de Ricqlès, L. Zylberberg and K. Padian. CRC Press, 2021. Chap. 34, pp. 688–723.

[160] F. Pirnay, M. Bodeux, J. M. Crielaard and P. Franchimont. 'Bone Mineral Content and Physical Activity'. In: *International Journal of Sports Medicine* 08.5 (1987), pp. 331–335. DOI: 10.1055/s-2008-1025679.

[161] T. Sugiyama, J. S. Price and L. E. Lanyon. 'Functional adaptation to mechanical loading in both cortical and cancellous bone is controlled locally and is confined to the loaded bones'. In: *Bone* 46.2 (2010), pp. 314–321. DOI: 10.1016/j.bone.2009.08.054.

[162] R. Rizzoli. 'Nutritional aspects of bone health'. In: *Best Practice and Research: Clinical Endocrinology and Metabolism* 28.6 (2014), pp. 795–808. DOI: 10.1016/j.beem.2014.08.003.

[163] K. Redlich and J. Smolen. 'Inflammatory bone loss: Pathogenesis and therapeutic intervention'. In: *Nature Reviews Drug Discovery* 11.3 (2012), pp. 234–250. DOI: 10.1038/nrd3669.

[164] Y.-C. Hou, C.-L. Lu and K.-C. Lu. 'Mineral bone disorders in chronic kidney disease'. In: *Nephrology* 23 (2018), pp. 88–94. DOI: 10.1111/nep.13457.

[165] R. P. Heaney, S. Abrams, B. Dawson-Hughes, A. Looker, A. Looker, R. Marcus, V. Matkovic and C. Weaver. 'Peak Bone Mass'. In: *Osteoporosis International* 11.12 (2001), pp. 985–1009. DOI: 10.1007/s001980070020.

[166] Q. Wang and E. Seeman. 'Skeletal growth and peak bone strength'. In: *Best Practice and Research: Clinical Endocrinology and Metabolism* 22.5 (2008), pp. 687–700. DOI: 10.1016/j.beem.2008.07.008.

[167] E. Seeman. 'Age- and Menopause-Related Bone Loss Compromise Cortical and Trabecular Microstructure'. In: *The Journals of Gerontology Series A: Biological Sciences and Medical Sciences* 68.10 (2013), pp. 1218–1225. DOI: 10.1093/gerona/glt071.

[168] I. J. Wallace, B. Demes and S. Judex. 'Ontogenetic and Genetic Influences on Bone's Responsiveness to Mechanical Signals'. In: *Building Bones: Bone Formation and Development in Anthropology*. Ed. by C. J. Percival and J. T. Richtsmeier. Cambridge University Press, 2017, pp. 233–253. DOI: 10.1017/9781316388907.011.

[169] R. Rizzoli, J.-P. Bonjour and S. Ferrari. 'Osteoporosis, genetics and hormones'. In: *Journal of Molecular Endocrinology* 26.2 (2001), pp. 79–94. DOI: 10.1677/jme.0.0260079.

[170] B. Javaheri, H. Razi, S. Gohin, S. Wylie, Y.-M. Chang, P. Salmon, P. D. Lee and A. A. Pitsillides. 'Lasting organ-level bone mechanoadaptation is unrelated to local strain'. In: *Science Advances* 6.10 (2020). DOI: 10.1126/sciadv.aax8301.

[171] J. G. Fleagle and D. E. Lieberman. 'Major Transformations in the Evolution of Primate Locomotion'. In: *Great Transformations in Vertebrate Evolution*. Ed. by K. P. Dial, N. Shubin and E. L. Brainerd. Chicago: University of Chicago Press, 2015. Chap. 15, pp. 257–280. DOI: 10.7208/9780226268392-016.

[172] M. P. Muehlenbein. *Basics in Human Evolution*. Elsevier Science & Technology Books, 2015, p. 584.

[173] H. Pontzer, C. Rolian, G. P. Rightmire, T. Jashashvili, M. S. Ponce de León, D. Lordkipanidze and C. P. E. Zollikofer. 'Locomotor anatomy and biomechanics of the Dmanisi hominins'. In: *Journal of Human Evolution* 58.6 (2010), pp. 492–504. DOI: 10.1016/j.jhevol.2010.03.006.

[174] R. L. Susman. 'Comparative and functional morphology of hominoid fingers'. In: *American Journal of Physical Anthropology* 50.2 (1979), pp. 215–236. DOI: 10.1002/ajpa.1330500211.

[175] R. D. Martin. 'Primate Evolution'. In: *Basics in Human Evolution*. Elsevier, 2015, pp. 31–41. DOI: 10.1016/b978-0-12-802652-6.00003-7.

[176] K. J. Fischer, F. Eckstein and C. Becker. 'Density-based Load Estimation Predicts Altered Femoral Load Directions For Coxa Vara And Coxa Valga'. In: *Journal of Musculoskeletal Research* 03.02 (1999), pp. 83–92. DOI: 10.1142/s0218957799000105.

[177] M. A. Bona, L. D. Martin and K. J. Fischer. 'A contact algorithm for density-based load estimation'. In: *Journal of Biomechanics* 39.4 (2006), pp. 636–644. DOI: 10.1016/j.jbiomech.2005.01.006.

[178] P. Christen, K. Ito, F. Galis and B. van Rietbergen. 'Determination of hip-joint loading patterns of living and extinct mammals using an inverse Wolff's law approach'. In: *Biomechanics and Modeling in Mechanobiology* 14.2 (2014), pp. 427–432. DOI: 10.1007/s10237-014-0602-8.

[179] M. J. Willemink, M. Persson, A. Pourmorteza, N. J. Pelc and D. Fleischmann. 'Photon-counting CT: Technical Principles and Clinical Prospects'. In: *Radiology* 289.2 (2018), pp. 293–312. DOI: 10.1148/radiol.2018172656.

[180] K. J. Fischer, C. R. Jacobs, M. E. Levenston, D. D. Cody and D. R. Carter. 'Bone Load Estimation for the Proximal Femur Using Single Energy Quantitative CT Data'. In: *Computer Methods in Biomechanics and Biomedical Engineering* 1.3 (1998), pp. 233–245. DOI: 10.1080/01495739808936704.

[181] K. J. Carlson and S. Judex. 'Increased non-linear locomotion alters diaphyseal bone shape'. In: *Journal of Experimental Biology* 210.17 (2007), pp. 3117–3125. DOI: 10.1242/jeb.006544.

[182] C. D. Byron, A. Herrel, E. Pauwels, A. D. Muynck and B. A. Patel. 'Mouse hallucal metatarsal cross-sectional geometry in a simulated fine branch niche'. In: *Journal of Morphology* 276.7 (2015), pp. 759–765. DOI: 10.1002/jmor.20376.

[183] C. M. Turcotte, K. N. Rabey, D. J. Green and S. C. McFarlin. 'Muscle attachment sites and behavioral reconstruction: An experimental test of muscle-bone structural response to habitual activity'. In: *American Journal of Biological Anthropology* 177.1 (2022), pp. 63–82. DOI: 10.1002/ajpa.24410.

[184] F. A. Karakostis, N. Jeffery and K. Harvati. 'Experimental proof that multivariate patterns among muscle attachments (entheses) can reflect repetitive muscle use'. In: *Scientific Reports* 9.1 (2019), p. 16577. DOI: 10.1038/s41598-019-53021-8.

[185] H. Pontzer, D. E. Lieberman, E. Momin, M. J. Devlin, J. D. Polk, B. Hallgrímsson and D. M. L. Cooper. 'Trabecular bone in the bird knee responds with high sensitivity to changes in load orientation'. In: *Journal of Experimental Biology* 209.1 (2006), pp. 57–65. DOI: 10.1242/jeb.01971.

[186] Z. J. Tsegai, M. M. Skinner, D. H. Pahr, J.-J. Hublin and T. L. Kivell. 'Systemic patterns of trabecular bone across the human and chimpanzee skeleton'. In: *Journal of Anatomy* 232.4 (2018), pp. 641–656. DOI: 10.1111/joa.12776.

[187] A. Colombo, N. Stephens, Z. Tsegai, M. Bettuzzi, M. Morigi, M. Belcastro and J.-J. Hublin. 'Trabecular analysis of the distal radial metaphysis during the acquisition of crawling and bipedal walking in childhood: A preliminary study'. In: *Bulletins et Memoires de la Societe d'Anthropologie de Paris* 31.1-2 (2019), pp. 43–51. DOI: 10.3166/bmsap-2018-0041.

[188] K. Komza and M. Skinner. 'First metatarsal trabecular bone structure in extant hominoids and Swartkrans hominins'. In: *Journal of Human Evolution* 131 (2019), pp. 1–21. DOI: 10.1016/j.jhevol.2019.03.003.

[189] S. Sukhdeo, J. Parsons, X. M. Niu and T. M. Ryan. 'Trabecular Bone Structure in the Distal Femur of Humans, Apes, and Baboons'. In: *The Anatomical Record* 303.1 (2018), pp. 129–149. DOI: 10.1002/ar.24050.

[190] L. J. D. DeMars, N. B. Stephens, J. P. P. Saers, A. Gordon, J. T. Stock and T. M. Ryan. 'Using point clouds to investigate the relationship between trabecular bone phenotype and behavior: An example utilizing the human calcaneus'. In: *American Journal of Human Biology* (2020), e23468. DOI: 10.1002/ajhb.23468.

[191] M. M. Skinner, N. B. Stephens, Z. J. Tsegai, A. C. Foote, N. H. Nguyen, T. Gross, D. H. Pahr, J.-J. Hublin and T. L. Kivell. 'Human-like hand use in Australopithecus africanus'. In: *Science* 347.6220 (2015), pp. 395–399. DOI: 10.1126/science.1261735.

[192] N. B. Stephens, T. L. Kivell, T. Gross, D. H. Pahr, R. A. Lazenby, J.-J. Hublin, I. Hershkovitz and M. M. Skinner. 'Trabecular architecture in the thumb of Pan and Homo : implications for investigating hand use, loading, and hand preference in the fossil record'. In: *American Journal of Physical Anthropology* 161.4 (2016), pp. 603–619. DOI: 10.1002/ajpa.23061.

[193] C. J. Dunmore, A. Bardo, M. M. Skinner and T. L. Kivell. 'Trabecular variation in the first metacarpal and manipulation in hominids'. In: *American Journal of Physical Anthropology* 171.2 (2019), pp. 219–241. DOI: 10.1002/ajpa.23974.

[194] C. J. Dunmore, T. L. Kivell, A. Bardo and M. M. Skinner. 'Metacarpal trabecular bone varies with distinct hand-positions used in hominid locomotion'. In: *Journal of Anatomy* (2019). DOI: 10.1111/joa.12966.

[195] Z. Tsegai, M. Skinner, D. Pahr, J.-J. Hublin and T. Kivell. 'Ontogeny and variability of trabecular bone in the chimpanzee humerus, femur and tibia'. In: *American Journal of Physical Anthropology* 167.4 (2018), pp. 713–736. DOI: 10.1002/ajpa.23696.

[196] L. Georgiou, T. L. Kivell, D. H. Pahr, L. T. Buck and M. M. Skinner. 'Trabecular architecture of the great ape and human femoral head'. In: *Journal of Anatomy* 234.5 (2019), pp. 679–693. DOI: 10.1111/joa.12957.

[197] L. Georgiou, C. J. Dunmore, A. Bardo, L. T. Buck, J.-J. Hublin, D. H. Pahr, D. Stratford, A. Synek, T. L. Kivell and M. M. Skinner. 'Evidence for habitual climbing in a Pleistocene hominin in South Africa'. In: *Proceedings of the National Academy of Sciences* 117.15 (2020), pp. 8416–8423. DOI: 10.1073/pnas.1914481117.

[198] L. Georgiou, T. Kivell, D. Pahr and M. Skinner. 'Trabecular bone patterning in the hominoid distal femur'. In: *PeerJ* 2018.7 (2018). DOI: 10.7717/peerj.5156.

[199] S. Judex and K. J. Carlson. 'Is Bone's Response to Mechanical Signals Dominated by Gravitational Loading?' In: *Medicine & Science in Sports & Exercise* 41.11 (2009), pp. 2037–2043. DOI: 10.1249/mss.0b013e3181a8c6e5.

[200] A. G. Robling. 'Is Bone's Response to Mechanical Signals Dominated by Muscle Forces?' In: *Medicine & Science in Sports & Exercise* 41.11 (2009), pp. 2044–2049. DOI: 10.1249/mss.0b013e3181a8c702.

[201] N. L. Griffin, K. D'Août, T. M. Ryan, B. G. Richmond, R. A. Ketcham and A. Postnov. 'Comparative forefoot trabecular bone architecture in extant hominids'. In: *Journal of Human Evolution* 59.2 (2010), pp. 202–213. DOI: 10.1016/j.jhevol.2010.06.006.

[202] H. Chirchir, A. Zeininger, M. Nakatsukasa, R. A. Ketcham and B. G. Richmond. 'Does trabecular bone structure within the metacarpal heads of primates vary with hand posture?' In: *Comptes Rendus Palevol* 16.5-6 (2017), pp. 533–544. DOI: 10.1016/j.crpv.2016.10.002.

[203] T. L. Mueller, M. Stauber, T. Kohler, F. Eckstein, R. Müller and G. H. van Lenthe. 'Non-invasive bone competence analysis by high-resolution pQCT: An in vitro reproducibility study on structural and mechanical properties at the human radius'. In: *Bone* 44.2 (2009), pp. 364–371. DOI: 10.1016/j.bone.2008.10.045.

[204] M. Sode, A. J. Burghardt, G. J. Kazakia, T. M. Link and S. Majumdar. 'Regional variations of gender-specific and age-related differences in trabecular bone structure of the distal radius and tibia'. In: *Bone* 46.6 (2010), pp. 1652–1660. DOI: 10.1016/j.bone.2010.02.021.

[205] A. Rubinacci, D. Tresoldi, E. Scalco, I. Villa, F. Adorni, G. L. Moro, G. F. Fraschini and G. Rizzo. 'Comparative high-resolution pQCT analysis of femoral neck indicates different bone mass distribution in osteoporosis and osteoarthritis'. In: *Osteoporosis International* 23.7 (2011), pp. 1967–1975. DOI: 10.1007/s00198-011-1795-7.

[206] N. B. Stephens, T. L. Kivell, D. H. Pahr, J.-J. Hublin and M. M. Skinner. 'Trabecular bone patterning across the human hand'. In: *Journal of Human Evolution* 123 (2018), pp. 1–23. DOI: 10.1016/j.jhevol.2018.05.004.

[207] J. Du, K. Brooke-Wavell, M. A. Paggiosi, C. Hartley, J. S. Walsh, V. V. Silberschmidt and S. Li. 'Characterising variability and regional correlations of microstructure and mechanical competence of human tibial trabecular bone: An in-vivo HR-pQCT study'. In: *Bone* 121 (2019), pp. 139–148. DOI: 10.1016/j.bone.2019.01.013.

[208] A. D. Sylvester and C. E. Terhune. 'Trabecular mapping: Leveraging geometric morphometrics for analyses of trabecular structure'. In: *American Journal of Physical Anthropology* 163.3 (2017), pp. 553–569. DOI: 10.1002/ajpa.23231.

[209] P. Gunz and P. Mitteroecker. 'Semilandmarks: a method for quantifying curves and surfaces'. In: *Hystrix, the Italian Journal of Mammalogy* 24 (2013). DOI: 10.4404/hystrix-24.1-6292.

[210] A. Myronenko and X. Song. 'Point Set Registration: Coherent Point Drift'. In: *IEEE Transactions on Pattern Analysis and Machine Intelligence* 32.12 (2010), pp. 2262–2275. DOI: 10.1109/tpami.2010.46.

[211] D. Rueckert, A. F. Frangi and J. A. Schnabel. 'Automatic Construction of 3D Statistical Deformation Models Using Non-rigid Registration'. In: *Medical Image Computing and Computer-Assisted Intervention – MICCAI 2001*. Springer Berlin Heidelberg, 2001, pp. 77–84. DOI: 10.1007/3-540-45468-3_10.

[212] A. Bijar, P.-Y. Rohan, P. Perrier and Y. Payan. 'Atlas-Based Automatic Generation of Subject-Specific Finite Element Tongue Meshes'. In: *Annals of Biomedical Engineering* 44.1 (2016), pp. 16–34. DOI: 10.1007/s10439-015-1497-y.

[213] T. H. Wenckebach, H. Lamecker and H.-C. Hege. 'Capturing Anatomical Shape Variability Using B-Spline Registration'. In: *Information Processing in Medical Imaging*. Ed. by G. E. Christensen and M. Sonka. Lecture Notes in Computer Science. Berlin, Heidelberg: Springer, 2005, pp. 578–590. DOI: 10.1007/11505730_48.

[214] A. H. Gee and G. M. Treece. 'Systematic misregistration and the statistical analysis of surface data'. In: *Medical Image Analysis* 18.2 (2014), pp. 385–393. DOI: 10.1016/j.media.2013.12.007.

[215] D. H. Pahr and P. K. Zysset. 'A comparison of enhanced continuum FE with micro FE models of human vertebral bodies'. In: *Journal of Biomechanics* 42.4 (2009), pp. 455–462. DOI: 10.1016/j.jbiomech.2008.11.028.

[216] H. S. Hosseini, A. Dünki, J. Fabech, M. Stauber, N. Vilayphiou, D. Pahr, M. Pretterklieber, J. Wandel, B. v. Rietbergen and P. K. Zysset. 'Fast estimation of Colles' fracture load of the distal section of the radius by homogenized finite element analysis based on HR-pQCT'. In: *Bone* 97 (2017), pp. 65–75. DOI: 10.1016/j.bone.2017.01.003.

[217] D. Rueckert, A. Frangi and J. Schnabel. 'Automatic construction of 3-D statistical deformation models of the brain using nonrigid registration'. In: *IEEE Transactions on Medical Imaging* 22.8 (2003), pp. 1014–1025. DOI: 10.1109/tmi.2003.815865.

[218] D. Rueckert and P. Aljabar. 'Non-rigid registration using free-form deformations'. In: *Handbook of Biomedical Imaging*. Springer US, 2015, pp. 277–294. DOI: 10.1007/978-0-387-09749-7_15.

[219] L. Steiner, A. Synek and D. H. Pahr. 'Femoral strength can be predicted from 2D projections using a 3D statistical deformation and texture model with finite element analysis'. In: *Medical Engineering & Physics* 93 (2021), pp. 72–82. DOI: 10.1016/j.medengphy.2021.05.012.

[220] F. L. Markley, Y. Cheng, J. L. Crassidis and Y. Oshman. 'Averaging Quaternions'. In: *Journal of Guidance, Control, and Dynamics* 30.4 (2007), pp. 1193–1197. DOI: 10.2514/1.28949.

[221] E. Taghizadeh, M. Reyes, P. Zysset, A. Latypova, A. Terrier and P. Büchler. 'Biomechanical Role of Bone Anisotropy Estimated on Clinical CT Scans by Image Registration'. In: *Annals of Biomedical Engineering* 44.8 (2016), pp. 2505–2517. DOI: 10.1007/s10439-016-1551-4.

[222] C. Zhu, R. H. Byrd, P. Lu and J. Nocedal. 'L-BFGS-B: Fortran subroutines for large-scale bound-constrained optimization'. In: *ACM Transactions on Mathematical Software* 23.4 (1997), pp. 550–560. DOI: 10.1145/279232.279236.

[223] J. R. Shewchuk. 'What Is a Good Linear Element? Interpolation, Conditioning, and Quality Measures'. In: *Eleventh International Meshing Roundtable (Ithaca, New York)*. 2002, pp. 115–126.

[224] T. Nichols and S. Hayasaka. 'Controlling the familywise error rate in functional neuroimaging: a comparative review'. In: *Statistical Methods in Medical Research* 12.5 (2003), pp. 419–446. DOI: 10.1191/0962280203sm341ra.

[225] K. Worsley, M. Andermann, T. Koulis, D. MacDonald and A. Evans. 'Detecting changes in nonisotropic images'. In: *Human Brain Mapping* 8.2-3 (1999), pp. 98–101. DOI: 10.1002/(SICI)1097-0193(1999)8:2/3<98::AID-HBM5>3.0.CO;2-F.

[226] R. J. Adler, K. Bartz, S. C. Kou and A. Monod. *Estimating thresholding levels for random fields via Euler characteristics*. 2017. arXiv: 1704.08562 [math.ST].

[227] A. A. Taha and A. Hanbury. 'Metrics for evaluating 3D medical image segmentation: analysis, selection, and tool'. In: *BMC Medical Imaging* 15.1 (2015), p. 29. DOI: 10.1186/s12880-015-0068-x.

[228] *Patran 2012 Reference Manual Part 3: Finite Element Modeling*. MSC Software. 2012.

[229] B. Wang, G. Mei and N. Xu. 'Method for generating high-quality tetrahedral meshes of geological models by utilizing CGAL'. In: *MethodsX* 7 (2020), p. 101061. DOI: 10.1016/j.mex.2020.101061.

[230] B. C. Lowekamp, D. T. Chen, L. Ibáñez and D. Blezek. 'The Design of SimpleITK'. In: *Frontiers in Neuroinformatics* 7 (2013). DOI: 10.3389/fninf.2013.00045.

[231] The CGAL Project. *CGAL User and Reference Manual*. 4.11. CGAL Editorial Board, 2017.

[232] P. Virtanen, R. Gommers, T. E. Oliphant, M. Haberland, T. Reddy, D. Cournapeau, E. Burovski, P. Peterson, W. Weckesser, J. Bright, S. J. van der Walt, M. Brett, J. Wilson, K. J. Millman, N. Mayorov, A. R. J. Nelson, E. Jones, R. Kern, E. Larson, C. J. Carey, İ. Polat, Y. Feng, E. W. Moore, J. VanderPlas, D. Laxalde, J. Perktold, R. Cimrman, I. Henriksen, E. A. Quintero, C. R. Harris, A. M. Archibald, A. H. Ribeiro, F. Pedregosa, P. van Mulbregt and S. 1. Contributors. 'SciPy 1.0: Fundamental Algorithms for Scientific Computing in Python'. In: *Nature Methods* 17 (2020), pp. 261–272. DOI: 10.1038/s41592-019-0686-2.

[233] E. Taghizadeh, V. Chandran, M. Reyes, P. Zysset and P. Büchler. 'Statistical analysis of the inter-individual variations of the bone shape, volume fraction and fabric and their correlations in the proximal femur'. In: *Bone* 103 (2017), pp. 252–261. DOI: 10.1016/j.bone.2017.07.012.

[234] J. H. Marangalou, K. Ito, F. Taddei and B. van Rietbergen. 'Inter-individual variability of bone density and morphology distribution in the proximal femur and T12 vertebra'. In: *Bone* 60 (2014), pp. 213–220. DOI: 10.1016/j.bone.2013.12.019.

[235] R. H. Tuttle. 'Knuckle-walking and the evolution of hominoid hands'. In: *American Journal of Physical Anthropology* 26.2 (1967), pp. 171–206. DOI: 10.1002/ajpa.1330260207.

[236] D. M. Doran. 'Comparative positional behavior of the African apes'. In: ed. by L. F. Marchant, T. Nishida and W. C. McGrew. Cambridge: Cambridge University Press, 1996, pp. 213–224. DOI: 10.1017/CBO9780511752414.018.

[237] J. G. H. Cant. 'Positional behavior of female bornean orangutans (Pongo pygmaeus)'. In: *American Journal of Primatology* 12.1 (1987), pp. 71–90. DOI: 10.1002/ajp.1350120104.

[238] S. K. Thorpe and R. H. Crompton. 'Orangutan positional behavior and the nature of arboreal locomotion in Hominoidea'. In: *American Journal of Physical Anthropology* 131.3 (2006), pp. 384–401. DOI: 10.1002/ajpa.20422.

[239] J. Cohen. *Statistical power analysis for the behavioral sciences*. L. Erlbaum Associates, 1988.

[240] K. Pearson. 'On lines and planes of closest fit to systems of points in space'. In: *The London, Edinburgh, and Dublin Philosophical Magazine and Journal of Science* 2.11 (1901), pp. 559–572. DOI: 10.1080/14786440109462720.

[241] S. S. Shaukat, T. A. Rao and M. A. Khan. 'Impact of sample size on principal component analysis ordination of an environmental data set: effects on eigenstructure'. In: *Ekológia (Bratislava)* 35.2 (2016), pp. 173–190. DOI: 10.1515/eko-2016-0014.

[242] S. P. Väänänen, L. Grassi, G. Flivik, J. S. Jurvelin and H. Isaksson. 'Generation of 3D shape, density, cortical thickness and finite element mesh of proximal femur from a DXA image'. In: *Medical Image Analysis* 24.1 (2015), pp. 125–134. DOI: 10.1016/j.media.2015.06.001.

[243] W. Yu, M. Tannast and G. Zheng. 'Non-rigid free-form 2D–3D registration using a B-spline-based statistical deformation model'. In: *Pattern Recognition* 63 (2017), pp. 689–699. DOI: 10.1016/j.patcog.2016.09.036.

[244] Y. Choi and S. Lee. 'Injectivity Conditions of 2D and 3D Uniform Cubic B-Spline Functions'. In: *Graphical Models* 62.6 (2000), pp. 411–427. DOI: 10.1006/gmod.2000.0531.

[245] L. Sarringhaus, J. C. Mitani and L. M. MacLatchy. 'The ontogeny of knuckle-walking and dorsal metacarpal ridge prominence in chimpanzees'. In: *American Journal of Biological Anthropology* 178.1 (2022), pp. 29–43. DOI: 10.1002/ajpa.24477.

[246] C. Figus, N. B. Stephens, R. Sorrentino, E. Bortolini, S. Arrighi, F. Lugli, G. Marciani, G. Oxilia, M. Romandini, S. Silvestrini, F. Baruffaldi, M. G. Belcastro, F. Bernardini, I. Erjavec, A. Festa, T. Hajdu, O. Mateovics-László, M. Novak, I. Pap, T. Szeniczey, C. Tuniz, T. M. Ryan and S. Benazzi. 'Human talar ontogeny: Insights from morphological and trabecular changes during postnatal growth'. In: *American Journal of Biological Anthropology* 179.2 (2022), pp. 211–228. DOI: 10.1002/ajpa.24596.

[247] F. Spoor, N. Jeffery and F. Zonneveld. 'Development, Growth and Evolution: Implications for the Study of the Hominid Skeleton'. In: ed. by P. O'Higgins and M. Cohn. 1st ed. Linnean Society Symposium Series. Academic Press, 2000. Chap. Imaging Skeletal Growth and Evolution, pp. 123–162.

[248] E. Le Garff, V. Mesli, E. Marchand, H. Behal, X. Demondion, A. Becart and V. Hedouin. 'Is bone analysis with μCT useful for short postmortem interval estimation?' In: *International Journal of Legal Medicine* 132.1 (2018), pp. 269–277. DOI: 10.1007/s00414-017-1696-1.

[249] P. J. Bishop, C. J. Clemente, S. A. Hocknull, R. S. Barrett and D. G. Lloyd. 'The effects of cracks on the quantification of the cancellous bone fabric tensor in fossil and archaeological specimens: a simulation study'. In: *Journal of Anatomy* 230.3 (2016), pp. 461–470. DOI: 10.1111/joa.12569.

[250] C. Zanolli, B. Schillinger, O. Kullmer, F. Schrenk, J. Kelley, G. E. Rössner and R. Macchiarelli. 'When X-Rays Do Not Work. Characterizing the Internal Structure of Fossil Hominid Dentognathic Remains Using High-Resolution Neutron Microtomographic Imaging'. In: *Frontiers in Ecology and Evolution* 8 (2020). DOI: 10.3389/fevo.2020.00042.

[251] T. L. Kivell, A. S. Deane, M. W. Tocheri, C. M. Orr, P. Schmid, J. Hawks, L. R. Berger and S. E. Churchill. 'The hand of Homo naledi'. In: *Nature Communications* 6.1 (2015), p. 8431. DOI: 10.1038/ncomms9431.

[252] N. Sarkalkan, H. Weinans and A. A. Zadpoor. 'Statistical shape and appearance models of bones'. In: *Bone* 60 (2014), pp. 129–140. DOI: 10.1016/j.bone.2013.12.006.

[253] L. C. Ebert, D. Rahbani, M. Lüthi, M. J. Thali, A. M. Christensen and B. Fliss. 'Reconstruction of full femora from partial bone fragments for anthropological analyses using statistical shape modeling'. In: *Forensic Science International* 332 (2022), p. 111196. DOI: 10.1016/j.forsciint.2022.111196.

[254] L. Steiner, A. Synek and D. H. Pahr. 'Femoral Bone Strength Prediction Using Isotopological B-Spline-Transformed Meshes'. In: *Biomechanics* 2.1 (2022), pp. 125–137. DOI: 10.3390/biomechanics2010012.

[255] I. A. Sigal, M. R. Hardisty and C. M. Whyne. 'Mesh-morphing algorithms for specimen-specific finite element modeling'. In: *Journal of Biomechanics* 41.7 (2008), pp. 1381–1389. DOI: 10.1016/j.jbiomech.2008.02.019.

[256] M. A. Baldwin, J. E. Langenderfer, P. J. Rullkoetter and P. J. Laz. 'Development of subject-specific and statistical shape models of the knee using an efficient segmentation and mesh-morphing approach'. In: *Computer Methods and Programs in Biomedicine* 97.3 (2010), pp. 232–240. DOI: 10.1016/j.cmpb.2009.07.005.

[257] L. Grassi, N. Hraiech, E. Schileo, M. Ansaloni, M. Rochette and M. Viceconti. 'Evaluation of the generality and accuracy of a new mesh morphing procedure for the human femur'. In: *Medical Engineering & Physics* 33.1 (2011), pp. 112–120. DOI: 10.1016/j.medengphy.2010.09.014.

[258] Z. Salo, M. Beek and C. M. Whyne. 'Evaluation of mesh morphing and mapping techniques in patient specific modelling of the human pelvis'. In: *International Journal for Numerical Methods in Biomedical Engineering* 28.8 (2012), pp. 904–913. DOI: 10.1002/cnm.2468.

[259] M. L. Staten, S. J. Owen, S. M. Shontz, A. G. Salinger and T. S. Coffey. 'A Comparison of Mesh Morphing Methods for 3D Shape Optimization'. In: *Proceedings of the 20th International Meshing Roundtable*. Ed. by W. R. Quadros. Berlin, Heidelberg: Springer, 2012, pp. 293–311. DOI: 10.1007/978-3-642-24734-7_16.

[260] S. Poelert, E. Valstar, H. Weinans and A. Zadpoor. 'Patient-specific finite element modeling of bones'. In: *Proceedings of the Institution of Mechanical Engineers, Part H: Journal of Engineering in Medicine* 227.4 (2013), pp. 464–478. DOI: 10.1177/0954411912467884.

[261] P. Pankaj. 'Patient-specific modelling of bone and bone-implant systems: The challenges'. In: *International Journal for Numerical Methods in Biomedical Engineering* 29.2 (2013), pp. 233–249. DOI: 10.1002/cnm.2536.

[262] G. Bergmann, A. Bender, F. Graichen, J. Dymke, A. Rohlmann, A. Trepczynski, M. O. Heller and I. Kutzner. 'Standardized Loads Acting in Knee Implants'. In: *PLOS ONE* 9.1 (2014), e86035. DOI: 10.1371/journal.pone.0086035.

[263] K. J. Fischer, C. R. Jacobs, M. E. Levenston and D. R. Carter. 'Different loads can produce similar bone density distributions'. In: *Bone* 19.2 (1996), pp. 127–135. DOI: 10.1016/8756-3282(96)00140-8.

[264] K. J. Fischer, C. R. Jacobs, M. E. Levenston, D. D. Cody and D. R. Carters. 'Proximal Femoral Density Patterns are Consistent with Bicentric Joint Loads'. In: *Computer Methods in Biomechanics and Biomedical Engineering* 2.4 (1999), pp. 271–283. DOI: 10.1080/10255849908907992.

[265] K. J. Fischer, J. A. Bastidas, H. J. Pfaeffle and J. D. Towers. 'A method for estimating relative bone loads from CT data with application to the radius and the Ulna'. In: *CMES - Computer Modeling in Engineering and Sciences* 4 (2003), pp. 397–403.

[266] M. A. Bona, L. D. Martin and K. J. Fischer. 'Density-based load estimation using two-dimensional finite element models: a parametric study'. In: *Computer Methods in Biomechanics and Biomedical Engineering* 9.4 (2006), pp. 221–229. DOI: 10.1080/10255840600792451.

[267] D. C. Tourolle né Betts, E. Wehrle, G. R. Paul, G. A. Kuhn, P. Christen, S. Hofmann and R. Müller. 'The association between mineralised tissue formation and the mechanical local in vivo environment: Time-lapsed quantification of a mouse defect healing model'. In: *Scientific Reports* 10.1 (2020). DOI: 10.1038/s41598-020-57461-5.

[268] S. D. Badilatti, P. Christen, S. J. Ferguson and R. Müller. 'Computational modeling of long-term effects of prophylactic vertebroplasty on bone adaptation'. In: *Proceedings of the Institution of Mechanical Engineers, Part H: Journal of Engineering in Medicine* 231.5 (2017), pp. 423–431. DOI: 10.1177/0954411916683222.

[269] P. Christen, K. Ito, I. Knippels, R. Müller, G. H. van Lenthe and B. van Rietbergen. 'Subject-specific bone loading estimation in the human distal radius'. In: *Journal of Biomechanics* 46.4 (2013), pp. 759–766. DOI: 10.1016/j.jbiomech.2012.11.016.

[270] W. Pistoia, B. van Rietbergen, E.-M. Lochmüller, C. A. Lill, F. Eckstein and P. Rüegsegger. 'Estimation of distal radius failure load with micro-finite element analysis models based on three-dimensional peripheral quantitative computed tomography images'. In: *Bone* 30.6 (2002), pp. 842–848. DOI: 10.1016/s8756-3282(02)00736-6.

[271] A. Synek and D. H. Pahr. 'Plausibility and parameter sensitivity of micro-finite element-based joint load prediction at the proximal femur'. In: *Biomechanics and Modeling in Mechanobiology* 17.3 (2017), pp. 843–852. DOI: 10.1007/s10237-017-0996-1.

[272] C. Lawson and R. Hanson. 'Solving least squares problems'. In: *Classics in applied mathematics*. Society for Industrial and Applied Mathematics, 1995. DOI: 10.1137/1.9781611971217.

[273] K. Daszkiewicz, G. Maquer and P. K. Zysset. 'The effective elastic properties of human trabecular bone may be approximated using micro-finite element analyses of embedded volume elements'. In: *Biomechanics and Modeling in Mechanobiology* 16.3 (2016), pp. 731–742. DOI: 10.1007/s10237-016-0849-3.

[274] T. Gross, D. H. Pahr and P. K. Zysset. 'Morphology–elasticity relationships using decreasing fabric information of human trabecular bone from three major anatomical locations'. In: *Biomechanics and Modeling in Mechanobiology* 12.4 (2012), pp. 793–800. DOI: 10.1007/s10237-012-0443-2.

[275] J. Panyasantisuk, D. H. Pahr, T. Gross and P. K. Zysset. 'Comparison of Mixed and Kinematic Uniform Boundary Conditions in Homogenized Elasticity of Femoral Trabecular Bone Using Microfinite Element Analyses'. In: *Journal of Biomechanical Engineering* 137.1 (2015). DOI: 10.1115/1.4028968.

[276] C. Flaig and P. Arbenz. 'A scalable memory efficient multigrid solver for micro-finite element analyses based on CT images'. In: *Parallel Computing* 37.12 (2011), pp. 846–854. DOI: 10.1016/j.parco.2011.08.001.

[277] D. Schenk and P. Zysset. 'Personalized loading conditions for homogenized finite element analysis of the distal sections of the radius'. In: *Biomechanics and Modeling in Mechanobiology* (2022). DOI: 10.1007/s10237-022-01656-4.

[278] N. Garijo, N. Verdonschot, K. Engelborghs, J. M. García-Aznar and M. A. Pérez. 'Subject-specific musculoskeletal loading of the tibia: Computational load estimation'. In: *Journal of the Mechanical Behavior of Biomedical Materials* 65 (2017), pp. 334–343. DOI: 10.1016/j.jmbbm.2016.08.026.

[279] K. O. T. Koo, D. M. K. Tan and A. K. S. Chong. 'Distal Radius Fractures: An Epidemiological Review'. In: *Orthopaedic Surgery* 5.3 (2013), pp. 209–213. DOI: 10.1111/os.12045.

[280] L. Engelhardt, F. Niemeyer, P. Christen, R. Müller, K. Stock, M. Blauth, K. Urban, A. Ignatius and U. Simon. 'Simulating Metaphyseal Fracture Healing in the Distal Radius'. In: *Biomechanics* 1.1 (2021), pp. 29–42. DOI: 10.3390/biomechanics1010003.

[281] A. Synek, Y. Chevalier, S. F. Baumbach and D. H. Pahr. 'The influence of bone density and anisotropy in finite element models of distal radius fracture osteosynthesis: Evaluations and comparison to experiments'. In: *Journal of Biomechanics* 48.15 (2015), pp. 4116–4123. DOI: 10.1016/j.jbiomech.2015.10.012.

[282] O. J. Lewis. 'Evolutionary change in the primate wrist and inferior radio-ulnar joints'. In: *The Anatomical Record* 151.3 (1965), pp. 275–285. DOI: 10.1002/ar.1091510309.

[283] O. J. Lewis. 'The hominoid wrist joint'. In: *American Journal of Physical Anthropology* 30.2 (1969), pp. 251–267. DOI: 10.1002/ajpa.1330300211.

[284] M. Ito, K. Tsurusaki and K. Hayashi. 'Peripheral QCT for the diagnosis of osteoporosis'. In: *Osteoporosis International* 7.3 (1997), pp. 120–127.

[285] A. Laib, H. J. Häuselmann and P. Rüegsegger. 'In vivo high resolution 3D-QCT of the human forearm.' In: *Technology and Health Care* 6.5-6 (5-6 1998), pp. 329–337. DOI: 10.3233/thc-1998-65-606.

[286] J. A. MacNeil and S. K. Boyd. 'Bone strength at the distal radius can be estimated from high-resolution peripheral quantitative computed tomography and the finite element method'. In: *Bone* 42.6 (2008), pp. 1203–1213. DOI: 10.1016/j.bone.2008.01.017.

[287] P. Varga, E. Dall'Ara, D. H. Pahr, M. Pretterklieber and P. K. Zysset. 'Validation of an HR-pQCT-based homogenized finite element approach using mechanical testing of ultra-distal radius sections'. In: *Biomechanics and Modeling in Mechanobiology* 10.4 (2010), pp. 431–444. DOI: 10.1007/s10237-010-0245-3.

[288] E. Dall'Ara, D. Pahr, P. Varga, F. Kainberger and P. Zysset. 'QCT-based finite element models predict human vertebral strength in vitro significantly better than simulated DEXA'. In: *Osteoporosis International* 23.2 (2012), pp. 563–572. DOI: 10.1007/s00198-011-1568-3.

[289] A. J. Arias-Moreno, H. S. Hosseini, M. Bevers, K. Ito, P. Zysset and B. van Rietbergen. 'Validation of distal radius failure load predictions by homogenized- and micro-finite element analyses based on second-generation high-resolution peripheral quantitative CT images'. In: *Osteoporosis International* 30.7 (2019), pp. 1433–1443. DOI: 10.1007/s00198-019-04935-6.

[290] L. Berger, D. Pahr and A. Synek. 'Articular contact vs. embedding: Effect of simplified boundary conditions on the stress distribution in the distal radius and volar plate implant loading'. In: *Journal of Biomechanics* 143 (2022), p. 111279. DOI: 10.1016/j.jbiomech.2022.111279.

[291] P. Christen, F. A. Schulte, A. Zwahlen, B. van Rietbergen, S. Boutroy, L. J. Melton, S. Amin, S. Khosla, J. Goldhahn and R. Müller. 'Voxel size dependency, reproducibility and sensitivity of an in vivo bone loading estimation algorithm'. In: *Journal of The Royal Society Interface* 13.114 (2016), p. 20150991. DOI: 10.1098/rsif.2015.0991.

[292] S. B. Chambers, M. E. McGregor, D. Isa, D. G. Langohr, J. A. Johnson and N. Suh. 'Loading at the distal radius and ulna during active simulated dart throw motion'. In: *Journal of Orthopaedics* 22 (2020), pp. 513–519. DOI: 10.1016/j.jor.2020.10.010.

[293] J. M. Smith, F. W. Werner and B. J. Harley. 'Forces in the Distal Radius During a Pushup or Active Wrist Motions'. In: *The Journal of Hand Surgery* 43.9 (2018), pp. 806–811. DOI: 10.1016/j.jhsa.2018.05.020.

[294] M. Stipsitz, P. Zysset and D. Pahr. 'Prediction of the Inelastic Behaviour of Radius Segments: Damage-based Nonlinear Micro Finite Element Simulation vs Pistoia Criterion'. In: *Journal of Biomechanics* 116 (2021). DOI: 10.1016/j.jbiomech.2020.110205.

[295] P. Varga, S. Baumbach, D. Pahr and P. K. Zysset. 'Validation of an anatomy specific finite element model of Colles' fracture'. In: *Journal of Biomechanics* 42.11 (2009), pp. 1726–1731. DOI: 10.1016/j.jbiomech.2009.04.017.

[296] L. I.-K. Lin. 'A Concordance Correlation Coefficient to Evaluate Reproducibility'. In: *Biometrics* 45.1 (1989), p. 255. DOI: 10.2307/2532051.

[297] M. Putnam, N. Meyer, E. Nelson, D. Gesensway and J. Lewis. 'Distal radial metaphyseal forces in an extrinsic grip model: Implications for postfracture rehabilitation'. In: *Journal of Hand Surgery* 25.3 (2000), pp. 469–475. DOI: 10.1053/jhsu.2000.6915.

[298] M. G. Mullender and R. Huiskes. 'Proposal for the regulatory mechanism of Wolffs law'. In: *Journal of Orthopaedic Research* 13.4 (1995), pp. 503–512. DOI: 10.1002/jor.1100130405.

[299] Z. Földhazy, A. Arndt, C. Milgrom, A. Finestone and I. Ekenman. 'Exercise-induced strain and strain rate in the distal radius'. In: *The Journal of Bone and Joint Surgery. British Volume* 87.2 (2005), pp. 261–266. DOI: 10.1302/0301-620x.87b2.14857.

[300] C. M. Court-Brown and B. Caesar. 'Epidemiology of adult fractures: A review'. In: *Injury* 37.8 (2006), pp. 691–697. DOI: 10.1016/j.injury.2006.04.130.

[301] J. A. Kanis. 'Diagnosis of osteoporosis and assessment of fracture risk'. In: *The Lancet* 359.9321 (2002), pp. 1929–1936. DOI: 10.1016/s0140-6736(02)08761-5.

[302] G. Iori, F. Heyer, V. Kilappa, C. Wyers, P. Varga, J. Schneider, M. Gräsel, R. Wendlandt, R. Barkmann, J. P. van den Bergh and K. Raum. 'BMD-based assessment of local porosity in human femoral cortical bone'. In: *Bone* 114 (2018), pp. 50–61. DOI: 10.1016/j.bone.2018.05.028.

[303] C. Geuzaine and J.-F. Remacle. 'Gmsh: A 3-D finite element mesh generator with built-in pre- and post-processing facilities'. In: *International Journal for Numerical Methods in Engineering* 79.11 (2009), pp. 1309–1331. DOI: 10.1002/nme.2579.

[304] B. Luisier, E. Dall'Ara and D. H. Pahr. 'Orthotropic HR-pQCT-based FE models improve strength predictions for stance but not for side-way fall loading compared to isotropic QCT-based FE models of human femurs'. In: *Journal of the Mechanical Behavior of Biomedical Materials* 32 (2014), pp. 287–299. DOI: 10.1016/j.jmbbm.2014.01.006.

[305] P. Yang, T.-Y. Lin, J.-L. Xu, H.-Y. Zeng, D. Chen, B.-L. Xiong, F.-X. Pang, Z.-Q. Chen, W. He, Q.-S. Wei and Q.-W. Zhang. 'Finite element modeling of proximal femur with quantifiable weight-bearing area in standing position'. In: *Journal of Orthopaedic Surgery and Research* 15.1 (2020), p. 384. DOI: 10.1186/s13018-020-01927-9.

[306] L. Cristofolini, M. Juszczyk, S. Martelli, F. Taddei and M. Viceconti. 'In vitro replication of spontaneous fractures of the proximal human femur'. In: *Journal of Biomechanics* 40.13 (2007), pp. 2837–2845. DOI: 10.1016/j.jbiomech.2007.03.015.

[307] M. Cazenave, T. L. Kivell, M. Pina, D. R. Begun and M. M. Skinner. 'Calcar femorale variation in extant and fossil hominids: Implications for identifying bipedal locomotion in fossil hominins'. In: *Journal of Human Evolution* 167 (2022), p. 103183. DOI: 10.1016/j.jhevol.2022.103183.

[308] D. O'Rourke, B. R. Beck, A. T. Harding, S. L. Watson, P. Pivonka and S. Martelli. 'Geometry and bone mineral density determinants of femoral neck strength changes following exercise'. In: *Biomechanics and Modeling in Mechanobiology* (2022). DOI: 10.1007/s10237-022-01642-w.

Image Credits

Chapter Images "Gorilla" by Samokhin Roman - stock.adobe.com
"Human" by Aleksander Kaczmarek - stock.adobe.com
"Orangutan" by Anna Kucherova - stock.adobe.com

Figure 1.1 "Gorilla" by Samokhin Roman - stock.adobe.com
"Human" by Aleksander Kaczmarek - stock.adobe.com
"Orangutan" by Anna Kucherova - stock.adobe.com

Figure 2.1 "Bone unit - Osteon 1" by Laboratoires Servier, CC BY-SA 3.0, via Wikimedia Commons[1]
"Bone unit - Osteon 3" by Laboratoires Servier, CC BY-SA 3.0, via Wikimedia Commons[2]
"Collagen" by Laboratoires Servier, CC BY-SA 3.0, via Wikimedia Commons[3]
"SEM deproteined bone - wistar rat - x10k" by Sbertazzo, CC BY-SA 3.0, via Wikimedia Commons[4] / cropped from original

Figure 2.1 "The Hierarchical Structure of Bone" is licensed under CC BY-SA 3.0 by Sebastian Bachmann

Figure 2.2 "Bone Remodelling" by Armin Kübelbeck, CC0, via Wikimedia Commons[5] / modified

Figure 2.3 "Femur (caput femoris) - bone structure detail (vertical cut) 2" by MAKY.OREL, CC0, via Wikimedia Commons[6] / modified

Figure 2.4 "Scheme human hand bones" by LadyofHats, Public domain, via Wikimedia Commons[7] / modified
"Orangutan" by Anna Kucherova - stock.adobe.com
"Chimpanzee" by JackF - stock.adobe.com

Figure 2.11 "Gorilla" by Samokhin Roman - stock.adobe.com
"Human" by Aleksander Kaczmarek - stock.adobe.com
"Orangutan" by Anna Kucherova - stock.adobe.com
"Chimpanzee" by JackF - stock.adobe.com

[1] https://commons.wikimedia.org/wiki/SMART-Servier_Medical_Art/Bones#/media/File:Bone_unit_-_Osteon_1_---_Smart-Servier.png
[2] https://commons.wikimedia.org/wiki/SMART-Servier_Medical_Art/Bones#/media/File:Bone_unit_-_Osteon_3_---_Smart-Servier.png
[3] https://commons.wikimedia.org/wiki/SMART-Servier_Medical_Art/Bones#/media/File:Collagen_2_---_Smart-Servier.png
[4] https://commons.wikimedia.org/wiki/File:Bertazzo_S_-_SEM_deproteined_bone_-_wistar_rat_-_x10k.tif
[5] https://commons.wikimedia.org/wiki/File:Bone_remodeling_01.svg
[6] https://commons.wikimedia.org/wiki/File:Femur_%28caput_femoris%29_-_bone_structure_detail_%28vertical_cut%29_2.jpg
[7] https://commons.wikimedia.org/wiki/File:Scheme_human_hand_bones-en.svg

“Puzzle pieces” by YummyBuum - stock.adobe.com
“Scientist” by Rudzhan - stock.adobe.com
“DNA simple” by Forluvoft, Public domain, via Wikimedia Commons[8] / cropped from original
“Outils néandertaliens” by Chauvière Françcois-Xavier, CC BY 2.5, via Wikimedia Commons[9] / cropped from original
“*H. naledi* pollical metacarpal (Mc1) morphology” by Kivell *et al.* [251], CC BY 4.0, via Wikimedia Commons[10] / cropped from original

Figure 3.18 “*H. naledi* pollical metacarpal (Mc1) morphology” by Kivell *et al.* [251], CC BY 4.0, via Wikimedia Commons[10] / cropped from original, modified

Detailed descriptions for the Creative Commons licences can be found at:

CC0	https://creativecommons.org/publicdomain/zero/1.0/
CC BY 2.5	https://creativecommons.org/licenses/by/2.5/
CC BY-SA 3.0	https://creativecommons.org/licenses/by-sa/3.0/
CC BY 4.0	https://creativecommons.org/licenses/by/4.0/

[8] https://commons.wikimedia.org/wiki/File:DNA_simple2.svg
[9] https://commons.wikimedia.org/wiki/File:Outils_n%C3%A9andertaliens.tif
[10] https://commons.wikimedia.org/wiki/File:Homo_naledi_pollical_metacarpal_(Mc1)_morphology.jpg